Photoionization Dynamics of Polyatomic Molecules

Thesis submitted to The University of Nottingham for the degree of Doctor of Philosophy

Paul Hockett

21st July 2009

Abstract

The work presented in this thesis was carried out with the ultimate aim of learning about the photoionization dynamics of polyatomic molecules. This is a complex problem; in order to obtain sufficient experimental data to shed light on the dynamics careful measurement of *photoelectron angular distributions* (PADs) is required. Ideally these measurements are *rotationally-resolved*, and the angular distributions measured correspond to the formation of the molecular ion in a single rotational state. The ionization event, in the dipole approximation, can be completely described by the dipole matrix elements. If sufficient experimental data to determine the radial components of the matrix elements and associated phases, the *dynamical parameters*, can be obtained the photoionization experiment may be said to be *complete*. Analysis of such experiments requires that the initial state of the molecular system is also known, to this end *resonance-enhanced multi-photon ionization* (REMPI) schemes can be used in order to populate a single quantum state prior to ionization. The experiments presented here follow this methodology, with various REMPI schemes used to prepare (*pump*) and ionize (*probe*) the molecule under study, and the *velocity-map imaging* (VMI) technique used to (simultaneously) record the photoelectron spectra and angular distributions.

Two molecules have been studied experimentally, acetylene (C_2H_2) and ammonia (NH_3). In both cases dynamical parameters pertaining to the formation of specific states (vibronic or vibrational) of the molecular ion have been determined from experimental data. Additionally, in the ammonia work, rotationally-resolved photoelectron images were obtained.

Acknowledgements

Prof. Katharine Reid has been an excellent PhD supervisor; she has been encouraging, supportive, and motivating over the last few years. Prof. Ivan Powis (co-supervisor) has contributed a wealth of technical knowledge and has always been approachable, and particularly helpful when things go wrong.

The experimental work presented in this thesis on acetylene was undertaken under the guidance of Dr Adrian King. Experimental work on ammonia was carried out with the help of Dr Dave Townsend and Mick Staniforth.

Thanks to everyone in the Reid group, past and present, who have contributed to the infrastructure and knowledge base which it is all too easy to take for granted. Data processing methods and experimental techniques have benefited greatly from the input of Chris Hammond, Mick Staniforth and Dr Julia Davies. The MATLAB image capture code used for the ammonia experiments was also developed by Mick.

Everyone in the Physical Chemistry Department has made the last few years enjoyable and stimulating. Special thanks go to Jay Jeffs and Dr Adrian Boatwright for discussions over tea, and frequent loans of equipment. The assistance of Neil Barnes (departmental technician) has also been invaluable, and the work presented here would not have been possible without his technical expertise and gentle mockery.

This thesis is dedicated to Amy Jane.

Overview

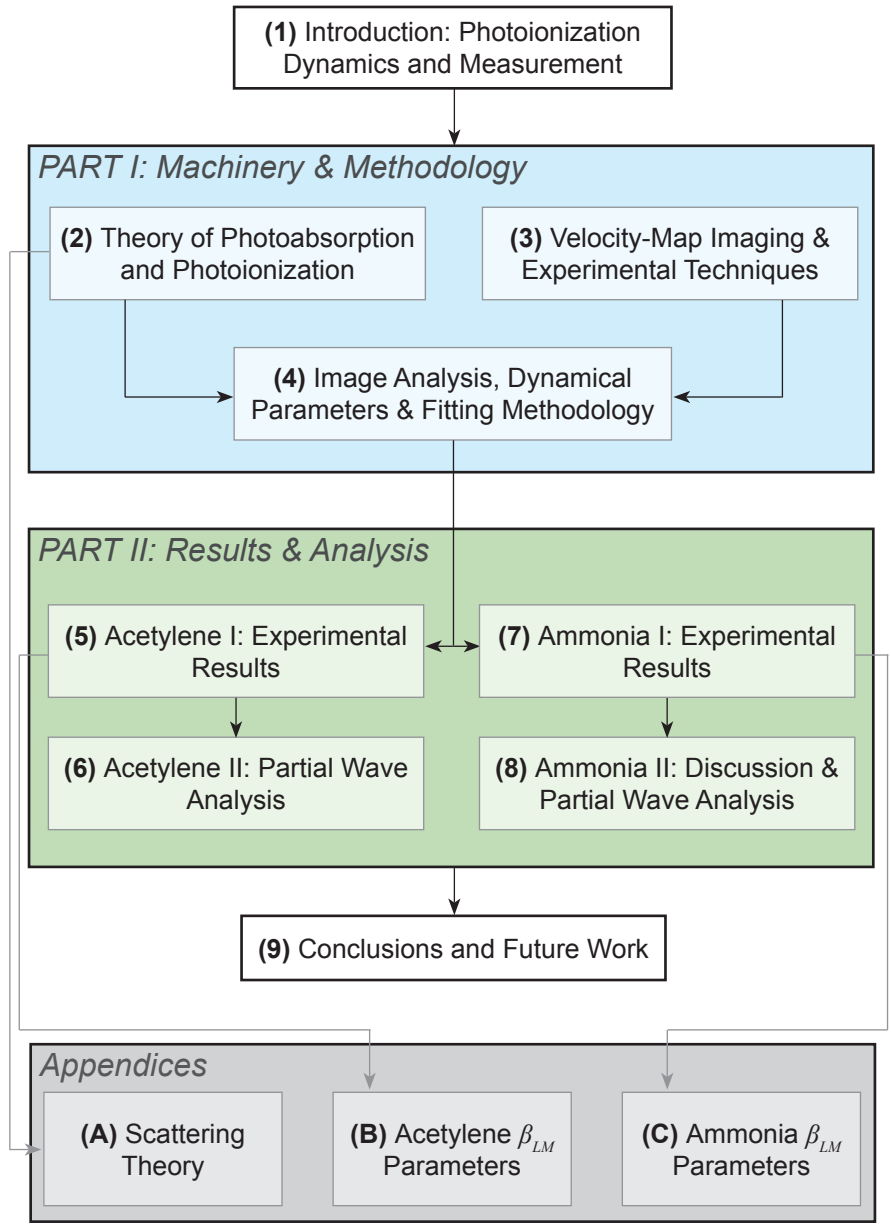
(1) Introduction: Photoionization Dynamics and Measurement
PART I: Machinery & Methodology
(2) Theory of Photoabsorption and Photoionization
(3) Velocity-Map Imaging & Experimental Techniques
(4) Image Analysis, Dynamical Parameters & Fitting Methodology
PART II: Results & Analysis
(5) Acetylene I: Experimental Results
(7) Ammonia I: Experimental Results
(6) Acetylene II: Partial Wave Analysis
(8) Ammonia II: Discussion & Partial Wave Analysis
(9) Conclusions and Future Work
Appendices
(A) Scattering Theory
(B) Acetylene β_{LM} Parameters
(C) Ammonia β_{LM} Parameters

Nomenclature

Quantum Numbers

J	Total angular momentum, inclusive of spin
N	Total angular momentum, exclusive of spin
K	Body-fixed projection of J or N (i.e. molecular frame of reference)
M	Space-fixed projection of J or N (i.e. lab frame of reference)
l	Orbital angular momentum of electron/photoelectron
λ	Body-fixed projection of l (i.e. molecular frame of reference)
m	Space-fixed projection of l (i.e. lab frame of reference)
μ_λ	Body-fixed projection of photon angular momentum

Sub & Super Scripts

The following modify quantum numbers as specified:

g	Ground state
i	Intermediate (excited) state
$+$	Ion
C	Molecular core states
Ryd	Rydberg electron
t	Transfer term

Abbreviations

BASEX	Basis Set Expansion (image inversion method)
CCD	Charge-coupled device
E_{KE}	Electron kinetic energy

FC	Franck-Condon
FWHM	Full-width at Half-maximum
LF	Lab frame
MCP	Microchannel plate
MF	Molecular frame
MQDT	Multi-channel quantum defect theory
MS	Molecular Symmetry
PAD	photoelectron angular distribution
pBASEX	Polar implementation of BASEX
PSD	Position sensitive detector
REMPI	Resonance enhanced multi-photon ionization
RT	Renner-Teller
S:N	Signal:Noise ratio
SE	Schrödinger equation
SEVI	Slow-electron velocity map imaging
Spec1	VMI Spectrometer #1
Spec2	VMI Spectrometer #2
V_r	Repeller plate voltage
V_e	Extractor plate voltage
T_{trans}	Translational temperature
T_{rot}	Rotational temperature
T_{vib}	Vibrational temperature
ToF	Time-of-flight
VMI	Velocity-Map Imaging

Contents

1 Introduction: Photoionization Dynamics and Measurement 11

1.1 Photoionization Dynamics . . . 11
1.2 Angle-Integrated Photoelectron Spectroscopy . . . 12
1.2.1 Magnetic bottle . . . 13
1.2.2 PFI-ZEKE . . . 14
1.3 Angle-Resolved Photoelectron Spectroscopy . . . 17
1.3.1 Field-free time-of-flight . . . 18
1.3.2 Photoelectron imaging . . . 19
1.4 Photoelectron Angular Distributions & Complete Experiments . . . 21
1.4.1 General form of photoelectron angular distributions . . . 21
1.4.2 Atomic photoionization . . . 22
1.4.3 Molecular photoionization - complete experiments . . . 23
1.4.4 Molecular photoionization - PADs as probes . . . 27
1.4.5 A note on theoretical methods . . . 28
1.5 Summary, Aims & Objectives . . . 28

I Machinery & Methodology 30

2 Theory of Photoabsorption and Photoionization 31

2.1 General Framework of Light-Matter Interactions . . . 32
2.1.1 Born-Oppenheimer approximation . . . 32
2.1.2 Frames of reference & angular momenta . . . 32
2.1.3 Dipole interactions & the weak field limit . . . 32
2.2 Photoabsorption . . . 35
2.2.1 Vibronic & rotational line strength factors . . . 35
2.2.2 Calculation of rotational line-strengths . . . 36
2.2.2.1 Symmetric tops . . . 36
2.2.2.2 Asymmetric tops . . . 37
2.2.2.3 Alignment . . . 38
2.2.3 Calculation of rotational energy levels . . . 39
2.3 Photoionization . . . 41
2.3.1 Photoelectron wavefunction . . . 42

2.3.2 Initial and final state wavefunctions . . . 43
2.3.3 Ionization matrix elements . . . 43
2.3.4 Observables . . . 45
2.4 Symmetry Selection Rules . . . 47
2.5 Calculation of PADs . . . 48
2.6 Summary . . . 49

3 Velocity-Map Imaging & Experimental Techniques 50
3.1 The VMI Spectrometer . . . 50
3.1.1 Electrostatic lens . . . 50
3.1.2 Position sensitive detector . . . 53
3.1.3 Supersonic molecular beam . . . 56
3.1.4 Field-free flight region . . . 57
3.2 Photoelectron Velocity & Energy Resolution . . . 57
3.2.1 Native VMI resolution . . . 58
3.2.2 Δv, ΔE and experimental considerations . . . 59
3.2.3 Angular resolution . . . 62
3.2.4 Improving image resolution with data processing . . . 62
3.3 Experimental Techniques . . . 63
3.3.1 Laser systems . . . 63
3.3.2 1-colour and 2-colour experimental set-up . . . 64
3.3.3 Ion images, timing and VMI focusing . . . 66
3.3.4 REMPI scans . . . 67
3.3.5 Photoelectron images . . . 67
3.4 Summary . . . 68

4 Image Analysis, Dynamical Parameters and Fitting Methodology 69
4.1 Image Processing . . . 69
4.1.1 Abel inversion of photoelectron images . . . 70
4.1.2 pBasex inversion of photoelectron images . . . 72
4.1.3 Comparison of Abel & pBasex methods . . . 75
4.1.4 Error analysis . . . 78
4.2 Energy Calibration . . . 79
4.3 Fitting Methodology . . . 81
4.3.1 Energy dependence of $r_{l\lambda}$ and $\eta_{l\lambda}$ . . . 81
4.3.2 Dataset size & statistical analysis . . . 83
4.3.3 Truncation of the partial wave expansion . . . 83
4.3.4 Fitness criteria . . . 84
4.3.5 Error analysis & χ^2 response . . . 85
4.4 Summary . . . 87

II Results & Analysis **88**

5 Acetylene I: Experimental Results **89**

5.1 Introduction . . . 89
5.2 Background . . . 90
5.2.1 Ground state $\tilde{X}^1\Sigma_g^+$ . . . 91
5.2.2 Excited state $\tilde{A}^1A_u$ . . . 92
5.2.3 Ion ground state $\tilde{X}^2\Pi_u$ . . . 92
5.2.3.1 Vibronic structure . . . 92
5.2.3.2 Rotational structure . . . 93
5.3 Experimental Details . . . 93
5.4 REMPI Spectra . . . 94
5.5 Photoelectron Images & Energy Spectra . . . 97
5.6 $V_0^4K_0^1$ Pump Transitions and the $\mathbf{4^1}\,^2\Sigma_u^-$ Vibronic Band . . . 100
5.6.1 Photoelectron spectra . . . 100
5.6.2 Photoelectron angular distributions . . . 100
5.7 $V_0^5K_0^1$ Pump Transitions and $K_+ > 0$ Vibronic Bands . . . 103
5.7.1 PADs . . . 103
5.8 Conclusions . . . 105

6 Acetylene II: Partial Wave Analysis **107**

6.1 Application of Photoionization Theory to C_2H_2 . . . 107
6.1.1 Angular momentum considerations . . . 107
6.1.2 Symmetry considerations . . . 108
6.2 Determination of Dynamical Parameters - $\mathbf{4^1}\,^2\Sigma_u^-$ Vibronic Band . . . 109
6.2.1 Fitting PADs . . . 109
6.2.2 Alignment and rotational-summation . . . 111
6.2.3 Rotational spectra and l=5 contribution . . . 113
6.2.4 Discussion of dynamical parameters . . . 117
6.3 Geometrical and Dynamical Parameters - $K_+ > 0$ Vibronic Bands . . . 118
6.3.1 Geometrical effects of ΔK . . . 119
6.3.2 Fitting PADs . . . 120
6.4 Conclusions . . . 123
6.5 Addendum . . . 123

7 Ammonia I: Experimental Results **125**

7.1 Background . . . 125
7.1.1 Ground state $\widetilde{X}^1A_1'$ . . . 125
7.1.2 $\widetilde{B}^1E''$ state . . . 127
7.1.3 $\widetilde{X}^2A_2''$ cation . . . 128
7.1.4 Rotational selection rules outline . . . 128
7.2 Experimental Details . . . 130
7.3 Preliminary 1-colour work . . . 131

7.3.1 REMPI spectra . . . 131
7.3.2 Photoelectron images & vibrational spectra . . . 133
7.3.3 Photoelectron angular distributions . . . 135
7.4 2-colour Photoelectron Images & Rotational Resolution . . . 137
7.4.1 Slow-electron VMI . . . 137
7.4.2 Probe wavelength & energy resolution . . . 139
7.4.3 2-colour data overview . . . 141
7.5 $v_2 = 4$ Dataset . . . 142
7.5.1 Rotational spectra . . . 142
7.5.2 Photoelectron angular distributions . . . 145
7.6 $v_2 = 3$ Dataset . . . 148
7.6.1 Rotational spectra . . . 148
7.6.2 PADs . . . 152
7.7 Probe Wavelength Revisited . . . 152
7.8 Conclusions . . . 154

8 Ammonia II: Discussion & Partial Wave Analysis 155
8.1 Application of Photoionization Theory to NH_3 . . . 155
8.1.1 Rotational spectator model . . . 155
8.1.2 Modelling scattering . . . 156
8.1.3 General symmetry selection rules . . . 158
8.2 Phenomenological Discussion of Scattering . . . 158
8.2.1 Scattering features . . . 158
8.2.2 Comparison with ZEKE/MATI spectra . . . 160
8.3 Extraction of Ionization Dynamics ($v_2 = 4$) . . . 162
8.3.1 Fit results . . . 162
8.3.2 Uniqueness of fit & rotational spectra . . . 166
8.3.3 Discussion of dynamical parameters . . . 169
8.4 Conclusions . . . 171

9 Conclusions & Future Work 172
9.1 Continuation of Experimental Work . . . 172
9.2 Experimental Development . . . 173
9.3 Theoretical Work . . . 174

III Appendicies & Bibliography 176

A Scattering Theory & Alternate Formalism 177
A.1 Scattering Theory . . . 177
A.1.1 General central potential . . . 177
A.1.2 Coulomb potential . . . 178
A.1.3 Coulomb potential plus short-range potential . . . 179
A.1.4 Coulomb potential plus *non-central* short-range potential . . . 180

A.2 Relation to Eigenchannels 181
A.3 Relation to Quantum Defects 182
A.4 Orbital Ionization Model 183

B β_{LM} Parameters from Acetylene Photoelectron Images **184**

C β_{LM} Parameters from Ammonia Photoelectron Images **187**

Bibliography **190**

Chapter 1

Introduction: Photoionization Dynamics and Measurement

In this chapter photoionization dynamics are discussed in a broad context, including an overview of some previous work in the field, and common experimental techniques used to probe ionization dynamics. Particular focus is placed on photoelectron angular distributions (PADs), which form a key aspect of the work presented in this thesis. More technical details of relevant theory and the experimental techniques used in the work presented here are given in Chapters 2 and 3, and Appendix A expands on the relation between the different theoretical methods mentioned here in passing.

1.1 Photoionization Dynamics

Photoionization is a complex process involving the interaction of a radiation field with an atomic or molecular system, and the subsequent ejection of a photoelectron. Photoelectron energy spectra provide a means to obtain detailed spectroscopic information on the energy levels of the ion created, and the relative population of rotational, vibrational and electronic states of the ion provides information on the dynamics of the ionization process [1]. The ionization process is defined by the ionization matrix element linking the initial state of the system to the continuum:

$$\boldsymbol{\mu_{i+}} = \langle \Psi_+;\, \phi_e | \hat{\mu}.\mathbf{E} | \Psi_i \rangle \tag{1.1}$$

where Ψ_i and Ψ_+ are the initial and final state wavefunctions of the atom or molecule, ϕ_e is the wavefunction of the photoelectron, $\hat{\mu}$ is the electronic dipole operator and $\mathbf{E}$ the electric vector of the ionizing radiation. Further details on the dipole approximation assumed here, and the explicit forms of the wavefunctions Ψ and ϕ_e, are discussed in Chapter 2; however, for the following discussion note that the photoelectron wavefunction is expanded in terms of *partial waves*, $|\mathbf{k}, l\lambda m\rangle$, where $\mathbf{k}$ is the photoelectron wave vector and l the orbital angular momentum with lab frame projection m and molecular frame projection λ. For ionization events involving a single initial state and a single final

state the ionization matrix elements can be expanded in terms of the partial waves, and determination of the dynamics amounts to obtaining information on the amplitudes of the different partial wave components. This is discussed in detail in Chapter 2 and Appendix A. An important point to note is that l is only a good quantum number in spherically-symmetric systems (e.g. atoms), and λ is a good quantum number for cylindrically symmetric systems. This means that molecular ionization is much more complex than atomic ionization and can involve many more partial wave components, this is discussed further in section 1.4.3. Partial waves are labelled in the same manner as atomic orbitals, thus $l = 0$ is an s-wave, $l = 1$ a p-wave and so on.

The ionization cross-section, I, is proportional to the magnitude squared of the ionization matrix element:

$$I \propto |\boldsymbol{\mu}_{i+}|^2 \tag{1.2}$$

Equation 1.2 shows how the ionization cross-section for population of a single quantum state of the ion is related to the initial state of the system, the ionizing radiation field and the outgoing photoelectron. All information on the dynamics is therefore contained in I, and hence the photoelectron spectrum, but in practice measurement of the integrated cross-section alone is not sufficient to gain quantitative insight into the dynamics. This is a consequence of the complexity of the wavefunctions involved, and the lack of coherence information in the integrated cross-section.

Angle-resolved, or differential cross-sections, have long been known to provide much more detailed information than angle-integrated measurements. The angle-resolved cross-section is given by the coherent square of the ionization matrix element, and can be defined as:

$$I(\theta, \phi) \propto \boldsymbol{\mu}_{i+}\boldsymbol{\mu}_{+i} \tag{1.3}$$

where $\boldsymbol{\mu}_{+i} = \boldsymbol{\mu}_{i+}^{\dagger}$, and the angles (θ, ϕ) are the polar and azimuthal angles in spherical polar coordinates. The full theoretical treatment of $I(\theta, \phi)$ is deferred until Chapter 2, but from the form of equation 1.3 it is apparent that measurements of the differential cross-section will contain more information than measurements of the angle-integrated cross-section. Angle-resolved measurements of photoelectrons provide deep insight into the composition of the photoelectron wavefunction, including phase information. As will be shown later, it is possible to quantitatively determine the photoionization dynamics from such photoelectron angular distributions (PADs).

1.2 Angle-Integrated Photoelectron Spectroscopy

Two common methods of photoelectron spectroscopy are the *pulsed-field ionization zero electron kinetic energy* (PFI-ZEKE) and *magnetic bottle* techniques, details of the techniques and some examples of work which probed photoionization dynamics using these methods are discussed in this section. In these techniques angle-resolved cross-sections

cannot be measured, but qualitative insight into the dynamics can still be obtained [1], and comparison with *ab initio* results presents a way of testing the predicted photoionization dynamics [2, 3].

Central to all of the experimental methods discussed here is the use of *resonance-enhanced multi-photon ionization* (REMPI) schemes, in which the system under study is prepared by a resonant absorption step in order to populate a single quantum state prior to ionization. These are often termed *pump-probe* experiments, and the absorption and ionization steps can be treated independently [1]. REMPI schemes are discussed further in Chapter 2.

1.2.1 Magnetic bottle

In a magnetic bottle spectrometer photoelectrons are parallelized and steered towards a detector by the use of diverging magnetic fields [4]. Measurement of electron flight-times provides an energy spectrum, and the magnetic field ensures a good collection efficiency of $\sim$50% [4]. Energy resolutions of $\sim$50 - 200 cm^{-1} are typically reported from such an instrument [4, 5, 6, 7]. The use of additional electric fields to advance or retard photoelectrons can be used to obtain some angular information, but the technique is not suitable for recording PADs. The presence of high strength magnetic fields may also have some effect on the ionization dynamics through l-mixing [5, 7], and these effects may be significant in some cases.

Vibrationally and rotationally resolved photoelectron spectra obtained from magnetic bottle instruments have been used to investigate photoionization dynamics by several groups, notably Pratt and co-workers [6, 7] (see also the review article by Pratt, ref. [1], and references therein), whose work on acetylene [6] and ammonia [7] is compared with the experimental results obtained in this work in the relevant Chapters.

De Lange and coworkers published magnetic bottle results recorded via high-lying Rydberg levels of NH [8], HCl [5] and HBr [9]. Rotational resolution was obtained in these cases by the preparation of high-lying rotational levels (typically $J/N > 10$), for which the rotational spacing was greater than the instrument resolution. From the experimental spectra they were able to draw qualitative conclusions about the dynamics of the photoionization, based upon the (calculated) angular momentum character of the Rydberg states ionized and the atomic-like propensity rule $\Delta l = \pm 1$. They were also able to compare their results with the *ab initio* calculations of Wang and McKoy [3, 9, 10] and good agreement was found. In this manner further, quantitative, insight into the dynamics was gained from the verification of the computational results. Example spectra from the HBr work [9] are reproduced in Figure 1.1; in this case both Rydberg states prepared prior to ionization are calculated to be $>$ 95 % p in character, so photoelectrons with s and d partial wave components are expected to dominate, leading to ionizing transitions $\Delta J \leq 7/2$ [9]. These qualitative conclusions are corroborated by the experimental results. The calculations were also able to account for small contributions from higher l components, and account for the differences in branching ratios between the odd and even parity

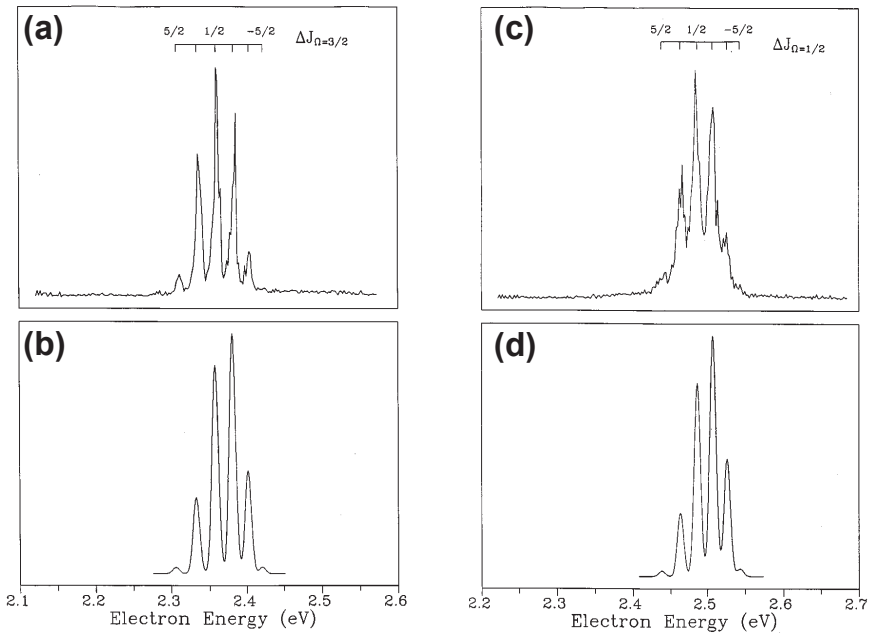

Figure 1.1: Photoelectron spectra and calculated spectra for HBr. (a) Ionization from $f^3\Delta_2(v=0)$ Rydberg state, prepared via $S(9)$ rotational transition, (b) corresponding *ab initio* result; (c) Ionization from $F^1\Delta_2(v=0)$ Rydberg state, prepared via $Q(10)$ rotational transition, (d) corresponding *ab initio* result. Figure reproduced from ref. [9].

components of each J_+ level [3].[1]

1.2.2 PFI-ZEKE

PFI-ZEKE offers the highest resolution of all methods of photoelectron spectroscopy. In ZEKE experiments a probe laser excites high-lying Rydberg states of the system under study. Each state of the ion is approached by a ladder of Rydberg levels, thus all ionic states can be accessed in this way [13]; a schematic of this is shown in Figure 1.2. Any prompt photoelectrons which arise from direct ionization have kinetic energies > 0 and rapidly depart the excitation region [14], while Rydberg states with high orbital angular momentum, l, values remain - these are the so-called ZEKE states and are formed from the laser-populated high-n Rydberg levels by l-mixing caused by stray fields[2] (Stark mixing) [12, 15]. After some short time, typically μs, a small voltage (usually $<$1 V/cm [12]) is pulsed over the region, this field-ionizes the long-lived ZEKE states and ejects the electrons towards a detector[3]. By scanning the laser wavelength a ZEKE spectrum can

[1] Note that the parity components are not resolved in the photoelectron spectra of ref. [9], but relative population of these components following ionization had been studied previously by laser-induced fluorescence [11].

[2] So-called stray fields may originate from sources external to the experiment, but ions present in the excitation region have also been shown to contribute to l-mixing, and in many cases may be the main source of l-mixing. For further general discussion of these points see [15]. Quantitative calculations by Softley and co-workers explore l- and m_l-mixing processes from time-dependent inhomogeneous fields in more detail [16, 17]. The strength of any fields present in the ionization region will of course depend on various experimental factors such as shielding of the vacuum chamber from external perturbations and number density of ions in the chamber.

[3] Note that there is a subtle, and often confusing, distinction between pulsed-field ionization of high *n*, *l* Rydberg states, and the original conception of ZEKE as a true threshold *photoelectron* spectroscopy

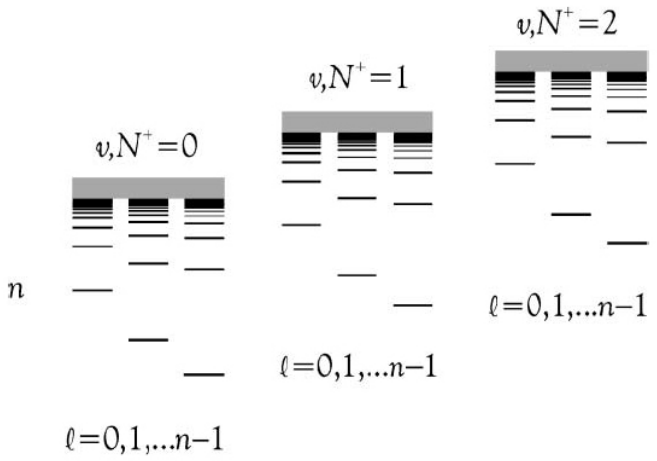

Figure 1.2: Schematic of the convergence of Rydberg series to different (rotational) states of the ion. Figure reproduced from ref. [12].

be built up, showing the detected electron intensity as a function of wavelength. As the detected electrons at a given laser wavelength originate from only the high-lying Rydberg states converging on a particular state of the ion, such a spectrum will reveal the spectroscopy of the ion with a resolution approaching the bandwidth of the laser (typically < 1 cm^{-1} for a ns pulsed dye-laser). By operating in this way ZEKE sidesteps the problem of the inherently poor resolution of electron kinetic energy analysis methods as used in other methods of photoelectron spectroscopy. The resolution is also highly dependent on the size of the extraction field used, this sets the size of the window of ZEKE states sampled and there is a consequent practical trade-off between resolution and signal strength. Currently the highest resolution ZEKE schemes employ a multi-pulse or stepped-pulse scheme, rather than a single ionizing pulse, allowing the 'window' or 'slice' of the ZEKE state manifold sampled to be varied over time. In this way a series of ZEKE spectra with different ionization field strengths are recorded in a single experiment as a function of delay time, and the results can be extrapolated to provide the "true" ionization threshold (zero order or field-free) [12]. The best experimental resolution to date has been achieved by Merkt's group [19], using such a stepped-pulse scheme they were able to achieve an energy resolution of better than 0.06 cm^{-1} in their ZEKE spectra of N_2. More typically resolutions on the order of 0.2 - 0.5 cm^{-1} are achieved experimentally [12]. An important variant of ZEKE is the mass-analysed threshold ionization (MATI) technique. This is conceptually identical to the ZEKE method described above except that ions are

[14, 18]. In some work this distinction is still maintained, but generally in the recent literature the acronyms PFI-ZEKE and ZEKE are used synonymously [12]. The view is now that all ZEKE is PFI-ZEKE, the physical justification for this being that any stray fields acting on true threshold photoelectrons will remove them from the ionization volume before the collection field is applied, so, given that it is practically impossible to remove all sources of Stark mixing, it really only is the high-lying Rydberg states which are probed. However, in early work this ionization mechanism was not fully understood thus there is still a conceptual distinction between ZEKE and PFI-ZEKE [12]. It should also be noted that there is a difference between performing a ZEKE experiment on neutral or cationic species, and anions. In the latter case there are no Rydberg states (there is no Coulomb potential acting between a positively charged core and a highly excited electron), so for anions ZEKE actually is a threshold photoelectron (or photodetachment) spectroscopy as originally envisaged.

detected instead of electrons. Consequently the experimental details are slightly different [12], but MATI allows different product ions to be distinguished.

The energy-resolution of ZEKE spectroscopy is excellent, however there is no ability to record angular data in such an experiment, so it is not a suitable technique if angular distributions are of interest. It can be viewed as a complementary technique to angle-resolved methods in cases where low-resolution spectra are too congested to make robust spectral assignments [20], although care should be taken regarding the different ionization mechanisms for the two techniques and consequent differences in peak intensities [15].

De Lange and co-workers, in a continuation of the magnetic bottle work discussed above, were able to compare their magnetic bottle results with ZEKE spectra [5, 9], and with *ab initio* calculations for direct ionization. Because there must be continuity of oscillator strength across the ionization threshold [1, 5], the calculations for direct ionization at threshold would be expected to match the ZEKE results. Figure 1.3 reproduces some of the ZEKE results for HCl. An interesting point is that the two ZEKE spectra, Figure 1.3(a) & (b), recorded under different experimental conditions, have different branching ratios. The calculated spectrum Figure 1.3(c) does not match either spectrum exactly, although the trend in the rotational features is reproduced. Figure 1.3(d) shows ZEKE spectra for a range of pump transitions, and recorded under the same conditions as Figure 1.3(a). In these spectra the dominant ΔN ionizing transition changes with the rotational level prepared, and transitions $\Delta N < 0$ are dominant. The magnetic bottle results (direct photoionization), on the other hand, showed $\Delta N = 0$ ionizing transitions to be dominant, and comparable intensities for $\Delta N < 0$ and $\Delta N > 0$ for the $P(8)$ and $S(8)$ cases. Transitions with $|\Delta N| > 3$ were not observed in the magnetic bottle results. Additionally, population of the $^2\Pi_{1/2}$ spin-orbit component of the ion dominated the direct photoionization spectra, but the lower-lying $^2\Pi_{3/2}$ component was far more intense in all of the ZEKE results. The differences between the ZEKE and direct spectra were attributed to spin-orbit autoionization of the ZEKE states, resulting in decay of the $^2\Pi_{1/2}$ component to the $^2\Pi_{3/2}$ continuum during the delay before pulsed-field ionization. The differences in rotational distributions were attributed to rotational autoionization from low-n Rydbergs, which converge to higher lying ion levels, into the high-n Rydberg quasi-continuum converging on lower lying ion states. In this way the optically prepared population of ZEKE states can undergo significant dynamics prior to pulsed-field ionization [15], resulting in the observation of different ionization dynamics than observed in direct photoionization. These results serve to illustrate the possible differences between ZEKE and direct photoionization processes.

The difference observed between Figure 1.3(a) and (b) also demonstrates how experimental conditions can affect ZEKE results; in particular the ZEKE states prepared, their lifetimes and the sampling of the states by field ionization, are dependent on experimental factors such as the magnitude of stray fields present in the spectrometer [21], the density of ions created [16, 17], and the pulsed-fields applied [15, 19].

Despite these complications several authors have shown that in many cases ZEKE results can provide insight into photoionization dynamics. Merkt and coworkers [22, 23,

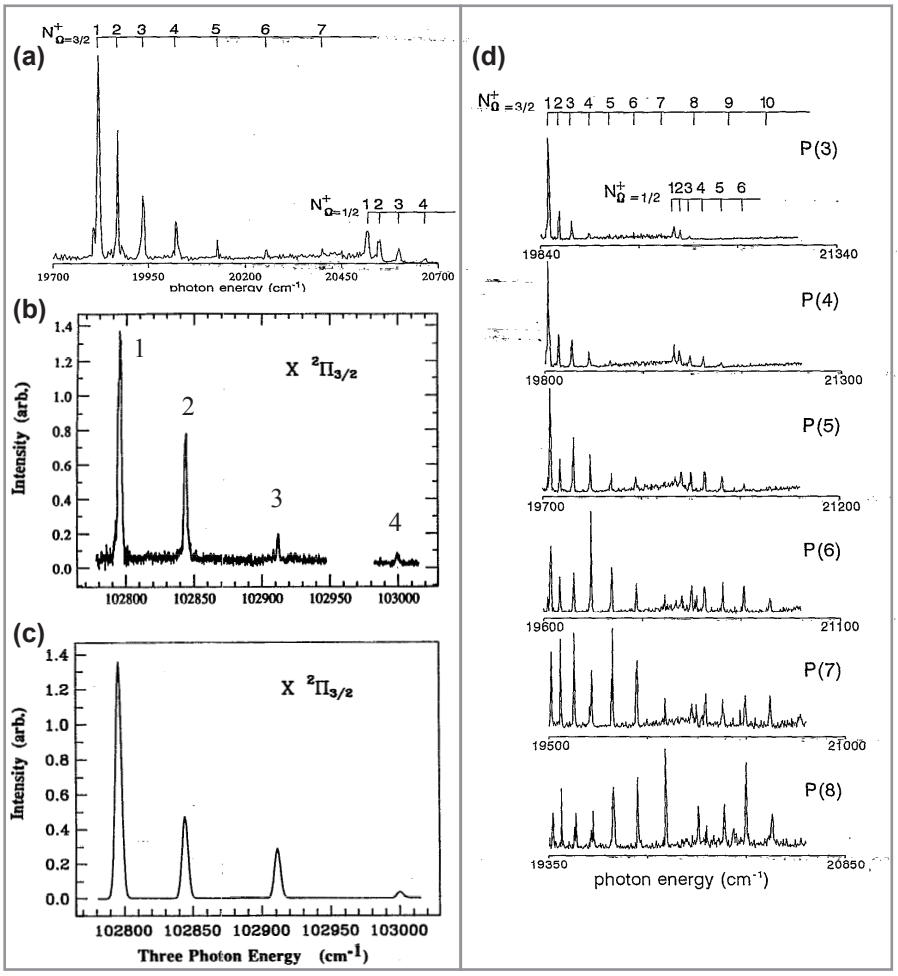

Figure 1.3: (a) & (b) ZEKE results for ionization of of HCl via $F^1\Delta_2(v = 0)$ Rydberg state, prepared via $S(0)$ rotational transition, (c) calculated spectrum for the same transition, (d) ZEKE results for different pump transitions as labelled. Spectra (a) and (d) reproduced from ref. [5], (b) & (c) from ref. [10] (original data for (b) was reported in ref. [21]).

24, 25, 26] have studied several systems, and shown good agreement with experimental results and simulations of the photoionization process based on their orbital ionization model (see Appendix A.4). Of particular relevance to the ammonia work presented in Chapters 7 and 8 is work by Müller-Dethlefs, which considered symmetry selection rules and rotational line intensities [27] in comparison with ZEKE results [28], and more recent work by Softley and coworkers [29, 30] who compared MATI results to calculations within the multi-channel quantum defect (MQDT) framework (see Appendix A.3 for further details of MQDT). These results are discussed in detail in the relevant chapters.

1.3 Angle-Resolved Photoelectron Spectroscopy

Methods of angle-resolved photoelectron spectroscopy are briefly outlined in this section, specifically field-free time-of-flight and imaging techniques are discussed. Work using

these techniques is discussed in section 1.4, along with details of photoelectron angular distributions.

1.3.1 Field-free time-of-flight

In a time-of-flight (ToF) scheme photoelectrons created with different kinetic energies are differentiated by their arrival time at a detector. The magnetic bottle technique described above is one type of ToF technique, another is field-free time of flight. In the field-free ToF technique photoelectrons created in the ionization region are not steered by any electric or magnetic fields, but are allowed to propagate to the detector under field-free conditions; in this way angular information is retained and PADs can be measured. A detector with a small solid-angle of collection will provide the best angular resolution by allowing only photoelectrons ejected towards the detector to contribute to the signal recorded, and energy resolution is maximized by studying only low energy photoelectrons [31]. Low energy electrons will take longer to reach the detector, and will therefore be more dispersed in time than high energy electrons which will have a narrow spread of arrival times [31]. PADs can be recorded either by rotating the polarization of the light[4] [32], or physically rotating the detector [33].

High resolution field-free ToF requires much care to be taken in minimizing any stray fields. Magnetic shielding of the flight region is essential, as is electrical shielding of the detector (typically a channeltron or MCP electron multiplier with a high operating voltage) and it is also important to keep ionization rates low. In their work on NO [32] Zare's group comment that at a yield of 4000 photoelectron/photoion pairs per laser shot Coulomb broadening is observed in the photoelectron ToF spectrum. Due to the low collection efficiency of a detector subtending a small solid-angle, typically 5x10^{-3} strad giving a detection efficiency on the order of 10^{-4}, this yield corresponds to only 2 photoelectrons detected per laser shot. To ensure the removal of Coulomb broadening the signal level used for high resolution work is reduced much further to around 1 photoelectron detection per 10 laser shots, corresponding to a photoionization yield of 150 per laser shot. This signal level is often used in ToF work using laser sources where all photoelectrons of interest are of relatively low energy (e.g. later NO work from the Zare group [34] cites 500 ions per laser shot, while ToF work from the group in Nottingham [31, 35] also used a signal level of 1 count per 10 laser shots)[5]. The main drawback of ToF methods is therefore the long experimental runs required in order to obtain statistically significant data-sets (i.e. good signal/noise ratio), and this problem is most acute when ToF spectra for a range of different detection angles are required for determination of PADs.

As with all methods of photoelectron spectroscopy it is hard to give a catch-all fig-

[4] Note that, in a pump-probe experiment, changing the polarization of the probe relative to the pump will also change the PAD, so the pump-probe polarization geometry must be maintained while recording ToF data at different probe-detector angles. Therefore, in a pump-probe experiment, the polarization of both beams must be rotated synchronously.

[5] It is worth noting that while ToF methods using synchrotron radiation sources are conceptually the same the range of kinetic energies studied (typically tens to hundreds of eV) leads to some different priorities, in particular at the much higher energies accessed space-charge effects are not so significant and photoelectron flight-times are much shorter.

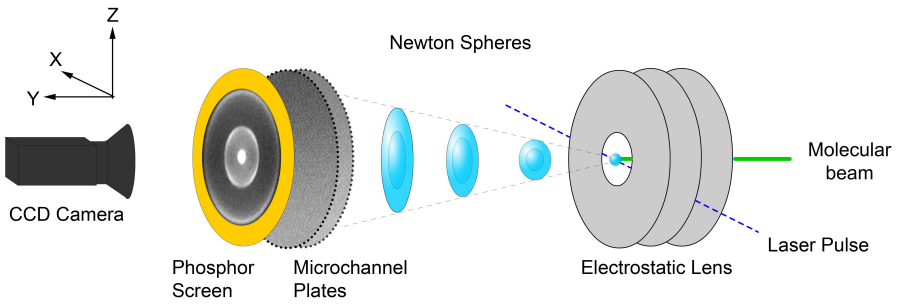

Figure 1.4: Schematic of the VMI set-up. The electrostatic lens focuses the Newton spheres onto the microchannel plates as a function of their initial velocity. Note that the action of the lens also compresses the Newton spheres in the y-direction. The 2D projection of the original 3D distribution is visualized by the phosphor screen.

ure for the resolution obtained in a ToF experiment due to the various factors which will affect this, and which may be biased differently for different experiments. This caveat aside, a typical figure for a ToF experiment looking at low energy photoelectrons ($E_{KE} < 5000$ cm^{-1}) generated from laser ionization might obtain an energy resolution of 15 - 40 cm^{-1} [32, 35] and resolution as high as 4 - 8 cm^{-1} has been reported [36].

1.3.2 Photoelectron imaging

In all imaging methods charged particles (ions or electrons), created in some defined interaction region, are steered towards a position sensitive detector using electrostatic optics. The resulting images can yield information on vector correlations within the system under study, for example photofragment kinetic energies and angular distributions [37]. Photoelectrons are ejected in all directions upon ionization, and in a field-free environment a set of nested *Newton spheres* would be propagated from the ionization region. At any given time after ionization the radii of the Newton spheres are proportional to the photoelectron speeds, and different Newton spheres (i.e. different photoelectron speeds and hence kinetic energies) correlate with the formation of different states of the ion. Imaging techniques can be split into two categories, 2D and 3D, depending on whether the final information is a 2D projection of the Newton spheres, or a full 3D map of the velocity distribution.

The major problem with early (2D) imaging methods was the poor spatial resolution, primarily due to the extended nature of the interaction region. The use of wire mesh grids as transmission elements of the electrostatic lens also led to distortions in the images due to field inhomogeneities [38]. The technique of velocity-map imaging (VMI), developed by Eppink and Parker [39, 40], offers significant advantages over previous imaging methods. By moving to open electrodes, and tuning the action of the electrostatic lens such that particles are focused onto the detector according to their initial velocity, the spatial resolution[6] is improved and the sensitivity to a large interaction volume removed.

[6]The spatial resolution of the image and energy resolution of the extracted data are linked, for further discussion see sections 3.1.2 and 3.2.

A schematic of the VMI set-up used in this work is shown in Figure 1.4. The ionization region is defined by the crossing of the laser beam and the supersonic molecular beam. In the VMI set-up the ensemble of expanding Newton spheres are repelled by the electrostatic lens towards the position sensitive detector, and focused according to initial photoelectron velocity. In other words, photoelectrons with the same initial velocity are mapped to the same point on the detector and, furthermore, this mapping is insensitive to the precise spatial location of their creation within the ionization volume. The detector is formed from two microchannel plates (in chevron arrangement) to amplify the incident photoelectrons, and a phosphor screen to visualize the (amplified) impacts. An image of the phosphor screen is captured by the CCD camera and sent to a PC; to build up an image with a good signal/noise ratio many camera frames are recorded and summed in an experimental run, typically $\sim$ 36000 frames, corresponding to 1 hour of experimental time at a 10 Hz repetition rate. Full experimental details are discussed in Chapter 3.

The 2D images obtained are processed to recreate a slice through the initial, (cylindrically symmetric[7]) 3D distribution. The radial component provides the photoelectron spectrum, and the angular component is also retained. PADs corresponding to each feature in the photoelectron spectrum can thus be obtained. Full details of image processing and data extraction are given in Chapter 4. It is difficult to give a single figure for the energy resolution of a VMI spectrometer as there are many caveats which must be considered (this is discussed in detail in section 3.2), but spectra with resolution of $\sim$100 cm^{-1} are routinely reported, typically corresponding to vibrational resolution in polyatomic systems. One important variation on the standard VMI technique is slow-electron velocity-map imaging (SEVI) [20, 42, 43, 44], in which high energy electrons are not recorded in order to obtain better energy resolution (see section 3.2). In the work presented on ammonia (Chapter 7) application of this technique enabled rotationally-resolved photoelectron images to be recorded.

Recently much progress has been made in experimental techniques which allow the recording of the full 3D distribution of photoelectrons [37, 45, 46, 47]. There are many variants of these techniques (see, for example, refs. [45, 48, 49]), but the common methodology is the combination of a 2D position sensitive detector with time-of-flight measurement [45], or the use of multiple, rotatable, energy analysers [50]. VMI may also be implemented in such a spectrometer [47, 49, 51]. Furthermore, if both ion and electrons are detected in coincidence, *vector-correlated* data can be obtained which may yield molecular frame angular distributions [52, 53]. If the molecule dissociates rapidly and the *axial-recoil approximation* holds, such measurements enable the orientation of the molecule during ionization to be inferred [54, 55], and hence molecular frame (or, more precisely, recoil frame) information can be obtained. Recent work has also demonstrated the possibility of making molecular frame measurements by probing a highly aligned sample [56, 57], circumventing the limitation of the axial-recoil requirement.

[7] This is a general requirement imposed by the image inversion procedure, see section 4.1, but may be circumvented using the Fourier-moment inversion technique [41], see Chapter 9.

1.4 Photoelectron Angular Distributions & Complete Experiments

1.4.1 General form of photoelectron angular distributions

Yang [58] formulated the most general expression for the angular distributions observed in work on nuclear reactions. The formulation relies on angular wavefunctions and invariance to frame rotation, and gives results which are generally applicable to any scattering system. This general form can be written

$$I(\theta,\phi) = \sum_{L=0}^{2n} \sum_{M=-L}^{L} \beta_{LM} Y_{LM}(\theta,\phi) \tag{1.4}$$

where the Y_{LM} are spherical harmonic functions, and the β_{LM} are the expansion parameters, often termed *anisotropy parameters*; L is the rank of the spherical harmonic (or multipole moment), and M the order of the spherical harmonic. The summation index, n, is discussed by Yang in terms of the highest orbital angular momentum component of the incoming wave in the scattering formalism; for a photoelectron angular distribution in the molecular frame (MF) this holds for the outgoing electron and $n = l_{max}$, the highest photoelectron orbital angular momentum component [59]. For the case of photoionization referenced to the lab frame (LF) n corresponds to the number of photons which interact with the system, because this determines the maximum anisotropy created in the lab frame [60, 61].

Additional symmetry restrictions may be placed on the allowed components of equation 1.4 in the LF depending on the experiment performed. For cases with reflection symmetry L must be even, and cylindrical symmetry defines $M = 0$; this is the case for photoionization with linearly polarized light. In a pump-probe experiment the polarization geometry of the two radiation fields may be parallel, and in this case cylindrical symmetry is preserved. If, however, the polarization of the probe laser is rotated relative to that of the pump laser the cylindrical symmetry is broken and terms with $M \neq 0$ can be present in the LF [62]. Reflection symmetry in the LF is broken by the use of circularly polarized light [63], or if the ionizing system is chiral [64] or oriented in space [61]. The term with $L = 0$ is proportional to the integrated cross-section.

In the MF the allowed terms in equation 1.4 are not determined by the experimental geometry, but by molecular symmetry. In general MF measurements therefore display much richer structure than LF measurements; some examples of this are discussed in section 1.4.3.

Equation 1.4 applies in many situations, for the PADs central to this work it provides a functional form with which experimental data can be fitted and the β_{LM} parameters determined. More detailed analysis of the PADs involves the derivation of the β_{LM} in terms of the ionization matrix elements and hence relates the angular distribution to the photoionization dynamics. Such a relation is complex, but enables the elucidation of the ionization matrix elements from the PAD by fitting the experimental data with the matrix

elements as fitting parameters: this is discussed in Chapters 2 and 4.

1.4.2 Atomic photoionization

Cooper & Zare [65, 66] derived the specific form of the angular distribution in the case of one-photon ionization of a one-electron atom. In this case only a single β-parameter is required, denoted β_{20} in the notation employed here,[8] and an expression is given for β_{20} in terms of two orbital angular momentum components of the photoelectron wavefunction, $l \pm 1$, which arise from ionization of a one-electron atomic orbital, with orbital angular momentum l:

$$\beta_{20} = \frac{l(l-1)\boldsymbol{r}_{l-1}^2(l+1)(l+2)\boldsymbol{r}_{l+1}^2 - 6l(l+1)\boldsymbol{r}_{l+1}\boldsymbol{r}_{l-1}cos(\eta_{l+1}-\eta_{l-1})}{2(2l+1)[l\boldsymbol{r}_{l-1}^2 + (l+1)\boldsymbol{r}_{l+1}^2]} \tag{1.5}$$

Here $\boldsymbol{r}$ denotes the radial dipole matrix element (see sections 1.1 and 2.3), and η is the phase shift of the l-wave. The selection rule $\Delta l = \pm 1$ comes from the application of the dipole approximation (see Chapter 2). The description of the photoelectron in terms of an expansion in orbital angular momenta l, and associated radial functions, is the *partial wave expansion* and is discussed further in section 2.3.1. The key result shown by this equation is contained in the cross-term involving terms in both $l+1$ and $l-1$, which shows that the observed anisotropy is dependent on not just the magnitudes, $\boldsymbol{r}_{l\pm1}$, but also the relative phases of the l-waves. The observed PAD is thus an *interference pattern*, and contains information on coherence which is lost in the integrated cross-section, as demonstrated by the form of equation 1.3.[9]

The classic example of this interference effect, as cited by Cooper & Zare [65], is the photodetachment of electrons from $O^-(^3P)$ and $C^-(^4S)$, reported by Hall & Siegel [68]. In both these cases s and d partial waves ($l = 0, 2$) are allowed, and the angular distribution observed in both cases was near to a $\sin^2\theta$ distribution. This is in contrast to single channel ionization, where a $\cos^2\theta$ angular distribution[10] would be expected. The single channel case was also demonstrated by Hall & Siegel [68] for photodetachment from $H^-(^1S)$. In that case $l = 1$ only, so there was no partial wave interference and the observed PAD resulted from a pure p-wave.

This form of the angular distribution suggests the idea of a *complete* photoionization experiment, defined as an experiment from which the radial dipole matrix elements and associated phases - termed the *dynamical* parameters - can be obtained. The first such experiment for photoionization of an atomic target was performed by Berry and coworkers

[8] In Cooper & Zare's work [65, 66] Legendre polynomials were used in place of spherical harmonics. For cylindrically symmetric problems these are interchangeable, differing only in normalization. Spherical harmonics are used in this work as they also allow for the more general case of non-cylindrical symmetry. See section 4.1.2 for further details.

[9] The existence of l-wave interference effects in *molecular* photoionization had earlier been posited by Cohen & Fano [67], based on photoabsorption spectra of N_2 and O_2, and they considered this using a two-centre interference model. While the conclusions of such an analysis are similar to those of Cooper & Zare, the conceptual approach is quite different, and the level of detail obtained in the angle-integrated spectra much lower.

[10] Physically this arises from the nature of the interaction of the ionizing radiation with the bound electron, see Chapter 2.

[69], who studied $\mathrm{Na}(^2P_{1/2}, {}^2P_{3/2})$. The difficulty in such an experiment is to obtain enough data to enable confident determination of the dynamical parameters, which may be obtained by fitting with a suitable functional form [62, 70] (see section 2.3) or by comparison with *ab initio* calculations [50], examples of this will be discussed later in the context of molecular photoionization.

From equation 1.5 it might be expected that the experimentally determined PAD would not yield enough data to obtain the dynamical parameters from a fitting procedure, so more complex experimental arrangements are required. For the work on sodium, Berry and coworkers [69] used a 2-photon scheme which allowed the preparation of the $^2P_{1/2}$ and $^2P_{3/2}$ states by absorption of one photon, followed by ionization upon absorption of a second photon, and control over the *polarization geometry*, the relative orientation of the polarization vectors of the preparation and ionizing light. The LF-PADs measured changed as a function of the polarization geometry, and contained contributions from many β_{LM}. The formalism relating these measured angular distributions to the dynamical parameters is therefore more complex than equation 1.5, but contains essentially the same elements. The experimental data was sufficient for the investigators to determine the ratio of the radial dipole matrix elements, $\boldsymbol{r}_0/\boldsymbol{r}_2$, and the phase difference $\eta_0 - \eta_2$. Further work by the same group examined the effect of nuclear spin on the PADs and photoelectron polarization [71], photoionization of Li [72], and the observation of quantum beats in the PADs observed from photoionization of Li [73].

In cases where spin is strongly coupled, measurement of the spin polarization of the photoelectrons can also be regarded as a requirement for a complete photoionization experiment [74, 75]. This has been extensively studied by Heinzmann and coworkers, particularly for photoionization of Xe [76, 77, 78]. An excellent review of atomic multiphoton ionization and PADs, including discussion of spin polarization, was provided by Smith and Leuchs [79].

Elliott and coworkers were able to probe the photoionization dynamics of rubidium using elliptically polarized light [80], and were able to determine magnitude and phases for s and d continua, the latter of which was further split by the presence of spin-orbit interactions [80, 81]. In related work on rubidium, Yin et. al. [82] demonstrated coherent ionization via 1-photon and 2-photon pathways using a two-colour laser field. The PADs recorded were asymmetric with respect to the laser polarization due to the interference of odd and even-l partial waves, and were sensitive to the relative amplitudes and phases of the laser fields. Although this work did not provide complete information, the potential of this technique for determination of the phase differences between odd and even-l continua was discussed [82].[11]

1.4.3 Molecular photoionization - complete experiments

Complete determination of the photoionization of molecular targets is a much more difficult problem than the atomic case. Because l is only a good quantum number in

[11] The technique was later applied to NO [83], demonstrating its applicability to molecular photoionization.

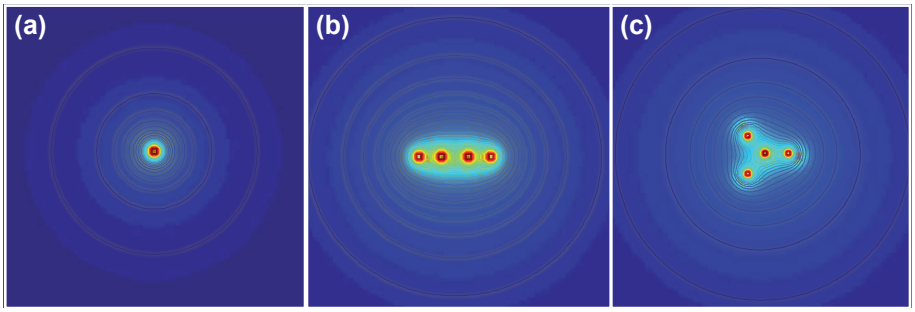

Figure 1.5: Illustration of electrostatic potential surfaces for (a) single-centre system, (b) four-centre linear system, (c) four-centre non-linear system. Potentials shown in (b) and (c) are highly anisotropic at short-range, but tend to pure Coulomb potentials asymptotically.

centrally-symmetric systems, the characterization of the initial molecular state in terms of a single orbital angular momentum is no longer valid. Similarly, the outgoing photoelectron is susceptible to l-mixing, which can be considered as scattering of the electron from the anisotropic molecular potential. Figure 1.5 shows plots of the electrostatic potential of single and four-centre systems to illustrate this idea. In the core region the potentials are highly anisotropic for multi-centre systems, but asymptotically these potentials tend to a pure Coulomb (isotropic) case. In reality the core region will be even more complex because the charge distribution over the atomic centres will not be uniform, and electron-electron interactions will also occur. The l-mixing means that the partial wave expansion may consist of many l components [55, 61, 84], and there will be more dipole matrix elements to determine in order to characterize the ionization dynamics. There is also a distinction introduced between the lab and molecular frames of reference, which is not applicable in the atomic case. These frames are related by the polarization vector of the radiation, by convention this defines the z-axis in both frames of reference (see section 2.1.2). The MF projection of l is defined by the quantum number $\lambda = l, l-1, ..., -l$.

Despite these inherent difficulties molecular photoionization is all the more interesting because of the rich dynamics which may occur, and the extensive information which the PAD carries about the potential experienced by the outgoing photoelectron. Successful examples of complete experiments in molecular photoionization have been limited to a handful of cases, which are discussed below.

Nitric oxide has become something of a benchmark system for complete experiments, and has been investigated by several groups. Zare and coworkers first showed that a complete experiment could be realised [32, 34, 62] for a molecule. Using a field-free time-of-flight instrument, lab frame PADs pertaining to the formation of individual rotational levels in NO^+ were recorded. A (1+1') ionization scheme was used, with ionization via $NO A^2\Sigma^+(v = 1,\ N = 22)$, and the use of a selection of polarization geometries allowed enough experimental data to be recorded to determine the magnitudes of seven dipole matrix elements, and five relative phases from a fit to the data (the signs of these phases were later determined with the aid of additional PADs recorded with circularly

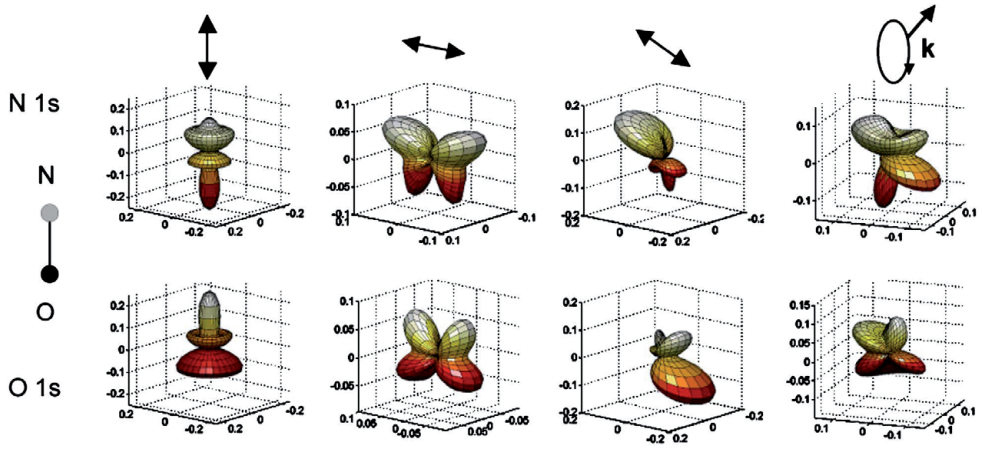

Figure 1.6: $\mathrm{N}(1s^{-1})$ and $\mathrm{O}(1s^{-1})$ MF-PADs at 418.3 eV and 550.5 eV, for a molecule aligned parallel, perpendicular, at the magic angle (54.7°) with respect to linearly polarized light, and for a molecule aligned perpendicular to the propagation axis of right-circularly polarized light. Reproduced from ref. [92].

polarized light [63]). The preparation of a high-N rotational level in the intermediate state ensured that the ion levels populated were sufficiently separated in energy to be resolved experimentally; as is clear from the discussion of experimental methods in sections 1.2 and 1.3, obtaining rotational resolution is experimentally very challenging and has often been the limiting factor in this type of work [31]. Further work from Zare's group probed the N-dependence of the ionization dynamics [85], the dynamics of vibrational autoionization [86], and also considered the treatment of the problem within the eigenchannel theoretical framework [87] (see Appendix A.2).

A very different set of experiments were performed by Geßner et. al. [88], who recorded molecular frame PADs pertaining to the $4\sigma^{-1}$, inner valence, 1-photon ionization of NO using a coincidence spectrometer. By recording MF-PADs using both linearly and circularly polarized light enough data was obtained to determine seven dipole matrix elements, and six phase differences by fitting the data [88].

Extensive work in this vein has been performed by Yagishita, Adachi and co-workers (see refs. [50, 89] and further work cited therein), who have recorded MF-PADs via core ionization of several diatomic molecules (including NO, $\mathrm{N_2}$, CO), and some linear triatomic systems ($\mathrm{N_2O}$, $\mathrm{CO_2}$). In many of these cases they were able to obtain dynamical parameters from their experimental data, and made comparisons with *ab initio* calculations in order to resolve any ambiguities in cases where several sets of dynamical parameters were found to model the experimental data. In using this approach they were also able to make extensive comparison of experimental and theoretical results over large ranges of photon energies, and look in detail at shape resonances in the ionization continuum. Dowek, Lucchese and co-workers have taken a similar approach, and have reported the determination of dynamical parameters using MF-PADs, and comparison with *ab initio* calculations, for NO [90, 91, 92]. Figure 1.6 shows an example of the MF-PADs reported in ref. [92], and the rich structure which is possible in such PADs.

These examples highlight the two main experimental approaches which have been employed in the investigation of photoionization dynamics, (a) the use of LF-PADs obtained via multi-photon ionization and (b) MF-PADs, typically obtained via single photon absorption and coincidence techniques [55]. Because the recording of MF-PADs requires that the axial-recoil approximation is applicable, the systems for which MF-PADs can be recorded in this manner are limited. High-energy processes that involve ejection of core electrons are the processes best suited to study as they typically cause rapid dissociation of the molecule. The benefit of MF-PADs is that they are not obscured by the averaging over molecular alignments, and consequently have more allowed terms in an expansion of the type given in equation 1.4, as compared with the LF case. For MF-PADs the index $n = 0...2l_{max}$, where l_{max} is the highest orbital angular momenta in the photoelectron wavefunction; additionally the symmetry restrictions imposed on the allowed Y_{LM} are lifted and odd-L is allowed [59]. This means that MF-PADs contain more information than LF-PADs. For molecular systems or ionization routes which are not suitable for study in this manner, for example valence ionization of polyatomic molecules, the measurement of LF-PADs obtained via REMPI schemes presents the best experimental approach.

Any experimental variables which do not affect the dynamical parameters can be exploited to maximize the data obtained from lab frame measurements. In the Zare group work discussed above [62, 34] the polarization geometry represented such a variable, and essentially changed the alignment in the ionization frame of reference (see section 2.2.2.3). Because the dynamical parameters vary only slowly with energy they are expected to be approximately constant over a range of rotational levels [85, 93] (see also discussion in section 4.3.1), so the preparation of different intermediate rotational levels prior to ionization represents another viable experimental scheme. This was demonstrated in work on NH_3 [31, 94], and is the approach used in the work presented in this thesis.

A final example is the creation of a time-dependent molecular axis alignment [95, 96, 97], such as that created by preparation of a rotational wavepacket. This approach again relies on the invariance of the dynamical parameters over a range of rotational levels, and also assumes that they show no time dependence. This approach has been demonstrated by Tsubouchi and Suzuki [98], who used a fs laser to prepare a rotational wavepacket in $NO A^2\Sigma^+$ prior to ionization. They were able to determine the dynamical parameters from LF-PADs recorded as a function of pump-probe delay time, and these parameters were comparable to those obtained in the Zare group work [87]. In a sense this technique also shows how the the MF and LF are related, essentially the LF-PAD is the MF-PAD averaged over a range of molecular orientations, so will approach the MF-PAD as the degree of alignment increases [56, 57, 96, 97, 99, 100].[12] For further detailed discussion of LF and MF measurements, and related topics, see refs. [61, 97, 100].

[12] There is however a distinction between *alignment*, where a plane of mirror symmetry is present, and *orientation,* where there is a distinction between "up" and "down" in the ensemble of molecules. Only in the case of orientation will the LF and MF be truly coincident.

1.4.4 Molecular photoionization - PADs as probes

The literature cited in the previous section shows the paucity of experimental measurements which provide detailed, quantitative, insight into photoionization dynamics. Such work is both experimentally and theoretically challenging, and to date has only been successful for a handful of cases. However, the determination of the dynamical parameters, in the sense of the complete experiments discussed above, is often not the goal of photoionization experiments, and may also be unfeasible if many partial waves are involved. PADs still provide extensive information on photoionization dynamics, and can also provide information on other dynamical processes.

The power of the PAD as an interference pattern has been explored further in high-energy experiments using the cold target ion-recoil momentum spectroscopy method (COLTRIMS), which is a variant of the coincidence experiments mentioned above. In these experiments single and double ionization of H_2, termed "the simplest double slit", has enabled the examination of interference and entanglement [101], and symmetry breaking [102] in multi-body systems.

The ability of PADs to give a direct insight into the molecular orbital structure of the ionized system is a very tempting prospect, although the relationship is very complex. As mentioned in the previous section, *ab initio* calculations have been compared to experimental PADs in some cases, and such comparisons present a good test of the calculations [2, 3]. Such calculations are very challenging, and several authors have also suggested correlations between observed PADs and molecular orbitals [50, 103, 104], or molecular structure [105], based on simplified or qualitative models. Although far from exact, such work does provide an appealing physical picture, albeit one which must be applied with care. Recent work on the ionization of small metal clusters [106] is an example of the more direct link between the observed PADs and bound states in simpler systems.[13]

The behaviour of PADs have also been explored in more exotic regimes, in particular the effects of laser intensity [79, 110] (see Figure 1.7) leading to strong field [111] and above-threshold ionization [112, 113, 114], have recently become popular topics with the widespread availability of intense, short-pulse laser sources. Non-dipole effects have also been explored by several authors, see for example refs. [115, 116, 117].

PADs are also a very powerful probe of other molecular processes because they carry the signature of changes to the initial and final molecular states - albeit in a complex manner. The sensitivity of the LF-PAD to a time-evolving molecular-axis distribution, discussed above, is one example of this [97, 118]. Other processes whereby the vibronic character of the molecule evolves in time will affect the PAD recorded in both the lab and molecular frame [46, 61]. Examples of this include inter-system crossing, dissociation [52, 57, 119, 120], intramolecular vibrational energy redistribution and isomerization [121].In many of these cases the PADs provide complementary information to the (angle-integrated) photoelectron spectrum.

[13] Photoionization dynamics is closely related to the dynamics of electron-ion recombination, as can be studied in high-harmonic generation (HHG) experiments [107]. Recent work [108, 109] has demonstrated the possibility of *tomographic reconstruction* of molecular orbitals from HHG measurements, so is linked to the work discussed here.

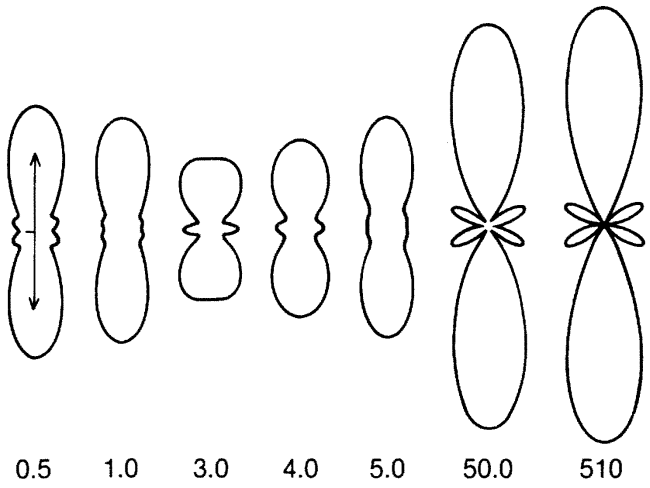

Figure 1.7: Calculated PADs for (2+1) ionization of sodium. Laser intensities are given in MW/cm^2. Reproduced from ref. [110].

1.4.5 A note on theoretical methods

In the preceding discussion several references have been made to *ab initio* calculations as a means to calculate directly the ionization dipole matrix elements, and predict the PADs which would be observed experimentally. The difficulty in these methods is the calculation of the bound-free matrix elements, which is a complicated computational problem due to the expansion of the photoelectron wavefunction over a large number of partial waves (the exact wavefunction is formally a sum over infinite l).

The formalism describing the partial wave expansion is presented in detailed in section 2.3, and related treatments of photoionization are discussed in Appendix A. Typically, the radial and angular parts of the matrix elements are separated. The angular part can be described analytically using standard angular momentum algebra, and therefore is readily calculated. The radial part cannot be solved analytically, and hence requires either experimental determination or numerical calculation through *ab initio* means. Broadly, the various *ab initio* approaches to calculating photoionization dynamics are very similar, but make different approximations or assumptions, or simply use different algorithms, in the numerical evaluation of the matrix elements.

Several different methods have been reported in the literature, and used to calculate the required dipole matrix elements. Examples include multiple-scattering [101, 122, 123], random phase approximation (RPA) [101, 75] and the Schwinger variational method [51, 90, 124]. The details of these methods are beyond the scope of this work.

1.5 Summary, Aims & Objectives

In this chapter some background to the work presented in this thesis has been discussed. The specific aim of this work is to study the ionization dynamics of polyatomic molecules through the use of PADs recorded using the VMI technique, following the preparation of

rovibronically selected levels. Results are presented for acetylene and ammonia, in the latter case rotational resolution has been obtained in the photoelectron images. Analysis of the experimental data has enabled the determination of dynamical parameters in both cases, presenting a significant addition to the limited number of successful experiments in this field.

Part I

Machinery & Methodology

Chapter 2

Theory of Photoabsorption and Photoionization

In this work a *pump-probe* methodology has been used to enable the recording of photoelectron angular distributions (PADs) from a state-selected species. As formulated by Dixit and McKoy [60], a resonance-enhanced multi-photon ionization (REMPI) process can be broken down into two steps:

1. An *excitation* or *pump* step which is used to prepare the system prior to ionization. In the work presented in this thesis this preparation step is used to select a single rovibronic quantum state of a molecule. Furthermore, this n-photon absorption also creates *alignment* in the molecular axis distribution of the sample, and the molecular ensemble is thus anisotropic in the lab frame of reference prior to ionization.

2. An *ionization* or *probe* step whereby m-photons ionize the prepared state. The photoelectron angular distribution observed will reflect both the intrinsic partial wave character of the ejected photoelectrons, and the molecular alignment created in the pump step.

In this chapter both steps in this $(n+m)$ REMPI scheme are addressed in turn (Sections 2.2 and 2.3). Specific results are derived for the intermediate state alignment, and for the form of the (lab frame) PADs observed from an ionization event. In the experimental work presented in this thesis (1+1), (2+1) and (2+1') REMPI schemes were used to study the photoionization dynamics of acetylene and ammonia. The theory presented is therefore derived with the specific cases of $n = 1, 2$ and $m = 1$ in mind, although it is readily extensible to any $(n + m)$ process. Further application of relevant parts of the theory to these specific molecules is shown in the corresponding chapters (5 and 7).

2.1 General Framework of Light-Matter Interactions

2.1.1 Born-Oppenheimer approximation

To begin, the approximations which underlie all of the following must be discussed. The starting point for many results in molecular quantum mechanics is the Born-Oppenheimer approximation, this states that the wavefunction of a system, Ψ, can be decomposed into a product formed from parts of a system which move on different timescales [125]. Nuclear motion is therefore decoupled from electron motion, and Ψ can be written [126]:

$$\Psi = \psi_{nuc}\psi_{elec}\psi_{vib}\psi_{rot} \tag{2.1}$$

The components here represent the nuclear, electronic, vibrational and rotational parts of the product wavefunction Ψ. As will be shown below, the separation of the rotational part of the wavefunction enables calculation of the angular momentum coupling between an incident photon and the initial state of the system (vital to PADs) without explicit consideration of the much harder problem of evaluating full (rovibronic) transition matrix elements. In addition, weak coupling between different product wavefunctions can be described as perturbations within the B-O framework; examples of this include vibronic coupling, spin-orbit coupling, the Jahn-Teller effect, and many others [127].

2.1.2 Frames of reference & angular momenta

Figure 2.1(a) illustrates the spatial coordinates used in this work. The lab frame Cartesian axes are defined by the laser polarization, $\bar{\mathbf{z}} = \bar{\mathbf{E}}$, and propagation direction, $\bar{\mathbf{x}} = \bar{\mathbf{k}}$, where quantities in bold are vectors and the bars indicate unit vectors. The coordinate origin is defined as the centre-of-mass of the molecular system. Spherical polar coordinates, ($\mathbf{r}$, θ, ϕ) are referenced to the same origin, spherical polar unit vectors ($\bar{\mathrm{r}}$, $\bar{\theta}$, $\bar{\phi}$) are also shown. Figure 2.1(b) shows the main angular momentum quantum numbers used in this work, in the lab and molecular frames of reference. J denotes the total angular momentum, with projection terms M_J and K; l is an electronic orbital angular momentum, with projection terms m_l and λ. Examples of spherical harmonics, Y_{lm}, in the lab frame and $Y_{l\lambda}$ in the molecular frame are also illustrated.

2.1.3 Dipole interactions & the weak field limit

Light-matter interactions can be treated in a classical picture as a charge distribution in the presence of an oscillating electromagnetic field. A semi-classical treatment can be developed from this, in which the charge distribution of a quantum system, e.g. an atom or molecule, is considered within the classical radiation field. Such a treatment is very briefly explored here.

The electronic part of the radiation field[1] is described as a plane wave, with wave

[1] The magnetic part of the radiation field is orders of magnitude smaller than the electronic part, and is neglected.

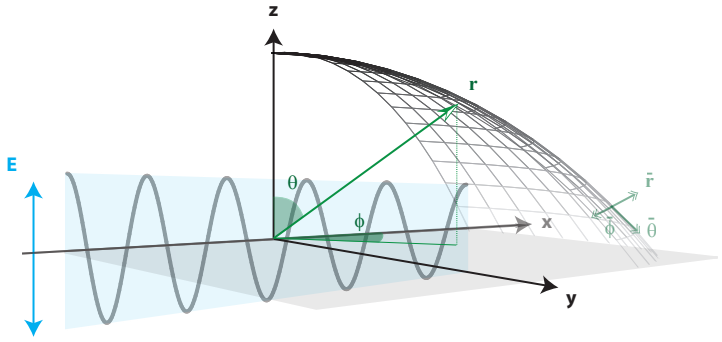

(a) Cartesian and polar spatial co-ordinates used in this work. The lab frame z-axis is defined by the laser polarization **E**, and the x-axis by the direction of the laser propagation; $\mathbf{r}$ is a radial vector in the spherical polar coordinate system. Unit vectors are denoted with a bar, e.g. $\bar{\mathbf{r}}$.

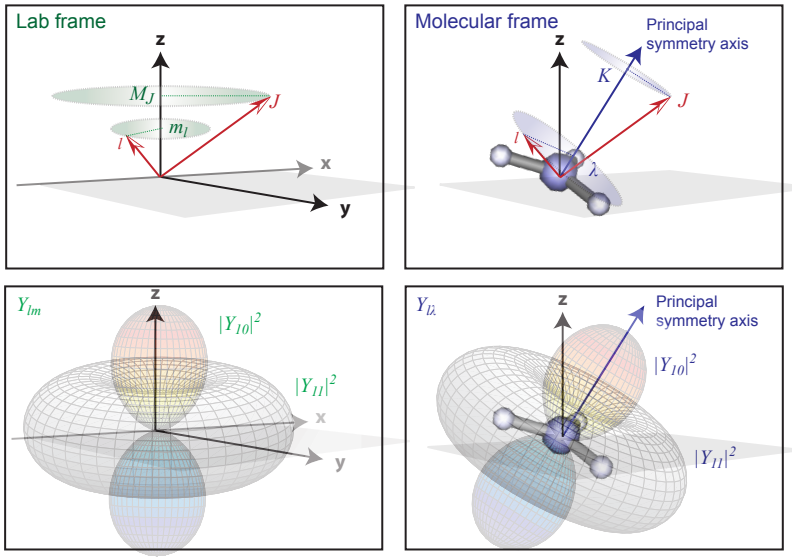

(b) Vector diagrams of the orbital angular momentum l, the total angular momentum J, and their projections in the lab and molecular frames. Spherical harmonics are also shown in both lab and molecular frames.

Figure 2.1: (a) Spatial coordinates. (b) Angular momentum vector diagrams.

vector $\mathbf{k}$, oscillating in time with angular frequency ω [128]:

$$\mathbf{E} = \mathbf{E_0}\cos(\mathbf{k}.\mathbf{r} - \omega t) \tag{2.2}$$

Here $\mathbf{r}$ is the radial vector from the coordinate origin (Figure 2.1), and $\mathbf{E_0}$ is the field at $t = 0$ and defines the field strength and polarization. If $\mathbf{k}.\mathbf{r}$ is taken to be small then $\mathbf{E}$ can be expanded as a power series [129]:

$$\mathbf{E} = \mathbf{E_0}[\cos(\omega t) + (\mathbf{k}.\mathbf{r})\sin(\omega t) - \frac{1}{2}(\mathbf{k}.\mathbf{r})^2\cos(\omega t) + ...] \tag{2.3}$$

The dipole approximation neglects all but the first-order term in this expansion. Higher-order, or multipole terms, are neglected; these are termed the electric quadrupole, octopole and so on. Physically the dipole approximation is good provided the light field

is constant over the spatial size of the system under study, for example, for an atom in a radiation field, where the coordinate origin is defined as the nucleus of the atom, $\mathbf{k}.\mathbf{r}$ is vanishingly small for optical wavelengths. Under this approximation the radiation field can be written:

$$\mathbf{E}(t) = \mathbf{E_0}\cos(\omega t) \tag{2.4}$$

If the field is weak, that is the interaction of the field with the system is small relative to the the potential of the unperturbed system, the full Hamiltonian in the dipole approximation can then be written, using perturbation theory, as [130]:

$$\hat{H}' = \hat{H}_0 - \hat{\mu}.\mathbf{E}(t) \tag{2.5}$$

where $\hat{H}_0$ is the Hamiltonian for the unperturbed system and $\hat{\mu}$ is the electric dipole operator:

$$\hat{\mu} = -e\sum_s \mathbf{r_s} \tag{2.6}$$

Here e is the electron charge and $\mathbf{r_s}$ the position vector of the s^{th} electron. The transition probability between some initial state of the system $|g\rangle$ and a final state $|i\rangle$ is now given by [130]:

$$\boldsymbol{P_{ig}} = |\langle i|\hat{\mu}.\mathbf{E_0}|g\rangle|^2 \frac{\pi t}{2\hbar^2}\delta(\omega - \omega_{ig}) \tag{2.7}$$

The $\delta(\omega - \omega_{ig})$ term is the Dirac delta function, and defines the condition that the radiation field (ω) is resonant with the transition frequency (ω_{ig}). The well-known Fermi's Golden Rule is essentially the time-independent form of equation 2.7. The matrix element in this equation is the *electric dipole matrix element*, henceforth denoted $\boldsymbol{\mu_{ig}}$:

$$\boldsymbol{\mu_{ig}} = \langle i|\hat{\mu}.\mathbf{E_0}|g\rangle \tag{2.8}$$

The transition dipole moment describes the coupling of the states g and i under a perturbing electric field. The resultant interactions are *electric dipole transitions*. For the interaction of a radiation field with an atom this leads to the selection rules:

$$\Delta l = \pm 1 \tag{2.9}$$

$$\Delta m = 0, \pm 1 \tag{2.10}$$

where l is the electronic orbital angular momentum and m is the projection of this onto the polarization axis of the light field (usually defined as the z-axis). These selection rules represent the transfer of angular momentum from the photon to the atom. In the work presented here both the weak field limit and dipole approximation are assumed. Explicit forms of the dipole matrix elements for absorption and ionization processes are given in Sections 2.2 and 2.3.

The strong field regime is not considered in this work. In this regime the coupling of the radiation field to the system is very strong, and the perturbative approach cannot be applied. Strong field treatments of PADs have been presented by other authors, for

example refs. [110, 131]. The effect of higher-order terms, such as electric quadrupole and magnetic dipole interactions, on PADs has also been studied, see for example refs. [79, 115, 116].

2.2 Photoabsorption

Following the above, the observed transition intensity for an electric dipole transition is found as the square of the modulus of the transition dipole moment:

$$\boldsymbol{S_{ig}} = |\boldsymbol{\mu_{ig}}|^2 = |\langle \Psi_i | \hat{\mu}.\mathbf{E} | \Psi_g \rangle|^2 \tag{2.11}$$

In this form the matrix elements are very difficult to evaluate as the entire wavefunction of the system is included. By application of the B-O approximation to split the wavefunction into product states equation 2.11 can also be written in terms of these product states, and only part of the transition need be considered as appropriate to the problem at hand. In the experimental work presented in this thesis the absorption of n photons is used to prepare a selected rovibronic state of the system under study, before single photon ionization of this prepared state. For a given set of experiments the electronic state and vibrational level are fixed, and only the rotational level prepared is varied, thus the focus is on rotational transition strengths in the following discussion. Additionally, the rotational profile of a band observed in a REMPI spectrum will provide information on the rotational temperature, T_{rot}, of the supersonic molecular beam used to deliver the sample to the ionization region (see Chapter 3); again it is the rotational transition strength which is of importance in such a calculation.

2.2.1 Vibronic & rotational line strength factors

Factorizing $\boldsymbol{S_{ig}}$ into B-O products for vibronic and rotational interactions yields [132]

$$\boldsymbol{S_{ig}} = \boldsymbol{S^{ev}_{ig}} \boldsymbol{S^{r}_{ig}} \tag{2.12}$$

$$\boldsymbol{S^{ev}_{ig}} = |\langle \chi_i | \langle E_i | \hat{\mu}_E.\mathbf{E} | E_g \rangle | \chi_g \rangle|^2 \tag{2.13}$$

$$\boldsymbol{S^{r}_{ig}} = \sum_{M_i, M_g} |\langle J_i M_i | \hat{\mu}_N | J_g M_g \rangle|^2 \tag{2.14}$$

$\boldsymbol{S^{ev}_{ig}}$ denotes the vibronic transition intensity, derived from the electronic and vibrational wavefunctions $|E\rangle$ and $|\chi\rangle$, and $\boldsymbol{S^{r}_{ig}}$ is the rotational line-strength determined by the rotational wavefunctions $|JM\rangle$ and includes a summation over the magnetic sublevels M, which are energetically degenerate in the absence of external fields. The dipole operator has been split into electronic and nuclear parts, denoted with subscript E and N respectively. Note, however, that in the remainder of this chapter these subscripts are omitted and the form of $\hat{\mu}$ can be inferred from context; for the majority of the derivations presented here only the rotational part of the transition intensity will be considered explicitly. Equation 2.13 can be further separated into vibrational and electronic components

by further application of the B-O approximation (i.e. no coupling between the vibrational and electronic motion)

$$\boldsymbol{S}^{\boldsymbol{v}}_{\boldsymbol{ig}} = |\langle \chi_i | \chi_g \rangle|^2 \tag{2.15}$$

$$\boldsymbol{S}^{\boldsymbol{e}}_{\boldsymbol{ig}} = |\langle E_i | \hat{\mu}_E . \mathbf{E} | E_g \rangle|^2 \tag{2.16}$$

Equation 2.15 now determines the vibrational part of the transition intensity and is the Franck-Condon factor [126]; equation 2.16 is the electronic part of the transition intensity.

2.2.2 Calculation of rotational line-strengths

The question now is how to calculate equation 2.14, the part of the transition intensity which is of interest in the following experimental work. This treatment follows that of Zare [132]. Consider equation 2.14 for a spherically symmetric case. For an isotropic excitation all components of $\hat{\mu}$ carry equal weight, so this vector form can be replaced with $3\hat{\mu}_z$:

$$\boldsymbol{S}(J_i, J_g) = 3 \sum_{M_i, M_g} |\langle J_i M_i | \hat{\mu}_z | J_g M_g \rangle|^2 \tag{2.17}$$

$\boldsymbol{S}^{\boldsymbol{r}}_{\boldsymbol{ig}}$ is now denoted $\boldsymbol{S}(J_i, J_g)$ to explicitly show the angular momenta of importance in the transition. In the spherically symmetric case the transition is completely described by the quantum numbers J_i and J_g, the total angular momenta of states i and g respectively. In general it is more useful to consider $\hat{\mu}$ in the molecule-fixed frame (MF), rather than the lab or space-fixed frame (LF). The two frames of reference can be related through the rotation matrix elements $D^k_{\mu_0 \mu_\lambda}(\phi, \theta, \chi)$, where k denotes the magnitude of an angular momentum vector with projections μ_0 and μ_λ in the two frames of reference linked by rotation of the axes through the Euler angles (ϕ, θ, χ). The incident photon carries one unit of angular momentum ($k = 1$), and for $\hat{\mu}_z$, $\mu_0 = 0$ and $\mu_\lambda = 0, \pm 1$:

$$\hat{\mu}_z = \mu(1, 0) = \sum_{\mu_\lambda} D^{1*}_{0\mu_\lambda} \mu(1, \mu_\lambda) \tag{2.18}$$

and

$$\boldsymbol{S}(J_i, J_g) = 3 \sum_{M_i, M_g} |\langle J_i M_i | E \sum_{\mu_\lambda} D^{1*}_{0\mu_\lambda} \mu(1, \mu_\lambda) | J_g M_g \rangle|^2 \tag{2.19}$$

Although this form of $\boldsymbol{S}(J_i, J_g)$ looks more formidable, it explicitly links the LF and MF, and is a more useful form when considering non-spherically symmetric cases because the angular momentum coupling can be written as LF and MF components, of which the LF component reduces to a degeneracy factor and the MF component to a Clebsch-Gordan coefficient.

2.2.2.1 Symmetric tops

In a symmetric top two of the moments of inertia about the body-fixed (a, b, c) axes are equal; $I_c = I_b > I_a$ for a prolate top and $I_c > I_b = I_a$ for an oblate top [133]. For a symmetric top the basis set is $|JKM\rangle$, where K is introduced as the projection of J

on the molecular frame. Unlike the LF terms M, energy levels with different K are not degenerate. In this case it can be shown that equation 2.19 can be written [132]:

$$\boldsymbol{S}(J_iK_i, J_gK_g) = (2J_g + 1)\langle J_iK_i, 1\mu_\lambda | J_gK_g\rangle^2 \tag{2.20}$$

$$= (2J_i + 1)(2J_g + 1) \begin{pmatrix} J_i & 1 & J_g \\ -K_i & K_i - K_g & K_g \end{pmatrix}^2 \tag{2.21}$$

The summation over M has been solved analytically and becomes part of the degeneracy term. $\boldsymbol{S}(J_iK_i, J_gK_g)$ are called the Hönl-London factors. In equation 2.20 the matrix element is a Clebsch-Gordan coefficient, this defines the angular momentum coupling between the incident photon and the states g and i; in the second form of the equation this C-G coefficient is rewritten as a Wigner $3j$ symbol, where

$$\begin{pmatrix} J_1 & J_2 & J_3 \\ K_1 & K_2 & K_3 \end{pmatrix} = (-1)^{J_1 - J_2 - K_3}(2J_3 + 1)^{-\frac{1}{2}}\langle J_1K_1, J_2K_2 | J_3K_3\rangle \tag{2.22}$$

Explicit values of the $3j$ terms can be calculated readily using the factorial methods developed by Racah [132, 134]. In equation 2.21, μ_λ, the MF projection of the photon angular momentum, has been written as $K_i - K_g$, explicitly showing that a particular $\triangle K$ transition is only contributed to by the component of $\hat{\mu}$ for which $\mu_\lambda = K_i - K_g$. This is a consequence of conservation of angular momentum, and such conservation rules are intrinsic to the properties of the $3j$ symbol, which is non-zero only if:

$$J_1 + J_2 \geq J_3 \geq |J_1 - J_2| \tag{2.23}$$

$$K_1 + K_2 + K_3 = 0 \tag{2.24}$$

Equations 2.23 and 2.24 show the rules subsumed into the $3j$ symbol for the vector coupling of the total angular momenta vectors J, and the conservation of the (scalar) projection terms K. These properties of the $3j$ symbol mean that the rotational selection rules are also encoded in 2.21; for the 1-photon absorption shown the rotational selection rules are seen to be $\triangle J = 0, \pm 1$ and $\triangle K = 0, \pm 1$, as is well known for symmetric top rotational transitions.

2.2.2.2 Asymmetric tops

To generalize these results further it is necessary to consider the case of asymmetric tops. Most molecules fall into this category as it defines the most general case where the three moments of inertia about the body-fixed axes are not equal, $I_a \neq I_b \neq I_c$ [126]. In this case K is no longer a good quantum number and is replaced by τ. In order to make use of the previous results the rotational wavefunctions may be expanded in the symmetric top basis set:

$$|\tau JM\rangle = \sum_K a_{\tau K}|JKM\rangle \tag{2.25}$$

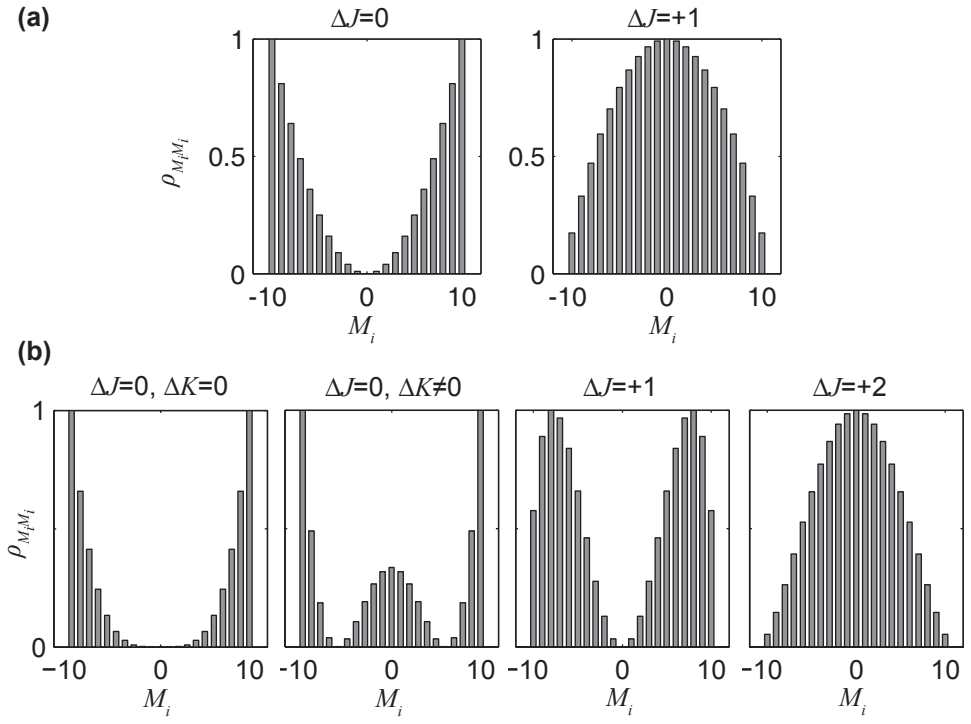

Figure 2.2: Lab frame alignments after (a) one-photon excitation, (b) two-photon excitation. In all cases $J_g = 10$ In most cases ΔK does not affect the alignment, the exception being the case for $\Delta J = 0$, $\Delta K = 0$ which is forbidden in the one-photon case.

The expansion coefficients $a_{\tau K}$ can be found by diagonalization of the asymmetric top Hamiltonian matrix. Substitution of 2.25 into the Hönl-London factors (2.21) gives

$$\boldsymbol{S}(\tau_i J_i, \tau_g J_g) = (2J_i + 1)(2J_g + 1) \left| \sum_{K_i} \sum_{K_g} a_{\tau_i K_i} a_{\tau_g K_g} \begin{pmatrix} J_i & 1 & J_g \\ -K_i & K_i - K_g & K_g \end{pmatrix} \right|^2 \tag{2.26}$$

Provided that the expansion coefficients $a_{\tau K}$ can be found, the calculation of $\boldsymbol{S}(\tau_i J_i, \tau_g J_g)$ is essentially the same as that of $\boldsymbol{S}(J_i K_i, J_g K_g)$ for the symmetric top case. The index $\tau = K_a - K_c$ can be used as a unique label [132] for each level in this expansion where K_a, K_c are the symmetric top quantum numbers in the prolate and oblate limits respectively. However, because many asymmetric molecules are near to these limits K_a or K_c can often be treated as a good quantum number and used to label asymmetric top energy levels.

2.2.2.3 Alignment

In the preceding treatment the lab frame terms M_g, M_i are reduced to degeneracy factors upon summation because the rotational line-strength depends only on molecular frame quantities. However, if the alignment of the system in the lab frame following photoabsorption is important then M_i is important because it defines this alignment, and this is indeed the case for the calculation of PADs (see Section 2.3.4, also refs. [62, 135]). The

LF alignment following absorption of linearly polarized light can be described in terms of a density matrix [62]:

$$ {}^{J_iK_i}\boldsymbol{\rho}_{M_iM_i} \propto \boldsymbol{S}(J_iK_i, J_gK_g) \sum_{M_g} \begin{pmatrix} J_g & 1 & J_i \\ M_g & 0 & M_i \end{pmatrix}^2 \tag{2.27} $$

In this form the density matrix is diagonal, and the elements provide the populations of each M_i sub-level. The summation over M_g, as written, assumes an isotropic initial distribution.[2] The presence of $\boldsymbol{S}(J_iK_i, J_gK_g)$ in this equation ensures that other factors appearing in the line strength are taken into account (for example, transitions $\Delta J = 0$, $\Delta K = 0$ are forbidden for $J = 0$). A formal treatment of density matrices is given in ref. [138], and the application to alignment is considered in more depth in ref. [132], including alternate expressions using state multipoles. Example alignments are shown in Figure 2.2 for one and two photon absorption.

This form of the density matrix is appropriate for the PAD calculations presented below (Section 2.3) provided the excitation and ionization reference frames are coincident. This amounts to the condition that the polarization vectors of the excitation and ionization laser pulses are parallel, thus there is no frame rotation between the two steps. For the more general case of non-parallel polarization vectors the situation is slightly more complex, and can be pictured as a frame rotation from the excitation frame to the ionization frame. In this case the rotation creates non-zero off-diagonal elements in the density matrix, which is denoted ${}^{J_iK_i}\boldsymbol{\rho}_{M_iM_i'}$ to signify the presence of off-diagonal elements $M_i \neq M_i'$. These off-diagonal elements represent coherences between different sub-levels which are created by the frame rotation. In the work presented here only parallel polarization geometries have been employed, so the more general form of ${}^{J_iK_i}\boldsymbol{\rho}_{M_iM_i'}$ is not considered explicitly, although the more general notation is used in Section 2.3.

2.2.3 Calculation of rotational energy levels

Section 2.2.2 considered rotational line strength factors. In order to simulate a rotational band in an absorption spectrum, the energy level structure of the rotational manifold is also required. Also, as mentioned above, in the case of an asymmetric top such a calculation will provide the coefficients $a_{\tau K}$ in the expansion of the wavefunctions in the symmetric top basis (equation 2.25).

For linear and symmetric rotors the rotational energy levels E_J have closed form equations which are easily deployed to calculate the energy levels and, when necessary, can be adapted to include terms to allow for effects such as centrifugal distortion and Coriolis coupling. In cases where there is extensive vibration-rotation coupling these closed formulae may not be appropriate and a full Hamiltonian may need to be constructed, but for the cases considered in this work they prove adequate.

[2] There is some experimental evidence that non-isotropic M_g distributions are created in molecular beams by collisional alignment (see ref. [136], Section 2.3.4 and ref. [137]), but deviations in the sub-level populations are typically $< 10\%$ from the isotropic case. Additionally, these results are for low backing pressures, and for the 2 bar backing pressures used in the experiments presented here the deviations from isotropic should be minimal.

For a linear rotor the energy levels are given by:

$$E_J = BJ(J+1) - DJ^2(J+1)^2 \tag{2.28}$$

Here B is the rotational constant and D is the centrifugal distortion constant.

For symmetric tops the prolate and oblate energy levels are given by

$$E_{JK} = BJ(J+1) + (A-B)K^2 - D_J J^2(J+1)^2 - D_{JK}J(J+1)K^2 - D_K K^4 \tag{2.29}$$

$$E_{JK} = BJ(J+1) + (C-B)K^2 - D_J J^2(J+1)^2 - D_{JK}J(J+1)K^2 - D_K K^4 \tag{2.30}$$

respectively. Here A, B and C are the rotational constants along each molecule-fixed axis, and three centrifugal distortion constants are included, relating to J, K or their cross-terms as denoted by the subscripts [126].

For an asymmetric top the prolate basis set is usually chosen for calculation of the matrix elements as many molecules approach the prolate limit. The matrix elements in K are then

$$\boldsymbol{H}_{K,K} = \langle JK|H|JK\rangle = \frac{1}{2}(B-C)[J(J+1) - K^2] + AK^2 \tag{2.31}$$

$$\boldsymbol{H}_{K,K\pm2}\langle JK \pm 2|H|JK\rangle = \frac{1}{4}(B-C)[(J^2 - (K\pm1)^2)((J+1)^2 - (K\pm1)^2)]^{\frac{1}{2}} \tag{2.32}$$

The Hamiltonian matrix thus has diagonal elements $\boldsymbol{H}_{K,K}$ and off-diagonal elements $\boldsymbol{H}_{K,K\pm2}$ representing coupling between different K of the same symmetry (odd/even). The specific cases relevant to the work in this thesis are the $\tilde{A}^1A_u$ electronic state of acetylene, and the $\widetilde{X}^1A_1'$ electronic state of ammonia. Calculations of the rotational energy levels in these cases are discussed in the relevant chapters.

That diagonalization of the Hamiltonian matrix is equivalent to solving the Schrödinger equation (SE) and finding the $a_{\tau K}$ coefficients discussed above can be seen by consideration of the SE in matrix form. The SE for a wavefunction Ψ is:

$$H\Psi = E\Psi \tag{2.33}$$

By expanding Ψ in the relevant basis set to the problem at hand, as shown in equation 2.25, the SE can be rewritten in matrix form using known basis functions:

$$H\sum_K a_{\tau K}|JKM\rangle = E\sum_K a_{\tau K}|JKM\rangle \tag{2.34}$$

Multiplying through by $\sum_{K'} a_{\tau K'}\langle JK'M|$ yields the matrix elements:

$$\sum_{K'} a_{\tau K'}\langle JK'M|H\sum_K a_{\tau K}|JKM\rangle = \sum_{K'} a_{\tau K'}\langle JK'M|E\sum_K a_{\tau K}|JKM\rangle \tag{2.35}$$

This simplifies to give

$$\sum_{KK'} a_{\tau K'} a_{\tau K} \langle JK'M|H|JKM\rangle = E \sum_{KK'} a_{\tau K'} a_{\tau K} \langle JK'M|JKM\rangle \tag{2.36}$$

$$\boldsymbol{AH_{KK'}} = \boldsymbol{A}E\delta_{KK'} \tag{2.37}$$

In this final form the matrix $\boldsymbol{A}$ is the unitary transformation matrix which diagonalizes the Hamiltonian matrix $\boldsymbol{H_{KK'}}$. The columns of $\boldsymbol{A}$ provide the eigenvectors in the basis $|JKM\rangle$, i.e. the expansion coefficients $a_{\tau K}$, and the diagonal elements of the matrix product $\boldsymbol{AH_{KK'}} = E$, the energy eigenvalues.

2.3 Photoionization

The ionization matrix elements are given in a similar manner to those for the (bound-bound) excitation step (equation 2.8), except that now the final state consists of a molecular ion and a continuum electron:

$$\boldsymbol{\mu_{i+}} = \langle \Psi_+;\, \phi_e|\hat{\mu}.\mathbf{E}|\Psi_i\rangle \tag{2.38}$$

Here the subscript i represents the state before ionization, as prepared by photon absorption and detailed in Section 2.2, and the subscript $+$ denotes the state of the ion populated by the ionization event. ϕ_e is the wavefunction of the photoelectron. As before the dipole approximation is assumed, so the dipole operator appears in the ionization, or transition dipole, matrix element.

For the discussion that follows it is useful to use a more specific notation, whereby the bra and ket vectors explicitly show the quantum numbers for the basis functions of relevance to the discussion, as with the $|JKM\rangle$ notation used above. The ionization matrix element is then written:

$$\boldsymbol{\mu_{i+}} = \langle \alpha_+ N_+ K_+ M_+ S_+;\, \mathbf{k}, l\lambda m|\hat{\mu}.\mathbf{E}|\alpha_i N_i K_i M_i S_i\rangle \tag{2.39}$$

Here N, K and M are the quantum numbers for the total angular momentum (excluding spin) and its projection onto the molecular and lab axes. For singlet states $N \equiv J$; this can also be applied in cases where the spin, S, is not strongly coupled to the system and can be neglected. α denotes any other quantum numbers required to uniquely define a state of the system (e.g. electronic and vibrational terms which are not explicitly shown). The photoelectron is labelled with the wave vector $\boldsymbol{k}$ and the orbital angular momentum l, which has projections λ in the molecular frame and m in the lab frame.

As for the bound-bound transitions discussed above it is necessary to find the square of the transition matrix elements to determine the transition probability. Furthermore, to calculate angular distributions $I(\theta, \phi)$, it is necessary to consider the *coherent* square of the transition matrix elements, rather than simply the magnitude squared. As will be shown later, the presence of coherence in the angular distributions makes them sensitive

to the relative phases of the photoelectron partial-waves, and hence a sensitive probe of the photoionization dynamics.

In the following treatment the various parts of the ionization matrix element are discussed, these parts are then combined as shown in equation 2.39 and the PAD derived as the coherent square of the ionization matrix element. This treatment follows that of Dixit and McKoy [60], and later work by Zare and co-workers [62, 93]. Aspects of this formalism have also been given, or developed, by other authors including Wang and McKoy ([3] and refs. therein) with respect to *ab initio* calculation of rotational spectra and PADs [2], and Dill [59] and Chandra [139] with regard to molecular frame PADs. It should also be noted that aspects of this treatment originate from scattering theory [140, 141]. The physical interpretation of some of the quantities derived here is considered within this framework in Appendix A, and related formalisms such as Multi-Channel Quantum Defect Theory (MQDT) and eigenchannel decomposition [93] are also discussed.

2.3.1 Photoelectron wavefunction

The photoelectron wavefunction, $|\mathbf{k}\rangle$, can be written as an expansion in radial and angular functions

$$|\mathbf{k}\rangle = \sum_{l\lambda} |\mathbf{k},\, l\lambda\rangle = \sum_{l\lambda} i^l e^{-i\eta_{l\lambda}} Y^*_{l\lambda}(\theta,\phi)\psi_{l\lambda}(r;\mathbf{k},R) \tag{2.40}$$

This is termed the *partial wave* expansion; each l-wave represents the photoelectron wavefunction for the orbital angular momentum l, i.e. an l-continuum wavefunction. In this expansion $\eta_{l\lambda}$ is the phase of the (l, λ) component of the wavefunction, $Y_{l\lambda}(\theta,\phi)$ is a spherical harmonic describing the angular structure of the wavefunction in spherical polar space (θ,ϕ), while $\psi_{l\lambda}(r;\mathbf{k},R)$ describes the radial part of the wavefunction. The angular part of the wavefunction is dependent on the direction of the wave vector; the radial component of the wavefunction is a function of r, the radial distance of the photoelectron from the origin (defined as the centre-of-mass of the molecule), and this wavefunction will also vary with the photoelectron energy ($\mathbf{k}$) and position of the nuclei defined by a set of nuclear coordinates R.

Equation 2.40 provides an exact solution to the photoelectron wavefunction in the asymptotic region, far from the ion core created by the ionization event. This is because the expansion describes the photoelectron under a central (e.g. Coulomb) potential [140], but in the ion-core region there will be a complex, non-central short-range potential. The short-range behaviour of the outgoing photoelectron may be highly sensitive to $\mathbf{k}$ and R and the asymptotic form of the wavefunction will reflect this. The continuum wavefunction, in the absence of any non-central fields, would also show a dependence on photoelectron energy, but no R dependence. In the calculation of PADs detailed below the explicit form of the radial part of the wavefunction is not considered, and it may be thought of as an expansion coefficient of $Y_{l\lambda}$ which essentially provides information on the contribution of each $Y_{l\lambda}$ to the photoelectron wavefunction. The exact form of the $\psi_{l\lambda}$ is discussed further in Appendix A. Physically, $\eta_{l\lambda}$, the total phase shift, arises from the interaction of the outgoing electron with the molecular potential. This is expanded on

in the discussions in Sections 6.2.4 and 8.3.3, in the context of the results derived from experimental data, and Appendix A.

The photoelectron wavefunction can also be cast into the LF using rotation matrix elements [62, 93], this will be useful later in terms of consideration of the LF angular distribution.

$$|\mathbf{k},\, l\lambda m\rangle = i^l e^{-i\eta_{l\lambda}} Y^*_{lm}(\theta,\phi) D^{l*}_{m\lambda} \psi_{l\lambda}(r;\mathbf{k},R) \tag{2.41}$$

2.3.2 Initial and final state wavefunctions

As discussed previously, the wavefunctions for a given state of the system can be factorized by application of the Born-Oppenheimer approximation. The states $|\alpha_i N_i K_i M_i S_i\rangle$ and $|\alpha_+ N_+ K_+ M_+ S_+\rangle$ can be expanded in electronic, vibrational and rotational components [60]:

$$|\alpha_i N_i K_i M_i S_i\rangle = \sqrt{\frac{(2N_i+1)}{8\pi^2}}\, \psi_{\alpha_i}(\{\mathbf{r_s}\};R)\chi_{v_i}(R) D^{N_i}_{M_i K_i}(\hat{R}) D^{S_i}_{M_{Si}\Sigma_i}(\hat{R}) \tag{2.42}$$

In this form $\psi_\alpha(\{\mathbf{r_s}\};R)$ is the electronic part of the wavefunction, dependent on the position vectors of the electrons in the system and the nuclear coordinates R; $\chi_v(R)$ is a vibrational wavefunction, and the rotation matrix elements are the wavefunctions for a symmetric rotor and electron spin respectively. All wavefunctions are taken to be anti-symmetrized as required by the Pauli principle. The form of $|\alpha_+ N_+ K_+ M_+ S_+\rangle$ is identical. Although spin is explicitly included in equation 2.42 it can be neglected in cases where it is uncoupled from the photoionization event. In both the acetylene and ammonia work presented in this thesis $S_i = 0$, so intermediate spin is omitted for the remainder of this derivation and $N_i \equiv J_i$.

2.3.3 Ionization matrix elements

The ionization matrix element can now be written in terms of the component wavefunctions discussed above [93]:

$$\begin{aligned}\langle \alpha_+ N_+ K_+ M_+ S_+;\, \mathbf{k}, l\lambda m|\hat{\mu}.\mathbf{E}|\alpha_i N_i K_i M_i\rangle = \\ &\left(\frac{4\pi}{3}\right)^{\frac{1}{2}} \frac{1}{8\pi^2}(2N_i+1)^{\frac{1}{2}}(2N_++1)^{\frac{1}{2}} i^{-l} e^{i\eta_{l\lambda}} Y_{lm}(\theta,\phi) \\ \text{x} \quad &\int d\Omega\, D^{N_+*}_{M_+K_+} D^{S_+*}_{M_{S+}\Sigma_+} D^{l}_{m\lambda} D^{1*}_{\mu_0\mu_\lambda} D^{N_i}_{M_iK_i} \\ \text{x} \quad &\int dR\, \chi_{v_+} \langle \psi_{\alpha_+};\, \psi_{l\lambda}| \sum_s r_s Y_{1\mu_\lambda} |\psi_{\alpha_i}\rangle \chi_{v_i}\end{aligned} \tag{2.43}$$

In writing this form of the matrix element the dipole operator has been expressed in a similar manner to that shown in equation 2.18, except that spherical harmonics are used:

$$\hat{\mu}.\mathbf{E} = \sum_s r_s \sum_{\mu_\lambda} D^{1*}_{\mu_0\mu_\lambda}(\hat{R}) Y_{1\mu_\lambda}(\hat{r_s}) \tag{2.44}$$

where equation 2.6 has been used to expand $\hat{\mu}$. The summation is over all electrons s, and over the MF projection μ_λ of the photon angular momentum.

The structure of equation 2.43 brings out some of the fundamental physics of the ionization process under the BO approximation. The two integrations, over angular space $d\Omega$ and the radial coordinate dR, allow the angular momentum part of the ionization matrix element to be separated from the radial part. The angular part can be readily calculated using standard angular momentum algebra, and will be generally applicable to any system in the same rotational basis (Hund's case) - this is usually termed the *geometric* part of the problem. The second integral, involving the vibrational and electronic wavefunctions, is a more complicated function of the electronic and nuclear coordinates of the system, and the radial part of the photoelectron wavefunction. The value of this integral is therefore dependent on the wavefunction overlap between the initial, final and photoelectron wavefunctions, which will include a dependence on the photoelectron energy/wave vector. This is usually termed the *dynamic* part of the problem, it will be unique to the system under study and may be said to determine the photoionization dynamics.

The two integrations can now be considered in more detail in order to derive a more useful form of equation 2.43. The integration over $d\Omega$ can be written in terms of the Wigner $3j$ symbols introduced previously:

$$\int d\Omega\, D^{N_+*}_{M_+K_+} D^{S_+*}_{M_{s+}\Sigma_+} D^{l}_{m\lambda} D^{1*}_{\mu_0\mu_\lambda} D^{N_i}_{M_iK_i} =$$

$$\begin{aligned}
& \sum_{N_t} 8\pi^2(2N_t+1)(-1)^{M_++\mu_\lambda} \begin{pmatrix} N_t & 1 & l \\ M_t & \mu_0 & m \end{pmatrix} \begin{pmatrix} N_+ & N_i & N_t \\ -M_+ & M_i & M_t \end{pmatrix} \\
\times & \begin{pmatrix} N_+ & N_i & N_t \\ -K_+ & K_i & K_t \end{pmatrix} \begin{pmatrix} N_t & 1 & l \\ -K_t & \mu_\lambda & -\lambda \end{pmatrix} \\
\times & \begin{pmatrix} N_+ & J_+ & S_+ \\ M_+ & M_{J+} & M_{S+} \end{pmatrix} \begin{pmatrix} N_+ & J_+ & S_+ \\ K_+ & P_+ & \Sigma_+ \end{pmatrix} \qquad (2.45) \\
= & \sum_{N_t} 8\pi^2 C(lm\lambda N_t M_i \mu_\lambda) \qquad (2.46)
\end{aligned}$$

In this form the first two $3j$ terms couple the angular momenta of the intermediate state (N_i), the ion (N_+), the photon (1) and the photoelectron (l) in the LF, through the coupling, or transfer, angular momenta N_t and its LF projection M_t. The next two $3j$ symbols couple the MF components of these angular momenta. The remaining two terms decouple the spin (S_+) from the total angular momentum (J_+) to give N_+; again there are terms for the LF and MF. Only spin terms for the ion state are included. As mentioned previously, in cases where spin is not important these terms can be omitted; in fact, they are only really relevant when geometric terms between different spin-orbit states are to be calculated and in these cases they will provide information on the relative transition intensities of the spin-orbit components. An important point regarding the angular momentum coupling scheme shown here is that the $3j$ symbols are readily computed, but that the complexity of the coupling through multiple interactions makes intuitive insight difficult. It should also be noted that while equivalent formalisms have been derived by

several authors there are often subtle differences in the phases and ordering of the terms within each $3j$ symbol, and the phase term appearing at the beginning of equation 2.46. These differences are generally not significant and simply reflect the cyclic-permutation behaviour of the $3j$ symbol.

In the final line of equation 2.46 the $3j$ terms are defined as the coefficient $C(lm\lambda N_t M_i \mu_\lambda)$. Here the terms in the bracket reflect the angular momenta for which coherences will be important when the coherent square of the matrix elements is derived. This definition allows for more compact notation without the need to explicitly write all the necessary $3j$ terms.

The radial integrals involved in the ionization matrix elements (equation 2.43) are difficult to calculate *ab initio* because, as discussed above, evaluation requires explicit evaluation of all the relevant wavefunctions. They are therefore designated as expansion parameters for l, λ, and the notation simplified to reflect this:

$$\boldsymbol{r}_{l\lambda} = \int dR\, \chi_{v_+} \langle \psi_{\alpha_+};\, \psi_{l\lambda} | \sum_s r_s Y_{1\mu_\lambda} | \psi_{\alpha_i} \rangle \chi_{v_i} \tag{2.47}$$

The $\boldsymbol{r}_{l\lambda}$ are the vibrationally-averaged radial components of the ionization matrix element linking the initial state of the system to the ionizing photon, the final ion state and the outgoing photoelectron. Following this, equation 2.43 can be written in a simplified form:

$$\begin{aligned}\langle \alpha_+ N_+ K_+ M_+ S_+;\, \mathbf{k}, l\lambda m | \hat{\mu}.\mathbf{E} | \alpha_i N_i K_i M_i S_i \rangle = \\ \left(\frac{4\pi}{3}\right)^{\frac{1}{2}} (2N_i+1)^{\frac{1}{2}} (2N_+ + 1)^{\frac{1}{2}} i^{-l} e^{i\eta_{l\lambda}} \boldsymbol{r}_{l\lambda} Y_{lm}(\theta,\phi) \\ \text{x} \quad \sum_{N_t} C(lm\lambda N_t M_i \mu_\lambda)\end{aligned} \tag{2.48}$$

2.3.4 Observables

As for the bound-bound line strengths discussed in Section 2.2.1, and indeed any real, physical observable, the square of the matrix elements is required in order to calculate the ionization flux of the system. Consideration of the coherent square of the transition matrix elements enables an expression describing the differential cross-section to be found, providing a full description of the PADs.

Making use of equations 2.46 and 2.48, the coherent square of the ionization matrix element can be found [60, 62]. This is denoted $I(\theta, \phi)$, the photoelectron flux as a function of angle. At this stage summations over the unobserved terms are also included, with coherent pairs of terms denoted with primes, for example ll' is used to label the

double sum over l and l'.

$$\begin{aligned} I(\theta,\phi) &= \sum_{M_+}\sum_{M_iM_i'}\sum_{ll'}\sum_{\lambda\lambda'}\sum_{mm'}\sum_{\mu_\lambda\mu_\lambda'}\langle\alpha_+N_+K_+M_+S_+;\ \mathbf{k},l\lambda m|\hat{\mu}.\mathbf{E}|\alpha_iN_iK_iM_iS_i\rangle \\ &\quad \langle\alpha_iN_iK_iM_iS_i|\hat{\mu}^*.\mathbf{E}|\alpha_+N_+K_+M_+S_+;\ \mathbf{k},l\lambda m\rangle^{J_iK_i}\boldsymbol{\rho}_{M_iM_i'} \\ &= \sum_{ll'}\sum_{\lambda\lambda'}\sum_{mm'}\boldsymbol{r}_{l\lambda}\boldsymbol{r}_{l'\lambda'}e^{i(\eta_{l\lambda}-\eta_{l'\lambda'})}Y_{lm}Y^*_{l'm'} \\ &\times\ (2N_i+1)(2N_++1)(-i)^{l'-l}\sum_{M_+}\sum_{M_iM_i'}\sum_{N_tN_t'}\sum_{\mu_\lambda\mu_\lambda'}{}^{J_iK_i}\boldsymbol{\rho}_{M_iM_i'} \\ &\times\ C(lm\lambda N_tM_i\mu_\lambda)C(l'm'\lambda'N_t'M_i'\mu_\lambda') \end{aligned} \tag{2.49}$$

The summation in the first line of equation 2.49 can be understood as a summation over all unobserved final states, where the initial M_i population is described by ${}^{J_iK_i}\boldsymbol{\rho}_{M_iM_i'}$. Coherences arise where multiple quantum pathways are available to the same final state, for example the photoelectron partial wave terms are coherent as different partial wave components can populate the same final ion state. As before this equation can be simplified and its structure emphasized, rewriting the second set of summations of equation 2.49 in a more compact notation gives:

$$I(\theta,\phi)=\sum_{ll'}\sum_{\lambda\lambda'}\sum_{mm'}\gamma_{N_+l\lambda ml'\lambda'm'}\boldsymbol{r}_{l\lambda}\boldsymbol{r}_{l'\lambda'}e^{i(\eta_{l\lambda}-\eta_{l'\lambda'})}Y_{lm}Y^*_{l'm'} \tag{2.50}$$

In this form the separation of geometrical and dynamical parameters in the photoionization problem is again highlighted, now $\gamma_{N_+l\lambda ml'\lambda'm'}$ denotes the *geometrical* parameters and incorporates all of the angular momentum coupling in the system, including the initial alignment (as shown explicitly in the final two lines of equation 2.49). The dynamical parameters $\boldsymbol{r}_{l\lambda}$ and associated phases $\eta_{l\lambda}$ are as previously, and the angular variation of the observed, LF, photoelectron flux arises as the product of the two spherical harmonics, $Y_{lm}Y^*_{l'm'}$.

Although equation 2.50 completely describes the observed PAD it is instructive to compare this form to the simpler expansion in Y_{LM} and β_{LM} which also parameterizes the observed angular distribution (see Section 1.4.1). For a $n+m$ REMPI scheme with linearly polarized light and parallel polarization vectors $M=0$, equation 1.4 can be written:

$$I(\theta,\phi)=\sum_{L=0}^{L_{max}}\beta_{L0}Y_{L0} \tag{2.51}$$

Here $L_{max}=2(n+m)$ and L can only take even values. The limit on the summation arises due to the anisotropy of the intermediate state created by absorption of n photons, the ionizing photon probes this anisotropic distribution so the highest multipole moment observed in the LF cannot be any greater than the angular momentum (and therefore anisotropy) imparted by the $(n+m)$ photon process. By comparison with equation 2.50, and using the Clebsch-Gordan series to rewrite the spherical harmonic product [132], the

β_{LM} can be expressed in terms of the dynamical and geometrical parameters:

$$\begin{aligned}\beta_{LM} &= \sum_{ll'}\sum_{\lambda\lambda'}\sum_{mm'}(-1)^m\sqrt{\frac{(2l+1)(2l'+1)(2L+1)}{4\pi}} \\ &\times \begin{pmatrix} l & l' & L \\ m & -m' & M \end{pmatrix}\begin{pmatrix} l & l' & L \\ 0 & 0 & 0 \end{pmatrix}\gamma_{N_+ l\lambda m l'\lambda' m'} \\ &\times \boldsymbol{r}_{l\lambda}\boldsymbol{r}_{l'\lambda'}\cos(\eta_{l\lambda}-\eta_{l'\lambda'})\end{aligned} \tag{2.52}$$

Again this form emphasizes the separation of the geometric and dynamic parts of the ionization. It also emphasizes how the form of the PAD arises from the interference of different partial wave components, as shown by the $\cos(\eta_{l\lambda}-\eta_{l'\lambda'})$ term. This interference is apparent in the full form of $I(\theta,\phi)$ shown in equation 2.50, but the reduction to a single spherical harmonic term makes interpretation of this physical process somewhat more intuitive. This interference is also the reason that measurements of the PAD are so powerful; they can now be seen to yield direct information on both the magnitudes and phases of the radial dipole matrix elements, and therefore have the potential to be used experimentally to determine the partial wave components of the photoelectron wavefunction.

2.4 Symmetry Selection Rules

Consideration of symmetry provides a means of determining which ionization matrix elements will be non-zero without the need for detailed calculations. In the molecular case, such considerations are vital to restrict the number of allowed partial wave components, which may otherwise be very large. Particularly lucid treatments of symmetry in molecular spectroscopy are given by Bunker and Jensen [127], and the specific case of photoionization is expanded on in the work of Signorell and Merkt [142]. The comments here are drawn primarily from these sources, although many other texts discuss the application of symmetry to dipole matrix elements.

For the dipole matrix element to be non-zero the direct product of the initial state, final state and dipole operator symmetries must contain the totally symmetric representation of the molecular symmetry (MS) group (isomorphic to the point group in rigid molecules):

$$\Gamma^f_{rve}\otimes\Gamma_{dipole}\otimes\Gamma^i_{rve}\supset\Gamma^s \tag{2.53}$$

Here Γ_{rve} is the rovibronic symmetry of the system (i.e. total symmetry excluding spin), with the i/f superscript denoting initial and final states respectively. Γ^s is the totally symmetric representation in the appropriate molecular symmetry group, and Γ_{dipole} is the symmetry of the dipole operator. Because the dipole operator is antisymmetric with respect to inversion,

$$\Gamma_{dipole}=\Gamma^* \tag{2.54}$$

where Γ^* is the antisymmetric representation in the MS group, and equation 2.53 reduces

to [127]:

$$\Gamma^f_{rve} \otimes \Gamma^i_{rve} \supset \Gamma^* \tag{2.55}$$

For the specific case of photoionization the final state is split into the symmetry species of the ion and the photoelectron [142]:

$$\Gamma^e \otimes \Gamma^+_{rve} \otimes \Gamma^i_{rve} \supset \Gamma^* \tag{2.56}$$

Here the superscript e denotes the symmetry of the photoelectron wavefunction, and $+$ the ion. At short range this equation represents the eigenchannel solutions to the molecular potential, and Γ^e must be considered in the appropriate MS group. Because the photoelectron symmetry depends on Y_{lm} this necessitates evaluating the symmetries of the spherical harmonics in the MS group, and the photoelectron wavefunction can be considered in a symmetry adapted basis which takes account of this [96, 139]. At long range the situation is considerably simpler as the photoelectron is considered in a central-potential, and the ion is considered as a point charge defining the coordinate origin. In this case symmetry need only be assigned with respect to coordinate inversion, so the photoelectron symmetry becomes [142]:

$$\begin{aligned} \Gamma^e &= \Gamma^s\,(even\,l) \\ &= \Gamma^*\,(odd\,l) \end{aligned} \tag{2.57}$$

The general selection rule, equation 2.56, can then be re-written for the even and odd l continua:

$$\Gamma^+_{rve} \otimes \Gamma^i_{rve} \supset \Gamma^*\,(even\,l) \tag{2.58}$$

$$\Gamma^+_{rve} \otimes \Gamma^i_{rve} \supset \Gamma^s\,(odd\,l) \tag{2.59}$$

The application of these rules to the specific ionization events considered in experiments on acetylene and ammonia is discussed in Chapters 6 and 8.

2.5 Calculation of PADs

As shown in equation 2.52, PADs can be calculated with knowledge of the geometrical and dynamical parameters. The angular momentum algebra involved in calculation of $\gamma_{N_+ l\lambda m l'\lambda' m'}$ is complex and non-intuitive, but can be readily evaluated using standard algorithms. To this end, code for the evaluation of $\gamma_{N_+ l\lambda m l'\lambda' m'}$ was developed in C, based upon the formalism of Racah [132, 134] and earlier implementations using FORTRAN by Zare and co-workers [132]. The code was tested for consistency against similar calculations by Reid and Leahy [143].

The *ab initio* evaluation of the dynamical parameters requires calculation of the initial and final state wavefunctions so that the radial integrals (equation 2.47) can be solved numerically (see also Section 1.4.5, and Appendix A). This is a difficult problem, and

beyond the scope of this work. Despite this limitation, by setting the dynamical parameters to arbitrary values the response of the PADs to the geometrical parameters can be probed. Because of the symmetry restrictions discussed above, limitations can also be placed on which matrix elements will be non-zero without explicit calculation of the radial integrals. In this manner model systems based on molecular symmetry can be examined [96, 144], and the response of the PAD to various effects, such as intermediate state alignment or ionizing transition, can be examined.

Combined with experimental PADs, calculation of the geometrical parameters presents the opportunity to determine $\boldsymbol{r}_{l\lambda}$ and $\eta_{l\lambda}$ by a fitting procedure [34, 94, 145], as discussed in Chapter 1. Because the experimental work detailed in this thesis made use of pump-probe schemes via single rotational levels in the intermediate state, the geometrical parameters could be calculated and, providing enough experimental data was obtained, fitting could be carried out to determine the dynamical parameters. The fitting procedure is detailed further in Section 4.3.

2.6 Summary

This chapter has outlined the theoretical treatment of photon absorption and photoionization, considered as a two-step, pump-probe, process. All of this machinery is used for the experimental work and analysis presented in the following chapters. The formalism described in Section 2.2 has been used to calculate REMPI spectra and intermediate state alignments. The formalism presented in Section 2.3 (along with the fitting methodology detailed in Section 4.3) is applied in order to calculate PADs and fit the experimental data to determine the dynamical parameters.

Chapter 3

Velocity-Map Imaging & Experimental Techniques

The aim of this chapter is to describe in detail the experimental technique of velocity-map imaging (VMI) and associated issues. An overview of the technique is presented, followed by specific details and considerations pertinent to the experimental apparatus used in this work. The final sections of this chapter detail the experimental techniques which were employed in recording the experimental data presented in Chapters 5 and 7.

3.1 The VMI Spectrometer

The general principles of VMI have been introduced in Section 1.3.2. A more detailed exploration of each component of the VMI spectrometer is presented in this section.

In this work two different VMI spectrometers were used, hereby referred to as Spec1 (constructed 2002) and Spec2 (constructed 2006/2007, from an existing vacuum chamber). For the experimental work on acetylene Spec1 was used, while work on ammonia used Spec2. Broadly speaking the two spectrometers can be viewed as identical, and are both based on the same Eppink and Parker design [39]. Figure 3.1 shows a detailed schematic and photographs. Each of the important elements of the spectrometer design is discussed in the following sub-sections and minor differences between the two spectrometers are highlighted where applicable.

3.1.1 Electrostatic lens

The action of the 3-element electrostatic lens used in VMI was first considered by Eppink and Parker [39], and is conceptually very similar to the Wiley-McLaren, grid-based 'ion-gun' originally developed in the 1950s for time-of-flight mass spectrometers [146]. In the Wiley-McLaren configuration flat electric field lines (i.e. a linear field gradient) are created using solid lens elements (referred to as repeller, extractor and ground as shown in Figure 3.2) with transmission grids to allow the ejection of ions or electrons towards a detector. The lens is space focusing, meaning that particles with the same mass, but

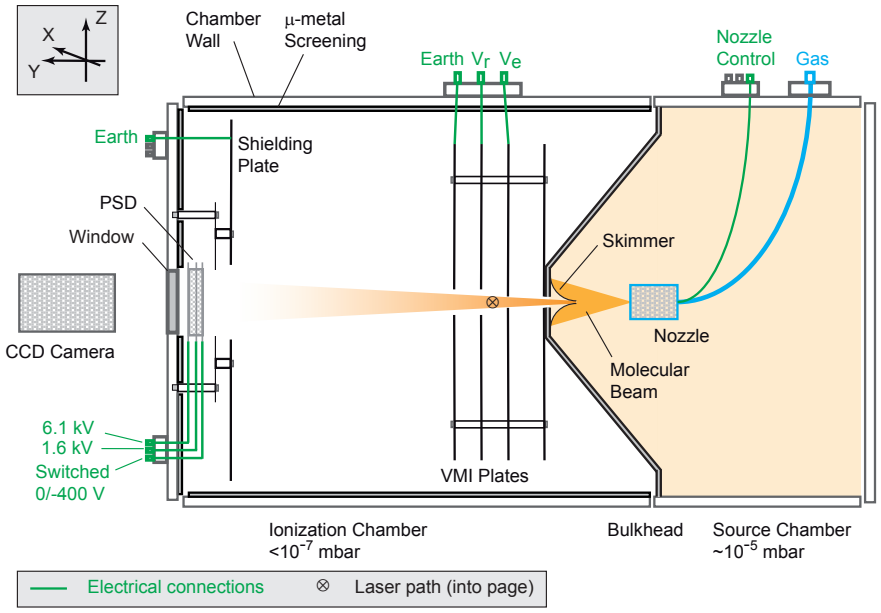

(a) Detailed schematic of the VMI spectrometer (Spec2 - see text).

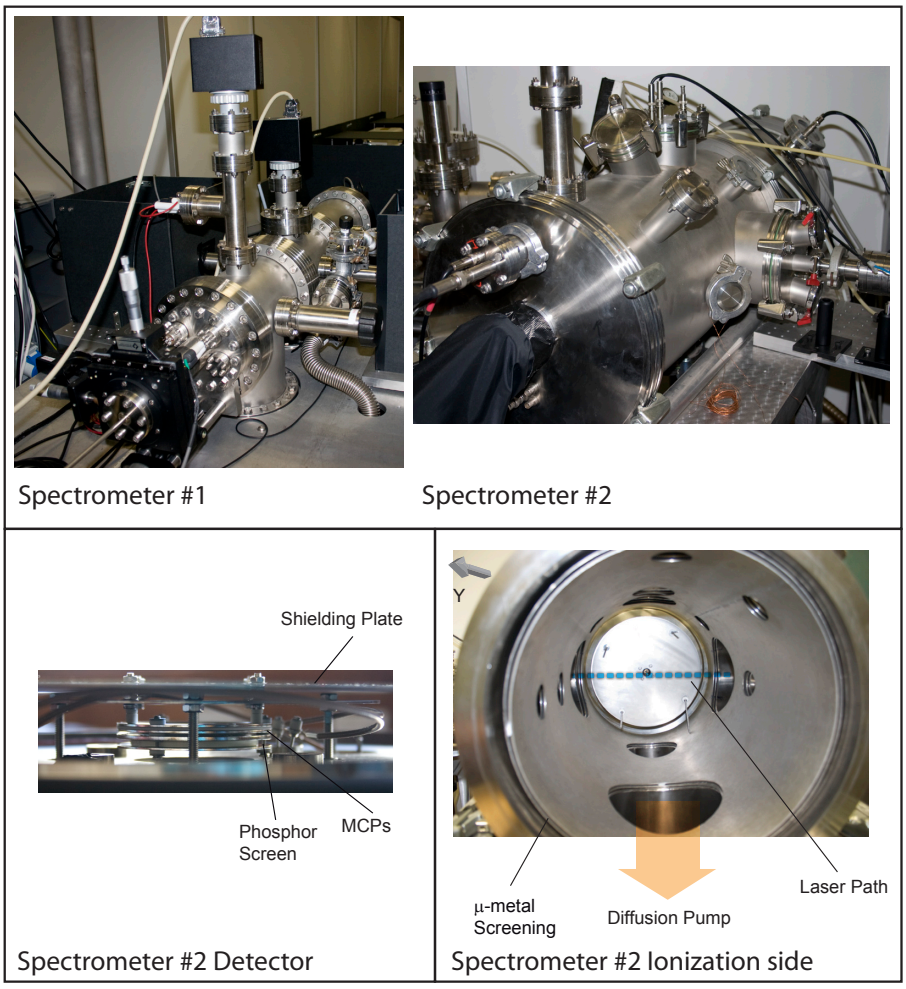

(b) Photographic detail of the spectrometers used in this work.

Figure 3.1: VMI spectrometer schematic and images.

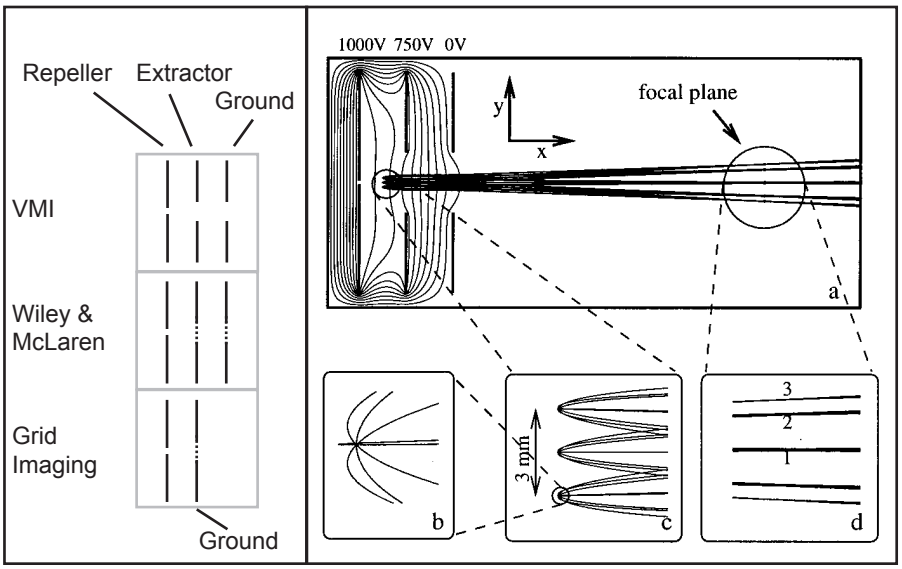

Figure 3.2: (Left panel) Comparison of different electrostatic lens configurations. (Right panel) Action of velocity-mapping electrostatic optics. Particles are velocity-mapped at the focal plane. Right panel reproduced from ref. [39].

born at different points in the ionization volume, will arrive at the detector with the same time-of-flight. In the VMI arrangement the removal of the grids and careful tuning of the field gradients between the lens elements results in velocity mapping, improving spatial resolution for imaging by removing the effects of an extended ionization region much as the Wiley-McLaren arrangement improves temporal resolution for time-of-flight work.

The main considerations for the design of the electrostatic lens are:

- Element material & homogeneity
- Element spacing
- Operational voltages
- Distortions of lensing electric fields

The lens elements in both spectrometers used in this work were manufactured from non-magnetic stainless steel, and the elements constructed with the same sized central holes, 4 mm in the repeller plate and 20 mm in the extractor and ground plates - similar to the original Eppink and Parker design [39]. The difference between the two spectrometers is the diameter of the lens elements, 150 mm in Spec1 and 260 mm in Spec2; the element spacing in Spec1 is fixed at 15 mm, while the lens assembly in Spec2 is designed to allow easy adjustment of this spacing over a range of 15-30 mm. The larger plate diameter in Spec2 is feasible because of the larger dimensions of the vacuum chamber. Simulations using SIMION 7 have shown that the larger diameter may have some benefits by acting to remove the edges of the plates and associated electric field distortions (*edge effects*) further from the ionization volume. There is also evidence from these simulations that a larger plate spacing improves the velocity-mapping action of the lens by allowing a reduction in the field gradients.

Mode	Gate	MCP front /kV	MCP rear /kV	Screen /kV
Ion	Off	**0**	1.2	6.1
	On	**-0.4**	1.2	6.1
Electron	Off	0	**1.2**	6.1
	On	0	**1.6**	6.1

Table 3.1: Typical operating voltages for MCP and phosphor screen

The exact voltages used for the repeller and extractor plates when recording a photoelectron image will depend on the energies of the photoelectrons. Imaging of higher energy electrons will require larger electric fields to create the necessary field gradients to steer fast electrons to the detector. Photoelectron kinetic energies of 1 eV (8000 cm^{-1}) require a repeller voltage $V_r \simeq 1.4$ kV in Spec1 (flight tube 300 mm, detector diameter 40 mm). For velocity-mapping the ratio of extractor to repeller voltages, V_e/V_r, is $\simeq 0.7$ [39], and the precise ratio will be a characteristic of the spectrometer. Optimal voltages for a given experiment correspond to good velocity mapping and maximum image size on the detector; in this way the best energy resolution can be obtained (see Section 3.2).

3.1.2 Position sensitive detector

In order to image the charged particle velocity distribution in 2D some kind of position sensitive detection (PSD) is required. In general the design of a PSD will involve amplification of the incident particles, and some method of recording impact locations. The amplification stage is handled by two microchannel plates (MCPs) arranged in a chevron stack (Spec1 - Photek, Spec2 - Burle). Usual operating voltages are shown in Table 3.1. The gain of the stack is $> 10^6$ when gated on, and the *dark signal* (i.e. MCP gate off) level is $< 1\%$ of the on signal [147]. Gating the detector thus allows discrimination against any background signal which could be picked up between laser pulses, and may also facilitate recording of only part of an ion signal if the gate width can be made small enough[1].

The gating was controlled by a high-voltage switching box (Photek GM1KV) which stepped the supplied voltages with a rise time on the order of 50 ns. During recording of photoelectron images the gate on-time was typically 1 μs, this was much longer than the spread of arrival times of the photoelectrons ($<<$ 1 ns) but short enough to gate out much of the background signal. Moving to shorter on times showed no significant reduction in background, but when set to $<$ 300 ns the signal intensity was observed to decrease, suggesting a longer rise time than the 50 ns specified for the GM1KV unit. In contrast, on times longer than 1 μs showed large increases in background noise, although the exact source of this noise was unclear.

The second part of the PSD is made up of a phosphor screen to convert the particle

[1]Such fast gating could be used, for example, to directly image slices through the Newton spheres of ions [148] (although slice imaging may also be achieved by other methods, see for example [149]). For electrons this scheme would not be practical due to the small spread in arrival times. Fast gating can also be used to provide mass selectivity of ions.

positions to visual data ("read out" the particle impacts), and a CCD camera to capture and digitize this data. Each frame of data from the camera is read into a PC via a Firewire connection, and frames are accumulated to produce the final image. Two software packages have been used for data capture, IFS32 supplied by Photek and code created in-house running within the MATLAB environment.

The shutter speed of the CCD was typically several hundred μs, much longer than the on time of the detector in order to capture the full fluorescence lifetime of the phosphor screen. A shorter shutter speed made no significant difference to the quality of the photoelectron images obtained, although signal intensity decreased for shutter speeds below $\sim$40 μs. Longer shutter speeds also had no significant effect on the photoelectron images, although the signal to noise ratio was seen to decrease. This reflects the fact that a CCD not exposed to any incident radiation will still generate *dark signal* due to thermal fluctuations in the CCD (and also due to any imperfections in the light-proofing of the camera enclosure), hence a longer exposure time without any increase in the fluorescence lifetime of the phosphor screen will result in a larger contribution from dark noise in the final image. Similarly, although the MCP dark signal is $< 1\%$ of the on signal, a long exposure time on the CCD could pick up some of this dark signal which would further contribute to the noise in the final image. Given that the duty-cycle in a 10 Hz experiment with ns laser pulses is very small, it might be expected that even a 1% dark signal could make a significant contribution to the final image if excessively long shutter speeds were used. These issues with dark signal could be an important consideration if on-chip integration, and hence much longer exposures recording several laser pulses, were used. This could be the case if the camera was free-running, rather than trigger-synched with the lasers.

The specifications of the detector are one of the main determining factors of the energy resolution of the spectrometer. A particle incident on the front MCP will eject electrons from the coated glass substrate, these cascade down the pore creating an electron avalanche which propagates along the pore [150]; this physical process is the source of the high gain of MCPs, and each MCP pore can be recognized as a continuous dynode. Figure 3.3(a) shows a schematic of an MCP chevron stack and the path of an electron avalanche signal. Consideration of the spreading of a charge cloud during this process illustrates how the spatial resolution of the MCP array will be determined by the physical size of the electron cloud ejected from the rear of the stack. In the limiting case of no transverse growth of the electron cloud between the rear MCP and the phosphor screen, the width of a spot on the screen is equal to the pore size of the MCPs [150], hence the smaller the pore size the better the spatial resolution of the detector. In practice there will be some dispersion of the electron cloud, and in a chevron stack there is the possibility of the cascade lighting up more than one pore on the second MCP, as shown in Figure 3.3. The pitch (pore-to-pore spacing) of the MCPs will also affect their spatial resolution, and this measurement takes into account the thickness of the substrate between neighbouring pores. For example, MCPs with 10 μm pores typically have a pitch of 12 μm. The front of the MCP therefore has structure which will be opaque to particle impacts, although

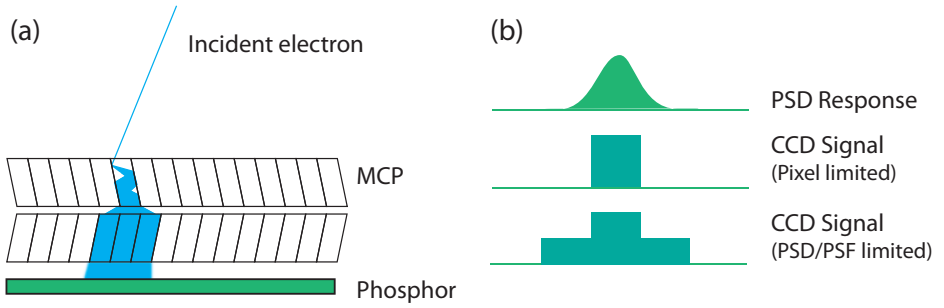

Figure 3.3: (a) MCP chevron stack operation, based on ref. [150]. (b) Detector response and limiting cases, see text for details.

this area is minimal relative to the pore area.

Both spectrometers used in this work are fitted with 40 mm diameter MCP stacks with 10 μm pore size and 12 μm pitch. A simple area calculation, using the pitch as the limiting factor, yields the area per pore as 78 μm^2, with 11 million pores in total. Spatial resolution is often quoted in lines per mm, or line pairs per mm, using this measurement gives a resolution of 40 line pairs (LP) per mm [151]. Assuming no change to the spatial resolution due to the phosphor screen, the CCD camera would require an 11 mega-pixel or better chip to record the full-resolution of the MCPs. The camera used for Spec1, a Basler A302f, features 8.3x8.3 μm pixels on a 0.5" (12.7 mm) chip, giving a total resolution of 582x782 pixels[152], or $\sim$0.5 mega-pixels. Spec2 uses a higher resolution camera, Basler A601f, capable of 1024x768 pixel resolution. In both cases, therefore, it seems as though the camera pixel resolution should be the limiting factor. Figure 3.3(b) illustrates how a Gaussian spot from the PSD might be recorded for pixel-limited and PSD limited cases.

Rough calculations can be used to determine the area, and therefore number of pores, imaged by the CCD. Taking the maximum pixel diameter of an imaged disc to be the shorter dimension of the CCD (i.e. 582 or 768 pixels for the two cameras mentioned above) the figures are 42 and 24 MCP pores per CCD pixel; these figures are consistent with the drop in pixel resolution to around 5-10% of the required 11x10^6 pixels. In terms of LP per mm these cameras give limits of 7 and 10 LP per mm respectively; this can be contrasted with the figure of $\sim$0.15 mm per event - or 3 LP per mm - quoted by Eppink and Parker in their original work on VMI [39] using a camera resolution of 384x286 pixels.

In practice single photoelectron impacts or spots which span several camera pixels with an approximately Gaussian intensity distribution are observed, typically a 3x3 pixel spot corresponding to a spot of $\sim$0.2 mm diameter on the phosphor. This immediately suggests that it is not the CCD chip which is the limiting factor in the PSD assembly, but in fact the size of the spot being imaged (as illustrated in Figure 3.3(b)). Although this spot size is much larger than calculations using the MCP pore size as a limiting factor suggest, it is consistent with some transverse spread of the MCP electron avalanche, and a significant point spread function[2] (PSF) for the phosphor screen and camera lens assembly. The PSF defined in this way will be dependent on both the response of the phosphor to the

[2]The point spread function is defined as the convolution of an instrument function, $g(x, y)$, and an image function, $f(x, y)$. It describes the instrumental broadening of each image point [128].

incident electron avalanche and the quality of the optics in the CCD camera. Houston et. al.[153] quote a 0.2 mm ion spot radius in their work yielding spot sizes on the order of 5x5 pixels, and attribute this to the action of the image intensifier (i.e. the MCP and phosphor screen). Eppink and Parker comment [37] that the phosphor response typically leads to impact spots of ∼0.1 - 0.2 mm, again consistent with the figures observed in this work. These considerations lead to the conclusion that although the MCP pore size will affect the spectrometer resolution in terms of the absolute spatial response of the MCPs to a particle impact on the front plate, the resolution of the recorded image is somewhat reduced from this limiting case, and this blurring is primarily due to the response of the phosphor.

Further discussion of spectrometer resolution, in terms of the overall velocity and energy resolution achieved, and factors other than the PSD which affect this resolution, will be presented in Section 3.2.1.

3.1.3 Supersonic molecular beam

The species under investigation is introduced into the spectrometer by a pulsed valve (General Valve Series 9, controlled by General Valve Iota 1 nozzle driver). Adiabatic cooling occurs as the sample gas, often seeded in an argon or helium carrier gas, is expanded from a high pressure reservoir (typically held at 2 bar) behind the pulsed valve (0.8 mm diameter orifice) to the vacuum chamber. Pulse lengths of ∼ 180 - 220 μs were typical in this work, although the optimum pulse length varied slightly during the experimental run due to aging of the poppet in the nozzle, or as a consequence of changes to the gas mixture used. The source chamber maintained a base pressure of $\sim 10^{-8}$ mbar, and a working pressure of $\sim 10^{-5}$ - 10^{-6} mbar.

Cooling occurs due to the large number of collisions within the gas as it passes through the orifice, and in the region of *hydrodynamic flow* immediately after. After this hydrodynamic region *molecular flow* is obtained, here the collisions have served to collapse the translational velocity distribution of the thermal sample to a well defined and directed beam velocity [133]. This produces a supersonic expansion, or supersonic molecular beam, with a very low translational temperature T_{trans} but high absolute velocity in the direction of the beam. Low rotational (T_{rot}) and vibrational (T_{vib}) temperatures are also achieved in the beam. Beam temperature will depend on a number of factors, such as orifice size, gas pressure, sample concentration and so on, but typical temperatures for a supersonic beam are $T_{trans} < 1K$, $T_{rot} < 10K$ and $T_{vib} < 100K$ [133]. The temperature of a beam can be found accurately by recording and analyzing an absorption spectrum via a REMPI scan (see Sections 3.3.4, 5.4 and 7.3), the features of the spectrum are dependent on the ground state vibrational and rotational populations of the system and will thus reflect T_{rot} and T_{vib}.

The velocity spread can be probed by looking at the Doppler profile of spectral lines [133]. By using a crossed-beam geometry (see Figure 3.1), where the laser beams are perpendicular to the beam propagation direction (and this propagation direction is towards the detector), only the transverse velocity spread of the molecular beam will be important.

This distribution is improved by collimation of the beam by a skimmer (Beam Dynamics, 0.7 mm orifice), mounted on a bulkhead which also serves to separate the *source* and *ionization* regions of the spectrometer. For photoelectrons a small ($\sim$few ms^{-1}) transverse velocity spread in the molecular beam is negligible relative to their velocity and will not serve to blur the photoelectron image - this situation can be contrasted with, for example, photofragment imaging where obtaining a small velocity spread in the molecular beam is vital to achieve high velocity resolution (for further discussion on this point see Chapter 2 in reference [37], and reference [45]). For these reasons characterization of the velocity profile of the molecular beam has not been performed in this work.

3.1.4 Field-free flight region

The main body of the ionization side of both spectrometers is a field-free, high vacuum region maintained at $\sim$10^{-7} - 10^{-8} mbar working pressure. The chamber is magnetically shielded using μ-metal, a specially developed alloy with high magnetic permeability [154] used for shielding experimental regions from the Earth's magnetic field as well as any locally-generated stray fields. Times of flight for ions are on the order of μs, while electron time of flight is on the order of ns as they are accelerated to much higher velocities by the VMI electric field. The flight time t scales as $\sqrt{m/qV_r}$, where m is the particle mass and q its charge [39]. For ions mass analysis can therefore be performed by measuring the arrival time to the detector.

For VMI the length of the field-free region is not critical but, as shown by Eppink and Parker [39], it will have some effect on the magnification factor of the spectrometer and hence the width (spread) and radius of rings in the final image. The optimum ratio for velocity-mapping, V_e/V_r, is also affected. In Spec1 the flight tube, as measured from the ionization region to the PSD, is $\sim$30 cm, while in Spec2 it is $\sim$50 cm. The larger size of Spec2 is a consequence of the size of the existing vacuum chamber, rather than a VMI spectrometer design decision. For photoelectrons of a given kinetic energy the resolution is thus expected to be similar in both spectrometers, but the voltages used for the electrostatic lens in Spec2 will be higher to compensate for the increased magnification due to a longer flight tube, but no increase in detector radius. As yet a systematic comparison of the two spectrometers has not been carried out due to the extended development period of Spec2.[3]

3.2 Photoelectron Velocity & Energy Resolution

The spatial resolution of the detection system has already been discussed, and it is expected that this is the limiting factor on the overall resolution of the VMI spectrometer, but this resolution has yet to be discussed in terms of velocity or energy. Further aspects which may also affect the resolution of the spectrometer are the efficacy of the velocity-mapping optics, the dynamic range of particle kinetic energies, the image pro-

[3] In part this was due to the concomitant development of a vacuum UV light source, this is briefly discussed with respect to future experimental work in Chapter 9.

cessing required to extract spectral data and the conversion of data from velocity to energy space. These points are addressed in this section, with the exception of image processing which is discussed in Section 4.1.

There is often some confusion regarding resolution figures. Here the resolution in velocity space is quoted as Δv, where Δv is difference in velocity between two particles which are just resolvable - in the limit where MCP pore size determines the image resolution Δv would correspond to the separation in velocity space of two adjacent pores. For perfect velocity mapping Δv is constant across the detector. Similarly, the resolution in energy space is given by ΔE. However, because $E \propto v^2$, ΔE is not constant across the detector. Resolution is also often quoted at a particular particle velocity, i.e. $\Delta v/v$, or $\Delta E/E$ in terms of energy. In both cases the value across the detector is not constant as all the terms, apart from Δv, change with position on the detector.

3.2.1 Native VMI resolution

The action of the VMI electrostatic optics to focus photoelectrons by their initial velocity can be termed the *native* resolution of the spectrometer. This resolution represents the ultimate limit in the VMI technique, but other limiting factors such as the spatial resolution of the PSD may lower the resolution realised practically. In order to consider this native resolution numerical simulations of the electrostatic optics can be performed using the SIMION package (or equivalent).

Eppink and Parker performed such calculations for electrons at 1 eV kinetic energy (E_{KE}) originating from a line-source with Gaussian intensity distribution width 2.12 mm; their results are reproduced in Figure 3.4. In these simulations the spread (S) in position of electrons, born with the same kinetic energy, at the detector is analysed. In all cases a deblurring of the initial 2 mm spread is observed, as expected in VMI, with $S < 0.05$ mm for very short flight lengths. For a longer apparatus S increases; a 400 mm flight tube yields $S = 0.4$ mm in these simulations. In this case the native resolution of the spectrometer in velocity space is less than the resolution of the detection system, with particles with the same initial velocity spread over more than one camera pixel. There is also some difference in S as a function of electron ejection angle from the ionization region, with a larger spread seen in electrons ejected parallel to the VMI lens axis.

Analysis of the spread of arrival positions for particles born with the same kinetic energy gives some insight into the behaviour of the VMI electrostatic optics, and these calculations show that in certain cases the native resolution may be the limiting factor. With $S = 0.4$ mm the effective pixel resolution of a 40 mm detector is reduced to 200 pixels, assuming that resolvable spots must be $S/2$ mm apart, yielding a maximum energy resolution of around 10 meV (80 cm^{-1}) for kinetic energies of 1 eV. However, these calculations summarize results for only a single E_{KE}, and in an existing system the behaviour of S as a function of the flight tube length may be somewhat academic. For experimental work a spread of E_{KE}s are likely, while other parameters, except the voltages applied to the VMI lens, will be fixed. In these circumstances it is more instructive to consider the resolution as $\Delta E/E$, and investigate how this changes with E_{KE} and the

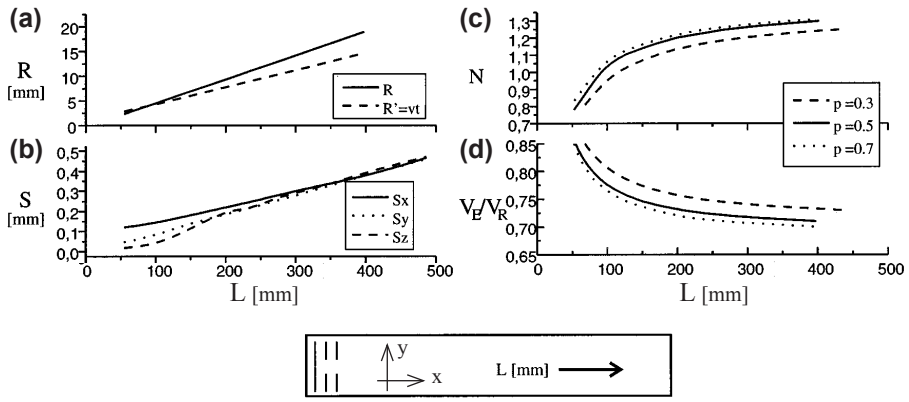

Figure 3.4: Characteristics of a VMI lens. R is the ring radius, S the residual spread in position, N the magnification factor and V_e/V_r the velocity-mapping voltage ratio. All quantities are plotted versus L, the length of the flight tube (or, equivalently, the distance of the detector from the ionization region). In all cases the ionization region was modelled as a line-source with Gaussian intensity distribution width 2.12 mm, V_r =1000 V and E_{KE} =1 eV. The laser focus was set at $p = 0.5$, defined as half-way between the repeller ($p = 0$) and extractor plates ($p = 1$) for (a) and (b), but was varied in (c) and (d). Reproduced from ref. [39]. Note that the axes are defined differently from the convention used in this thesis.

VMI lens voltages. This is considered in the next section.

3.2.2 Δv, ΔE and experimental considerations

An important experimental aspect concerning resolution which has yet to be mentioned is the *dynamic range* to be imaged on the PSD. Intuitively it may be realised that the smaller the total spread of velocities to be imaged the smaller the velocity steps, Δv, between pores of the MCP become. This is a consequence of the fixed size of the MCP, and hence a fixed number of pores. Thus the smaller the dynamic range the better the resolution should become, provided that the action of the VMI lens is constant for all E_{KE}s. Experimentally this idea can be employed by ionizing near threshold, thereby only creating low-energy electrons. Alternatively, the electron cloud can be enlarged such that only the central part of the photoelectron distribution is imaged, thus restricting the energy range to only record slow electrons. Such slow-electron images have been shown to be capable of yielding photoelectron spectra with line-widths (ΔE) as narrow as 1.1 cm^{-1} [42]. The restriction in energy range can also be overcome (at the cost of experimental timescale) by recording slow-electron velocity map images (SEVI) over a range of probe laser wavelengths, as demonstrated by Neumark and co-workers [42, 43], although analysis and compilation of a spectrum from a set of SEVI images can be challenging [20, 44].

In order to investigate these issues further it is instructive to consider ΔE for a range of kinetic energies while keeping all other parameters fixed. Such calculations have been performed by Garcia et. al. [155] using custom code for the electrostatic simulations. By varying only the VMI voltages the dynamic range imaged is adjusted, as shown in Figure 3.5. As V_r is increased the dynamic range increases, and higher kinetic

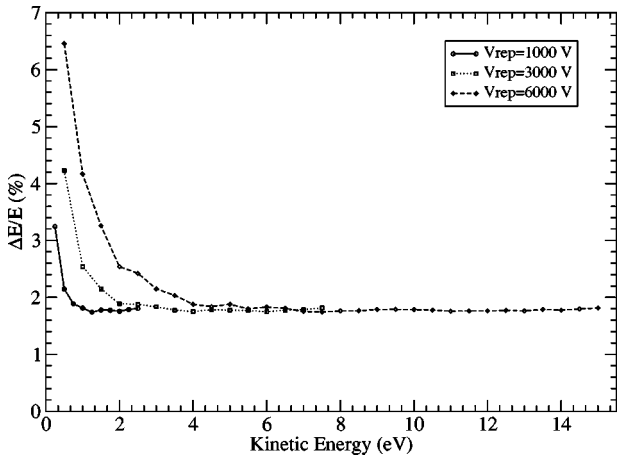

Figure 3.5: $\Delta E/E$ behaviour as a function of VMI voltages. The simulations used a source region 0.5x0.5x4 mm. Reproduced from ref. [155].

energy electrons are focused onto the PSD. The resolution follows approximately a $1/r$ dependence, equivalently $1/\sqrt{E}$. One surprising result of these simulations is that the energy resolution obtained near the edge of the detector (highest E_{KE}) tends towards the same value in all cases. The resolution towards the centre of the detector is, however, markedly worse for high V_r.

Although numerical simulations are required to investigate the VMI optics, the relationship between radius and energy resolution can also be examined analytically. As already defined by the velocity-mapping condition, the conversion from radial position to velocity is linear across the detector [39]:

$$r = Nvt \tag{3.1}$$

Here N is defined as the magnification factor of the VMI lens, t is the time of flight (approximately the same for all electrons in VMI), and r is the radius of the ring appearing on the detector, i.e. the case where $v = v_x$. From this it is clear that

$$dr = Ntdv \tag{3.2}$$

dr represents the (continuous) radial resolution of the PSD in velocity space. The discrete form realised experimentally will be the radial step per pixel of the camera, Δr, which will also depend on the spatial resolution of the imaging system as discussed in Section 3.1.2. Similarly dv is the native resolution of the spectrometer, and is constant across the detector. This relation can also be considered in energy space:

$$\begin{aligned} E &= \frac{1}{2}mv^2 \\ &= \frac{1}{2}m\left(\frac{r}{Nt}\right)^2 \end{aligned} \tag{3.3}$$

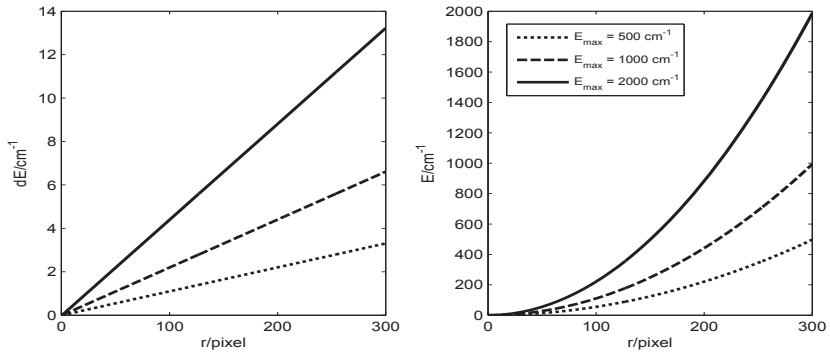

(a) Plots showing the behaviour of E and dE as a function of pixel radius for three different maximum kinetic energies (dynamic ranges).

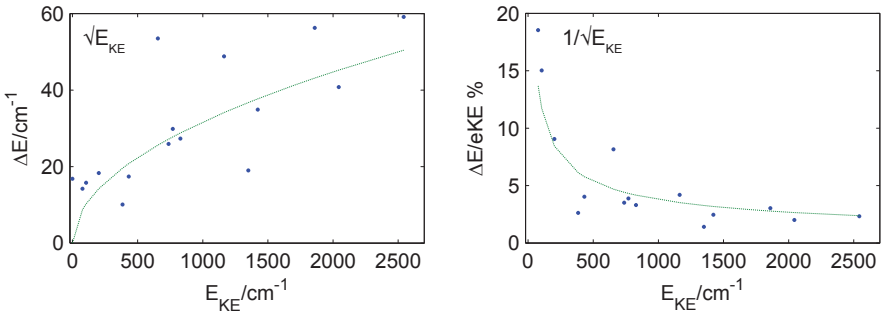

(b) Experimental results showing ΔE and $\Delta E/E$. Dotted lines show $\Delta E \propto \sqrt{E}$ and $\Delta E/E \propto 1/\sqrt{E}$ plots. ΔE is approximated here using the peak widths from a Lorentzian fit to the experimental spectrum. The data used is from the acetylene experiments, $V_0^5 K_0^1 R_1$ pump transition (see Section 5.7); peak widths will also reflect underlying rotational structure as well as native VMI resolution.

Figure 3.6: Plots showing the behaviour of E and dE. (a) Analytic and (b) experimental.

and

$$dE = \frac{mr}{Nt} dr \tag{3.4}$$

This proves the previous statement that dE is not constant over the detector, and shows that it is $\propto r$ for constant dr. Using equations 3.3 and 3.4 it can also be seen that

$$\frac{dE}{E} = \frac{2Nt}{r} dr \tag{3.5}$$

$$\propto \frac{1}{r} \tag{3.6}$$

which agrees with the results shown in Figure 3.5. These equations also highlight the importance of *how the resolution is defined*. $\triangle E \propto r$, so increases with r, while $\triangle E/E$ decreases with r. In this sense the definitions are opposing: the narrowest features in the spectrum will be obtained for small r, so features arising from closely-spaced energy levels are most likely to be resolved in this region of the spectrum, yet the resolution in percentage terms is actually worst at low r.

Finally, the question of dynamic range can be re-examined. Reducing the maximum velocity of the photoelectrons imaged (and adjusting the VMI voltages such that the image still uses the full area of the PSD) will mean that a smaller velocity range is recorded over

the same number of pixels, so dr is decreased with a consequent effect on dE. Figure 3.6 shows the behaviour of E and dE as a function of r for three different maximum energies.

From this discussion the main points pertinent to the final energy resolution of the spectrometer can be summarised:

- dr defines the resolution limit of the PSD, and is dependent on the velocity range mapped onto the detector. This is the key point, and in experiments on ammonia (Chapter 7) rotational resolution is obtained by keeping the dynamic range to $\sim$300 cm^{-1}.
- dv defines the native resolution of the spectrometer.
- dv may be improved experimentally by reducing the length of the ionization region.

In addition, other factors could further affect the experimental resolution, for example aberrations in the VMI lens which could cause dv to vary as a function of E_{KE}. From the discussion in Section 3.1.2 it may be surmised that $dv < \Delta r$, and the PSD is the limiting factor experimentally.

3.2.3 Angular resolution

For accurate measurement of PADs the angular resolution, $\Delta\theta$, is also important. The angular resolution is dependent on the number of MCP pores around a ring of given radius, which is given by:

$$\text{No. of pores} = \frac{2\pi r}{\text{pore diameter}} \tag{3.7}$$

The angular resolution is defined as the angular step per pore, so is given by:

$$\Delta\theta = \frac{2\pi}{\text{No. of pores}} \tag{3.8}$$

$$\propto \frac{1}{r} \tag{3.9}$$

Using the 12 μm MCP pitch as the limiting case shows that the angular resolution rapidly becomes $\ll 1^\circ$ as r increases. Using a pixel scale, rather than the native MCP spatial resolution, shows that any rings appearing at $r > 10$ pixels will have excellent angular resolution, $\ll 1^\circ$. This highlights the benefits of using VMI for measuring PADs: the angular resolution is excellent except in the central region of the image. Experimentally the angular resolution will be slightly worse, due to the limitations of the PSD as previously discussed, but is still expected to be $< 1^\circ$.

3.2.4 Improving image resolution with data processing

A final consideration is how the radial (energy) resolution, now seen as a limitation in the data visualization and collection part of the PSD, might be improved upon. Houston and

co-workers [153] demonstrate a significant improvement in spatial resolution by an ion-counting method which assigns each recorded particle impact to a single camera pixel by analysis of the recorded intensity distribution. Further improvement of spatial resolution using image processing techniques has been demonstrated by Suits and co-workers [156], by finding the "centre-of-mass" of each impact spot they are able to achieve sub-pixel resolution. At this point they comment that the limiting factors in the spectrometer resolution are no longer due to the detector, but arise from the behaviour of the rest of the spectrometer. A centroiding algorithm, similar to that used by Houston et. al. [153], is implemented in the IFS32 software, but use of this feature yielded little improvement in resolution in experimental photoelectron images (see ref. [20] for further detail on centroiding in IFS32, including example photoelectron images and spectra). The reason for this is unclear, but may be due to deficiencies in the VMI lensing, or the drop in signal/noise ratio and concomitant graininess of a centroided image.

3.3 Experimental Techniques

The details of the VMI spectrometer have been consider in the preceding sections, the remainder of this chapter looks in more detail at the practical aspects of the experimental work: the overall set-up of the spectrometer and ancillary equipment, the various techniques employed in order to optimize the set-up, the recording of resonance-enhanced multi-photon ionization (REMPI) spectra, and the recording of photoelectron images. Naturally some of the techniques described here evolved over the course of various experimental runs, so not all of the methods were employed in the earlier acetylene work (Chapter 5). In particular, the description of 2-colour experiments is relevant only to the ammonia experiments (Chapter 7). It should also be noted that the parameter space of such an experimental set-up is large, so often these procedures had to be iterated several times to achieve satisfactory results.

3.3.1 Laser systems

Three Nd:YAG pumped, nano-second pulsed dye-laser systems were used in the work presented in this thesis:

1. Continuum Surelite I & Sirah Cobra
2. Continuum Surelite III & Continuum ND6000
3. Continuum Powerlite 8010 & Sirah Cobra-Stretch

All of these systems operate by the same principles, but the specifications of the output laser power and wavelengths are somewhat different. In brief: the YAG-rod is flash-lamp pumped and lases at 1064 nm with a 5-7 ns pulse duration; this radiation is then frequency-doubled (λ = 532 nm) or tripled (λ = 355 nm) before input to the dye-laser. The dye-laser uses a dye solution and a finely-ruled diffraction grating to create wavelength-tunable radiation from the broad-band dye fluorescence. The exact dye used

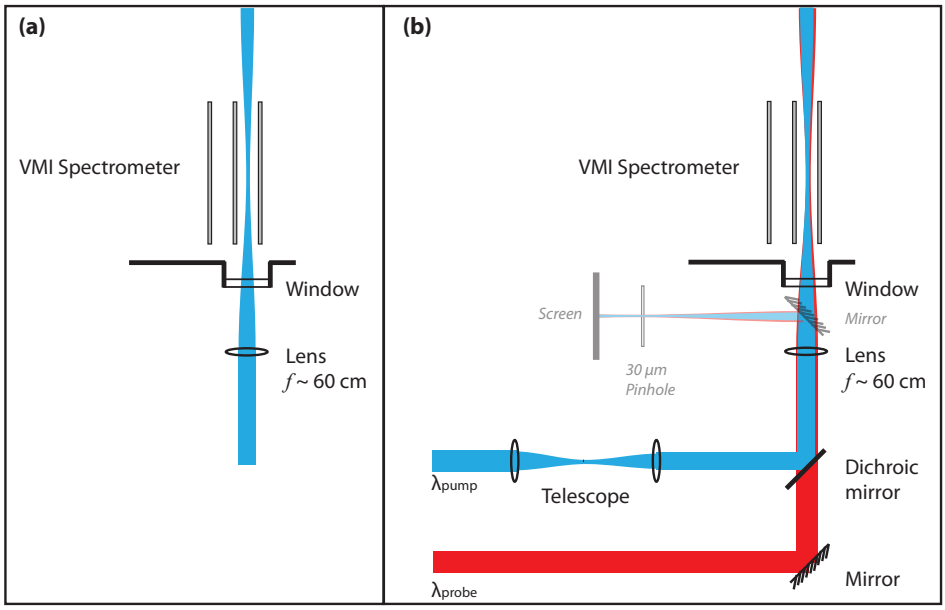

Figure 3.7: Schematic of the experimental set-up for (a) 1-colour and (b) 2-colour work.

will depend upon the laser wavelength required experimentally. Dyes which lase in the blue region of the spectrum (e.g. Courmarin 102) have lower efficiencies and lifetimes than those in the red region of the spectrum (e.g. DCM). The output dye-laser beam may be doubled or tripled if required, using appropriate non-linear crystals (BBO or KDP). Typical output powers in the UV are in the range 1 - 3 mJ per pulse, but can be much higher in some cases - particularly if the dye fundamental is used without further wavelength conversion. The linewidth of the dye-laser fundamental varies slightly depending on the wavelength and laser system, but is specified to be better than 0.002 nm ($\sim$0.05 cm^{-1} at 600 nm, $\sim$0.1 cm^{-1} at 400 nm) in all cases.

The work presented in this thesis used systems 1 & 2 to generate light in the region of 316 nm and 430 nm for experiments on ammonia, and system 3 to generate light in the range 207 - 216 nm for experiments on acetylene. Full details of the dyes used and laser power obtained are given in the relevant chapters.

3.3.2 1-colour and 2-colour experimental set-up

In a 1-colour experiment (Figure 3.7(a)) a single laser pulse is used to both prepare (*pump*) and ionize (*probe*) the system under study. For acetylene (Chapter 5) this took the form of a (1+1) REMPI scheme, for ammonia (Chapter 7) a (2+1) REMPI scheme was employed.[4] A 1-colour experiment represents the simplest experimental set-up, where a single laser beam is directed through the spectrometer. Initially the set-up can be arranged by aligning the laser path to the centre of the input and output windows on the spectrometer, thus ensuring the beam path is parallel to the VMI plates and crosses the spectrometer axis. A focusing lens can then be introduced into the beam, with appropriate focal length

[4]Full details of wavelengths, laser power etc are reported in the relevant chapters.

to bring the laser into focus at the spectrometer axis. The focal length used will also affect the *tightness* of the focus, characterized by the beam waist and the Rayleigh range [128]; this is one of many factors which can affect the ionization yield and quality of the photoelectron images. The difference in physical size of Spec1 and Spec2 meant that the minimum focal length which could be used was ∼30 cm in the former case, and ∼60 cm in the latter.

After the laser is geometrically aligned to the spectrometer axis the pulsed nozzle is activated to introduce sample gas, the VMI plates are turned on, and the PSD is gradually turned up to operating voltage. The rough alignment of the laser to the spectrometer axis is usually sufficient to obtain an ionization signal, assuming the laser wavelength and timing of the pulsed nozzle are also set correctly. Fine adjustment of the experimental set-up can then be initiated, and is further detailed in Section 3.3.3.

A 2-colour scheme (Figure 3.7(b)) enables the maximum photoelectron energy to be controlled independently of the pump step by adjustment of λ_{probe}. Photoelectron images recorded for low kinetic energies and with a small dynamic range provide the best resolution in VMI (see Section 3.2), so a 2-colour scheme is desirable in order to optimize energy resolution. Additionally, a 2-colour scheme allows the study of photoionization dynamics as a function of photoelectron kinetic energy; such a study can be performed by fixing λ_{pump} and recording photoelectron images for different λ_{probe}.[5]

A 2-colour scheme was employed in experiments involving ammonia. In this case the pump beam was aligned as described above, and a (2+1) REMPI signal was obtained. Once optimized (see Section 3.3.3) this path could be defined using irises, and the probe beam could then be precisely aligned to this defined path. A flip-mounted mirror, a pinhole and a screen were then positioned as shown in Figure 3.7(b). This is an *equivalent plane* set-up, arranged such that the laser path from the final focusing lens to the pinhole is equal to the path length from the focusing lens to the ionization point, where the ionization point is defined by the pump beam focal spot. The probe beam waist can then be aligned to the pinhole by maximizing the spot intensity on the screen (or by optimization of Airy discs if a small enough pinhole is used), ensuring spatial overlap of the two lasers which will be replicated in the VMI chamber when the flip-mirror is removed from the beam path. With a 30 μm pinhole such a procedure was sufficient to obtain a 2-colour ionization signal from ammonia via a (2+1') process, the alignment could then be fine-tuned in-situ by making small adjustments to the final turning mirror and the focusing lens while observing the total 2-colour ionization signal. The 2-colour signal can be monitored by observing the total ion yield and checking for enhancement in the yield relative to the pump only and probe only yields. In the ammonia experiments observation of the real-time photoelectron images also proved a useful procedure, in this case the large kinetic energy difference between photoelectrons produced via (2+1) and (2+1') processes (Section 7.4) meant that the different sets of photoelectrons were well separated in the images and could be used to qualitatively optimize the 2-colour part of

[5] A 2-colour scheme also allows for independent control over the polarization of the pump and probe beams, as mentioned in Sections 2.2.2.3 and 4.3, such control can be used in order to record angular distributions with different polarization geometries.

the signal.

Additional telescope optics are also shown in Figure 3.7(b). These are optional, but may be required in order to ensure that the effective focal length of the final lens is the same for both pump and probe beams. Preferentially these would be placed in the probe beam path, so that they could be used for fine adjustment of the pump-probe overlap without moving the (already optimized) pump beam. However, in the ammonia experiments the dichoric mirror was not optically flat and caused the pump beam to be slightly divergent, so telescope optics were placed in the pump beam path to correct for this.

The temporal overlap of the beams at the equivalent plane was achieved using a fast photodiode to monitor fluorescence from the UV beams impinging on white paper. The precision of this overlap was estimated to be on the order of 1 ns, defined by the temporal response of the photodiode, and the temporal envelope of each laser pulse was on the order of 5 ns. The temporal overlap was further tuned by observing the effect of changing the timings on the 2-colour photoelectron signal, although little change was observed in the ionization signal over a range of approximately ± 1 ns.

3.3.3 Ion images, timing and VMI focusing

The ionization yield can be monitored via the *integrated count rate* from the PSD using *ion detection mode*. In this mode the VMI plates are set to +ve voltages, so cations are repelled towards the detector, and the operating voltages for the PSD are set as listed in Table 3.1. The integrated count represents the total ion yield, as distinct from the ion image which provides a velocity-mapped ion signal. Initial optimization of the 1-colour signal was performed by adjusting various experimental parameters in order to obtain a good ion yield:

- The relative timing of the laser pulse, the pulsed nozzle and the PSD gate. Timing was controlled by an 8-channel pulse generator (BNC 565).
- Laser & molecular beam paths.
- Gas pulse length.
- Laser wavelength.

Once a good ion yield was obtained, indicating a good laser-molecular beam spatial overlap and correct timing sequence, the ion image was optimized in order to ensure that the observed signal originated from a cold part of the molecular beam, and the VMI conditions were correct.

In the *zone of silence*, the translationally cold region of the molecular beam (away from the initial shock-front - see discussion in Section 3.1.3), the transverse velocity spread of the beam is small. Ions born in this part of the supersonic expansion thus appear on the detector as a single pixel in the limit of perfect velocity mapping. Ions created from a hotter part of the molecular beam have a larger velocity spread, and create a diffuse circle

on the detector. Observation of the real-time ion image thus provides a way of optimizing the timing of the laser and pulsed nozzle, and the cold part of the molecular beam can be found. The VMI voltages can also be fine-tuned so that the ion spot size is pixel-limited.

3.3.4 REMPI scans

REMPI scans were recorded by monitoring the total ion yield while scanning the (pump) laser wavelength. Once the timing had been optimized as described above, REMPI scans could be recorded and analysed to provided more quantitative information on the vibrational and rotational temperature of the molecular beam. REMPI data was also used for calibration of laser wavelength. REMPI scans are discussed further, with examples and details of the analysis procedure, in Sections 5.4 and 7.3.

3.3.5 Photoelectron images

After optimizing the set-up in ion detection mode, the spectrometer was switched into *electron detection mode*. In this mode the VMI voltages are -ve, and the voltages on the PSD are also slightly different (see Table 3.1). The timing of the PSD gate is adjusted for electron detection because the flight times are much faster than for ions, but no other experimental parameters are changed. If the photoelectron yield was sufficient, the real-time photoelectron image observed at this point revealed whether the spectrometer was working correctly, or if further adjustments were necessary. In cases where the photoelectron yield was low, short accumulations of a few minutes duration were required to determine this.

In an ideal case the experimental variables optimized in ion detection mode would not require any adjustment. However, because the size of the photoelectron image on the detector is important, changes to the VMI plate voltages were often required to maximize the image size. During experiments on ammonia, optimization of ion images for different V_r showed that the VMI voltage ratio, V_e/V_r, for optimum velocity mapping, changed slightly over the range $150 < V_r < 1500$ V, so this ratio also required small adjustments.

In electron mode background signal can be a problem. Such background arises from electrons which are not produced in the previously defined ionization volume, but still arrive at the detector within the gated on period. The main cause of these electrons was thought to be scattered light liberating electrons from the chamber walls or VMI plates, although ionization of background gas present in the spectrometer may also have contributed to the background signal. In order for the former processes to occur the work function of the material must be less than the photon energy, so background signal will become worse for shorter wavelengths of light and also for higher VMI plate voltages. A small amount of scattered light is unavoidable, but the problem is worsened if the laser path is too close to the VMI plates, or not parallel to the VMI plates; in the latter case back-reflections from the output window could cause significant scattered light. Background noise was a particular problem in the acetylene experiments, where it was exacerbated by the short wavelengths required ($<$ 220 nm) and the low ionization cross-section. In the acetylene

experiments some reduction in the background signal was achieved by installing baffles in the input and output arms of the spectrometer to ensure good collimation of the laser beam and block some of the scattered light.

3.4 Summary

In this chapter various details of the VMI spectrometers used in this work have been considered. General discussion of the main components of such an instrument have been discussed, with particular focus on the PSD specifications and energy resolution in the images obtained. These considerations were especially relevant to experimental work on ammonia (Chapter 7). Experimental techniques have also been discussed, providing an overview of VMI from a practical perspective.

Chapter 4

Image Analysis, Dynamical Parameters and Fitting Methodology

This chapter serves to bridge the gap between the photoelectron images obtained experimentally using the velocity map imaging technique (see Chapter 3) and the theoretical treatment of PADs within the partial wave expansion of the ionization continuum (Section 2.3).

The photoelectron images obtained in VMI must be processed in order to obtain a slice through the original distribution, as distinct from the 2D projection of the full 3D distribution which is recorded experimentally. Once processed, the photoelectron spectra and angular distributions can be extracted, and these represent the final form of the experimental data. This procedure is detailed in Section 4.1.

The experimentally determined PADs provide a set of β_{LM} parameters (see Sections 1.4.1 and 2.3.4). These can be fitted with equation 2.52 in order to deduce the dynamical parameters. Due to the complexity of this fit there are several aspects to consider regarding the assumptions made and the methodology employed. These are detailed in Section 4.3, and are applicable to the analysis of PADs obtained from experiments on both acetylene (Chapters 5 and 6) and ammonia (Chapters 7 and 8).

4.1 Image Processing

The photoelectron image obtained in a VMI experiment is a 2D projection of the full 3D photoelectron distribution, this is illustrated in Figure 4.1. In order to obtain reliable transition intensities from such an image it is necessary to back-transform the projected image and recreate a slice through the centre of the original velocity distribution. There are several methods of performing such an image inversion. In this work the Abel and pBasex inversion methods have been used; these are discussed below, and compared in Section 4.1.3, which also provides example images and data. These methods are only

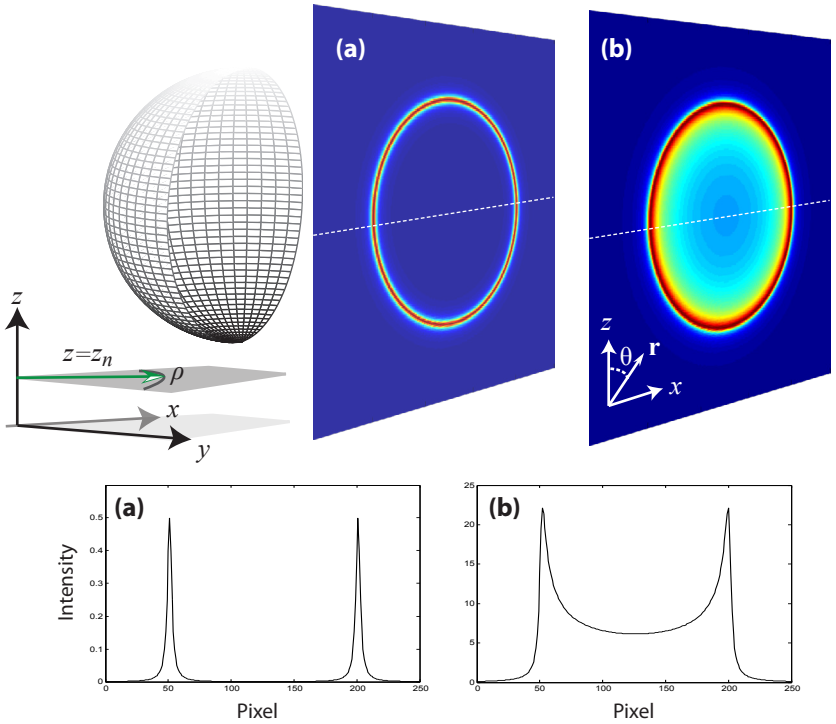

Figure 4.1: Simulated 3D & 2D photoelectron distributions. (Top) Image (a) shows the central slice through a 3D photoelectron velocity sphere for an isotropic angular distribution with a Lorentzian radial profile. Image (b) shows a 2D projection of the velocity sphere, using a 250 x 250 pixel array. (Bottom) Cuts through the central row ($z = 125$) of images (a) and (b), as marked in the images by the dashed line. Coordinate systems used in the text are defined, the general Cartesian axes (x, y, z) are the same as those previously defined (Figure 2.1), cylindrical coordinates (ρ, z) in the plane $z = z_n$, and polar coordinates (r, θ) in the plane of the detector.

applicable for the reconstruction of cylindrically symmetric distributions. For an overview of other image inversion methods see Chapter 3 of reference [37] and references therein.

4.1.1 Abel inversion of photoelectron images

The Abel transform describes the projection of a 3D distribution onto a 2D plane. Taking the detector as the (x, z) plane the projected imaged is described, in Cartesian coordinates, as [37]:

$$p(x, z) = \int_{-\infty}^{\infty} i(x, y, z)dy \tag{4.1}$$

Here $p(x, z)$ describes the 2D projection in the plane of the detector, while $i(x, y, z)$ is the initial 3D distribution. Equation 4.1 shows that the projected image is simply the summation of the original 3D distribution in the plane of the detector, as would be intuitively expected. For a cylindrically symmetric distribution equation 4.1 can be rewritten in cylindrical coordinates (ρ, z) using the substitutions $\rho = \sqrt{x^2 + y^2}$ and $dy = \rho(\rho^2 - x^2)^{-\frac{1}{2}} d\rho$:

$$p(x,\, z) = 2\int_{x}^{\infty} \frac{i(\rho,\, z)\rho}{\sqrt{\rho^2 - x^2}} d\rho \tag{4.2}$$

This form of the projection is known as the (forward) Abel transform. This expression replaces the summation over y in Cartesian coordinates with a summation over $\rho \geq x$, where ρ is the radial coordinate. Equation 4.2 can be seen to describe each row, $p(x;\, z = z_n)$, in the final image.

The advantage of the Abel transform is that the inverse or back transform can be analytically found:

$$i(\rho;\, z_n) = \frac{1}{\pi}\int_{\rho}^{\infty} \frac{p'(x;\, z_n)}{\sqrt{x^2 - \rho^2}} dx \tag{4.3}$$

Here $p'(x;\, z_n) = dp(x;\, z_n)/dx$. Equation 4.3 provides a method for recovering $i(\rho;\, z_n)$, the initial radial distribution in the plane z_n, from a row of the projected image. As the 3D distribution is cylindrically symmetric, applying this reconstruction to all rows z is equivalent to recovering the desired slice through the original distribution $i(\rho,\, z)$. The inverse Abel transform is thus well suited to images obtained from a CCD camera as it can be applied row by row to the recorded image (i.e. $(x,\, z)$ pixel array), making it computationally simple to reconstruct $i(\rho,\, z)$.

In reality some problems arise with the Abel inversion due to noise. The inversion has the effect of magnifying noise, and accumulating it along the centre-line (z-axis) of the image [157]. The magnification of noise is due to the term in $p'(x)$ in equation 4.3, while the accumulation along the centre-line is due to the row-by-row application of the transform - the noise from each row is worst in the centre of the row [158] (see Figure 4.3). It also assumes a symmetrized image and artefacts may arise in the inversion from any left-right asymmetry in the recorded image [37], either due to noise or inhomogeneities in the detector, distortions in the initial distribution, or a non-cylindrically symmetric initial distribution. However, in most cases photoelectron images with cylindrical symmetry and good signal-to-noise can be inverted using equation 4.3 with only minimal loss of data along the centre-line. Inverted images and data are discussed further in Section 4.1.3, in comparison with pBasex results.

The inverted image presents the desired *vertical* slice through the original photoelectron distribution. To prevent confusion with the planes of constant z considered above, this slice is written in polar coordinates as $i(r,\, \theta)$, where $r = \sqrt{x^2 + z^2}$ (see Figure 4.1). The final stage of processing is to extract the radial and angular information from the image, and convert this raw data to photoelectron spectra and angular distributions.The radial information is extracted by summing over the angular coordinate:

$$i(r) = r^2 \sum_{\theta_1}^{\theta_2} i(r,\, \theta) \tag{4.4}$$

Here the factor of r^2 normalizes the intensities. This factor allows for the spread of the

photoelectrons over the full surface area of the 3D Newton sphere. The angular limits, θ_1 and θ_2, are typically chosen as 0 and 2π to encompass all of the data, but may also be chosen to average over only part of the image in order to avoid image artefacts. When extracted from a square pixel array, $i(r)$ may also need to be averaged to allow for the summation over a different number of pixels with each radial step. The intensity scale obtained is arbitrary and derived from the pixel values in the inverted image. With suitable calibration of the detection system it should be possible to scale this directly to the photoelectron count.

At this stage the peak intensity ratios are correctly scaled, but the ordinate is still just a pixel value. This axis can be converted to velocity or, more usually for photoelectron spectra, converted to an energy scale. The conversion to energy, and resolution considerations, has been discussed in Section 3.2; calibration of energy scales is discussed in Section 4.2.

The angular data $i(\theta)$ is extracted in an analogous manner:

$$i(\theta) = \sum_{r_1}^{r_2} i(r, \theta) \tag{4.5}$$

The limits in this summation define a radial window, chosen to encompass a feature in the spectrum. The angular data needs no further processing; this data is the PAD for the spectral feature within the radial window defined by r_1 and r_2. To obtain β_{LM} parameters from the data it is necessary to fit the data with appropriate spherical harmonics or Legendre polynomials (equation 1.4).

4.1.2 pBasex inversion of photoelectron images

The pBasex method [157], a polar coordinate adaptation of the (Cartesian) Basex method (Basis Set Expansion) [159], is somewhat different in approach. In pBasex a set of known polar basis functions are used, comprised of a Gaussian radial component and Legendre polynomial angular component:

$$f_{kL}(R, \Theta) = e^{-(R-R_k)^2/\sigma} P_L(\cos\Theta) \tag{4.6}$$

Here σ is the width of the Gaussian part of $f_{kL}(R, \Theta)$, R_k is the centre of the k^{th} Gaussian, and $P_L(\cos\Theta)$ is the L^{th} order Legendre polynomial in $\cos\Theta$. Polar coordinates (R, Θ) are used to distinguish the general case of 3D, ϕ invariant, basis functions from the (r, θ) coordinates defined in the plane of the 2D detector (Figure 4.1); the coordinate systems are coincident for $\phi = 0$ and for the remainder of this section no distinction is made between them. These basis functions can describe a cylindrically symmetric distribution:

$$i(r, \theta) = \sum_{k=0}^{k_{max}} \sum_{L=0}^{L_{max}} c_{kL} f_{kL}(r, \theta) \tag{4.7}$$

The 2D projection of this distribution can be found analytically using the forward Abel transform, similar to that shown in equation 4.2 for cylindrical coordinates. Furthermore, the projected image $p(r, \theta)$, where the coordinates now refer to the plane of the detector, can also be written as an expansion in basis functions $g_{kL}(r, \theta)$:

$$p(r, \theta) = \sum_{k=0}^{k_{max}} \sum_{L=0}^{L_{max}} c_{kL} g_{kL}(r, \theta) \tag{4.8}$$

These functions are therefore related to $f_{kL}(r, \theta)$ by the Abel transform [157]:

$$g_{kL}(r, \theta) = 2 \int_{|x|}^{\infty} \frac{f_{kL}(r, \theta) r}{\sqrt{r^2 - x^2}} dr \tag{4.9}$$

Thus the projected image can be fitted to the Abel transformed basis functions $g_{kL}(r, \theta)$ to obtain the coefficients c_{kL}. As these coefficients are the same as those appearing in the original distribution (equation 4.7) this fitting is equivalent to reconstructing $i(r, \theta)$. The pBasex method is therefore a fitting procedure, although the Abel transformation of the basis functions is analytically solved. The radial spectrum is obtained in a similar fashion to the angular summation shown in equation 4.4, but using the basis functions the integration can be re-cast as a sum over k for the zero-order Legendre polynomial $L = 0$ (a sphere) [157]:

$$i(r) = \frac{r^2}{i_{max}} \sum_{k=0}^{k_{max}} c_{ko} f_{ko}(r, \theta) \tag{4.10}$$

In this expression note that a normalization factor of r^2 is present, as in equation 4.4, and the output from the pBasex code also normalizes the data to i_{max}.

The β_L parameters which describe the PAD are similarly obtained by summing over k for $L \neq 0$:

$$\beta_L(r) = \frac{r^2}{i(r) i_{max}} \sum_{k=0}^{k_{max}} c_{kL} f_{kL}(r, \theta) \tag{4.11}$$

Note that the β_L parameters extracted in this way correspond to the anisotropy over some small radial window as described by σ, the Gaussian width of the radial part of the basis functions. This width is usually set to be 1 or 2 pixels wide, so this extracted data can be thought of as providing a $\beta_L(r)$ radial spectrum (see Figure 4.2). In order to obtain β_L for a given feature in the spectrum, which may cover several or tens of pixels in the image, an intensity weighted average of the $\beta_L(r)$ spectrum is required:

$$\beta_L = \frac{1}{N} \sum_{r_1}^{r_2} i(r) \beta_L(r) \tag{4.12}$$

Here N is the number of discrete data points averaged over, $r_1$and r_2 are the inner and outer radial limits for the feature of interest.

Note that the β_L parameters correspond to an angular expansion in Legendre poly-

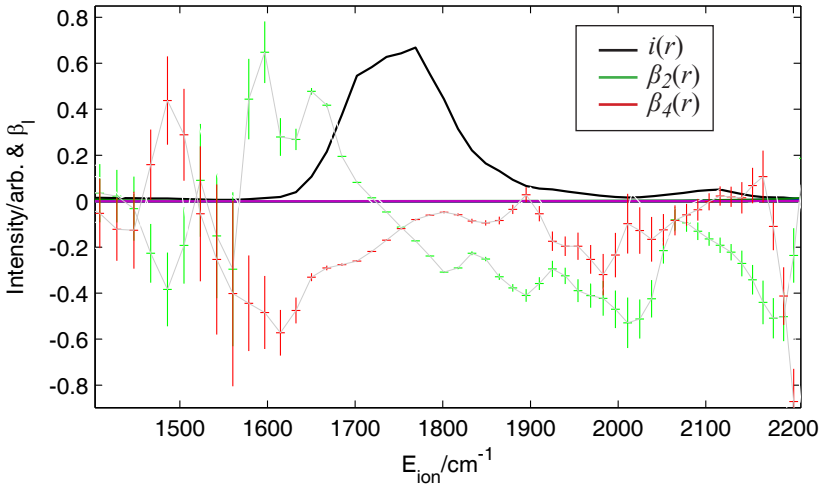

Figure 4.2: Example of pBasex extracted radial and β_L spectra. Error bars are shown on the β_L data. In regions of low intensity in the radial spectrum, the β_L spectrum shows oscillatory behaviour and large error bars, this is a result of undefined angular functions in these regions. Over features in the radial spectrum the β_L values are well-behaved with small error bars; these regions provide meaningful anisotropy parameters over which an intensity-weighted average can be found, yielding the β_L parameters for the feature.

nomials $P_L(\cos\theta)$, not the more general expansion in spherical harmonic functions Y_{LM} (equation 1.4). For $M = 0$ the spherical harmonics reduce to the Legendre polynomials but with an additional normalization factor,

$$Y_{LM} = \sqrt{\frac{(2L+1)(L-M)!}{4\pi(L+M)!}} P_L(\cos\theta) e^{iM\phi} \tag{4.13}$$

$$Y_{L0} = \sqrt{\frac{2L+1}{4\pi}} P_L(\cos\theta) \tag{4.14}$$

The pBasex extracted anisotropy parameters must therefore be re-normalized before direct comparison with anisotropy parameters derived from spherical harmonic expansion. In the work presented in this thesis *all* β parameters are quoted according to equation 1.4, i.e. they are β_{LM} terms, and pBasex outputs are always re-normalized appropriately. Additionally, values are always normalized before plotting PADs such that $\beta_{00} = 1$.

The main advantage of the pBasex method is that the effect of noise in an image is much reduced; the fitting acts as a smoothing filter for most random noise and any artefacts are accumulated in the centre of the image ($r = 0$), rather than along the centre-line. This is due to the polar nature of the fitting, as opposed to the row-by-row application of the Abel inversion. Additionally the use of basis functions means that β_L parameters are directly obtained from the photoelectron images, as shown in equation 4.11, rather than requiring further fitting of the angular data. Extensive comparison of pBasex with other inversion methods [37] also shows that it typically performs better than Abel inversion methods when processing test images; this is discussed further in the

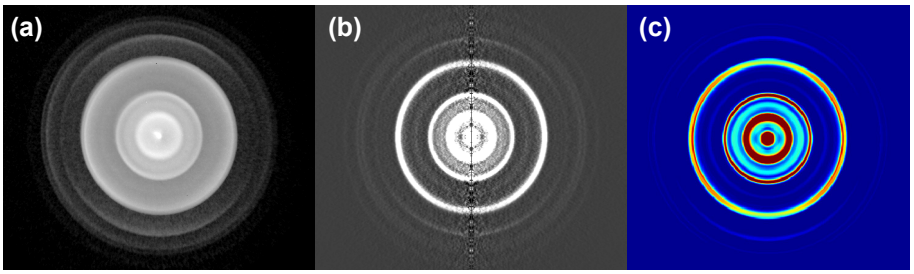

Figure 4.3: Illustration of inversion methods. (a) Raw photoelectron image; (b) Abel-inverted image; (c) pBasex inverted image. Data shown is from acetylene work (Chapter 5), $V_0^5 K_0^1 R_1$ pump transition.

following section.

4.1.3 Comparison of Abel & pBasex methods

In the experimental work presented in this thesis pBasex was the preferred inversion method, while previous work in Nottingham used the Abel inversion.[1] In the literature the pBasex method has been shown to outperform the Abel inversion in most cases (see ref. [157], also ref. [37] which covers the similar Basex method in detail). Work was also undertaken in Nottingham using simulated images in order to ensure the consistency of the radial and angular data obtained using the two different methods [160]. Additionally, consistency checking was carried out using a representative sample of photoelectron images from the acetylene and ammonia experimental work presented in Chapters 5 and 7.

Figures 4.3 and 4.4 illustrate the differences in the Abel and pBasex results. Figure 4.3 shows a raw photoelectron image, and the results of the Abel and pBasex inversion; centre-line noise is clearly visible in the Abel case. Figure 4.4(a) shows a comparison of radial spectra. The Abel inverted data has not been smoothed so exhibits low-level noise not present in the pBasex extracted data. Only at very small radii ($r \lesssim 15$ pixels) is there some difference in these spectra, and in both cases it is expected that any inversion problems will be most noticeable in this region where there are fewer data points and noise may have a more significant effect. The intense image centre is also prone to saturation [20]; consequently this data is usually discarded.

Figure 4.4(b) compares PADs extracted with the two different inversion methods; the β_{LM} parameters pertaining to these plots are listed in Table 4.1(a). Note, as mentioned previously, that in all cases β_{LM} are normalized such that $\beta_{00} = 1$. In general the angular data showed more variation between the two methods than was seen in the radial data, but analysis of simulated images with known angular distributions suggests that the

[1] Previous work in Nottingham [35] has also investigated whether any significant differences arise between ToF methods and VMI results processed with the Abel inversion. In that work some difference was seen in the the β_{LM}-parameters extracted from the data, although PADs were qualitatively the same. Small differences in (vibrational) branching ratios were also observed between the two methods, but the work concluded that these were most likely due to changes in detection efficiency in the ToF spectrometer with photoelectron energy and not due to any inherent problems with the VMI results or image processing.

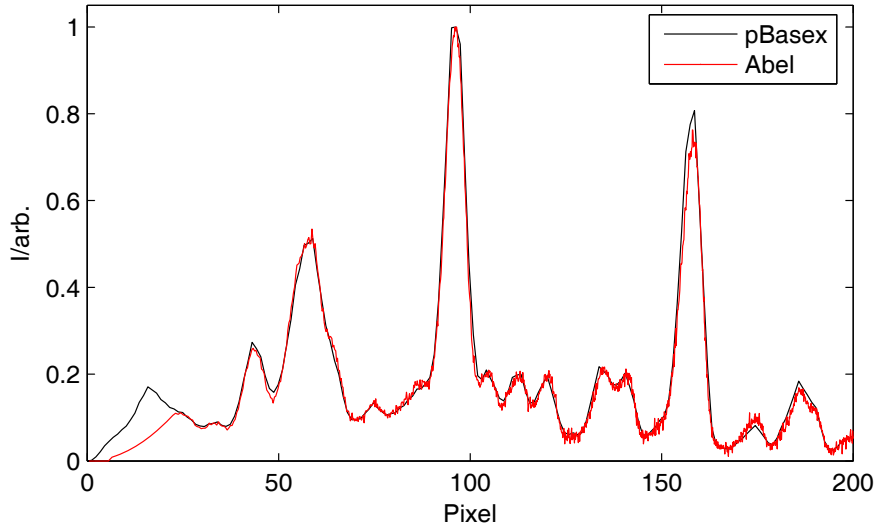

(a) Comparison of pBasex and Abel extracted radial spectra. Data shown is from acetylene work (Chapter 5), $V_0^6 K_0^1 R_1$ pump transition.

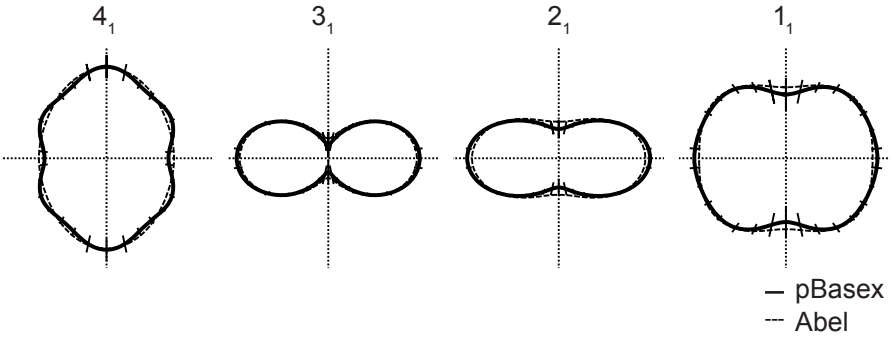

(b) Comparison of pBasex and Abel extracted PADs. Data shown is from ammonia work (Chapter 7), $v_2 = 4$, $1_1 \rightarrow 1_0$ pump transition. PADs are labelled according to ion rotational level, and plotted in polar form (i, θ).

Figure 4.4: Radial & angular data comparison for pBasex and Abel inversion methods.

pBasex extracted data are more reliable [157, 160]. In particular, for examples of the kind shown here where $L_{max} = 6$, pBasex produced much larger β_{60} terms. This difference is reflected in the PAD labelled 4_1 in Figure 4.4(b) which shows the most significant difference between the Abel and pBasex inversion, and is attributable primarily to an order of magnitude difference in the β_{60} parameter. The values quoted in Table I of ref. [157] suggest that the magnitude of this disagreement is not unusual, but that the pBasex result is likely to be closer to the true value. This is most likely a direct consequence of the centre-line noise in the Abel inverted data, which may affect the sensitivity of the extracted data to different β_{LM}. The performance of pBasex in this case is also corroborated by the data in Table 4.1(b), which shows the results output by pBasex from simulated images with small β_{LM} values. An interesting result in this case is that all of the pBasex results are very close to the inputs, even when the errors are significant. In particular, when $\beta_{60} = 0$ for the input image (denoted image 1 in Table 4.1(b)) pBasex produces very large errors, but the β_{LM} parameters which are much closer to the inputs than expected

Feature	β_{20}		β_{40}		β_{60}	
	pBasex	Abel	pBasex	Abel	pBasex	Abel
4_1	0.08(2)	0.08	*-0.02(2)*	0.02	0.04(2)	0.00
3_1	-0.36(2)	-0.33	*0.01(2)*	0.01	*0.00(2)*	0.00
2_1	-0.29(1)	-0.24	0.04(1)	0.03	*-0.01(1)*	0.00
1_1	-0.06(1)	-0.03	-0.03(2)	-0.04	*-0.01(2)*	0.00

(a) Comparison of pBasex and Abel determined β_{LM} parameters, data as plotted in Figure 4.4(b).

Image	β_{20}		β_{40}		β_{60}	
	Input	pBasex	Input	pBasex	Input	pBasex
1	-0.2	*-0.24(30)*	-0.04	*-0.05(10)*	0.00	*0.00(6)*
1*		-0.23(2)		-0.05(2)		-
2	-0.2	-0.23(2)	-0.04	*-0.04(2)*	0.01	*0.01(2)*
3	-0.2	-0.23(2)	-0.04	*-0.03(2)*	0.02	*0.02(2)*

(b) pBasex results for simulated images with small β_{LM} values. Three simulated PADs were tested, with increasing β_{60} values. The row marked 1* is the result of a pBasex inversion omitting β_{60}, and produces much smaller errors for the case where $\beta_{60} = 0$.

Table 4.1: Evaluation of extracted β_{LM} parameters for (a) experimental and (b) simulated images. Uncertainties in pBasex results are shown in parenthesis, and parameters in italics have >50 % error and can be regarded as undefined. Uncertainties have not been calculated for the Abel derived results (see Section 4.1.4).

from the magnitude of these errors. In this case the errors can be reduced by omitting the $L = 6$ terms from the inversion (row 1* in Table 4.1(b)); this produces very similar outputs but with smaller errors, presumably because there is less uncertainty in the fit when fewer terms are allowed in equation 4.8. These results again demonstrate the good performance of the pBasex method, and furthermore give confidence that the small β_{60} parameters found in the ammonia data (Chapter 7) are significant.

A final point of note regarding the extracted radial spectra from the pBasex inversion method is the nature of the peak shapes. The features obtained are often asymmetric, with jagged tops. This is a result of pixellation, because the pBasex output only produces 256 data points. Identical peak shapes can be produced by generating Gaussian peaks and plotting them on a coarse pixel grid, this is illustrated in Figure 4.5. A consequence of this is that for experimental data where more than one transition may contribute to the observed feature, the peak profiles may be slightly misleading and should be approached carefully. One method of analysis is the fitting of Gaussian or Lorentzian peaks to the observed spectrum using the same coarse pixel grid (see Figure 4.5), and this may allow the resolution of peaks into component parts. The Abel extracted data does not show pixellation, but the software used to extract the data from the Abel inverted images actually interpolates to sub-pixel steps, leading to excessive noise at high pixel values (see Figure 4.4). This noise can be minimized by re-binning or smoothing the data, but again

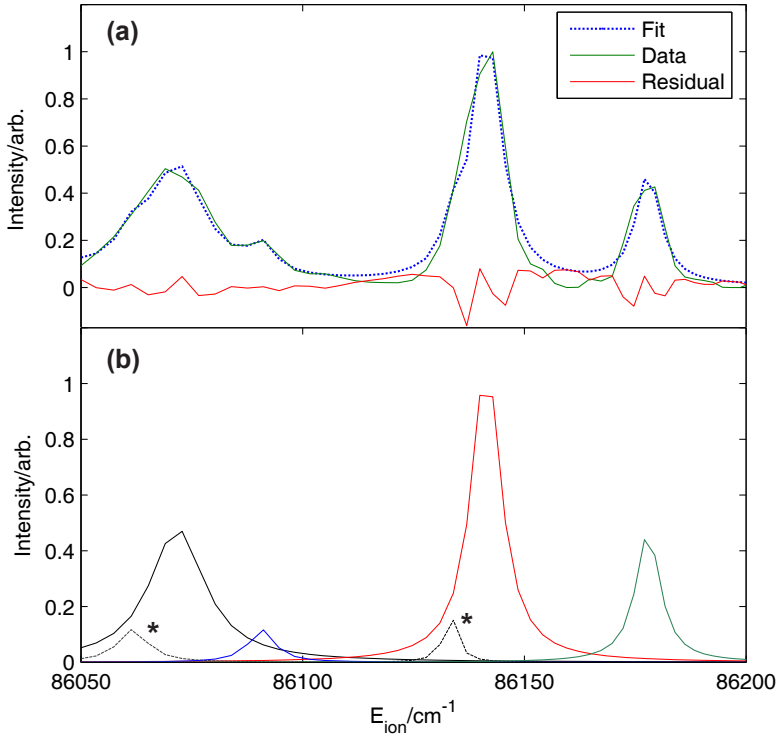

Figure 4.5: Illustration of pixellation and fitting to pBasex extracted data. (a) Experimental data, fit and residual. (b) Lorentzian components of the fit, peaks marked * represent the position of known features which may underlie the intense peaks, but are ambiguous in this data. The quality of the fit is almost identical if they are omitted. Data shown is from ammonia work (Chapter 7), $v_2 = 4$, $1_1 \rightarrow 3_2$ pump transition.

the resultant peak shapes may not be indicative of underlying features.[2]

4.1.4 Error analysis

The raw experimental data, that is the photoelectron count per pixel in the photoelectron image, is a discrete quantity and should obey Poisson statistics. As such the random error in each data point (pixel) gives a standard deviation $\propto \sqrt{N}$ [161], where N is the number of counts. The pBasex algorithm takes N as the pixel intensity in the image and propagates this error through the fitting procedure to give a final uncertainty on the extracted spectrum and β_{LM} parameters. Because the pixel values in the work presented here are uncalibrated they do not actually represent N so this uncertainty may be an underestimate. However, the uncertainties output in tests using simulated data with comparable pixel values has been found to be provide a reasonable error estimate on the pBasex results (see Table 4.1, also ref. [160]). Typical uncertainties are around 1% for data-points in the radial spectra and on the order of a few percent for β_{LM}-parameters, although can be much higher for features near the centre of the image, with β_{LM} parameters near zero (Table 4.1(b)), or with very low intensities (as shown in the Figure 4.2). Because the final β_{LM} parameters obtained for a given feature in

[2] A typical example of this is the long tail often observed to the low-velocity side of features, which is an artefact of the inversion process. This is discussed in ref. [20].

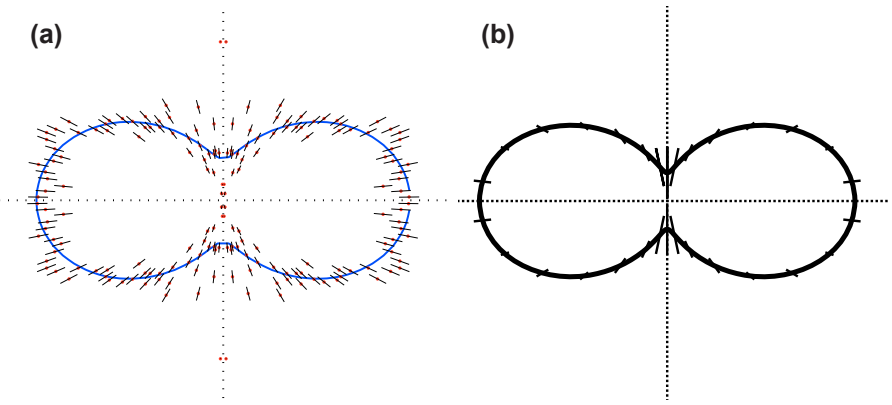

Figure 4.6: Polar plots of PAD extracted from Abel and pBasex inverted data. (a) Abel data, extracted from the inverted image in 1° steps, and fitted form (equation 1.4). Centre-line noise has not been removed in the plot although it was ignored for the purposes of fitting. Error bars are plotted on each data point as $\sqrt{N}$. Note that the data is symmetrized by the inversion process. (b) pBasex derived PAD. Error bars are calculated from the uncertainties in each β_{LM} parameter and plotted at 12° intervals, but *do not represent data points*. PAD shown is 3_1 example from Figure 4.4(b).

the spectrum are obtained by the intensity-weighted average of the $\beta_L(r)$ data-points (equation 4.12), the error in the peak-averaged values is typically quite small - even in cases where the $\beta_L(r)$ uncertainties are large.

The Abel inversion discussed above was only used for testing and consistency checking in this work, so errors were not derived for the fitted β_{LM}, but are expected to be approximately twice those of the pBasex derived results [157].

One important point regarding the plotted PADs shown in this thesis is that they are derived from the pBasex results. These results represent a set of (fitted) β_{LM} values and associated uncertainties, as such there are *no data-points plotted in the PADs*. This in in contrast to Abel extracted data which are in a rawer form, and PADs can be plotted as data points $i(\theta)$ (see equation 4.5), which are then fitted to obtain β-parameters.[3] Figure 4.6 demonstrates this with the comparison of Abel derived angular data and a fit to this data, and the equivalent pBasex derived data plotted directly from β_{LM} values. In the latter case error bars are derived from the uncertainties in the β_{LM}, but the 12° plotting interval is arbitrary and does not represent experimental data points.

4.2 Energy Calibration

Radial spectra obtained from the photoelectron images require calibration to determine the magnification factor (see equation 3.1), allowing the image pixels to be converted to meaningful velocity ($\propto r$) or energy ($\propto r^2$) scales. There are essentially two ways to

[3]Similarly, angular data obtained from techniques which do not require 2D to 3D reconstruction, such as time-of-flight data, is usually plotted as data points $i(\theta)$ which are then fitted to obtain β_{LM}-parameters. There is, however, another subtle difference here in that the Abel extracted data is symmetrized by the inversion process, so again is slightly removed from the raw data which could show differences in each quadrant of the image.

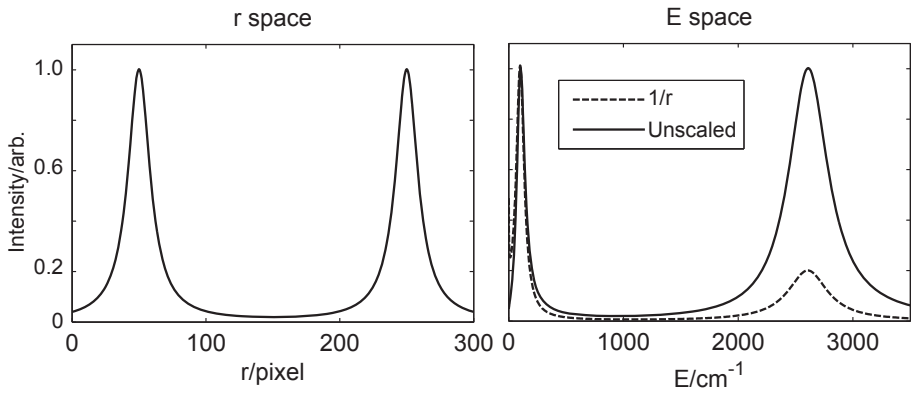

Figure 4.7: Illustration of the conversion from $r \rightarrow E$ space for two identical Lorentzian peaks in r (velocity) space. Peak heights are preserved in the unscaled conversion, division by r normalizes the energy spectrum to peak area.

calibrate photoelectron images, either through the use of known features in the spectrum, or by changing the probe wavelength. Both methods are described below.

The photoelectron kinetic energy associated with a known feature is determined, by conservation of energy, as:

$$E_{KE}(E_+) = \frac{mhc}{\lambda_{probe}} + E_i - E_+ \tag{4.15}$$

Where m defines the number of probe photons absorbed, E_i is the rovibronic energy of the intermediate state and E_+ the rovibronic energy of the ion state formed. The notation, $E_{KE}(E_+)$, is used to show that the kinetic energy calculated is correlated with formation of a given ion state. Equation 3.3 is linear in r^2, and can be rewritten in a simplified form to define the mapping $r^2 \rightarrow E$ in terms of a known peak position:

$$E_{KE} = \frac{E_{KE}(E_+)}{r(E_+)^2} r^2 \tag{4.16}$$

Here the energy, $E_{KE}(E_+)$, and radial position, $r(E_+)$, of the known feature is used to determine the gradient of the transformation, and the energy scale is then found as a function of r^2.

The second method of calibration is to make use of a series of images recorded at different λ_{probe}. Under the assumption that any offset in the probe laser calibration is constant over the range studied, the energy scaling of the images can be deduced by the change in pixel position of a given peak as a function of λ_{probe}. For two different probe wavelengths, λ_1 and λ_2, the change in peak position is given by:

$$\begin{aligned} \Delta E(\lambda_1, \lambda_2) &= hc\left(\frac{1}{\lambda_1} - \frac{1}{\lambda_2}\right) \\ &= m\Delta r(\lambda_1, \lambda_2)^2 \end{aligned} \tag{4.17}$$

where $\Delta E(\lambda_1, \lambda_2)$ is the change in peak position in energy space, and $\Delta r(\lambda_1, \lambda_2)^2$ the change in peak position in units of pixels squared. The gradient, or calibration constant, m, then defines the linear mapping from $r^2 \rightarrow E$. The advantage of this method is that it does not require known features in the spectrum, and is also independent of the absolute calibration of λ_{probe}. The error in this calibration is estimated to be on the order of dE, the minimum energy range covered by a single pixel. For the 2-colour ammonia data (Chapter 7), which was calibrated initially using this method, the error was estimated at $\sim$5 cm^{-1}.

A final note on the conversion from velocity to energy space is the effect on peak shape. Because the mapping from $r \rightarrow E$ is non-linear, peak widths for (resolved) features in the spectrum are constant in velocity space, but *not in energy space* (see also discussion in Section 3.2.1). This is illustrated in Figure 4.7. After mapping from $r \rightarrow E$, two identical Lorentzian peaks in r (velocity) space are no longer identical. Peak heights are preserved under mapping of the type given in equations 4.16 and 4.17, while division by r normalizes the converted peaks by area.

4.3 Fitting Methodology

As defined in Chapter 1, the aim of "complete" photoionization experiments is to fully describe the ionization process by determining the radial dipole matrix elements and phases, $\boldsymbol{r}_{l\lambda}$ and $\eta_{l\lambda}$, the parameters which define the dynamics of the photoionization. Experimentally PADs can be recorded and β_{LM} anisotropy parameters obtained, as discussed above. Providing that the experimental data set is large enough there is then the possibility of obtaining the dynamical parameters by fitting the experimental data with equation 2.52. In such a fitting procedure the geometrical parameters must be calculated, so knowledge of the initial and final states of the system, including alignment, is essential. The ideal data for a complete determination of the photoionization dynamics would thus consist of angular distributions pertaining to population of individual rotational states of the ion (rotationally-resolved PADs), where ionization occurs from a single rotational state of the neutral. The rotationally resolved photoelectron images obtained from photoionization of ammonia (Chapter 7) provide such data-sets. If rotational resolution of the ion is not achieved the data may still be sufficient for a complete determination of the dynamics if the (rotationally-summed) PADs are sensitive to the intermediate state prepared; this is explored further in the acetylene work presented in Chapters 5 and 6.

In order to carry out a fit for a given dataset several points need to be considered, and a logically consistent and rigorous fitting scheme must be followed. These points are discussed in the following sub-sections, which are applicable to both sets of experiments detailed in Chapters 5 and 7.

4.3.1 Energy dependence of $r_{l\lambda}$ and $\eta_{l\lambda}$

In selecting the data to be included in the fit it is imperative to first consider whether the dynamical parameters are expected to be constant for all of the data. This question is

considered extensively by Park & Zare [87, 93], who conclude that the magnitudes of the dipole matrix elements, and associated phases, can be approximated as constant over the rotational levels of a single vibrational manifold for most small diatomic molecules. This is also known as the slowly-varying continuum approximation [111, 131].

These conclusions arise from consideration of the form of the radial part of the photoelectron wavefunction, $\psi_{l\lambda}(r;\mathbf{k},R)$. Asymptotically the wavefunction is composed of regular and irregular Coulomb functions, and these show little dependence on $\mathbf{k}$ at short range. Although the Coulomb functions are not the solutions to $\psi_{l\lambda}(r;\mathbf{k},R)$ in the core region, the boundary conditions (at the surface where the molecular potential is defined to become Coulombic) mean that the short-range dependence of the Coulomb functions must also be reflected in the short-range eigenchannels. Additionally, the variation in $\mathbf{k}$ is small, $<$ 0.01 a.u, over several rotational levels. The energy range for which this assumption holds is given by Park & Zare [93] as around 100 meV ($\sim$800 cm^{-1}). The phases $\eta_{l\lambda}$ are more sensitive to the photoelectron energy at short range, but the phase differences $(\eta_{l\lambda} - \eta_{l'\lambda'})$ do not vary rapidly and can again be approximated as constant over this energy range [93].

Any sharp resonant phenomena in the ionization continuum would, however, invalidate these approximations. An example of such a feature is the Cooper minimum present in the ionization of the NO $D\,^2\Sigma^+$ state, as investigated by Park & Zare [87]. This is diagnosed through the intensity difference observed in ionizing transitions arising from $\Delta N > 0$ and $\Delta N < 0$ for the same $|\Delta N|$ (note $K = 0$ in this work), and allowed for in the fitting procedure by explicitly including a linear energy dependence for the relevant dipole matrix elements. In the NO case this analysis was supported by extensive theoretical work which was extant in the literature. Another common example of this type of resonant phenomena is autoionization [86, 162]. Generally it is expected that a fit to a given dataset will reveal any resonant phenomena by the insufficiency of the fit; if there is any resonant behaviour the fit will not satisfactorily reproduce the experimental data, highlighting a problem with the assumptions and model used.

Further experimental evidence on the response of the dipole matrix elements to energy can be found in the work of Yagishita and co-workers. Here ionization of 1s core-levels of CO and NO [50], $\mathrm{CO_2}$ [163] and $\mathrm{CS_2}$ [164] were studied using synchrotron radiation and a "multi-coincidence" spectrometer to enable MF-PADs to be obtained. The results, and accompanying *ab initio* calculations, show the dipole matrix elements and phases as smooth, slowly varying functions, with significant changes occurring on the scale of eV ($\sim$8000 cm^{-1}), consistent with the approximations discussed above. One point of note however is that "slow" photoelectrons arising from near-threshold valence ionization might be expected to be more sensitive to small changes in the molecular potential than high energy photoelectrons from the core ionization processes probed in these experiments. On a similar note Becker et. al. highlight that valence photoemission should reflect orbital structure rather than molecular topology [55].

The data from Yagishita and co-workers also show shape resonances [50], defined as significant changes in the PADs with photoelectron energy, which occur when certain

partial wave channels become dominant due to continuum resonances. Shape resonances are broad when compared to the energy range of a few rotational levels, and may be several eV in width. It is therefore generally possible that a shape resonance is present, but this will not affect the validity of the approximations discussed here. Related work, studying the response of PADs to photoelectron energy in para-difluoro benzene (pDFB), has been carried out in Nottingham [123, 165]. In this work the dipole matrix elements were not extracted from the data, but the evolution of the PADs with ionizing wavelength along with *ab initio* calculations allowed for the investigation of a near-threshold shape resonance, and small changes in the PADs are seen over energies of $\sim$200 cm^{-1}. As before the response is smooth, with no sharp features on a scale which would contradict the assumptions above.

4.3.2 Dataset size & statistical analysis

Another question to consider, and try to approach in a systematic and methodical fashion, is how large a dataset is required to provide robust results from the fitting procedure? Generally, the larger the dataset the better, particularly when the upper bound for l is unknown and may be large, necessitating many matrix elements to be determined from the fit. Statistically the fit parameters should be more accurately determined for a larger dataset, and there must be at least as many data points as fit parameters for the problem to be soluble. The transition intensities should also be considered, because for weak transitions the errors in the experimental β parameters will be larger.

Statistical analysis of the fitted parameters derived from repeated fits to the same dataset (using random seed values to initialize the fit) can be employed to probe the behaviour of the fitting algorithm, and also to gain information on how well the experimental data defines each fitted parameter. This is accomplished by plotting histograms of the fitted parameters. A large scatter in the value of a given fit parameter over a range of fits to the same data suggests a poorly defined parameter; a consistent result meanwhile shows that a particular parameter is well defined by the dataset. The experimental data can show different sensitivities to different parameters depending on the type of ionizing transitions present, because different transitions will (according to the magnitude of the geometrical parameters and symmetry constraints) be more sensitive to certain partial waves. Additionally, the presence of multiple-minima in the fit may be revealed by the presence of more than one feature in the histogram, reflecting more than one "best" fit result. This is discussed further in Section 4.3.5.

4.3.3 Truncation of the partial wave expansion

The size of the partial wave expansion, as defined by l_{max}, is generally not known *a priori*, so decisions must be made about this cut-off in a fitting procedure. The expectation in photoionization is that the expansion is truncated at low l, due to the centrifugal barrier in the scattering Hamiltonian [61] (see Appendix A for further discussion). In this context "low" has been suggested to be $l \leq 5$ for photoelectron energies $<$50 eV [75].

As a means of making an initial guess for l_{max} the rotational spectra can be used. Angular momentum coupling (equation 2.46) defines that

$$\Delta N \leq l + 1 \tag{4.18}$$

This means that the ionizing transition with largest ΔN observed experimentally can be related to l_{max}. However, there is also the possibility of destructive interference of partial waves leading to near-zero intensities for certain ΔN that are otherwise allowed by angular momentum coupling, so the lack of large ΔN ionizing transitions does not necessarily indicate a lack of high l partial waves [1]. An example of this was seen in the $\mathrm{NO}(A \rightarrow X^{+})$ ionization studied in Zare's group [34, 62, 87] where $\Delta N = \pm 4$ transitions were not observed due to destructive interference of $f\sigma$ and $f\pi$ partial waves. In some cases the maximum L observed in the lab frame PADs may also provide information on l_{max} as is seen in work on ammonia (Section 7.5.2).

The procedure to determine l_{max} is therefore to take an initial value based on the available experimental data, and use this in fitting. The goodness of fit can then be evaluated, as described below. Other values of l_{max} can then be tested and compared to the first guess value.

4.3.4 Fitness criteria

Fitting is carried out using a least-squares type test to evaluate a fit parameter χ^2:

$$\chi^2 = \sum_i \frac{W_i}{\sigma_i^2}[y_i - y(x_i)]^2 \tag{4.19}$$

Here y_i is an experimental data point measured at x_i, $y(x_i)$ is a calculated value at the same point according to the function being fitted and σ_i are the experimental uncertainties [161]. W_i is a weighting term to allow further control over the fit, and the summation is over all data points i. For fitting to PADs $y_i = \{\beta_{LM}\}$ for each observed PAD, where the size of the set of β_{LM} parameters depends on the experiment performed (see Section 1.4.1). The fitting procedure minimizes χ^2 by varying the parameters which affect the fitting function $y(x_i)$. Fitting was performed in MATLAB (R2006b) using the `LSQCURVEFIT` algorithm.[4]

If available, rotational spectra also provide another means to test the fitted parameter set. The calculated β_{00} values are proportional to the angle-integrated photoelectron yield, so can be used to produce calculated rotational spectra (or lower resolution spectra by summation of underlying features). As shown later (Section 6.2.3), comparison with spectra is particularly important when investigating where to truncate the partial wave expansion. As l_{max} is increased it is often possible to find excellent fits to the PADs, but from parameter-sets which produce very poor rotational spectra. The reason for this is that adding more basis functions (i.e. more partial waves) into the fit allows for increasing fidelity in the calculated PAD, but this is just a consequence of the basis set

[4] This algorithm implements a subspace trust region method and is based on the interior-reflective Newton method to minimize χ^2, details can be found in the MATLAB documentation.

expansion and does not necessarily represent a physically meaningful result. The rotational spectrum, when used in tandem with the PADs, can provide the necessary insight as small contributions of high l can drastically change peak intensities and the range of ΔN accessed. The observed intensities can be included directly in the χ^2 function (this corresponds to including β_{00} in the fit), or compared with calculated values after fitting of normalized PADs only (i.e. $\beta_{00} = 1$). Weighting β_{LM} parameters according to the observed intensity of the associated ionizing transition is a similar, but not identical, method of incorporating rotational branching ratios into the fitting procedure.

4.3.5 Error analysis & χ^2 response

The general assumption is that minimization of χ^2 results in the best fit to the data. However, for complex non-linear fitting it is possible that the n-dimensional χ^2 parameter space contains local minima [161], or non-singular global minima. To eliminate these possibilities it is important not only to objectively evaluate fit results, but also to probe the behaviour of χ^2. In essence, this amounts to removing the black-box nature of the fitting algorithm by explicitly looking at the gradient and curvature of χ^2 as a function of the fitting parameters, rather than looking at only the final fitted results. Additionally, the curvature with respect to a given parameter can be used to provide uncertainty estimates on the fitted parameters [161]:

$$\sigma_j^2 = 2\left(\frac{\partial^2\chi^2}{\partial a_j^2}\right)^{-1} \tag{4.20}$$

where σ_j is the uncertainty in parameter a_j. Equation 4.20 relates the response of χ^2 to a given parameter; the sharper the response the better a_j is defined by the data and hence the smaller the uncertainty. Figure 4.8(a) shows an example of a 2D cut through a χ^2 hypersurface, and $\partial^2\chi^2/\partial a_j^2$ in the region of the minima. These plots were generated using the data obtained from experiments on ammonia, as detailed in Chapter 7.

To illustrate the existence of multiple minima χ^2 can be examined with respect to $\eta_{l\lambda}$. In this case the response should be periodic because the phase differences appear as $\cos(\eta_{l\lambda} - \eta_{l'\lambda'})$ in equation 2.52, but the exact form of χ^2 will be more complex due to the existence of multiple phases. Figure 4.8(b) shows the variation of χ^2 with respect to each fitted phase, plotted as a sequence of 1D cuts through the hypersurface. The periodic nature of the function is clear. It is also apparent, as mentioned above, that χ^2 is more sensitive to some parameters and shows a larger response. This will be reflected in the uncertainties calculated from equation 4.20.

The complex, non-linear nature of the fitting is illustrated in the behaviour of χ^2 as a function of $r_{l\lambda}$ (Figure 4.8(b)). In these 1D cuts many of the individual dimensions do not show narrow minima, however the overall value of χ^2 (Figure 4.8(c)) does show a minimum. This reflects the fact that interference is present, so there is a complicated multi-dimensional dependence of χ^2 which depends on relative, rather than absolute, values of the parameters. Another method of probing this behaviour further would be to re-fit the data at each trial value of a_j [88], in this case minima would be expected, and

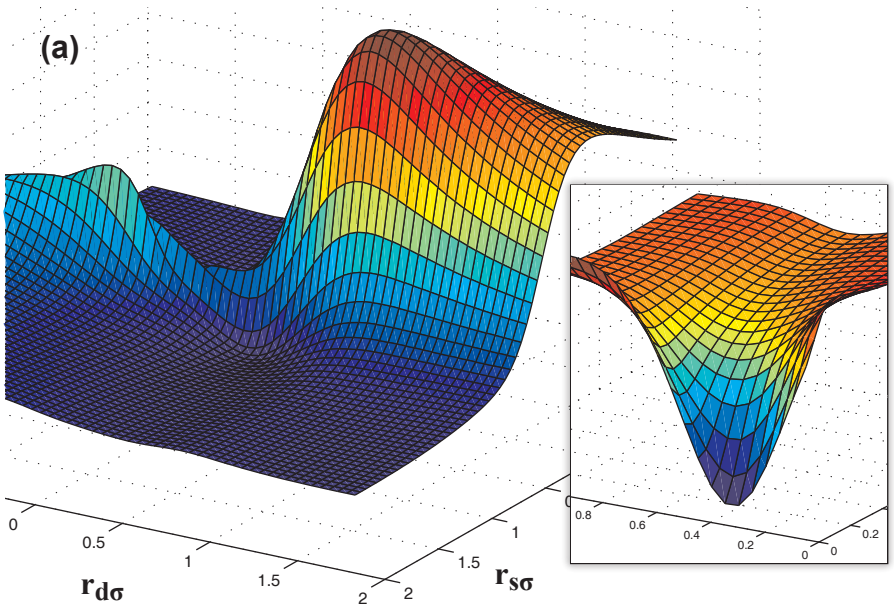

(a) Example of a 2D cut through a χ^2 hypersurface (left) and $\partial^2\chi^2$ in the region of the minima (inset).

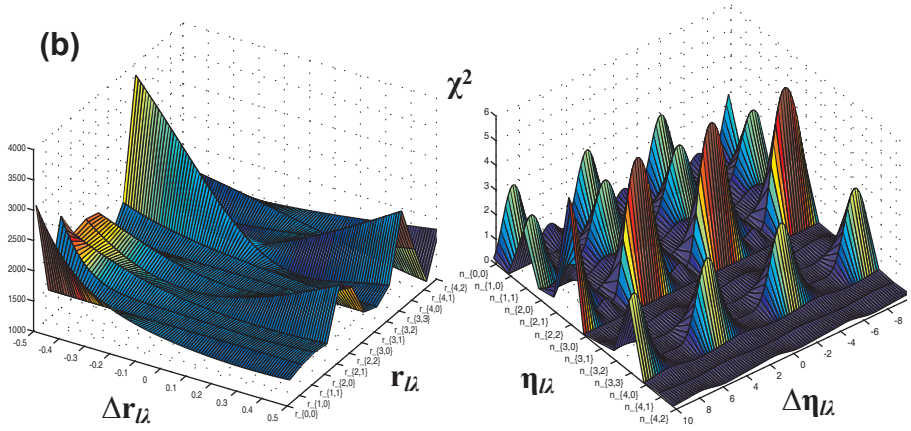

(b) Illustration of χ^2 response with respect to $r_{l\lambda}$ (left) and $\eta_{l\lambda}$ (right). $\Delta r_{l\lambda}$ and $\Delta\eta_{l\lambda}$ are the changes in the parameters away from the best-fit value.

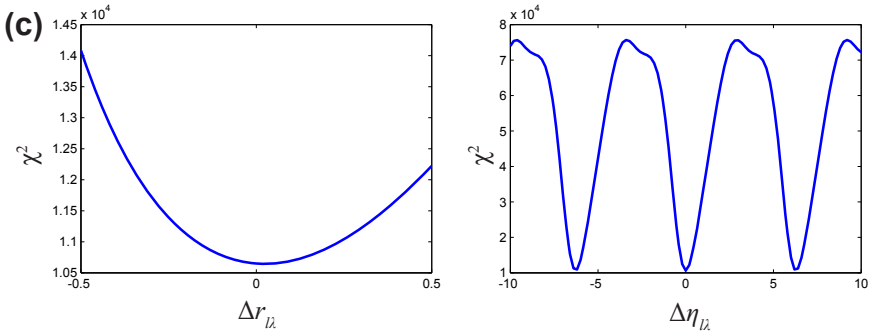

(c) Overall response of χ^2 to $r_{l\lambda}$ and $\eta_{l\lambda}$. (Odd-l continuum.)

Figure 4.8: Illustration of χ^2 mapping and response. Data used is from ammonia, see chapter 8.

the 1D cuts should follow the valley in the χ^2 hypersurface, always tracing the minimum value along the a_j coordinate.

The utility of this analysis, apart from the obvious use of determining uncertainties associated with the fitted parameters, is that it reveals whether the automated fitting routine has searched a large section of parameter space and if the fitted parameters can be confidently accepted as the unique global minima. It also shows the limitations placed on the fit by the function being fitted, in this case $\eta_{l\lambda}$s are determined $\mathrm{mod}(2\pi)$ and are unsigned (due to the even symmetry of cosine). In the case of the $r_{l\lambda}$ parameters it is the relative magnitudes which are important, so final values from the fits are re-normalized so that the total ionization cross section is unity. When running multiple fits with random seed values this is even more apparent, in these cases different sets of unnormalized $r_{l\lambda}$ may be found, if these equate to the same best-fit values when normalized then the fitting algorithm is seen to be searching a large solution space.

4.4 Summary

This chapter has detailed the image processing and data analysis techniques applicable to the work presented in this thesis. Extraction of radial and angular data from inverted images provides the final form of the experimental data: photoelectron spectra and associated PADs. All data presented in the experimental chapters has been processed using pBasex. All PADs presented in this chapter have been plotted as polar plots, with $\theta = 0$ coincident with the z-axis (as defined in Figure 4.1) and normalized such that $\beta_{00} = 1$; this convention is employed throughout the rest of this work. The calibration of spectra in energy space has also been discussed.

Further analysis of experimental data in order to determine the dynamical parameters has also been considered. This involves calculation of the geometrical parameters and fitting of the dynamical parameters. The application of this methodology to specific experimental data-sets is presented in Chapters 6 and 8.

Part II

Results & Analysis

Chapter 5

Acetylene I: Experimental Results

This chapter details experimental work studying the ionization of acetylene via rovibronically selected levels of the $\tilde{A}^1A_u$ electronic state. In these experiments a (1+1) REMPI scheme was used (see Chapter 2). Best resolution was obtained in images recorded via pump transitions $\tilde{X}^1\Sigma_g^+|v_{4(g)}=0, J_gK_g\rangle \rightarrow \tilde{A}^1A_u|v_{3(i)}=4, J_iK_i\rangle$; in these cases the maximum photoelectron kinetic energy was ~600 cm^{-1} and partial rotational resolution is obtained in the photoelectron spectra, with peak widths (FWHM) of ~30 cm^{-1}.

Images were also recorded via $v_{3(i)}=5$ and ($v_{1(i)}=1$, $v_{3(i)}=2$), in these cases the maximum photoelectron kinetic energy was ~2600 cm^{-1} and only vibronic resolution was obtained, although many more ion levels could be accessed. In all cases the PADs obtained are *vibronically-resolved*, they are correlated with the formation of a vibronic band in the photoelectron spectrum and are thus *summed over any underlying rotational structure*. The strict rotational selection rules applicable for population of Σ ($K=0$) vibronic bands in the ion mean that these bands have only a few rotational levels populated, the rotationally summed PADs are found to be most sensitive to the pump transitions in these cases.

Images recorded via $v_{3(i)}=6$, and were also obtained. In these cases the maximum photoelectron kinetic energy was ~4500 cm^{-1} and the resolution obtained in the photoelectron spectra was 100 - 200 cm^{-1}.

5.1 Introduction

Acetylene (C_2H_2) has long been studied spectroscopically. Early work on the $\tilde{X}^1\Sigma_g^+ \rightarrow \tilde{A}^1A_u$ system was carried out by Ingold and King [166], who conclusively established the geometry change from linear to *trans*-bent upon excitation. This means that the molecular structure changes from a linear rotor to a near-prolate asymmetric top upon excitation (see Figure 5.1), giving rise to *axis-switching* effects which can be observed in the spectrum. Extensive work on the characterization of the $\tilde{A}^1A_u$ state was performed

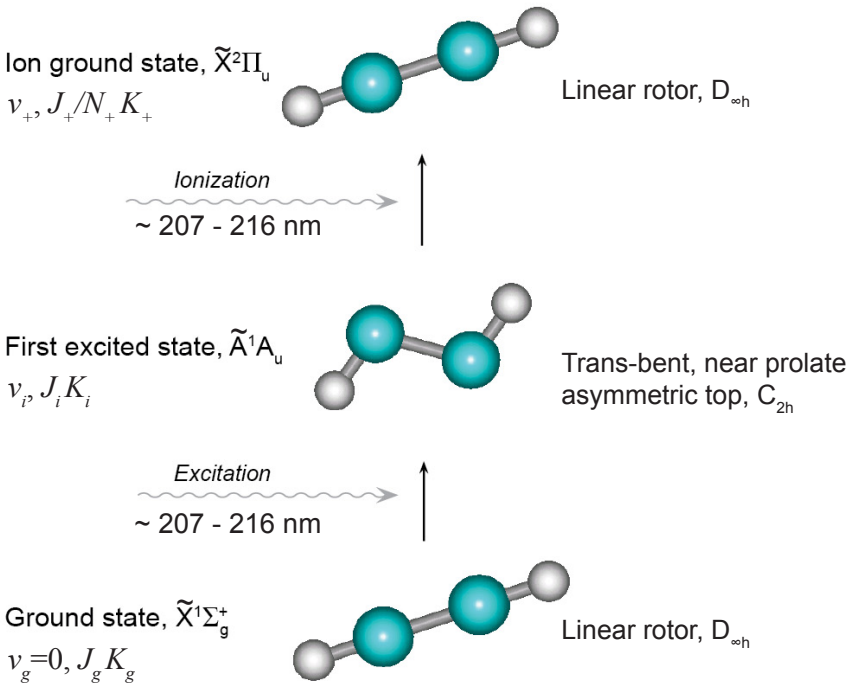

Figure 5.1: Overview of the (1+1) REMPI scheme used.

by Watson and co-workers [167, 168], who developed effective Hamiltonians describing the rotational structure.

There are rich dynamics possible in the $\tilde{A}$-state. The *trans*-bent form can undergo isomerization to the *cis*-bent form if the total energy is $>$ 47400 cm^{-1}; this threshold lies between 5 and 6 quanta in the *trans*-bending mode [169, 170]. Predissociation, mediated by inter-system crossing to metastable triplet states, is also a possibility [171, 172]. In the work presented here these dynamics have not been investigated; possible experiments to probe the intermediate state dynamics are briefly discussed in Chapter 9.

The ground state of the cation, $\tilde{X}^2\Pi_u$, is linear and presents a prototypical system for the Renner-Teller (RT) effect in tetra-atomic systems [173]. The RT effect results in the splitting of vibrational bands into vibronic sub-bands due to the coupling of vibrational and orbital angular momenta. Previous photoelectron studies, most notably by Pratt, Dehmer & Dehmer [6], ZEKE work by the same investigators [174], and ZEKE work by Tang et. al. [175], have been able to assign vibronic and rotational features in the ion, and the Renner-Teller coupling has been analysed. Extensive theoretical studies of the cation have also been conducted by Perić and co-workers, including the RT effect [173].

5.2 Background

In this section the salient details of the electronic states accessed in this work are discussed. Particular attention is paid to the form of the rotational labelling in the linear and

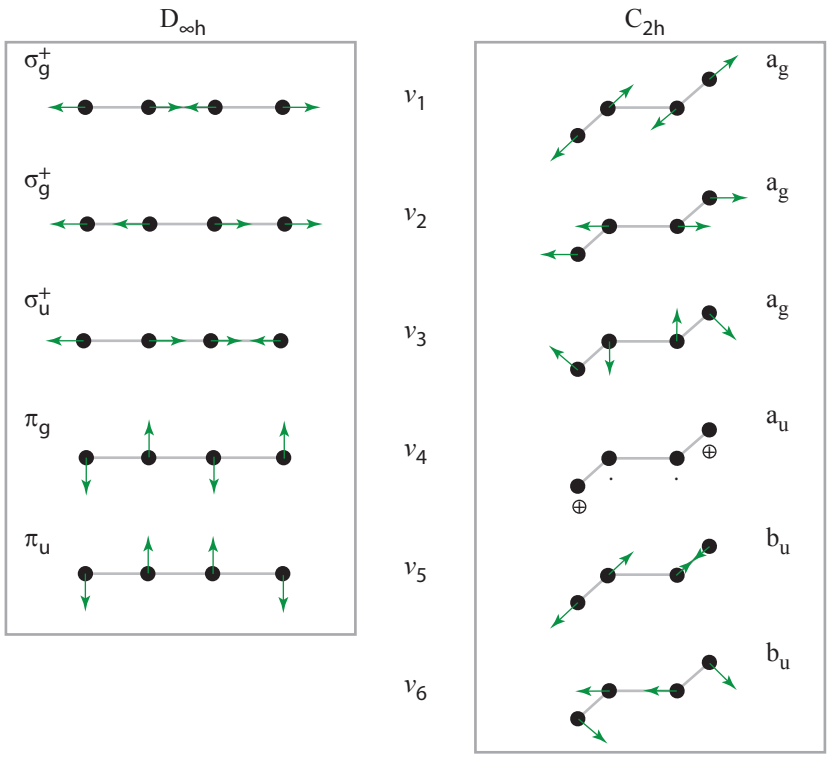

Figure 5.2: Vibrational modes and vibrational symmetry of C_2H_2 in linear and *trans*-bent geometries. Based on ref. [6].

trans-bent geometries, the effects of Renner-Teller splitting in the ion, and the symmetry selection rules imposed on the ionization. Figure 5.1 shows a schematic overview of the excitation and ionization steps, and relevant quantum numbers.

5.2.1 Ground state $\tilde{X}^1\Sigma_g^+$

The geometry of the electronic ground state is linear ($D_{\infty h}$) and has rotational constant $B_0 = 1.176608$ cm^{-1} [167]. The only significant deviation of the rotational behaviour from that of an ideal linear rotor is l-type doubling, which arises due to Coriolis coupling of vibrational and rotational motion (see, for example, [176]). However, this doubling has little effect until relatively high J, around $J = 13$ for $v_4 = 1$. In the jet-cooled case with a rotational temp of order 10 K a Boltzmann calculation shows that $J > 6$ will not be significantly populated. Similarly at a vibrational temperature below 100 K there will be little or no vibrational population above $v_4 = 0$. Consequently for the jet-cooled case the l-doubling can be neglected and a simple linear rotor model (see Section 2.2.3) is sufficient to describe the rotational structure.

In a linear rotor a non-zero molecular axis projection, K_g, of the total angular momentum J_g can only arise from vibronic contributions. In this case of a singlet electronic state $K_g \equiv l_4$, so for $v = 0$, $K_g = 0$ only. The vibrational modes are shown in Figure 5.2, and correlated with their equivalent modes in C_{2h} symmetry (as appropriate for the $\tilde{A}$-state). Due to the linear→*trans*-bent change in the geometry upon excitation the *trans*-bending

vibrational mode is preferentially excited, and long progressions in this mode are observed in the excitation spectrum [167]. This mode is labelled as v_4 in $D_{\infty h}$, and v_3 in C_{2h}, so in general vibrational transitions involving this mode are denoted V_m^n, where the transition is of the form $\tilde{X}^1\Sigma_g^+|v_4 = m\rangle \rightarrow \tilde{A}^1A_u|v_3 = n\rangle$.

5.2.2 Excited state $\tilde{A}^1A_u$

The $\tilde{A}$-state is *trans*-bent and is a near-prolate asymmetric top, point group C_{2h}. The axial projection of the total angular momentum, K_i, is now equated with K_a, the asymmetric top (or total) axial angular momentum quantum number. The strongest sub-bands in the $\tilde{X} \rightarrow \tilde{A}$ transition are those with $\Delta K = \pm 1$, although sub-bands with $\Delta K = 0, \pm 2$ are also observed due to axis-switching upon excitation [167]. As a result of the ΔK propensity rule, in this work only $K_i = 1$ levels were prepared in order to prepare sufficient intermediate state population.

The rotational structure of the $\tilde{A}$-state is accurately modelled by Watson and coworkers [167, 168] using an effective Hamiltonian based on the standard near-prolate asymmetric top case with the addition of centrifugal distortion constants D^J, D^{JK} and D^K. Calculation of the energy levels using this effective Hamiltonian follows the procedure detailed in Section 2.2.3; relevant molecular constants are listed in ref. [167].

5.2.3 Ion ground state $\tilde{X}^2\Pi_u$

5.2.3.1 Vibronic structure

The acetylene ionization potential is 91953.5(5) cm^{-1} [177, 178]. The electronic ground state of the ion is linear ($D_{\infty h}$ point group), with symmetry $^2\Pi_u$. There is the possibility of vibronic coupling between the axial components of the vibrational (l_+) and electronic ($\Lambda_+ = 1$) angular momenta. This is Renner-Teller (RT) coupling, and results in vibronic levels $K_+ = |l_+ + \Lambda_+|$. The vibronic structure dominates both the rotational structure ($B_0 = 1.10463(2)$ cm^{-1} [179]) and the spin-orbit splitting ($|A_0| = 30.91(2)$ cm^{-1} [179]). The RT parameter, ε_{4+}, is 0.30 (dimensionless) [174] for a $K_+ = 0$ level with $v_{4(+)} = 1$ and $v_{5(+)} = 0$, resulting in a splitting between the sub-bands of approximately 400 cm^{-1} [175]. A fuller discussion of the Renner-Teller structure can be found in Refs. [173, 174, 175, 180]; for the purposes of this work it is sufficient to be able to assign the RT states in the photoelectron energy spectra. RT states are labelled according to their value of K_+, i.e. Σ, Π, Δ..., and are preceded by X^m which denotes the parent vibrational level. For example, $4^3\triangle$ denotes the $K_+ = 2$ component of the $v_{4(+)} = 3$ vibrational level. The ungerade symmetry of the $^2\Pi_u$ state means that only RT states with

$$K_+ + v_{4(+)} = odd \tag{5.1}$$

are allowed, hence for even $v_{4(+)}$ only odd K_+ levels exist, and vice versa [180].

5.2.3.2 Rotational structure

Generally there are no additional selection rules on the N_+ levels which can be accessed, beyond those arising from conservation of angular momentum,

$$|\triangle N| \leq l + 1 \tag{5.2}$$

where l denotes the photoelectron orbital angular momentum. However, in the case of $^2\Sigma^{+/-}$ (i.e. $K_+ = 0$) vibronic bands, which have overall even or odd parity, nuclear spin considerations do place additional symmetry restrictions on the N_+ levels accessed. For the $^2\Sigma^-$ state, rotational levels with odd N_+ must be associated with nuclear spin states which are anti-symmetric with respect to exchange of nuclei, while rotational levels with even N_+ must be associated with nuclear spin states which are symmetric with respect to exchange of nuclei [174]. The situation is reversed for $^2\Sigma^+$ vibronic states.

The consequence of the rotational level structure for the Σ states is that the allowed ΔN transitions for the $\tilde{A}^1A_u \rightarrow \tilde{X}^2\Sigma_u^{+/-}$ ionization are dependent on the nuclear spin of the prepared $\tilde{A}^1A_u$ state. Because spin is conserved in electronic dipole transitions, the nuclear spin of the intermediate state is dependent on the nuclear spin of the singlet ground state, in which odd/even J_g correlates with anti-symmetric/symmetric nuclear spin states [174]. The outcome of these nuclear spin consideration is that for R and P branch pump transitions ($\Delta J = \pm 1$), and population of a $^2\Sigma^-$ state in the ion, $\Delta N =$ odd, and for Q branch transitions $\Delta N =$ even. Hence in a rotationally-resolved spectrum from a single rovibronic intermediate state only *alternate* rotational levels will be populated. This is discussed further with respect to the experimentally obtained photoelectron spectra in Sections 5.6 and 6.2.3.

5.3 Experimental Details

The acetylene experiments followed the 1-colour experimental set-up detailed in Section 3.3 and additional details are given here. In these experiments spectrometer #1 was used. UV radiation in the range 207 - 218 nm (sufficient to access several vibrational levels in the $\tilde{A}$-state) was produced using the frequency tripled output from a dye laser (Sirah Cobra-Stretch) with DCM in methanol dye solution. The pulse energy was 2 - 3 mJ at the laser output. The dye laser was pumped with the second harmonic output from a 10 Hz Nd:YAG (Continuum Powerlite Precision II 8010) with a pulse energy of 600 mJ and a pulse duration of 5 - 7 ns.

Acetylene (BOC, $>$ 98.5% pure) was introduced into the spectrometer via a pulsed nozzle (General Valve Series 9), creating a supersonic jet expansion. The UV beam was focused into the VMI spectrometer using a 30 cm focal length lens, and crossed with the supersonic molecular beam. Neat acetylene was typically used in the expansion to keep T_{rot} high enough to populate a range of rotational levels. The rotational temperature was characterized by recording (1+1) REMPI spectra, which were compared with simulated absorption spectra based upon the effective Hamiltonians of Watson et. al. [167] (see

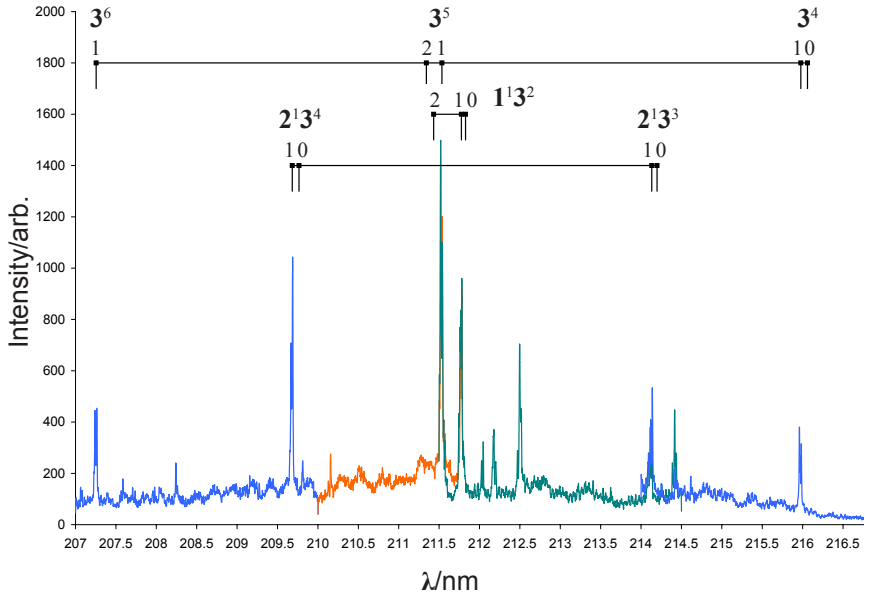

Figure 5.3: Composite REMPI scan over λ = 207 - 216.5 nm. Features are labelled by mode, quanta and K_i, e.g. $\mathbf{3}^5$ denotes $v_{3(i)} = 5$, and the sub-bands $K_i = 1, 2$ are marked.

Section 5.4). Rotational temperatures in the range 20 - 30 K were typically achieved with a 2 bar acetylene gas backing pressure. Additionally, the REMPI spectra offered a method of calibration of the laser wavelength.

5.4 REMPI Spectra

Figure 5.3 shows an extended REMPI scan over the range 207 - 216.5 nm, showing the vibrational bands in this region. The scans shown here are normalized by intensity at peaks which overlap in different scans, but they are not corrected for any drift in laser power. The key levels prepared in this work were $v_{3(i)} = 4$ and 5; ionization from these levels produced uncongested photoelectron spectra showing long progressions in $v_{4(+)}$ due to the *trans*-bent $\rightarrow$ linear geometry change [6], hence the dominant Franck-Condon (FC) factors are of the form $\langle v_{4(+)}|v_{3(i)}\rangle$. Additionally, ionization via $v_{3(i)} = 4$ in a 1-colour experiment provided the lowest photoelectron energy and therefore the best resolution in a velocity-mapped image (see Section 3.2.1). Ionization via $v_{3(i)} = 6$ and the combination band $v_{1(i)} + 2v_{3(i)}$ was also studied.

Figure 5.4 shows the rotational structure in the region of $v_{3(i)} = 4$ and 5, along with simulated spectra and rotational assignments. The data shown here are for a 10% mixture of C_2H_2 seeded in Ar carrier gas. The rotational temperatures are on the order of 5 K. In these spectra it is clear that the R-branch is well resolved and intense, the P-branch is weak and the Q-branch transitions are overlapped. For this reason the majority of the photoelectron images were recorded via R-branch transitions. In order to accumulate a sufficiently large data-set to enable fitting of PADs to determine the dynamical parameters it was necessary to record photoelectron images following the preparation of a number

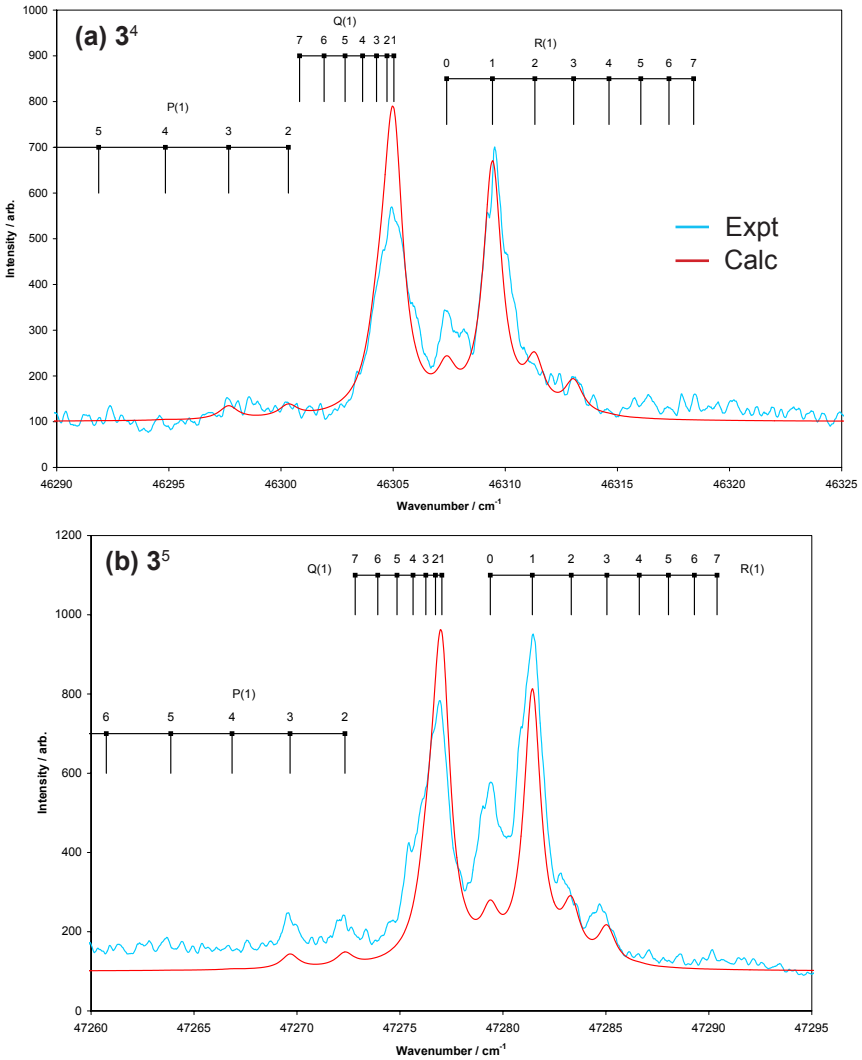

Figure 5.4: Examples of experimental (blue) & simulated (red) REMPI spectra in the region of (a) $V_0^4 K_0^1$ and (b) $V_0^5 K_0^1$. Experimentally a 10% mixture of $\mathrm{C_2H_2}$ seeded in Ar was used. In the simulations $T_{rot} = 5$ K.

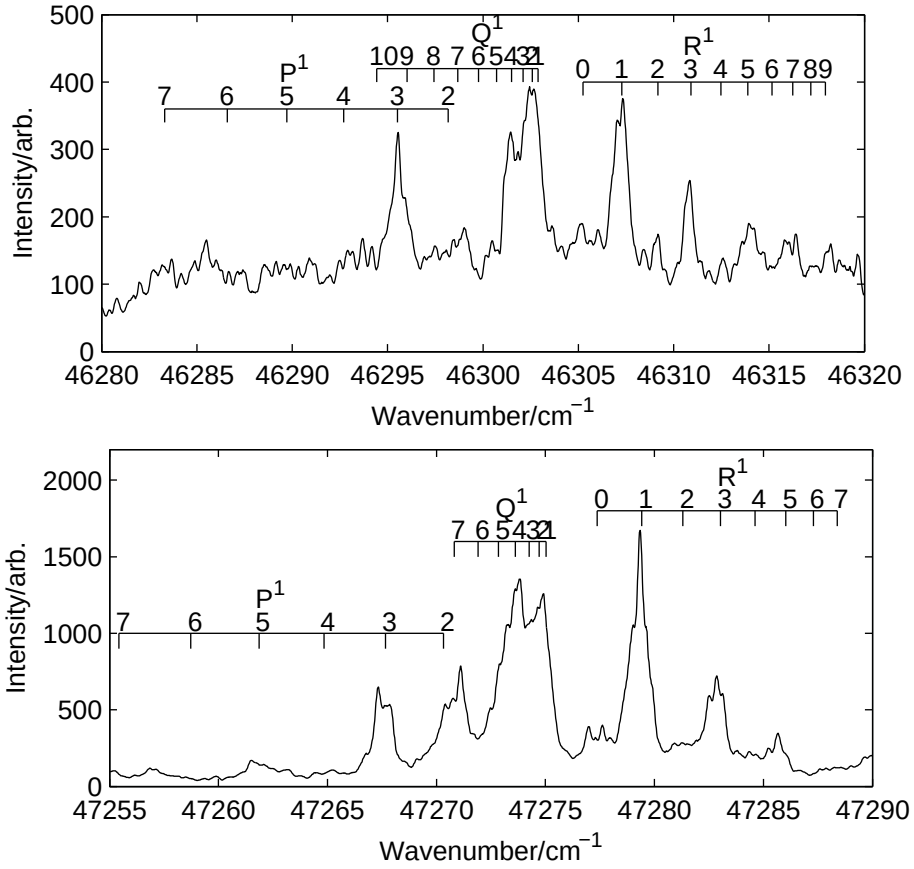

Figure 5.5: REMPI spectra recorded using neat C_2H_2 in the region of the $V_0^4K_0^1$ (top) and $V_0^5K_0^1$ (bottom) bands. The data is shifted by 0.8 cm^{-1} to agree with the calculated line positions.

of different rotational levels in the $\tilde{A}$-state; to allow for this requirement neat acetylene was used. This meant a hotter molecular beam so that more rotational transitions could be accessed. Additionally it increased the number density of acetylene targets, leading to greater intermediate state population and a greater ion yield.

Example REMPI spectra for a neat acetylene expansion are shown in Figure 5.5. The spectra show an increased ground state rotational temperature (∼15 K), leading to population of more rotational levels upon excitation. It can also be seen that the signal:noise (S:N) ratio is much better in the V_0^5 case; this reflects the increased transition strength (as can also be seen in Figure 5.3), and thus intermediate population, due to increased FC factors relative to V_0^4. Again R-branch transitions are well resolved, while Q-branch transitions are overlapped. Simulations of these spectra provide information on which Q-branch transitions are dominant, enabling the assignment of mixed lines in terms of the main components of the unresolved feature.

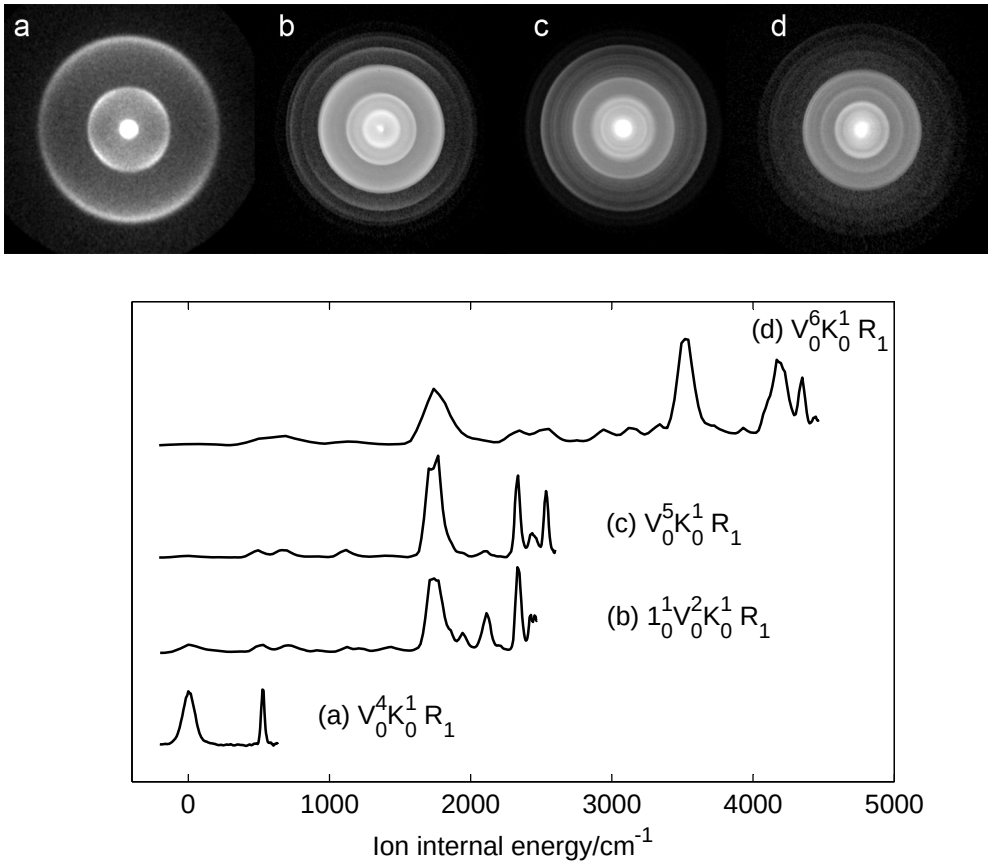

Figure 5.6: (top) Photoelectron images and recorded via pump transitions (a) $V_0^4K_0^1\,R_1$ (b) $1_0^1V_0^2K_0^1\,R_1$ (c) $V_0^5K_0^1\,R_1$ (d) $V_0^6K_0^1\,R_1$. Non-linear intensity scaling has been applied to enhance the contrast of the outer features in images (b)-(d). (bottom) Photoelectron spectra extracted from the images.

5.5 Photoelectron Images & Energy Spectra

Velocity-mapped photoelectron images were recorded as detailed above (Section 5.3, see also Chapter 3) following preparation of rovibrationally selected levels in the $\tilde{A}$-state. Example images recorded via the vibrational bands V_0^4, $1_0^1V_0^2$, V_0^5 and V_0^6 are shown in Figure 5.6, along with photoelectron spectra extracted from these images using pBasex (see Section 4.1) and plotted as a function of ion internal energy. The vibrationless origin peak was used for calibration. In all cases the $K_0^1R_1$ rotational transition presented the most intense single line in the $\tilde{X} \rightarrow \tilde{A}$ system, enabling photoelectron images with good S:N to be recorded and optimized. Once optimized, the laser wavelength was adjusted and further images recorded following preparation of different J_i levels within the vibrational manifold.

In these images the total energy available, and therefore the number of ion states accessible, changes with pump transition because the pump transition defines the laser wavelength and thus the energy of the ionizing photon. The sequence of images (a)-(d) in Figure 5.6 show the consequence of this. For $v_{3(i)} = 4$ only two rings are seen in the image and the maximum electron kinetic energy (E_{KE}) is ~600 cm^{-1}, while for $v_{3(i)} = 5, 6$

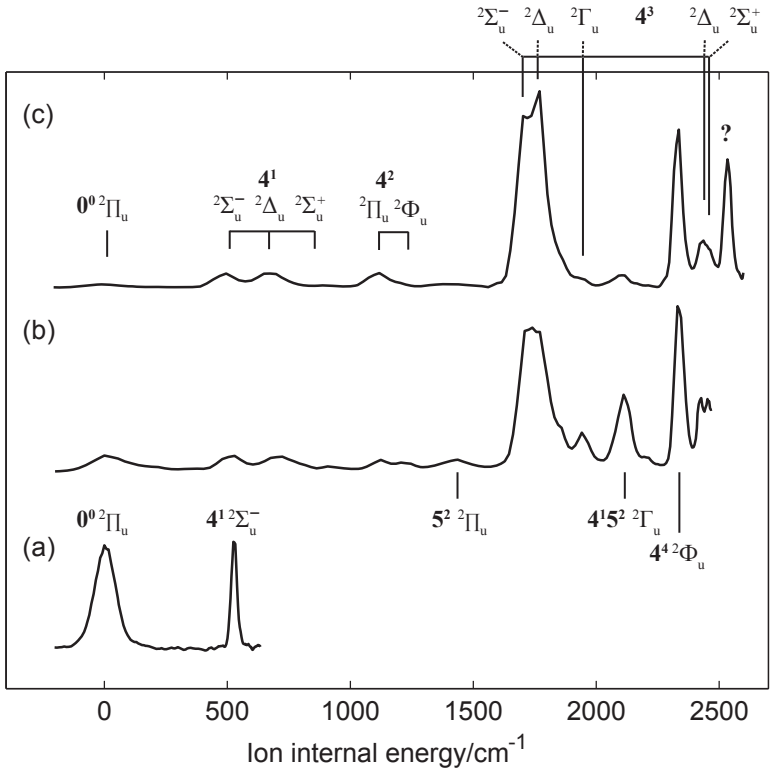

Figure 5.7: Photoelectron spectra recorded via pump transitions (a) $V_0^4 K_0^1\, R_1$, (b) $1_0^1 V_0^2 K_0^1$, (c) $V_0^5 K_0^1\, R_1$, and vibronic band assignments.

there are many more rings visible in the images, and the maximum E_{KE} is ∼2500 and 4500 cm^{-1} respectively. Of particular note in these images is the low intensity of the outer rings in (b)-(d); this reflects the small FC factors for population of $\tilde{X}|v_{4(+)} = n\rangle$ where $n = 0-2$.[1] This effect can also be seen clearly in the photoelectron spectra (Figure 5.6 (b)-(d)), where any features below $E_{ion} = 1500$ cm^{-1} are very weak compared to the dominant features. For ionization following preparation of the $V_0^4 K_0^1\, R_1$ band (Figure 5.6 (a)), the photoelectron yield is small as a consequence of the FC factors, and the S:N not as good as for the other pump bands studied. However, in this case the energy resolution is much better due to the small range of E_{KE} imaged, and peak widths (FWHM) are ∼30 cm^{-1}, compared with 50-80 cm^{-1} for ionization via $V_0^5 K_0^1$. In the images recorded via $V_0^4 K_0^1$ partial rotational resolution was obtained (see Section 5.6).

Due to the large RT effect in the acetylene ion (Section 5.2.3) the features resolved in these spectra are *vibronic* bands, and assignments of these bands have been made up to $E_{ion} \sim 2500$ cm^{-1}. These assignments are shown in Figure 5.7, and compared with literature values in Table 5.1. The RT assignments shown have been based upon previous photoelectron [6] and ZEKE [174, 175] studies, as well as on *ab initio* calculations [173, 184].

[1] These observations can be compared with FC calculations on the $\tilde{X} \rightarrow \tilde{A}$ system [181] which should show the same trends as $\tilde{A} \rightarrow \tilde{X}(+)$ ionization, showing an order of magnitude increase in the calculated FC factors between $n = 0$ and 1, and similarly between $n = 2$ and 3.

Assignment	E_{vib}/cm^{-1}	Literature		
		Pratt et. al. [174]	Tang et. al. [175]	Perić et. al. [173]
$\mathbf{0^0}\,^2\Pi_u$	0		0	
$\mathbf{4^1}\,^2\Sigma_u^-$	499 (12)	485 (3)	487	485
$\mathbf{4^1}\,^2\Delta_u$	686 (19)	668 (3)	666	661
$\mathbf{4^1}\,^2\Sigma_u^+$	859 (40)	903 (3)	897	924
$\mathbf{4^2}\,^2\Pi_u$	1114 (7)	1098 (3)	1095	1095
$\mathbf{4^2}\,^2\Phi_u$	1193 (22)[a]		1325	1320
$\mathbf{5^2}\,^2\Pi_u$	1381 (20)		1379	1452/1488
$\mathbf{4^3}\,^2\Sigma_u^-$	1711 (21)	1672 (3)	1673	1702
$\mathbf{4^3}\,^2\Delta_u$	1752 (19)	1738 (3)	1733	1754
$\mathbf{2^1}$	1805 (22)	[1829 (3)[b], 1811 (30)[c]]		
$\mathbf{4^3}\,^2\Gamma_u$	1917 (33)			
$\mathbf{4^1 5^2}\,^2\Gamma_u$	2101 (10)	2025 (3)	2104	
$\mathbf{4^4}\,^2\Pi_u$	2202 (30)		2288	2358
$\mathbf{4^4}\,^2\Phi_u$	2333 (5)	[2320 (100)[d]]	2387	2436
$\mathbf{4^3}\,^2\Delta_u$	2426 (4)			2481
$\mathbf{4^3}\,^2\Sigma_u^+$	2455 (3)			2555
?	2529 (6)		2508/2524[e]	2554/2565[e]

Table 5.1: Vibronic state assignments. E_{vib} values are derived from Lorentzian peak fits to the experimental spectra, and averaged over all spectra obtained via the $V_0^5K_0^1$ and $1_0^1V_0^2K_0^1$ vibronic bands. Values in parentheses represent the error assigned from the standard deviation of this analysis. Literature values quoted from Pratt et. al. [174] show experimental uncertainties in parentheses; the values from Tang et. al. [175] have been rounded to zero decimal places and the quoted experimental errors are omitted at this level of accuracy, representing an error in the second decimal place. The values in the final column, taken from ref. [173], are from *ab initio* calculations and no uncertainties are given in the source article.
(a) Tang et. al. [175] assign a feature at 1195 cm^{-1} to the $\mathbf{4^1 5^1}\,^2\Pi_g$ state, this matches well in energy with the feature assigned here but is not expected to be observed in this data due to the requirement for overall ungerade symmetry. However, emission of even-l partial waves could allow this state to be populated, although the propensity for this process to occur is expected to be very small [174].
(b) Ref. [182].
(c) Ref. [183].
(d) Ref. [6].
(e) Possible assignment as $\mathbf{4^2 5^2}\,\Pi_u$ or Φ_u state.

To make these assignments spectra obtained from photoelectron images recorded via $V_0^5K_0^1$ (six rotational lines - see Section 5.7) and $1_0^1V_0^2K_0^1$ (two rotational lines) were fitted to Lorentzian lineshapes. Peak positions were averaged over the dataset and errors assigned from the standard deviation of the fits to each peak. The values obtained are in good agreement with literature values within the experimental uncertainties, and in most cases unambiguous assignments can be made. Further support for the K_+ assignments was also provided by the PADs, as is discussed in Section 5.7.1.

Robust assignments of higher energy features ($E_{ion} > 2500$ cm^{-1}) have not been attempted. The lower experimental resolution and increasing congestion of the spectrum (and lack of data in the literature) renders assignments in this region problematic. The fact that 6-quanta of the *trans*-bend is above the isomerization barrier in the $\tilde{A}$-state may also drastically change the spectrum, resulting in an increased propensity for population of

the *cis*-bending mode in the cation. At the resolution of the spectra recorded via $V_0^6K_0^1$ it may be hard to tell if this is the case because many of the vibronic levels originating from the *cis*-bend lie close in energy to those of the *trans*-bend [173]. The significant change in the branching ratio between the cluster of features at ∼2500 cm^{-1} and the features at ∼1800 cm^{-1} between spectra recorded via $V_0^5K_0^1$ and $V_0^6K_0^1$ (Figure 5.6(c) and (d)) may indicate that this is the case; in the absence of significant isomerization the $\mathbf{4^4}\,^2\Phi_u$ feature would be much more intense in 5.6(d).

Spectra recorded via $1_0^1V_0^2K_0^1$ and $V_0^5K_0^1$ show interesting differences, in the former case the features assigned as $\mathbf{4^15^2}\,^2\Gamma_u$ and $\mathbf{4^3}\,^2\Gamma_u$ are much more intense, suggesting that the coupling of $v_{1(i)}$ and $v_{3(i)}$ in the intermediate state leads to enhanced FC factors for excitation of the *cis*-bend in the cation and also leads to an increased propensity for $\triangle K = 3$.

5.6 $V_0^4K_0^1$ Pump Transitions and the $4^1\,^2\Sigma_u^-$ Vibronic Band

5.6.1 Photoelectron spectra

Images recorded via $V_0^4K_0^1(P,Q,R)$ pump transitions provided the highest resolution data, as shown in the previous section. Two vibronic bands, $\mathbf{0}^0\,^2\Pi_u$ and $\mathbf{4}^1\,^2\Sigma_u^-$, are observed in this region of the spectrum. The $\mathbf{4}^1\,^2\Sigma_u^-$ state is of particular interest because the parity selection rules (see Section 5.2.3) result in population of only alternate rotational levels. The observed spectrum is therefore less congested than if all N_+ levels were accessible.

Figure 5.8 shows a series of spectra in the region of the $\mathbf{4}^1\,^2\Sigma_u^-$ vibronic band. Five different pump transitions, $V_0^4K_0^1(R_{1,3,5,7,9})$, are shown. As J_i increases the single feature visible in the spectrum recorded via $V_0^4K_0^1R_1$ broadens and resolves into two peaks. This is due to population of higher N_+ $(= J_i \pm 1)$ rotational levels in the ion and a concomitant increase in the rotational level spacing (see equation 2.28). For high N_+ the line spacing is large enough (30 cm^{-1}) that partial rotational resolution is observed in the spectra. The spectra shown here are consistent with the ZEKE studies of Tang et. al. [175], although these authors do not observe the small features seen at ion energies above 600 cm^{-1}. As will be show later (Section 6.2.3) these can be attributed to $\Delta N = +3$ peaks. The peaks in these spectra are too broad for accurate rotational energy assignments. However, they do reveal the underlying rotational structure of the vibronic state, and therefore provide important information for the calculation of the PADs. Obtaining partial rotational resolution in these spectra also provided the impetus for 2-colour work on NH_3 where much higher resolution was obtained in the photoelectron images (see Chapter 7).

5.6.2 Photoelectron angular distributions

The PADs extracted from the images for the pump transitions $V_0^4K_0^1(R_{1,3,5,7,9})$ are shown in Figure 5.9. These PADs are averaged over the $\mathbf{4}^1\,^2\Sigma_u^-$ vibronic band, and therefore

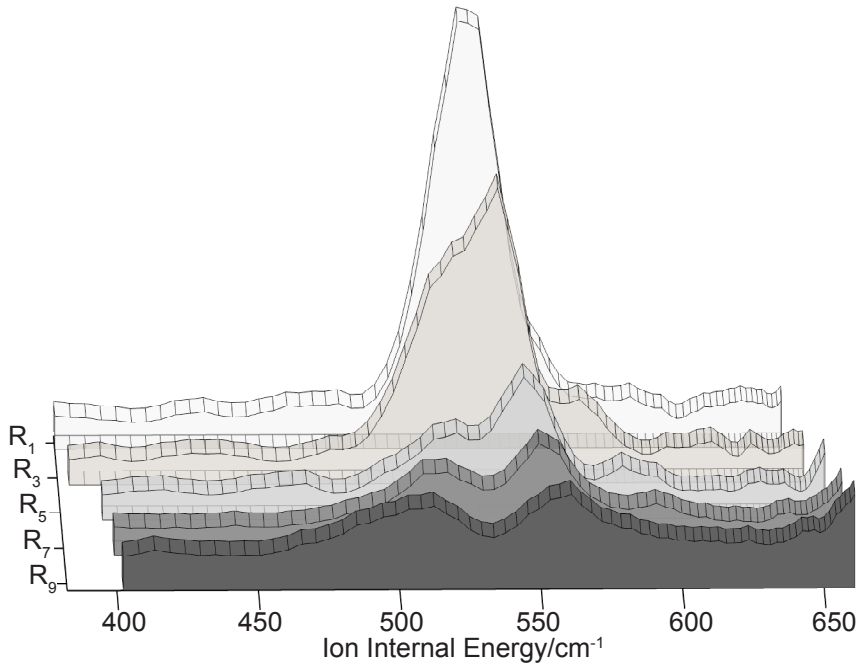

Figure 5.8: Photoelectron spectra in the region of $\mathbf{4}^1\,^2\Sigma_u^-$ vibronic band. Five different pump transitions, $V_0^4K_0^1(R_{1,3,5,7,9})$ are shown. For $J_i \geq 6$ rotational lines of alternate N_+ levels become partially resolved.

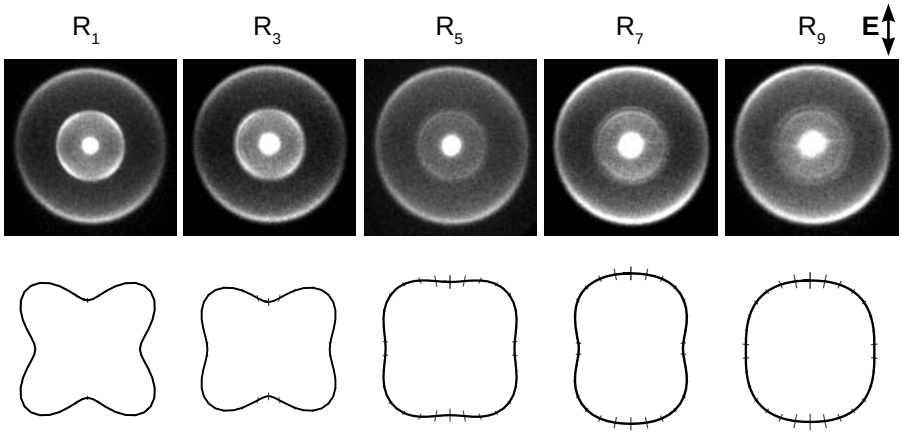

Figure 5.9: Photoelectron images recorded via pump transitions $V_0^4K_0^1(R_{1,3,5,7,9})$, and PADs correlated with the formation of the $\mathbf{4}^1\,^2\Sigma_u^-$ vibronic state of $C_2H_2^+$ (inner ring of the photoelectron images). PADs for pump transitions $V_0^4K_0^1(Q_{3,5,7})$ are shown in Figure 6.1.

Pump Transition	J_i	β_{20}	β_{40}
R_1	2	0.07(1)	-0.15(1)
R_3	4	*0.00(1)*	-0.11(1)
R_5	6	0.04(2)	-0.06(2)
R_7	8	0.13(2)	-0.04(2)
R_9	10	*0.03(2)*	*-0.03(2)*
Q_3	3	*-0.02(1)*	-0.08(1)
Q_5	5	*-0.02(1)*	-0.07(1)
Q_7	7	0.08(1)	-0.05(1)

Table 5.2: Normalized β_{LM} parameters for PADs correlated with the formation of the $\mathbf{4}^1\,^2\Sigma_u^-$ vibronic band via $V_0^4K_0^1(J_i)$. Values in parentheses are errors in the final digit. Parameters shown in *italics* are undefined with respect to the experimental errors ($>$ 50% error) and can be regarded as zero.

represent a sum of the PADs correlated with individual rotational levels (here after referred to as *rotationally-resolved PADs*). Although the images recorded via high J_i show partial rotational resolution, it was found that rotationally-resolved PADs could not be reliably extracted from this data due to excessive noise in the angular data extracted over a small energy range. Only by averaging over a larger energy range could reliable PADs be obtained, with consequent loss of N_+ selectivity. For this data, recorded via a (1+1) REMPI scheme with parallel polarization geometry, equation 1.4 is reduced to three terms with $L = 0,\ 2,\ 4$ and $M = 0$. β_{L0} parameters for these PADs are listed in Table 5.2.

Of particular note in these PADs is the strong four-fold symmetry, and correspondingly large β_{40} parameter. For PADs recorded via higher J_i intermediate levels a reduction in this anisotropy can be seen, with the R_9 ($J_i = 10$) PAD showing very little angular structure. The more isotropic PADs seen for high J_i are reflected in the decrease in magnitude of the β_{20} and β_{40} values for these PADs. The loss in anisotropy correlates with a decreasing alignment of the intermediate state as J_i increases; this point is discussed further in Section 6.2.2. The loss in image fidelity correlates with the increase in the errors attributed to the extracted β_{L0} parameters.

During the recording of these images the effect of laser power was not directly investigated. However, as already noted, the ionization signal observed was very weak, even at the maximum powers available, due to low absorption cross-section and unfavourable FC factors for both the pump and probe transitions. The presence of large β_{40} components in the lab frame PADs suggests that neither the excitation nor ionization transition are saturated. If saturation of M_{Ji} or M_{N+} levels was present, the consequent loss in alignment and therefore lab frame anisotropy would be expected to yield $\beta_{40} \approx 0$.

From angular momentum coupling (see equation 2.52) the non-zero value of β_{40} reveals the presence of partial waves with $l \geq 2$ in the photoelectron wavefunction. As has been shown in Section 2.3, the coupling of the partial waves into the LF-PAD is complex, so it is hard to draw further conclusions without more quantitative calculations. Such calculations are explored in Chapter 6.

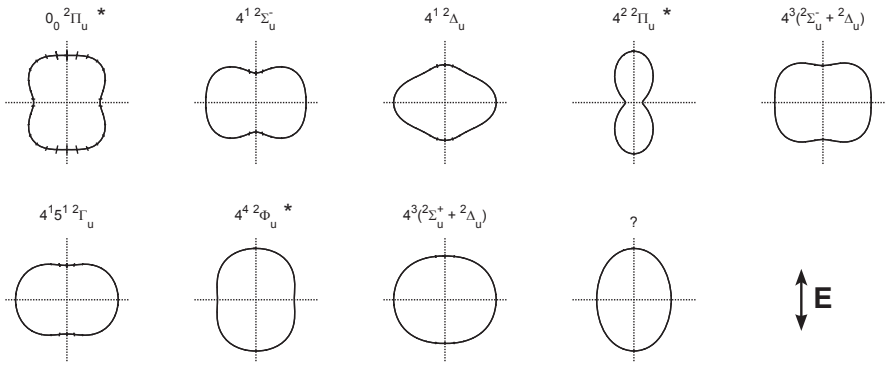

Figure 5.10: Vibronically-resolved PADs recorded via the $V_0^5K_0^1R_1$ pump transition. Vibronic bands are labelled as detailed in the text, and * denotes PADs correlated with vibronic bands for which K_+= odd.

5.7 $V_0^5K_0^1$ Pump Transitions and $K_+ > 0$ Vibronic Bands

The photoelectron spectra shown in Section 5.5 show that, for the $V_0^5K_0^1$ pump transitions, many more vibronic states are accessible in the ion. The energy resolution is much lower than that obtained from the images recorded via the $V_0^4K_0^1$ band, with typical feature widths of around 50-80 cm^{-1}. The Renner-Teller structure of the ion allows K_+ levels to be resolved in most cases (with the exception of some overlapping features), but J_+/N_+ levels cannot be resolved in the data.

Images were recorded via various P, Q and R branch transitions. All transitions and experimentally determined β_{L0} parameters are listed in Appendix B. Because rotational structure was not resolved and, furthermore, is more complicated in the $K_+ > 0$ bands (Section 5.2.3) little change in the peak profiles, or intensities, is observed in the photoelectron spectra recorded via different pump transitions. The PADs extracted for the vibronic bands maintain their sensitivity to K_+, and also show small changes with pump transition.

5.7.1 PADs

Figure 5.10 shows examples of vibronically-resolved PADs recorded via the $V_0^5K_0^1R_1$ pump transition. The PADs show behaviour that is dependent on the value of K_+. For K_+ = odd (marked * in Figure 5.10) the PAD is vertically oriented, i.e. the maximum intensity lies parallel to the laser polarization axis. For K_+ = even the PAD is horizontally oriented, i.e. the maximum intensity lies perpendicular to the laser polarization. This flip in orientation corresponds to a change in sign of β_{20}, which is positive for vertical alignment (peaking at θ = 0, π) and negative for horizontal alignment (see Appendix B for tabulated values). The β_{40} values also show sign changes, but these do not correlate with K_+. In fact, in most cases the β_{40} values are small, and do not make a significant contribution to the PAD. Exceptions are $\mathbf{0^0}\ ^2\Pi_u$ (for R_1, β_{40}= -0.070(20)) and

$\mathbf{4^1}\,^2\Delta_u$ (for R_1, β_{40}= 0.049(8)). In both these cases $\beta_{40} \approx \beta_{20}/2$ so makes a significant contribution to the PAD.

The PADs are also seen to become, in general, more isotropic for the high-lying vibronic states. In particular the $\mathbf{4^3}\,^2\Sigma_u^- + \mathbf{4^3}\,^2\Delta_u$(upper component) and unassigned (?) bands show very little angular structure. This is most likely due to congestion in this region of the spectrum (see Figure 5.7); even though the PADs are extracted from the pBasex inversion by intensity-weighting over the FWHM of a feature, they are likely to contain contributions from more than one vibronic feature in heavily congested regions.

Changes in the PAD according to the prepared J_i state are also observed. Some examples are shown in Figure 5.11, and a full list of experimentally determined β_{L0} parameters is given in Appendix B. There are no clear patterns seen in this data, although in general the PADs do become more isotropic with higher J_i, as may be expected from the loss of intermediate state alignment. Of the examples shown in Figure 5.11, the $\mathbf{4^3}\,^2\Sigma_u^- + \mathbf{4^3}\,^2\Delta_u$ (lower component) PADs clearly exhibit this behaviour, while the PADs for the formation of the $\mathbf{4^1}\,^2\Sigma_u^-$ band show anomalous changes between R_1 and R_3. These changes may simply reflect the low intensity of this band, which can be seen in the spectra (Figure 5.7), rendering the extracted β-parameters less reliable. Despite this uncertainty, the 4-fold structure (i.e. significant β_{40}) observed in the $V_0^4K_0^1$ data (Section 5.6) is visible in the PADs, suggesting that the dynamical parameters may not change substantially between the two intermediate vibrational levels studied. This point is discussed in further detail in Section 6.3.2.

The orientation changes of the PAD (which are consistent over the dataset) may be due to several factors which contribute to the observed PADs:

- Change in the angular momentum coupling between ΔK = even and ΔK = odd.
- Vibrational dependence of the dynamical parameters ($r_{l\lambda}$, $\eta_{l\lambda}$).
- Contribution of more/different partial wave components for different ΔK.
- Photoelectron kinetic energy dependence of the dynamical parameters. The range of photoelectron energies accessed is ~2600 cm^{-1}, so small but possibly significant changes might be expected. (See 4.3.1 for further discussion of this point.)

Of these factors, it is the change in ΔK that appears to correlate strongly with the orientation flips. However, because of the selection rules on the RT vibronic bands (Section 5.2.3) there are no cases where odd/even ΔK can be compared for the same parent vibration, so any vibrational dependence of the dynamical parameters could also contribute to the observed behaviour, and would be difficult to separate from geometric contributions. Changes in the dynamical parameters due to photoelectron energy would not be expected to be significant or periodic on the energy scale of different K_+ states, so are unlikely to produce the observed flips. The contribution of different partial wave components (discussed further in Sections 6.1.1 and 6.3.1) may, like the vibrational dependence, contribute to the observed behaviour and would be difficult to disentangle in this data.

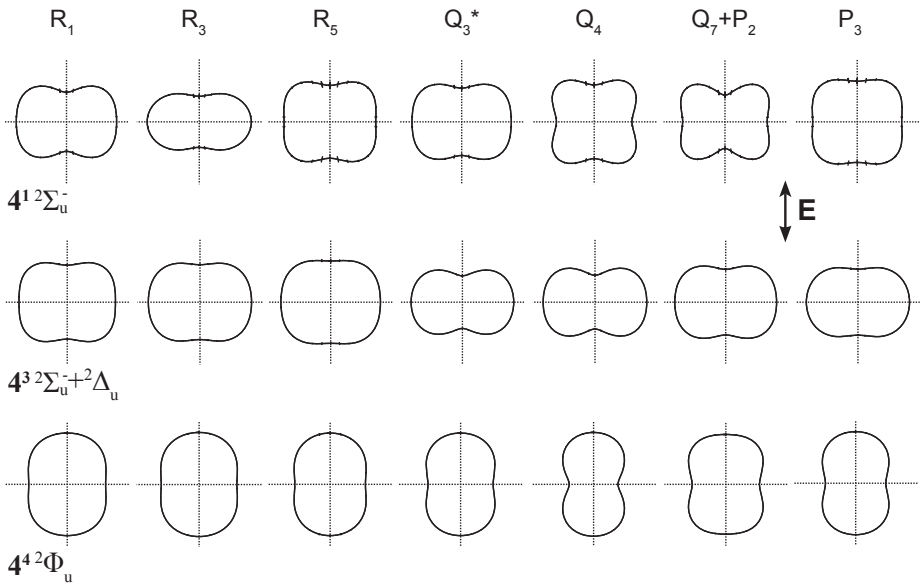

Figure 5.11: PAD response to pump transition for the $\mathbf{4^1}\,^2\Sigma_u^-$, $\mathbf{4^3}\,^2\Sigma_u^- + \mathbf{4^3}\,^2\Delta_u$ (lower component) and $\mathbf{4^4}\,^2\Phi_u$ vibronic bands. * Mixed with Q_1 and Q_2.

These considerations show how problematic it can be to attribute changes in the PADs to a single factor, and highlight the limitations of a 1-colour experiment. In a 2-colour scheme the vibrational and kinetic energy dependence could be probed independently and systematically.[2] However, the considerations above suggest that only significant changes in the partial wave phases could be responsible for the observed flips in the PAD, and their periodic nature. This would most likely arise from a change in sign of the geometrical parameters which correlated with ΔK. This conclusion is reinforced by the fact that the features $\mathbf{4^3}\,^2\Sigma_u^- + \mathbf{4^3}\,^2\Delta_u$(lower component), $\mathbf{4^1 5^2}\,^2\Gamma_u$ and $\mathbf{4^4}\,^2\Phi_u$ all lie close in energy, and will show significant differences in FC factors $\langle\chi_{v(+)}|\chi_{v(i)}\rangle$, yet exhibit the same orientational flips in the associated PADs.

In order to explore this behaviour in detail calculations are required, not least because the angular momentum coupling is complicated (see equation 2.46) and quite unintuitive. As will be discussed in Section 6.3.1, limiting case calculations are able to reproduce the observed flips in the orientation of the PADs in this case (for a given set of dynamical parameters), showing that the observed behaviour can be attributed primarily to angular momentum coupling. This supports the above conclusion that changes in the dynamical parameters over the states accessed do not make significant contributions to the observed PADs.

5.8 Conclusions

In this chapter photoelectron images recorded via selected rovibrational levels of the $\tilde{A}^1A_u$ electronic state of C_2H_2 have been presented. Photoelectron spectra extracted from the

[2]Work on ammonia (Chapter 7) shows some examples of how the vibrational and kinetic energy dependence can be probed in this way.

images allowed assignment of Renner-Teller bands in $C_2H_2^+(\tilde{X}^2\Pi_u)$. The best experimental resolution was obtained in the region of the $4^1\,^2\Sigma_u^-$ vibronic band, following pump transitions $V_0^4K_0^1$, and partial rotational resolution was achieved. Angular distributions were observed to be sensitive to the prepared rotational level, even in cases where the rotational structure of the ion was not resolved. Orientational flips in the PAD, with respect to the laser polarization, were observed and correlated with changes in the geometrical parameters.

Elucidation of the dynamical parameters from sub-sets of this data are presented in Chapter 6, along with further discussion of the photoionization dynamics.

Chapter 6

Acetylene II: Partial Wave Analysis

In this chapter a quantitative analysis of the C_2H_2 data (presented in Chapter 5) is presented. Using the theory and fitting methodology discussed in Chapter 2, and the data presented in Section 5.6 pertaining to the formation of the $\mathbf{4}^{\mathbf{1}2}\Sigma_u^-$ vibronic level, it has been possible to perform a full analysis of the $\tilde{X}^1\Sigma_g^+|v_{4(g)}=0, J_gK_g\rangle \rightarrow \tilde{A}^1A_u|v_{3(i)}=4, J_iK_i\rangle \rightarrow \tilde{X}^2\Pi_u|v_{4(+)}=1, J_i, K_i=0\rangle$ ionizing transition. The radial components of the dipole matrix elements, and associated phases, are thus determined from the experimental measurements. Ion rotational spectra have been calculated and compared with ZEKE data, and are shown to provide a powerful means of evaluating the fitted parameters.

Data pertaining to the formation of higher-lying vibronic bands have also been analysed. Some fitting has been attempted and, although there is insufficient data in these cases for the confident determination of a unique parameter-set, the parameters obtained do begin to provide some insight into the dependence of the dipole matrix elements on intermediate vibrational level. Calculations have also been performed to explore limiting cases by employing additional assumptions in the analysis. The orientational flips observed in the PADs with ΔK odd/even can be reproduced in this way.

6.1 Application of Photoionization Theory to C_2H_2

6.1.1 Angular momentum considerations

As discussed in Chapter 5, the Σ vibronic levels have negligible spin-orbit splitting so are described by Hund's case (b) coupling [174]. In this case the angular momentum coupling scheme given in equation 2.46, with the spin terms omitted, is appropriate. For the $0 < K_+ \leq \nu_{4(+)}$ vibronic levels spin-orbit coupling is significant, and the system is best described as a mix of Hund's cases (a) and (b) [174]. This means that it is necessary to include spin in order to model different spin-orbit bands.

Selection rules due to the conservation of angular momentum, which are encoded in the coupling scheme, can be used to place an upper limit, l_{max}, on the photoelectron partial wave expansion. In particular, equation 5.2 shows:

$$|\Delta N_{max}| \leq l_{max} + 1 \tag{6.1}$$

The partially rotationally-resolved data observed for the formation of the $\mathbf{4^1}\,^2\Sigma_u^-$ vibronic level shows $\Delta N_{max} = \pm 3$. The ZEKE spectra obtained by Pratt et. al. [174] and Tang et. al. [175] show $\Delta N_{max} = \pm 3$ for the $\mathbf{4^1}\,^2\Sigma_u^-$ vibronic state, and for $K_+ > 0$ vibronic levels show $\Delta N_{max} = \pm 4$. These observations are all consistent with $l_{max} = 3$. Additionally, both groups suggest that the π_g molecular orbital from which the electron can be considered to be removed upon ionization of the $\tilde{A}^1A_u$ state[1] is "similar to" [174], or "roughly the same shape as" [175] an atomic d-orbital, so p and f partial waves may be expected to dominate in a simplified, atomic-like, picture. This simplified description is useful as a first approximation, or zero-order model, with which to gain some physical insight into the ionization dynamics. However, it should be noted that in this work there is no direct determination of the $\tilde{A}^1A_u$ state character, and in the following analysis *no assumptions are made about the character of this state*.

As noted elsewhere (Section 4.3), the absence of higher $\triangle N$ transitions is not an unambiguous indication of the lack of higher l because destructive interference of the partial waves may cause the transition intensity to become negligible. However, the use of equation 6.1 does provide a useful starting point in the analysis. As will be shown later, in this case the limit imposed by this selection rule is consistent with the fits (using equation 2.52) to the experimental PADs.

Restrictions are placed on λ, the projection of l onto the molecular axis, because it is coupled to K. In particular, for $K_i = 1$, the third and fourth $3j$ terms appearing in equation 2.46 define:

$$\begin{aligned} |\lambda| &= K_t,\, K_t \pm 1 \\ |K_t| &= \Delta K \end{aligned} \tag{6.2}$$

6.1.2 Symmetry considerations

For acetylene the selection rules detailed in Section 2.4 can be considered in terms of just the inversion symmetry (*gerade*/*ungerade*) of the initial state and final photoelectron-ion complex. For the overall *ungerade* vibronic states observed in this work, equation 2.56 becomes

$$\Gamma^e \otimes u \otimes u = u \tag{6.3}$$

Hence,

$$\Gamma^e = u \tag{6.4}$$

[1] In the molecular orbital picture this would leave a π_g hole. *Ab initio* calculations in ref. [185] characterize the cation ground electronic state ($\tilde{X}\,\Pi_u$) as 88% π_g^{-1}, suggesting that molecular orbital theory is a reasonable framework to use in this case.

and only odd-l partial waves are symmetry allowed. This conclusion agrees with the comments in ref. [174], and also the related conclusions of ref. [142] with respect to diatomic molecules in the $D_{\infty h}$ molecular symmetry group. Additionally, because the *cis*-bending mode in the ion has *ungerade* inversion symmetry, population of vibronic levels with $v_{5(+)} = odd$ will mean that only even-l waves fulfil equation 2.56 because the vibronic state is *gerade*. Population of such vibronic states is observed in ref. [175], although the transition intensities are weak. Note that there are no symmetry restrictions placed on the rotational levels (except for $K_+ = 0$ as discussed in Section 5.2.3) by these rules because for every J_+ level ψ_{nuc} can be antisymmetric or symmetric, so there is always an allowed combination of appropriate parity which can be populated upon ionization [174].

Although these symmetry rules do not provide any information on the amplitudes of different partial wave components, they do allow the ionization to be considered in terms of either odd-l or even-l continua for a given vibrational state. When combined with the angular momentum selection rules discussed in Section 6.1.1, it is clear that for *ungerade* vibronic states $l = 1, 3$ components are expected to be dominant, while higher odd-l waves may also make a contribution to the photoelectron wavefunction.

6.2 Determination of Dynamical Parameters - $4^1\,^2\Sigma_u^-$ Vibronic Band

Photoelectron spectra and angular distributions recorded for the ionizing transition $\tilde{A}^1A_u|v_{3(i)} = 4, J_iK_i\rangle \rightarrow \tilde{X}^2\Pi_u|v_{4(+)} = 1, J_+, K_+ = 0\rangle$, following the pump step $\tilde{X}^1\Sigma_g^+|v_{4(g)} = 0, J_gK_g\rangle \rightarrow \tilde{A}^1A_u|v_{3(i)} = 4, J_iK_i\rangle$, were presented in Section 5.6. As discussed there, these data represent the best opportunity for performing a "complete" analysis by extracting the dynamical parameters from a fit to the data. This procedure is detailed here, along with discussion of the assumptions applied and the validity of the final results.

6.2.1 Fitting PADs

Figure 6.1 shows the results of fitting the data obtained via $V_0^4K_0^1(Q, R)$ pump transitions using equation 2.52. In order to carry out this fit PADs were calculated for all rotational levels unresolved in the data, i.e. formation of $N_+ = N_i \pm 1$, $N_i \pm 3$ for R-branch pump transitions, and $N_+ = N_i$, $N_i \pm 2$ for Q-branch pump transitions (see Section 5.2.3), and these were summed to produce a *vibronically-resolved* PAD which could be compared with the experimental data. Limits were placed on the partial wave components allowed to contribute to the PAD as discussed above; in this case $l = 1, 3$ only (see Section 6.2.3 for more on this point) and $|\lambda| = 0, 1$.[2] Phases were determined relative to $\eta_{p\sigma}$, which was fixed at zero. Weighting was applied to the dataset to allow for differences in image fidelity.

[2] See addendum, Section 6.5.

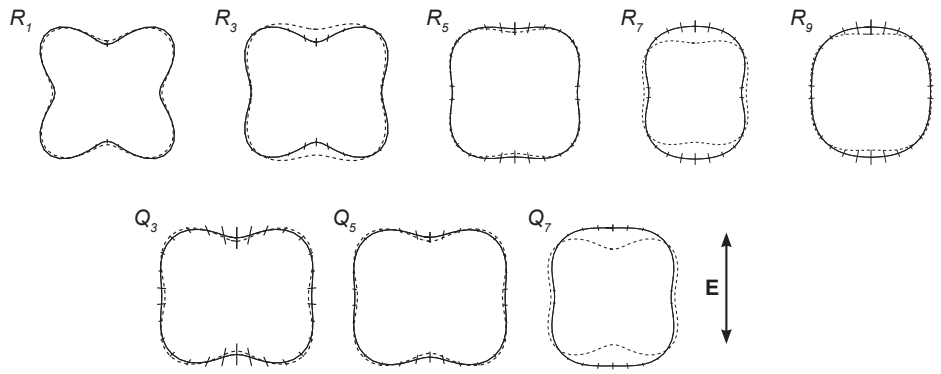

Figure 6.1: Experimental (solid lines) and fitted (dashed lines) PADs for the formation of the $4^1\,^2\Sigma_u^-$ vibronic band following pump transitions $V_0^4 K_0^1(Q,R)$.

Unconstrained fitting was repeated around 100 times, with random seed values, to ensure the uniqueness of the fit. Various sets of $\{r_{l\lambda},\, \eta_{l\lambda}\}$ were found in this way. All phases were converted to $modulo(360)$. Each set of magnitudes was normalized, and re-expressed in terms of the partial wave cross-section (F_l) and degree of parallel character (Γ_l):

$$\sum_l r_{l\sigma}^2 + 2r_{l\pi}^2 = 1 \tag{6.5}$$

$$F_l = r_{l\sigma}^2 + 2r_{l\pi}^2 \tag{6.6}$$

$$\Gamma_l = \frac{r_{l\sigma}^2}{F_l} \tag{6.7}$$

Once recast in these relative terms, necessary because the absolute cross-section measurements required to determine absolute values of $r_{l\lambda}$ are not made in this work, all the parameter sets which were found to fit the data were seen to be equivalent. The range of both magnitudes and phases found to fit the data demonstrated that the fitting algorithm sampled a large solution space, ensuring that the final parameters determined from the fit are unique.

The dynamical parameters determined from this fit are shown in Table 6.1, including uncertainties in the fitted parameters estimated as detailed in Section 4.3.5. As can be seen in Figure 6.1, the fitted PADs match the experimental data well. The agreement is slightly poorer for the R_7 and Q_7 cases, although the experimental uncertainties are also larger in these cases (this is linked to the loss in signal intensity for higher J_i as discussed in Chapter 5) and the fit is weighted in favour of the lower J_i data. The match to the R_3 data is also not quite as satisfactory, although there are no obvious reasons why this should be the case.

The fit shows the $p\pi$ component as the dominant contribution to the asymptotic photoelectron wavefunction, with approximately equal contributions from the $p\sigma$, $f\sigma$ and

l	λ	$r_{l\lambda}$	$\eta_{l\lambda}$/deg	Γ_l/%	$r_{l\lambda}^2$/%	F_l/%
p	σ	0.299 (19)	0*	12 (3)	9.0 (26)	78 (3)
	π	0.587 (6)	117 (1)		68.8 (18)	
f	σ	0.311 (5)	355 (3)	43 (2)	9.7 (7)	22 (2)
	π	0.251 (7)	70 (1)		12.6 (20)	

Table 6.1: Fitted dynamical parameters. $r_{l\lambda}$ are normalized such that the total cross-section is unity. $\eta_{l\lambda}$ are relative to $\eta_{p\sigma}$, which is fixed at zero. Γ_l represents the degree of parallel character, $r_{l\lambda}^2$ the partial cross-section and F_l the l-wave cross-section.

$f\pi$ components. The four-fold structure observed in the PADs can be correlated with the non-zero f-wave contribution to the photoelectron wavefunction, as $\beta_{40} \neq 0$ in this case requires either $l = 1, l' = 3$ or $l = l' = 3$ (see equation 2.52). Significant phase shifts between the various components are also deduced. The associated uncertainties from the fit are small because the PADs are very sensitive to the relative phases. In particular the large β_{40} terms show that the f-wave phases are well-defined by the experimental data despite the small associated magnitudes.

The following subsections (6.2.2 and 6.2.3) examine various aspects of these calculations, including the validity of $l_{max} = 3$, and subsection 6.2.4 explores the physical interpretation of these dynamical parameters in further depth.

6.2.2 Alignment and rotational-summation

As noted in Section 5.9, the loss in anisotropy with increasing J_i can be attributed to the loss in intermediate state alignment. This effect is illustrated in Figure 6.2, where the calculated PADs are compared with the alignments prepared in the intermediate state (see also Section 2.2.2.3 for more on alignment). Interestingly, in both the R and Q branch cases, the four-fold structure observed in the PAD remains. These two cases have "opposite" alignments, with maximum population at $M_i = 0$ (*perpendicular* alignment) for R-branch pump transitions and at $M_i = J_i$ (*parallel* alignment) for Q-branch transitions. The parallel and perpendicular terminology here referring to the alignment with respect to the lab frame z-axis as defined by the laser polarization. The presence of four-fold PADs in both cases illustrates the complex coupling of many angular momenta shown in equation 2.49, rendering the effect of differing alignments far from intuitive. Also, for these PADs different ΔN levels are accessed, so there are potentially other unresolved differences which give rise to the observed similarities in the vibronic PADs. This is considered further below.

At higher J_i the PADs recorded via R-branch transitions appear to lose strong four-fold structure more quickly than those recorded via the Q-branch. This observation can be explained by consideration of the main contributions to the vibronically resolved PADs. For the R-branch case there are two rotational lines observed with almost equal intensity in the photoelectron spectra, correlated with $\Delta N = \pm 1$, and much weaker features for $\Delta N = \pm 3$ (see Section 5.6). The rotationally-summed PADs are therefore composed primarily of just two components. For the Q-branch case there are three N_+ lines observed

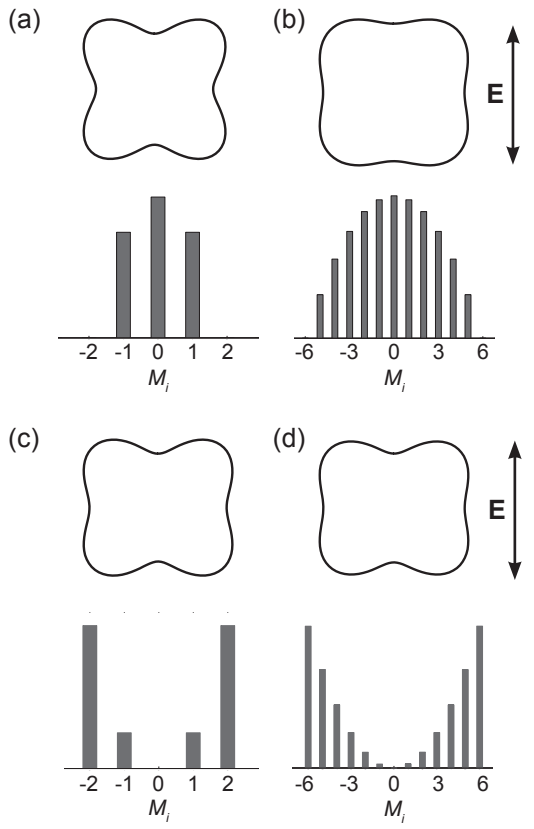

Figure 6.2: Calculated PADs for pump transitions $V_0^4 K_0^1$ (a) R_1, (b) R_5 (c) Q_2 and (d) Q_6. Intermediate state alignments are shown in terms of the relative population of M_i levels in each case.

with almost equal intensity, correlated with $\Delta N = 0, \pm 2$. Although this means that the PADs recorded via the Q-branch contain three major components, the higher ΔN transitions are coupled more strongly to the f-wave through the geometrical parameters, and exhibit larger β_{40} parameters. This is illustrated by the calculated rotationally-resolved PADs shown in Figure 6.3.

Figure 6.3 (left panel) shows how the vibronic PADs for the R_1 and Q_3 cases look similar, despite quite different forms of the rotational PADs in the two cases. It is therefore not surprising that the evolution of the PAD with J_i is different for the R and Q pump transitions. It is not only a consequence of alignment, but the behaviour of the different rotational transitions accessed in the two cases. For the Q-branch pump transitions the $\Delta N = \pm 2$ PADs are quite similar, while for the R-branch pump transitions there is an apparent rotation of $\pi/2$ between $\Delta N = +1$ and -1.

The right panel of Figure 6.3 shows all the calculated PADs for $J_i = 4$ assuming (a) parallel intermediate alignment and (b) perpendicular intermediate alignment (i.e. maximum population for $M_i = J_i$ for the Q_4 case and for $M_i = 0$ for the R_3 case, similar to the alignments shown in Figure 6.2). Significant differences are found between different $|\Delta N|$, and also between ΔN positive or negative. In the parallel case the $\Delta N = \pm 2$

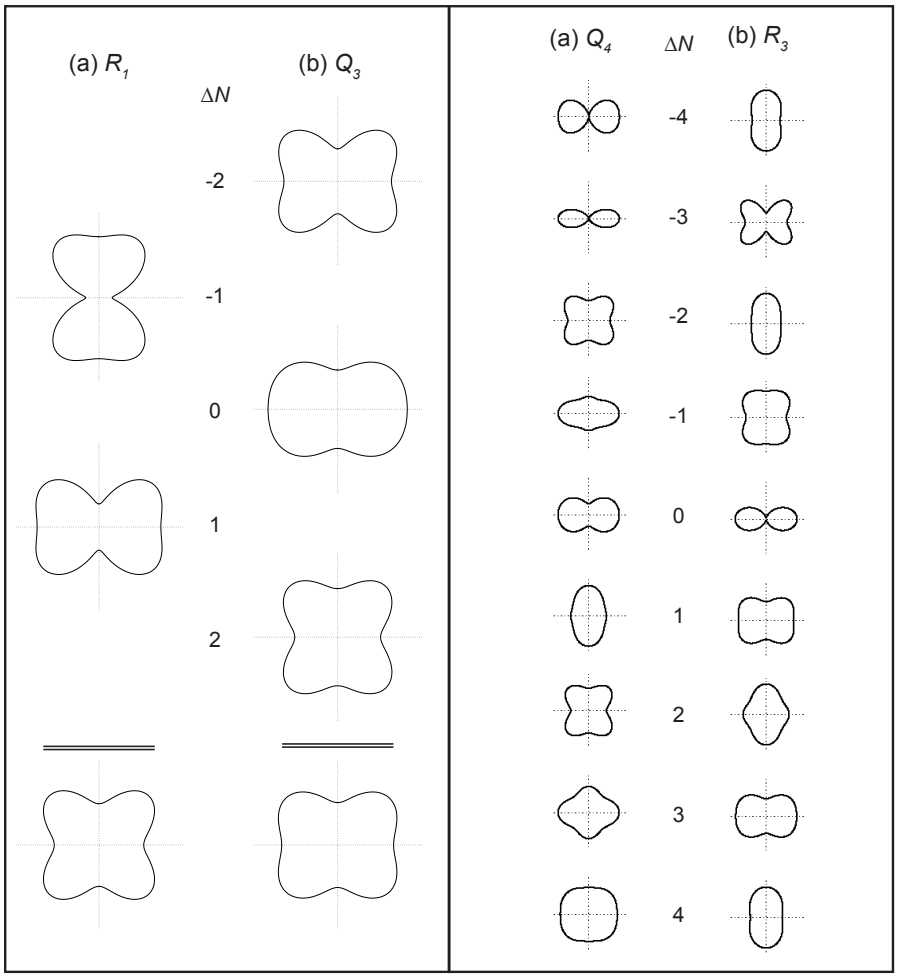

Figure 6.3: Calculated rotationally-resolved PADs. (left panel) Major contributions to the calculated PAD for the lowest J_i (a) R-branch and (b) Q-branch pump transitions observed experimentally. (right panel) Calculated PADs for the J_i=4, (a) R-branch and (b) Q-branch pump transitions.

PADs are similar, thus the observed four-fold structure in the rotationally-summed PAD remains to higher J_i. The PADs for $\Delta N = \pm 1$ and perpendicular alignment show less anisotropy overall, and a $\pi/2$ rotation between $\Delta N = +1$ and -1, so will sum to a much more isotropic vibronic PAD. The PADs calculated here also demonstrate how much information is lost in the rotationally-summed PADs, even in this simple case of only two or three rotational components substantial information is washed out by summation. Rotationally-resolved PADs have since been obtained for NH_3 (Chapter 7 & 8), and provide further experimental confirmation of significant changes in the PADs with ΔN.

6.2.3 Rotational spectra and l=5 contribution

As a means of further testing the extracted dynamical parameters, and the assumptions made about l_{max}, simulated rotationally-resolved photoelectron spectra can be produced from the calculated β_{00} parameters. Figure 6.4 shows calculated spectra which can be

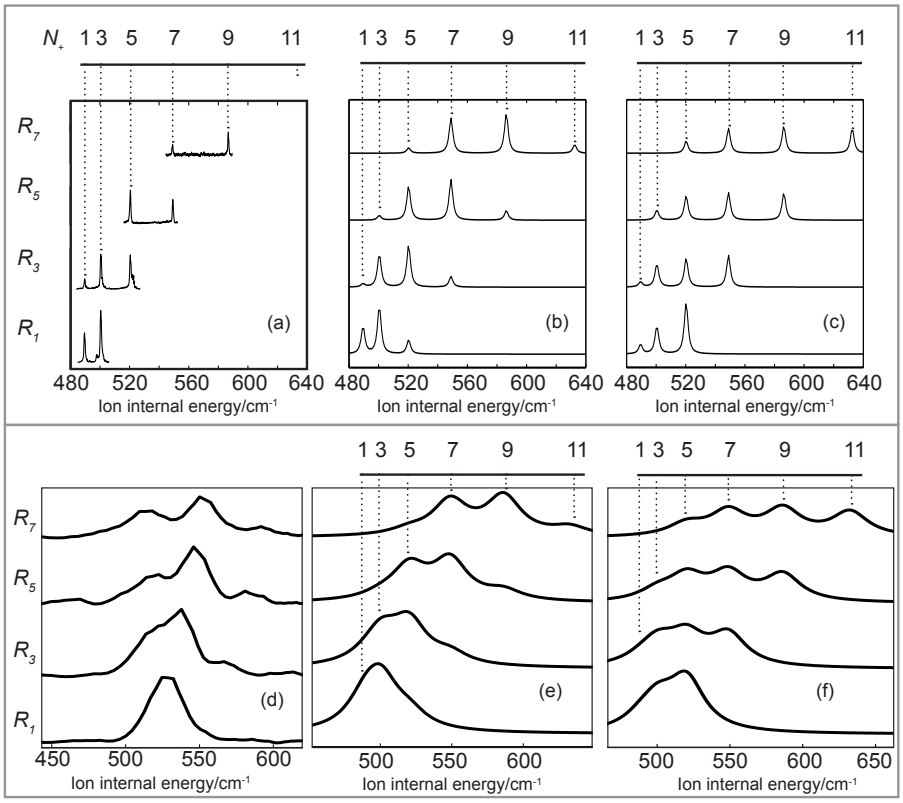

Figure 6.4: Comparison of calculated and experimental rotationally-resolved photoelectron spectra. (a) ZEKE spectra reproduced from ref. [175]. (b) & (c) Calculated rotational spectra with $l_{max} = 3$ and $l_{max} = 5$ respectively. (d) Photoelectron spectra from photoelectron images (see Chapter 5). (e) & (f) Calculated spectra as (b) & (c) but with broader peaks to match imaging data.

compared with the ZEKE spectra shown in panel (a) and the imaging data in panel (d). The calculated spectra in panels (b) and (e) show the results using the dynamical parameters in Table 6.1, and Lorentzian peak widths (FWHM) of 5 cm^{-1} and 30 cm^{-1} respectively. The calculated spectra in panels (c) and (f) show the calculated spectra using an alternate set of dynamical parameters, obtained from fitting the PADs with l_{max}=5.

There are several points of note regarding Figure 6.4. Firstly, comparison of panels (a) and (d) shows that there are marked differences in the observed intensities of the rotational features between the ZEKE [175] and photoelectron imaging experiments. This is apparent at high J_i (>5) where partial rotational resolution is achieved in the images. This discrepancy is attributed to the differences between ZEKE and photoelectron imaging measurements; these differences are expanded on further in Chapter 7 in reference to the fully rotationally-resolved spectra obtained from NH_3. The ZEKE data does not show the $|\Delta N| = 3$ features, with the exception of $N_+ = 1$ in the R_3 spectra. This is most likely a consequence of the low intensity of these features (which may be even weaker in the ZEKE experiment), and this becomes a bigger problem at high J_i because the

	$\Delta N=-3$	$\Delta N=-1$				$\Delta N=+1$				$\Delta N=+3$
	CI	CI	*CII*	*CIII*	*Expt.*	CI	*CII*	*CIII*	*Expt.*	CI
R_1	-	30	*36*	*30*	*49*	54	*64*	*70*	*51*	16
R_3	3	37	*44*	*41*	*41*	47	*56*	*59*	*59*	12
R_5	5	39	*46*	*44*	*38*	46	*54*	*56*	*62*	11
R_7	6	39	*47*	*45*	*44*	45	*53*	*55*	*56*	10
R_9	0	50	*50*	*50*	*47*	50	*50*	*50*	*53*	0

	$\Delta N=-2$		$\Delta N=0$		$\Delta N=+2$	
	Calc.	Expt.	Calc.	Expt.	Calc.	Expt.
Q_3	24	26	33	32	43	42
Q_5	30	14	28	41	42	46
Q_7	33	19	26	65	41	16

Table 6.2: Calculated and experimental branching ratios (%) for $V_0^4K_0^1$ R-branch (left) and Q-branch (right) pump transitions. For the R-branch CI are the full calculated results including $\Delta N=\pm3$ features, *CII* shows calculated values excluding $\Delta N=\pm3$ features and *CIII* shows calculated values after summing $\Delta N=\pm1,\pm3$ features. *CII* and *CIII* can be compared directly with the experimentally derived results, *CIII* should provide a better match for low J_i, and *CII* for higher J_i where $\Delta N=\pm3$ features do not underlie the $\Delta N=\pm1$ features.

ZEKE spectra become quite noisy.[3] Comparison of the peak positions shown in the ZEKE and imaging data also show discrepancies. In this case slight mis-calibration of the photoelectron spectra obtained from the images is the cause of the differences, and the rotational features do not move to high enough energy as N_+ increases. The error in the calibration increases with J_i and is around 40 cm^{-1} for the R_7 case. For the analysis performed in this work this error is not significant, as the partial wave analysis of the PADs does not depend on this energy.

Comparison of panels (a) & (b) and (d) & (e) in Figure 6.4 allows for comparison of the spectra calculated from the fitted dynamical parameters with the experimental spectra. The match to the imaging data (panel (d)) is good, and the shoulders observed in these spectra to high N_+ can be unambiguously assigned as the $\Delta N=3$ features which appear with similar intensities in the calculated spectra. As J_i increases the $\Delta N=+1$ and -1 features tend towards the same intensity in the calculated spectra, but the experimental spectra show the $\Delta N=+1$ as more intense than the $\Delta N=-1$ line. It is unclear whether this difference is significant, or arises as a result of the loss in fidelity of the images to high J_i which may result in image processing artefacts.

A more quantitative comparison can be made by fitting Lorentzians to the experimental data, and comparing the branching ratios so derived to those calculated. The Lorentzian positions in the fit are fixed according to the known rotational spacings, and the peak areas floated as free parameters. Table 6.2 shows the results of this analysis. For the R-branch pump spectra only the $\Delta N=\pm1$ features were fitted, so the calculated branching ratios (CI in Table 6.2) are adapted for comparison by either omitting or summing the $\Delta N=\pm3$ features (CII and CIII in Table 6.2). The agreement is good; in most cases the

[3] This is a consequence of lower intermediate state population for higher J_i, the same effect is observed in the photoelectron images, see Section 5.5.

l	λ	$r_{l\lambda}$	$\eta_{l\lambda}$/deg	Γ_l/%	$r_{l\lambda}^2$/%	F_l/%
p	σ	0.348	0*	24	12	52
	π	0.444	181		40	
f	σ	0.288	334	83	8	10
	π	0.091	101		2	
h	σ	0.578	61	87	33	38
	π	0.159	107		5	

Table 6.3: Fitted dynamical parameters, as Table 6.1 but for $l_{max} = 5$. $r_{l\lambda}$ are normalized such that the total cross-section is unity. $\eta_{l\lambda}$ are relative to $\eta_{p\sigma}$, which is fixed at zero. Γ_l represents the degree of parallel character, $r_{l\lambda}^2$ the partial cross-section and F_l the l-wave cross-section. Uncertainties in the fit have not been calculated for these results, but will be of similar magnitude to those given for the $l_{max} = 3$ case shown in Table 6.1. These parameters were used to calculate the rotational spectra shown in Figure 6.4, panels (c) and (f).

calculated and experimental ratios are within a few percent. The worst agreement is for the R_1 case although, in the case of this unresolved feature, the Lorentzian fit may not be reliable. The calculated R_1 ratios are, however, in good agreement with the ZEKE data shown in Figure 6.4, despite the differences in the two experiments. For the Q-branch data the agreement is less convincing. As with the R_1 case, the experimental data is not sufficiently resolved to unambiguously fit the profiles, so there are questions about the validity of the Lorentzian fits in this case. Unfortunately there are no equivalent ZEKE spectra recorded via $V_0^4K_0^1$ Q-branch transitions in the literature for comparison.

Panels (c) and (f) in Figure 6.4 show the spectra calculated including $l = 5$. In this case the PADs were fitted as before, but with $l_{max} = 5$. A good fit to the experimental PADs was found. The dynamical parameters from this fit are shown in Table 6.3. In this fit the $p\pi$ component is still the main contribution to the photoelectron wavefunction, but a large $h\sigma$ component is also found. Such a large contribution from high l appears somewhat suspect in light of the general observation in photoionization that the summation over l converges rapidly [61], which arises due to the centrifugal barrier contribution to the scattering Hamiltonian (see discussion in Appendix A), but cannot be ruled out by the fitted PADs alone. The calculated rotational spectra, however, are very different from the experimental spectra, showing much larger $\Delta N = +3$ features which have similar intensities to the $\Delta N = \pm 1$ features.

Constrained fitting was also carried out, in which upper bounds were placed on F_h, ranging from 1% - 5%, to examine the sensitivity of the spectra to the h-wave contribution. Again good fits to the PADs could be found, but even for $F_h \approx 1\%$ significant differences in the calculated rotational spectra were observed, with 20% - 30% population of $N_+ = N_i + 3$ versus 10% - 16% population as shown in Table 6.2 for the $l_{max} = 3$ results. This analysis shows that the rotational spectra are a very sensitive probe of the contribution of high l partial waves, and in this case any contribution from $l > 3$ can be assumed to be negligible ($F_h \ll 1\%$).

This work also highlights a general point about fitting, namely that adding more

basis functions into a fit - in this case more l-waves - can often produce better fits to a dataset because there are more variable parameters and therefore more freedom to fit any functional form. This is analogous to the basis set considerations made in *ab initio* calculations, or the number of Fourier components required in a series expansion to accurately model an arbitrary function. This means that, when dealing with fits to PADs, it is important to thoroughly test the effect of changing l_{max} and consider extra criteria which may be applied to the fits in order to resolve any ambiguities, such as the comparison with rotational spectra demonstrated here. Physical arguments, such as the general result of the rapid convergence of the partial wave expansion with l, may also be deployed in order to select from a set of fitted parameters, although such arguments are not rigorous so quantitative methods based on the experimental data are preferred, allowing for unbiased, objective testing.

6.2.4 Discussion of dynamical parameters

In the preceding sub-sections a fit to the experimental PADs with $l_{max} = 3$ has been presented, and its validity discussed in terms of both the PADs and rotational spectra. The question now becomes: what is the physical insight into the photoionization process given by these parameters?

The predominantly $p\pi$ character of the photoelectron wavefunction is consistent with ejection of a valence electron, which is close to the molecular framework and thus will experience a highly anisotropic short-range potential (see Figure 1.5). In contrast, if the electron were in a diffuse Rydberg orbital prior to ionization, more atomic-like behaviour would be expected. In the context of the assertion made by other authors that the $\tilde{A}^1A_u$ state is similar to an atomic d-orbital (see Section 6.1.1), atomic-like behaviour would mean that roughly equal p and f contributions would be expected, and similarly equal magnitudes of the σ and π components.[4] The difference in magnitudes between the partial waves could therefore be interpreted as the signature of molecular ionization, and the dominance of the $p\pi$ channel reflects the coupling of the π_g valence orbital (see Section 6.1.1) to the ionization continuum. To put this another way, the radial integrals $r_{l\lambda}$ (equation 2.47) are largest for coupling into the $p\pi$ continuum. By analogy with bound-bound transitions, the ionization dipole moment could be defined as perpendicular to the molecular axis.

The phases show $|\eta_{p\sigma} - \eta_{f\sigma}| = 355^\circ$ (as previously noted phases are determined $mod(360)$ and unsigned), so these components are almost in-phase. $\eta_{l\lambda}$ is the total phase shift, which will contain both an l-dependent Coulombic (σ_l) contribution, and a scattering contribution ($\delta_{l\lambda}$) which may vary with both l and λ. The calculated Coulomb phase shift, $\sigma_p - \sigma_f$ ~170°, suggesting there is a large scattering contribution to the total phase for $\lambda = 0$. The $p\pi$ and $f\pi$ channels show considerable phase shifts relative to the $p\sigma$ and $f\sigma$ channels, suggesting very different scattering contributions in these channels.

The scattering phases arise from the interaction of the partial waves with the short-

[4] This is akin to the rotational spectator approximation, discussed in Section 8.1 in the context of ionization of the ammonia $\widetilde{B}^1E$" state, an n=3 Rydberg state.

range molecular potential, so can be considered as a measure of the strength of this interaction relative to a purely Coulombic potential (see Appendix A). For a linear molecule it is not surprising that the effect of the short-range potential on the σ and π components is very different. Because the sign of these phases cannot be deduced in this work it is not known whether the scattering advances or retards the π components relative to the $p\sigma$ reference phase, although physical arguments suggest that the σ components, directed along the molecular axis, will interact more strongly with the nascent ion core. Following this argument, it might also be expected that the sharper angular structure of the $f\sigma$ component would interact with the molecular potential more strongly than the $p\sigma$ component, and that the $p\pi$ and $f\pi$ components would experience a weaker interaction. Similarly, it might be expected that the π components would couple more strongly to the continuum, and this is indeed reflected in the dominance of the $p\pi$ wave, as discussed above.

6.3 Geometrical and Dynamical Parameters - $K_+ > 0$ Vibronic Bands

The experimental data presented in Section 5.7 detailed the observation of PADs correlated with the formation of different vibronic states in the acetylene ion, obtained via pump transitions $V_0^5 K_0^1(P, Q, R)$. The rotational structure underlying the $K_+ > 0$ features was discussed, and from this arose the expectation that the rotationally-summed PADs are not likely to provide enough information to determine the dynamical parameters. However, it was also observed that there were significant changes in the PADs with K_+, so not all rotational information is washed out in this data.

These observations suggested two approaches to the further analysis of this data. Firstly, a qualitative approach, whereby model calculations are performed for arbitrary dynamical parameters in order to study the geometrical effect of changes in K_+. Secondly, after the dynamical parameters for the $\tilde{A}^1 A_u | v_{3(i)} = 4, J_i K_i\rangle \rightarrow \tilde{X}^2\Pi_u | v_{4(+)} = 1, J_i, K_i = 0\rangle$ ionization had been successfully determined, as detailed above, a more quantitative analysis could be attempted under the assumption that there will only be small changes in the radial integrals with $\langle v_{4(+)} | v_{3(i)}\rangle$. Working from this supposition, it is possible that fitting sets of experimental PADs, then evaluating the fits both in terms of deviation of the parameters from those determined for the formation of the $\mathbf{4}^1\,^2\Sigma_u^-$ level, and through comparisons of the calculated rotational spectra with the ZEKE spectra of Tang et. al. [175], may provide enough information for a full determination of the dynamical parameters for the formation of other K_+ levels. Extra complications which arise here are the increased number of $l\,\lambda$ components allowed (see equation 6.2), the inclusion of spin in the calculation and the greater range of photoelectron kinetic energies sampled by the data. These calculations, and associated issues, are pursued and discussed in this section.

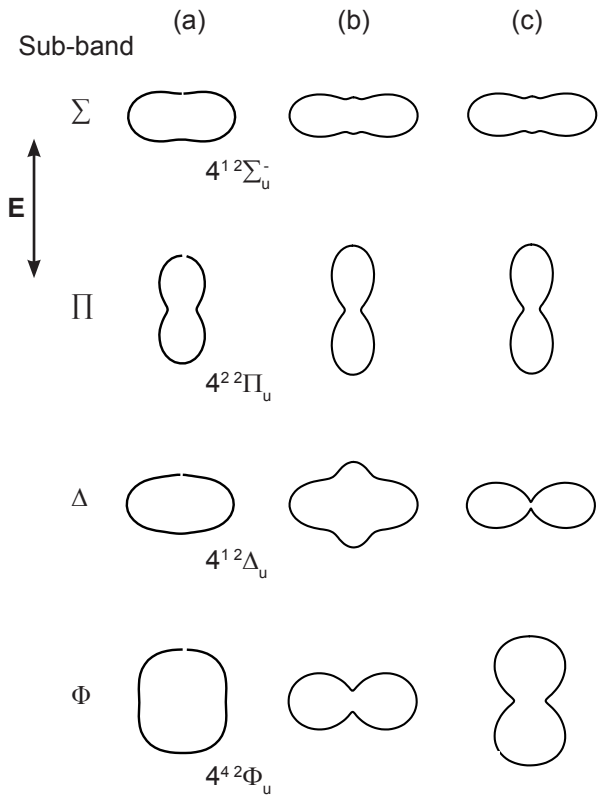

Figure 6.5: Experimental (a) and calculated (b) & (c) PADs as a function of K_+. Experimental PADs were recorded via the $V_0^5 K_0^1 R_1$ pump transition. Calculated PADs are shown for (b) all $r_{l\lambda} = 1$, all $\eta_{l\lambda} = 0$; (b) all $r_{l\lambda} = 1$, $\eta_{l\lambda} = 0$ except $\eta_{f(\lambda>0)} = \pi$.

6.3.1 Geometrical effects of ΔK

The vibronically-resolved PADs presented in Figure 5.10 show how the orientation of the PAD flips, between vertical and horizontal orientation with respect to the laser polarization, according to $\Delta K =$ odd/even. The possible causes of this behaviour were discussed in Section 5.7.1 in terms of the geometrical parameters, and also possible changes to the dynamical parameters over the different vibrational states accessed. PADs for different ΔK transitions were calculated to explore this behaviour in more detail; the results are shown in Figure 6.5 along with representative experimental data. In all cases the pump transition was $V_0^5 K_0^1 R_1$, as shown in Figure 5.10.

The calculated PADs show that the flip observed between the Σ, Π and Δ vibronic levels is reproduced by the calculations when all partial waves are in phase ($\eta_{l\lambda} = 0$), but the change between the Δ and Φ levels is not reproduced, although there is a change in the exact form of the PAD. By adjusting the f-wave phases for the $\lambda > 0$ components so that these components are exactly out of phase (π radians, or 180°) with the $p\sigma$, $p\pi$ and $f\sigma$ components, the forms of the PAD calculated for the Δ and Φ levels are changed, and the flip in orientation of the PAD for the Φ level is reproduced.

These calculations serve to highlight the complexity of the geometrical terms. The only difference between each calculated PAD in column (b) or (c) of Figure 6.5 is ΔK, and

the geometrical parameters will exhibit changes with K_t (see equation 2.46). Additionally, because of the angular momentum constraints on λ, the PADs will show dependence on different partial wave components as K_t changes (equation 6.2). This means that the flip observed between the PADs for $K_+ = 0, 1$ may arise solely from the change in parity of $3j$ terms involving K_t, and thus a change in the overall geometrical phase, but may also be affected by the inclusion of extra $f\lambda$ components. The same is true for the PADs calculated for $K_+ > 1$, but in these cases the effect of higher λ components is evident, and the phase of these components is seen to change the PAD considerably; this significant phase effect is not observed for the $K_+ = 0, 1$ PADs, most likely because components $f(\lambda > 0)$ do not make a large contribution to the geometrical parameters.

The necessity of a phase shift in the f-wave components in order to reproduce the observed behaviour of the $K_+ = 2, 3$ PADs highlights the sensitivity of the PADs to the partial wave phases. Again the complex interdependence of the geometrical and dynamical parameters is apparent, as both will influence the PADs in this case. A change in parity of the geometrical parameters with ΔK or λ, leading to a change in the geometrical phase (± 1) is equivalent to a π phase shift in the dynamical phase difference between the same partial wave components. The requirement of a non-zero phase for qualitative calculation of these PADs illustrates how the interferences which give rise to the observed PAD are highly sensitive to these considerations.

6.3.2 Fitting PADs

The similarity of the qualitative PAD calculations (Figure 6.5) to the experimental results is quite surprising given the fact that all $r_{l\lambda} = 1$ in these calculations. This may reflect the fact that the summation over many underlying rotational levels washes out some of the finer details shown in the rotationally-resolved PADs; the summed PADs thus show less sensitivity to the magnitudes of the dipole matrix elements. However, the sensitivity to the phases, and the possibility of following the methodology discussed in Section 6.2.3 (whereby fitted dynamical parameter sets are further tested by the comparison of calculated rotational spectra to ZEKE spectra) mean that there is some hope that a complete analysis of the PADs pertaining to the $K_+ > 0$ bands is feasible despite the reduced information in the experimental dataset. With this in mind some, limited, fitting of the $K_+ > 0$ bands was attempted. It is noted that this fitting was not as thorough as that discussed above, and is presented as preliminary (and incomplete) work which may nonetheless be a useful stepping stone toward future work on acetylene.

Three sets of PADs were fitted, pertaining to formation of the vibronic bands:

1. $\mathbf{4}^1\,{}^2\Sigma_u^-$, ${}^2\Delta_u$
2. $\mathbf{4}^2\,{}^2\Pi_u$
3. $\mathbf{4}^3\,{}^2\Sigma_u^- + {}^2\Delta_u$

following $V_0^5 K_0^1(P, Q, R)$ pump transitions. In cases (1) and (3) the Σ and Δ vibronic bands lie close in energy, and originate from the same parent vibrational band - $\mathbf{4}^1$ and

l	λ	1. $4^1\,^2\Sigma_u^-,\,^2\Delta_u$			2. $4^2\,^2\Pi_u$			3. $4^3\,^2\Sigma_u^- +^2\Delta_u$		
		$r_{l\lambda}^2/\%$	$\eta_{l\lambda}/^\circ$	$F_l/\%$	$r_{l\lambda}^2/\%$	$\eta_{l\lambda}/^\circ$	$F_l/\%$	$r_{l\lambda}^2/\%$	$\eta_{l\lambda}/^\circ$	$F_l/\%$
p	σ	45	0*	74	43	0*	71	1	0*	33
	π	29	179		28	63		32	88	
f	σ	16	63	26	13	147	29	3	308	67
	π	7	112		8	325		0	33	
	δ	3	0		8	205		64	95	
	ϕ	0	-		0	-		0	-	

Table 6.4: Fitted dynamical parameters, as Table 6.1 but for fitting to three different datasets as discussed in the text. $\eta_{l\lambda}$ are relative to $\eta_{p\sigma}$, which is fixed at zero. $r_{l\lambda}^2$ is the partial cross-section (%) and F_l the l-wave cross-section (%).

4^3 respectively - so the assumption that the dynamical parameters will show little change over the dataset should hold. The available data is slightly different in the two cases; for case (1) the two vibronic states are resolved, but the photoelectron intensity is weak (see Figure 5.7) so the associated experimental errors are significant; for case (3) the features are much more intense, but the vibronic states are not resolved so the calculated PADs must include incoherent summation over $K_+ = 0,\,2$ as well as the underlying rotational J_+ levels. Table 6.4 shows the dynamical parameters found for fitting of the three different datasets.

As discussed above, as a reasonable first approximation it may be assumed that the dynamical parameters for the formation of the $4^1\,^2\Sigma_u^-,\,^2\Delta_u$ states following preparation of $v_{3(i)} = 5$ are little different from those obtained following preparation of $v_{3(i)} = 4$. Following this rationale, the F_l determined for case (1) (Table 6.4) look to be around the anticipated values, and are similar to those shown in Table 6.1. However, closer inspection shows large changes in the partial cross-sections, with a large shift in magnitude from $r_{p\pi}$ to $r_{p\sigma}$. There are also shifts in the phases, with a large change in $\eta_{p\pi} - \eta_{f\sigma}$ of 122°, and a smaller, but still significant, shift in $\eta_{p\sigma} - \eta_{p\pi}$ of 62°. Similar comments apply to case (2); again the $p : f$ split, as expressed by F_l, is close to that shown in Table 6.1, while there are significant differences in $r_{p\sigma}$ and $r_{p\pi}$ and all $\eta_{l\lambda}$. Comparison of the parameters obtained for case (1) and (2) also shows large changes in $\eta_{l\lambda}$, although little change in $r_{l\lambda}$, between the two fits. Case (3) yields a completely different parameter set, with very different magnitudes and phases from any of the previous fits. In particular there is a shift in magnitudes to $f\delta$, which is found to be the dominant component in this case.

Inspection of these fitted parameters is therefore somewhat inconclusive. The changes seen in the parameters for case (1) and (2), although large, do not seem physically unreasonable; if correct they indicate a strong vibrational dependence of the phases of the partial wave components, but a weaker vibrational dependence of the magnitudes. This may be the case if the change in the FC factors appearing in the radial integrals is small, but the effect of the vibrational wavefunction on the short-range potential, and thus on $\delta_{l\lambda}$, is significant. These parameter sets may not, however, represent unique fits to the data and there may be other parameter sets which equivalently minimize χ^2. As discussed in Section 6.2.1 there are various checks which can be performed to confirm the uniqueness of a parameter set, but such checks are hampered by the lack of experimental data.

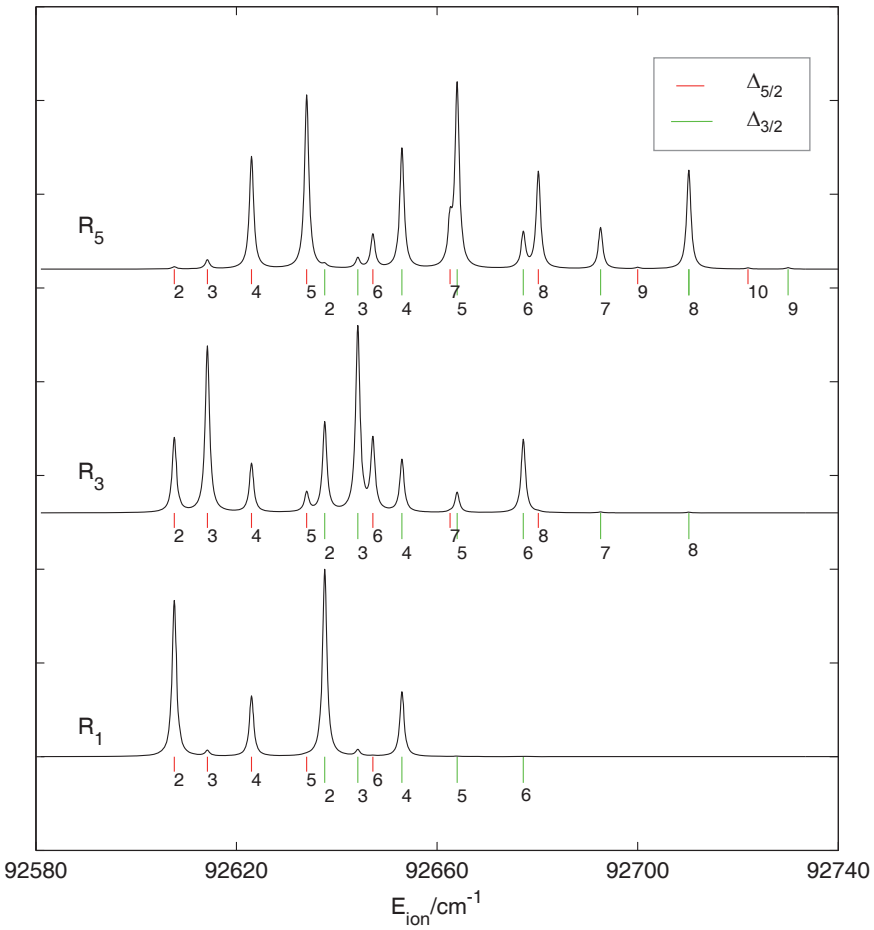

Figure 6.6: Calculated rotational spectra for the $4^1\,^2\Delta_u$ vibronic band. The spin-orbit splitting was set to -30 cm^{-1}.

Comparison with ZEKE spectra is discussed further below, but seen to be inconclusive. The parameters found for case (3) do seem likely to be spurious (based on the same physical considerations) and reflect the further loss of information in the experimental data from the PADs summed over two vibronic states. Again it is stressed that these parameters may reflect only one of several minima in χ^2.

The results of the calculation of uncertainties, based on the curvature of χ^2 (see Section 4.3.5), for these fits is not shown here. Such calculations produced uncertainties of similar magnitude to those shown in Table 6.1, but do not necessarily reveal the presence of multiple minima in the full parameter space because they only evaluate 1-dimensional cuts around a single minima. The validity of such calculations must be treated carefully for this reason.

As demonstrated in Section 6.2.3, calculations of the rotational spectra based on fitted parameter sets is a useful way to assess the validity of a fit. Examples of such calculations are shown in Figure 6.6, where the parameters given in Table 6.4, case (1), were used to calculate the rotational spectra for the $\tilde{A}^1A_u|v_{3(i)} = 5, J_i, K_i = 1\rangle \rightarrow \tilde{X}^2\Pi_u|v_{4(+)} = 1, J_i, K_i = 2\rangle$ ionizing transition, for $J_i = 2$, 4, 6 and R-branch excitation. Comparison

of these calculations with the available ZEKE spectra (Figure 5 in ref. [175]) show reasonable agreement with the intensities of the first two peaks ($N_+ = 2, 3$; $J_+ = 5/2, 7/2$) for the R_1 and R_3 cases, and with the relative magnitudes of the upper and lower spin orbit components, but poorer agreement with higher J_+ lines (although this comparison is hindered by overlapping features in the ZEKE data). Unfortunately this comparison is rather limited and somewhat ambiguous, and is as likely to reflect subtle differences between field ionization and direct photoionization, as it is to shed light on the verisimilitude of the fitted parameters.

6.4 Conclusions

It has been demonstrated that the PADs obtained relating to the formation $\mathbf{4^1}\,^2\Sigma_u^-$ vibronic band following $V_0^4K_0^1$ pump transitions provide enough data to uniquely determine the magnitudes and phases of the radial dipole matrix elements and phases which determine the ionization dynamics. Calculation of rotational spectra using these parameters provided a sensitive means of testing the fitted parameters, and of testing the validity of the truncation of the partial wave expansion at $l_{max} = 3$.

PADs relating to the formation of $K_+ > 0$ vibronic states have been investigated qualitatively and through fitting. The qualitative, limiting-case, calculations reveal that changes in the geometrical parameters alone can describe the observed flips of the PADs with $K_+ = 0,\, 1,\, 2$, while non-zero phases are additionally required for $K_+ = 3,\, 4$.

Preliminary work on fitting of the PADs from the currently available experimental data, and comparison with other studies from the literature, has been shown to be insufficient for a confident assignment of the fitted parameters (as determined for the formation of the $\mathbf{4}^1\,^2\Sigma_u^-$, $^2\Delta_u$, $\mathbf{4}^2\,^2\Pi_u$ and $\mathbf{4}^3\,^2\Sigma_u^-$, $^2\Delta_u$ vibronic states) as the unique set of dynamical parameters which describe the ionization events. The parameters obtained are suggestive of little change in the partial wave character, but large phase shifts, for vibronic states arising from the $\mathbf{4}^1$ and $\mathbf{4}^2$ parent vibrations, while the parameters obtained for the $\mathbf{4}^3\,^2\Sigma_u^-$, $^2\Delta_u$ vibronic states are likely to be spurious and may represent only one of several minima in the fit. The fact that this analysis goes some way to obtaining these parameters, despite the unresolved rotational features in the data, suggests that with more experimental data a full analysis should be possible. A 2-colour, slow-electron experiment similar to that carried out on NH_3 (Chapter 7 & 8), should be capable of providing the required, higher resolution, data. Future work on acetylene is planned with this in mind.

6.5 Addendum

In the course of re-visiting this work two issues with the original analysis have come to light. These issues have not been discussed in the preceding work, and there is some deviation from the previously published treatment [186] which is addressed here.

1. The selection rules given in equation 6.2 are correct as given here, but were previously given as $|\lambda| = 0, 1 ... K_+ + 1$ [186]. This is incorrect. The consequence

of this is that, for the $4^1\,^2\Sigma_u^-$ analysis reported in Section 6.2, the $f\delta$ component is allowed, and $r_{f\delta}$ is not necessarily zero as assumed in the analysis. Ideally this analysis should be redone, with the $f\delta$ component included in the fitting. However, given the good agreement of the calculated and experimental results, and the small $f\delta$ component found for the formation of the same band after excitation via $V_0^5 K_0^1$ (3%, see Section 6.3.2 and Table 6.4) this component is likely to be negligible.

2. The phase factor of $(-i)^{l'-l}$ given in equation 2.49 was omitted from the calculations. This does not have any effect on the validity of the results, but is equivalent to an additional π phase shift between the p and f continua. This correction has been applied to the results presented in this chapter. Without this correction, the phases presented in Table 6.1 are $\eta_{f\sigma} = 175°$, $\eta_{f\pi} = 250°$, as published in ref. [186].

Chapter 7

Ammonia I: Experimental Results

This chapter details experimental work in which the ionization of ammonia via rovibrationally selected levels of the $\widetilde{B}^1E''$ electronic state was studied. In these experiments a (2+1') REMPI scheme was used to enable the creation of photoelectrons with very low kinetic energies (<300 cm^{-1}), enabling maximal resolution in the velocity-mapped photoelectron images. The excitation step was of the form $\widetilde{X}^1A_1'|v_{2(g)}=0, J_{gK_g}\rangle \rightarrow \widetilde{B}^1E''|v_{2(i)}=\{3,\,4\}, J_{iK_i}\rangle$; upon ionization cation states $\widetilde{X}^2A_2''|v_{2(+)}=v_{2(i)}, N_{+K_+}\rangle$ were populated. Rotational resolution of the ion was achieved, enabling the observation of PADs correlated with the formation of individual rotational levels, N_{+K_+}, of NH_3^+.

Relevant background details are discussed in Section 7.1, followed by experimental details (Sections 7.2) and preliminary work (Sections 7.3 and 7.4). Section 7.5 presents data obtained via $v_{2(i)}=4$; this represents the most complete dataset, so forms the majority of the work presented in this chapter. The $v_{2(i)}=4$ data is further analysed, in order to extract the dynamical parameters, in Chapter 8. Section 7.6 presents data recorded via $v_{2(i)}=3$ and Section 7.7 presents a brief look at data recorded using different λ_{probe} (via $\widetilde{B}^1E''|v_{2(i)}=4, 3_2\rangle$ intermediate), although both of these datasets require further analysis.

7.1 Background

A schematic overview of the pump-probe ionization scheme used is shown in Figure 7.1, along with the rotational level structure of each electronic state. (2+1) and (2+1') REMPI schemes are also illustrated. In the following sub-sections the important characteristics of each electronic state are described in detail.

7.1.1 Ground state $\widetilde{X}^1A_1'$

The ground electronic state of ammonia, $\widetilde{X}^1A_1'$, has pyramidal geometry and belongs to the C_{3v} point group. Consideration of the form of ψ_{nuc} for three identical H nuclei results

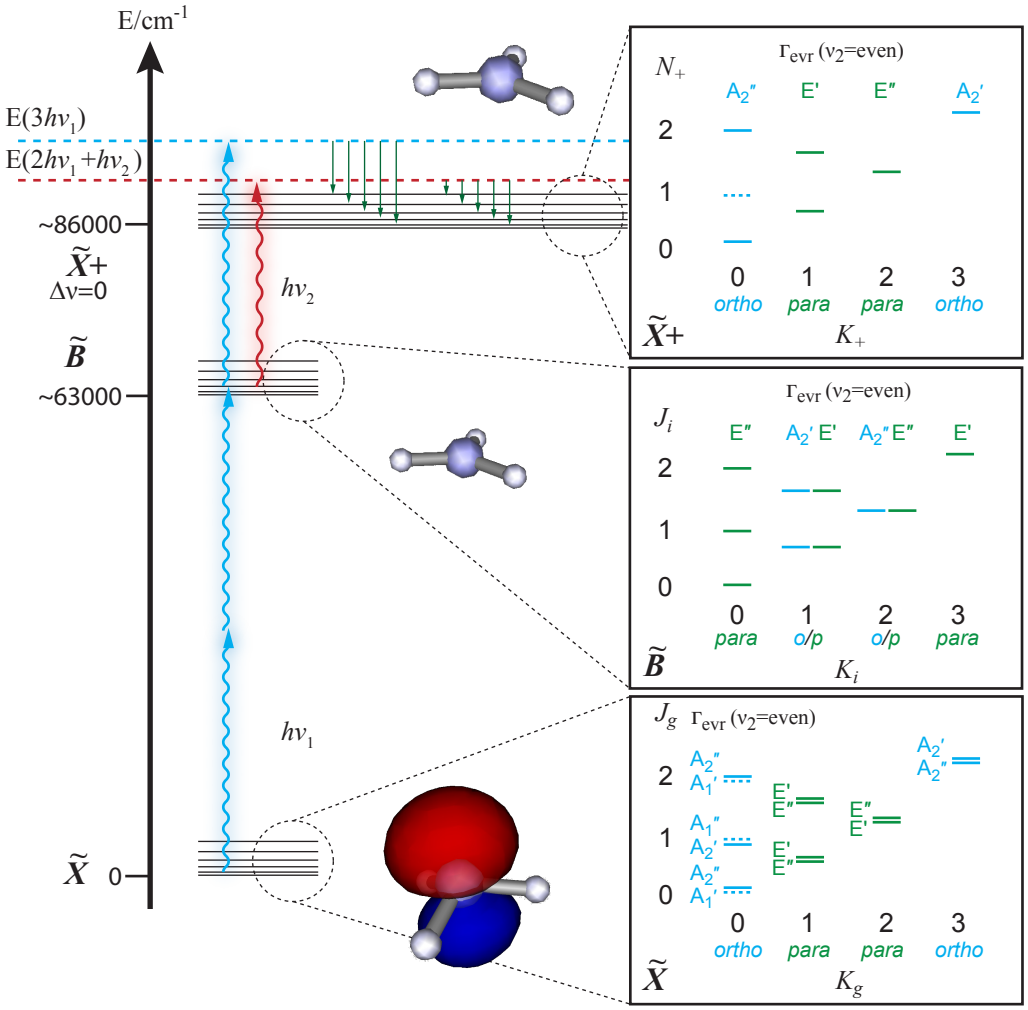

Figure 7.1: Schematic of (2+1) and (2+1') REMPI via the $\widetilde{B}$-state. The rotational structure of each electronic state is illustrated, see main text for details. The highest occupied molecular orbital (HOMO) for the $\widetilde{X}^1A_1'$ state is also illustrated, as calculated using the Gaussian package. No calculations have been run for the $\widetilde{B}^1E''$ or $\widetilde{X}^2A_2''$ electronic states.

in two distinct forms, *ortho* (I=3/2, A_1 symmetry) and *para* (I=1/2, E symmetry), with a 1:2 statistical weighting. The energy barrier to inversion of the molecule (nitrogen nucleus passing through the plane described by the three hydrogen nuclei) is small, resulting in tunnel splitting of the vibrational levels which are assigned parity labels + (symmetric, lower level) and - (anti-symmetric, upper level). For the vibrationless ground state the tunnel splitting is only 0.8 cm^{-1}. This inversion doubling also means that the $\widetilde{X}^1A_1'$ state is more appropriately classified in the D_{3h} molecular symmetry group, rather than the C_{3v} point group which describes only the rigid geometry.[1]

The general requirement that the complete molecular wavefunction, Ψ, must be anti-symmetric with respect to exchange of any two fermions implies that the two components of the inversion doublet, when paired with either the ortho or para form of the nuclear spin wavefunction, will result in only certain combinations of vibrational and rotational levels fulfilling the correct symmetry requirements:

$$\psi_{evr} \supset A_2\,(\mathrm{ortho}) \tag{7.1}$$

$$\psi_{evr} \supset E\,(\mathrm{para}) \tag{7.2}$$

The resulting rotational level structure is shown in Figure 7.1. As the symmetry classification changes with K it is possible to uniquely assign a given K stack of levels to ortho or para nuclear spin. For v_2 = even levels with $K = 0, 3, 6...$ must be ortho-NH_3, while those with $K = 1, 2, 4, 5...$ must be para-NH_3; for v_2 = odd the situation is reversed. As nuclear spin states cannot inter-convert upon excitation or ionization, this separation of spin states provides strict selection rules on $\triangle K$.

7.1.2 $\widetilde{B}^1E''$ state

The $\widetilde{B}^1E''$ electronic state is an $n = 3$ Rydberg state with planar geometry (D_{3h} point group), lying 59225 (1) cm^{-1} [187] above the $\widetilde{X}^1A_1'$ state. As in the ground state, the allowed rotational energy levels are restricted by the allowed symmetries of Ψ. The rotational structure is shown in Figure 7.1. As was the case for the $\widetilde{X}^1A_1'$ state, levels with $K_i = 0,\ 3,\ 6...$ are ortho, but for all other K_i both ortho and para levels exist [29].

The electronic character of the $\widetilde{B}$-state is known to be predominantly $p\pi$ with an admixture of $d\delta$ character [28, 29, 30, 31]. This mixed character arises because of the low-n nature of the Rydberg state; in this case a hydrogenic orbital solution is less applicable than it would be for a high-n Rydberg state. In a non-central potential (i.e. non-spherically symmetric), l and λ are not good quantum numbers, hence the electronic character of the Rydberg orbital must be considered as an expansion in the $|l\lambda\rangle$ central-potential basis, where all basis states of the same symmetry may contribute. This expansion reflects the incomplete separation of the Rydberg electron from the molecular core. The $n =$

[1] No specific references have been cited here because these points are discussed in numerous books and articles. For general discussion on these points see refs. [127, 126, 180], and for points related to the experimental work presented here see refs. [28, 29, 31, 22].

3 Rydberg electron has some finite probability of being near to the core, and angular momentum may be exchanged through the interaction of the Rydberg electron with the short-range molecular potential - classically this can be thought of as a torque between the Rydberg electron and the molecular core. At long range (as $n \rightarrow \infty$) the potential experienced by the Rydberg electron approaches a purely Coulombic potential, and the Rydberg orbitals approach the hydrogenic case. A related question to be explored in this work is how the outgoing photoelectron experiences this complex molecular potential, and how much angular momentum exchange (or scattering) is seen during ionization.

Further insight into the nature of the $\widetilde{B}$-state can be gained by considering the Rydberg orbital in terms of *eigenchannels.* Such an approach is employed in the multi-channel quantum defect (MQDT) formalism (see Appendix A) and has been applied to model ionization from the $\widetilde{B}$-state in MATI experiments by Dickinson, Rolland and Softley [29, 30]. The symmetry restrictions on the eigenchannels, $|\alpha\rangle$, are considered under D_{3h} symmetry, and it is shown that only channels of e' symmetry are allowed. The eigenchannels of appropriate symmetry are expanded only over a small sub-set of partial waves with the appropriate symmetry behaviour:

$$|\alpha\rangle^{e'} = \sum_{even-l} A_{l\lambda}|l, \lambda = \pm 2\rangle + \sum_{odd-l} A_{l\lambda}|l, \lambda = \pm 1\rangle \tag{7.3}$$

$A_{l\lambda}$ denote the expansion coefficients. The lowest l-waves in this expansion are $p\pi$ and $d\delta$, and the description of the the $\widetilde{B}$-state Rydberg character in terms of just two angular momentum components appears reasonable as only a very few low-l components are symmetry allowed. In the work reported in ref. [30], Softley and co-workers found best agreement between their MATI results (reproduced in Section 8.2.2) and MQDT calculations with a $1/3$ $d\delta$ contribution to the $\tilde{B}$-state. The conclusion from the MATI work is that the description of the $\widetilde{B}$-state in terms of just two $|l\lambda\rangle$ components is justified by both symmetry arguments, and the agreement of the MQDT calculations with experimental MATI spectra.

7.1.3 $\widetilde{X}^2A_2''$ cation

The ammonia cation in its ground electronic state ($\widetilde{X}^2A_2''$) is, like the $\widetilde{B}$-state, a planar symmetric top. The rotational energy levels are those of an oblate symmetric rotor. The rotational structure is shown in Figure 7.1, and rotational selection rules are discussed in Section 7.1.4. The structure of the $\widetilde{X}^2A_2''$ state has been extensively studied by ZEKE and MATI spectroscopy [27, 28, 29, 30].

7.1.4 Rotational selection rules outline

In-depth analysis of the selection rules for ionization is withheld until the following chapter. However, to facilitate discussion of the experimental data presented in this chapter, a brief outline of the *rotational spectator approximation* is given here. This provides a useful model to build on and is quite intuitive. If the orbital angular momentum of the Rydberg

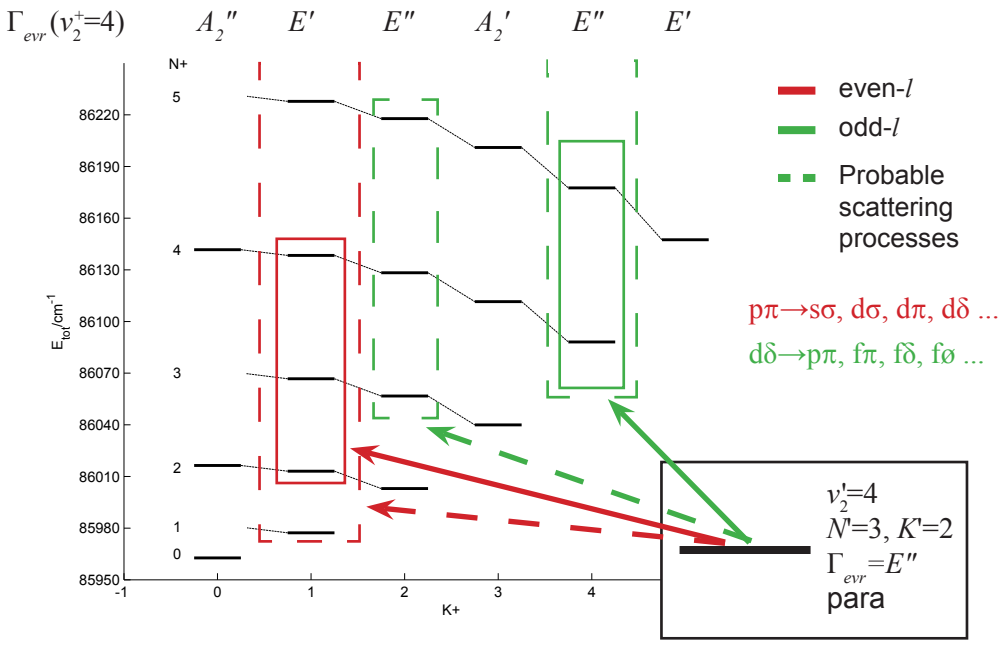

Figure 7.2: Ionization pathways from $\tilde{B}|v_2 = 4, 3_2\rangle$. Solid lines show the levels accessible in the rotational-spectator, or atomic-like, ionization model; dashed lines show rotational levels which may be accessed by scattering.

electron in the $\widetilde{B}$-state is assumed to be completely decoupled from the molecular core, as it would be in a central-potential, then the angular momentum of the molecular core will be determined by the Rydberg character. In this decoupled model the angular momentum of the molecular core is conserved upon ionization, so the final rotational levels populated in the ion are determined by the Rydberg components of the $\widetilde{B}$-state, and the rotational selection rules which arise are:

$$p\pi \begin{cases} \triangle N = & 0, \pm 1 \\ \triangle K = & \pm 1 \end{cases} \tag{7.4}$$

$$d\delta \begin{cases} \triangle N = & 0, \pm 1, \pm 2 \\ \triangle K = & \pm 2 \end{cases} \tag{7.5}$$

The expectation is that these rules, generally termed *atomic-like* in the following discussion, will hold as propensity rules, and account for the strongest features in the rotational spectrum. Population of rotational levels in the ion which are forbidden by these rules represents a break-down of this decoupled model, and hence reflects further interaction of the Rydberg/outgoing photoelectron with the molecular core. This is generally termed as *scattering* in the following discussion. Strict symmetry limitations are placed on the rotational levels which can be populated by scattering, according to partial wave parity. A schematic of ionization pathways is shown in Figure 7.2. The symmetry rules for ionization are discussed in detail in Chapter 8, but the conclusions relevant to the experimental

results presented in this chapter can be summarised as:

1. The symmetry allowed rovibronic levels follow the same rules as those of the ground state, given in equations 7.1 and 7.2 (see also Figure 7.1); for $v_{2(i)}$ =even, para-NH_3 has levels $K_+ \neq 0, 3, 6...$, and ortho-NH_3 has levels $K_+ = 0, 3, 6....$

2. Population of a given K_+ stack must correlate with ionization to the l-even or l-odd continua.

7.2 Experimental Details

The experimental set-up used for 2-colour photoelectron VMI measurements has been detailed in Section 3.3, further specific details relating to NH_3 are given here. The set-up was broadly similar to that used for the (1+1) acetylene experiments detailed in Chapter 5, the major differences between the equipment used in the two experiments were as follows:

1. Two laser systems, with the beams arranged in a co-propagating geometry, were used.

2. Spectrometer #2 was used in this work.

3. Image capture was performed using code developed in-house running within the MATLAB environment.

Points 2 & 3 do not have any bearing on the reliability of the experimental results, although, as discussed in Chapter 3, the differences between the two VMI spectrometers have implications on the energy resolution obtained in the photoelectron images. The move from a 1-colour to a 2-colour pump-probe scheme is, however, a critical difference between the two experiments, and enabled better photoelectron energy resolution to be obtained by the use of long probe wavelengths.

Wavelengths in the range 315 $< \lambda_{pump} <$ 317 nm were obtained from the frequency-doubled output of a Continuum ND6000 dye laser, using DCM dye in methanol and pumped by the second harmonic of a Continuum Surelite III YAG, 10 Hz repetition rate. This range was sufficient to access vibrational levels $v_{2(i)}$= 3, 4 in the $\widetilde{B}$-state. The pulse energy from the doubling unit was set to be $\sim$ 2 mJ by increasing the Q-switch on the YAG from its optimum setting (177 μs to 290 μs, corresponding to a drop in the YAG power at 532 nm from 4 W to 2 W). The laser power input to the spectrometer was controlled further downstream by the use of a variable attenuator, and was typically reduced to 0.5 - 1.0 mJ.

Wavelengths in the range 420 $< \lambda_{probe} <$ 432 nm were obtained from the fundamental output of a Sirah Cobra dye laser, using Exalite 428 dye in para-dioxane solvent and pumped by the frequency-tripled output of a Continuum Surelite I YAG. This range of wavelengths was sufficient to span the rotational levels accessible in NH_3^+ for a $\triangle v = 0$ ionizing transition (dominant in the ionization of the $\widetilde{B}$-state), and create photoelectrons

with kinetic energies up to 900 cm^{-1}. The maximum output power obtainable was 4 mJ at the laser output. Higher powers would have been available if required, but at the cost of beam shape due to ongoing problems with the internal alignment of the Sirah Cobra. The power input to the spectrometer was again tuned using a variable attenuator, and input powers in the range 0.5 - 2.0 mJ were used.

Generally, the intensity of the probe beam was kept much higher than the pump beam in order to maximize the possibility of a molecule already pumped to the $\widetilde{B}$-state absorbing a probe photon. Above a certain level increasing the intensity of the probe beam made little difference to the signal due to depletion of $\widetilde{B}$-state population. However, increasing the pump beam to compensate for this also increased the yield of 1-colour photoelectrons so, as with any set of competing multi-photon processes, a compromise with the best ratio of 1- to 2-colour signal was found. Furthermore, when the pump beam power was $>$ 1.0 mJ, distortion of the velocity-mapped ion spot on the detector was observed, signifying space-charge effects in the ionization region due to the large number of ions created. Although it was not clear how sensitive the photoelectrons were to this effect, pump power was kept below 1.0 mJ to minimize space-charge. The ratio of pump:probe power was therefore typically 1:2. Tests were also performed to check for saturation effects in the angular distributions at these pump power levels.

Before introduction into the spectrometer, ammonia (Sigma-Aldrich, liquefied, 99.9999% pure) was mixed with argon in a mixing volume. Typically a 10% mixture was used, with 0.5 bar NH_3 allowed to mix overnight with 4.5 bar Ar. This mixture was regulated down to provide a 2 bar backing pressure to the pulsed nozzle. The temperature of the molecular beam was optimised and characterized with (2+1) REMPI, example spectra are presented and discussed in the following section.

7.3 Preliminary 1-colour work

The experiment described above was initially set up using the pump laser only, this enabled the apparatus to be tested, the laser-molecular beam overlap to be optimized, REMPI scans to be recorded and so on. Additionally, data comparable to the previous 1-colour time-of-flight work [31, 94] could be obtained as a consistency check. During this work several problems with the VMI spectrometer were identified and remedied, the most serious of which was the inadequate electrical screening around the MCP and phosphor screen assembly, leading to severe distortions in the photoelectron images. Fixing such problems was, of course, one of the aims of this preliminary work. However, there was also a lot of down-time while the spectrometer was worked on and many early photoelectron images proved to be unreliable, so the dataset obtained in this preliminary work was somewhat smaller than initially envisaged.

7.3.1 REMPI spectra

Figure 7.3 shows examples of REMPI spectra recorded in the region of (a) $v_{2(i)} = 3$ and (b) $v_{2(i)} = 4$. Rotational assignments are shown; these assignments were made with the

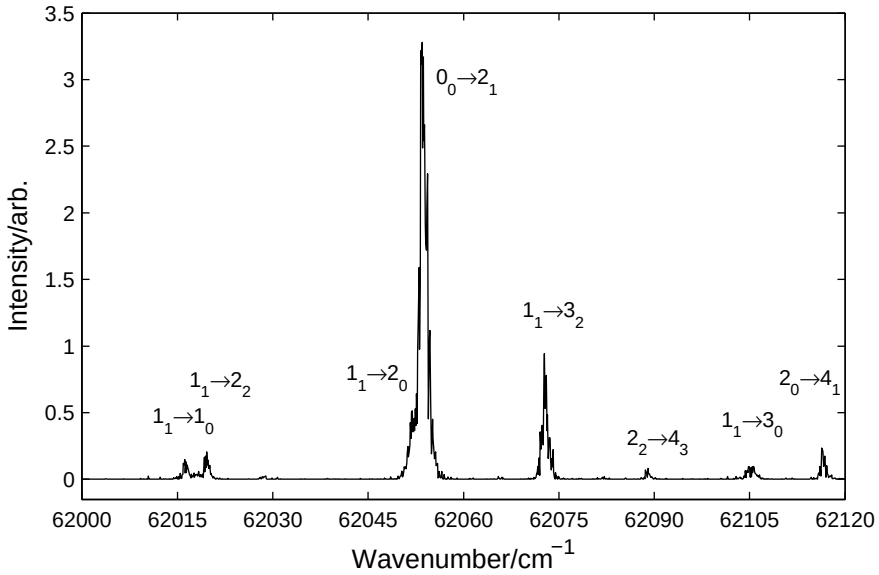

(a) $v_{2(i)} = 3$ region, recorded with 50% NH_3 in Ar. Experimental data is shifted by 164.5 cm^{-1} to match calculated line positions.

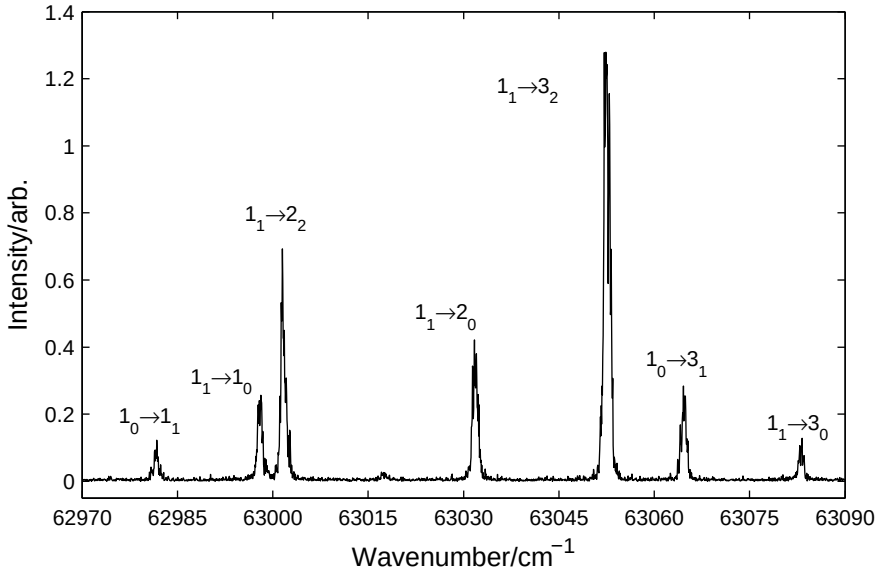

(b) $v_{2(i)} = 4$ region, recorded with 10% NH_3 in Ar. Experimental data is shifted by 167 cm^{-1} to match calculated line positions.

Figure 7.3: REMPI spectra. (a) $v_{2(i)} = 3$ region, (b) $v_{2(i)} = 4$ region. Transitions are labelled $N_{gK_g} \rightarrow N_{iK_i}$. Experimental data are shifted to match calculated line positions, see text for details.

aid of simulations of the $\tilde{X} \rightarrow \tilde{B}$ excitation, based on previous work on this system by D. Townsend [31]. These spectra enabled the characterisation of the molecular beam temperature, and the accurate calibration of λ_{pump}. Figure 7.3(a) shows the result from a 50% NH_3 in Ar mixture. The majority of the ortho population is collapsed into the rotation-less ground state (see Figure 7.1), and the $0_0 \rightarrow 2_1$ transition dominates the spectrum. Several less intense peaks are observed, correlated with transitions from the lowest-lying para level, $J_K = 1_1$. A very small feature originating from the ortho 2_0 level is also observed. The exact rotational temperature has not been deduced from this spectrum, but qualitative comparison with the simulations indicates that $T_{rot} < 15$ K. Excepting the $1_1 \rightarrow 2_0$ transition, which appears as a shoulder to the low energy side of the $0_0 \rightarrow 2_1$ feature, all rotational lines are well-resolved under these experimental conditions. Moving to a less concentrated mixture appeared to make little difference to the spectrum recorded, except that the reduced target density led to a reduced signal intensity, and the smaller features shown in Figure 7.3(a) disappeared completely.

Figure 7.3(b) shows the REMPI spectrum in the $v_{2(i)} = 4$ region using a 10% NH_3 in Ar mixture. Transitions originating from the lowest-lying ortho 0_0 level are forbidden in this case, so only the ortho 1_0 level in the $\tilde{X}$-state is observed to contribute to the spectrum. Several lines are seen which originate from the para 1_1 level. As before the rotational temperature has only been approximately determined, but is < 10 K. In this case, because more transitions to the $\tilde{B}$-state are allowed for $v_{2(i)}$ =even, the spectrum was more sensitive to temperature and only a slight increase in concentration led to many more rotational transitions appearing.

The laser wavelength calibration was slightly different for the two regions, with the offset in λ_{pump} determined to be 0.858 nm and 0.844 nm for spectra (a) and (b) respectively. The large absolute offset found is unsurprising given the age of the laser system used (approximately 12 years old). The change in the offset between λ_{pump} ~323 nm and ~318 nm indicates that the calibration changes as a function of the wavelength, and there may be a non-linear relation between them. However, because λ_{pump} is always chosen to be resonant with a selected transition in order to record photoelectron images, the precise details of the calibration were not an issue for the experiments reported here. If the $\tilde{X} \rightarrow \tilde{B}$ transition was not already well-characterized in the literature then accurate calibration may have been required in order to make the assignments. Calibration of λ_{probe}, as discussed later, is a more pertinent issue for the results presented in this chapter.

7.3.2 Photoelectron images & vibrational spectra

Figure 7.4 shows three example photoelectron images recorded via $v_{2(i)} = 4$. Figure 7.4(a) shows an example of the distortions seen in the photoelectron images due to insufficient shielding around the detector. The distortion observed is a result of penetration of the high voltages applied to the rear of the MCPs, and the phosphor screen, into the field-free region. The front MCP is held at 0 V, so these penetrating fields are only significant for photoelectrons near the edge of the detector. Because the velocity-mapping was good

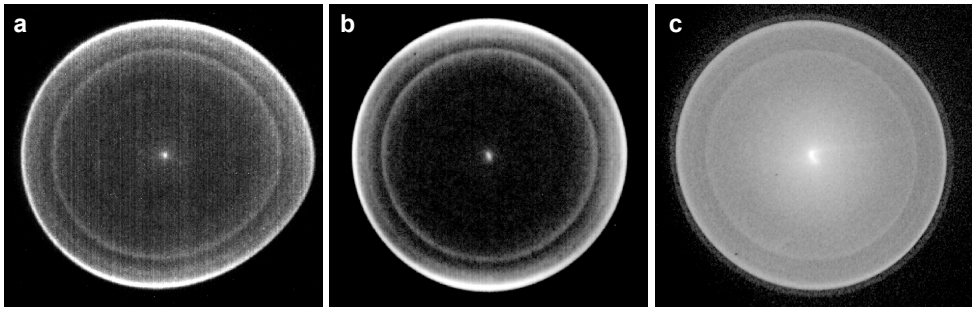

Figure 7.4: Photoelectron images. (a) & (b) recorded via $\widetilde{X}^1A_1'|v_{2(g)} = 0, 1_0\rangle \rightarrow \widetilde{B}^1E''|v_{2(i)} = 4, 3_1\rangle$ pump transition, (c) via via $\widetilde{X}^1A_1'|v_{2(g)} = 0, 1_1\rangle \rightarrow \widetilde{B}^1E''|v_{2(i)} = 4, 3_2\rangle$. (a) Shows distortion due to insufficient detector shielding. (b) Image with good contrast. (c) Image showing poor contrast, but sharper features.

over the majority of the image the penetrating fields must have been significant only in the region close to the MCPs; longer range effects would have been more likely to significantly compromise the velocity-mapping. Figure 7.4(b) shows an image recorded after a small adjustment in the laser path, and a slight increase in the VMI voltage. These adjustments moved the photoelectrons further from the edge of the detector and enabled an undistorted image to be obtained.

Later in the experimental work the edge effects were eliminated with the addition of a shielding plate around the MCP, as shown in Figure 3.1, thereby removing the necessity to use higher voltages and reduce the effective area of the detector. Slow electron images could not have been recorded without this correction to the instrument. Figure 7.4(c) shows an image recorded much later in the experimental run, for the same pump transition and $V_r = 2700$ V, $V_e = 1874$ V. Although this image has poor contrast, partly due to significant background contributions to the image[2], the rings are much sharper than those seen in (b), consequently the photoelectron spectrum extracted from this image is sharper. Figure 7.5(a) shows the spectrum obtained from 7.4(c), and the insert shows the spectrum obtained from 7.4(b). Figure 7.5(b) & (c) show comparable spectra from the literature. Thorough evaluation of vibrational peak positions has not been attempted, the assignments shown in Figure 7.5(a) were made by comparison with the spectra in ref. [7]. The significance of these spectra is that they compare well with other methods of photoelectron spectroscopy, showing that the VMI results are consistent with more established techniques. In fact, VMI shows some improvement in resolution over the magnetic bottle results (7.5(c)), and the problem of the drop in signal intensity as a function of flight time inherent in field-free time-of-flight methods is also removed [35].

[2]The background referred to here is the photoelectron signal obtained with the pulsed nozzle off. The origin of this signal is unknown but most likely originated from significant ejection of electrons from the VMI plates due to scattered light. Although these images were actually recorded after the 2-colour work which is the main focus of this chapter, and the laser path had consequently already been carefully optimized to minimize scatter, the switch to high VMI voltages may have caused a large increase in background signal. Also, the focusing of the laser after reflection from the dichoric mirror used in the 2-colour experiments (see Figure 3.7) may not have been as tight as that achieved in the initial 1-colour set-up, and this may also have had a significant affect on the level of background signal. See Section 3.3.5 for more details regarding background signal.

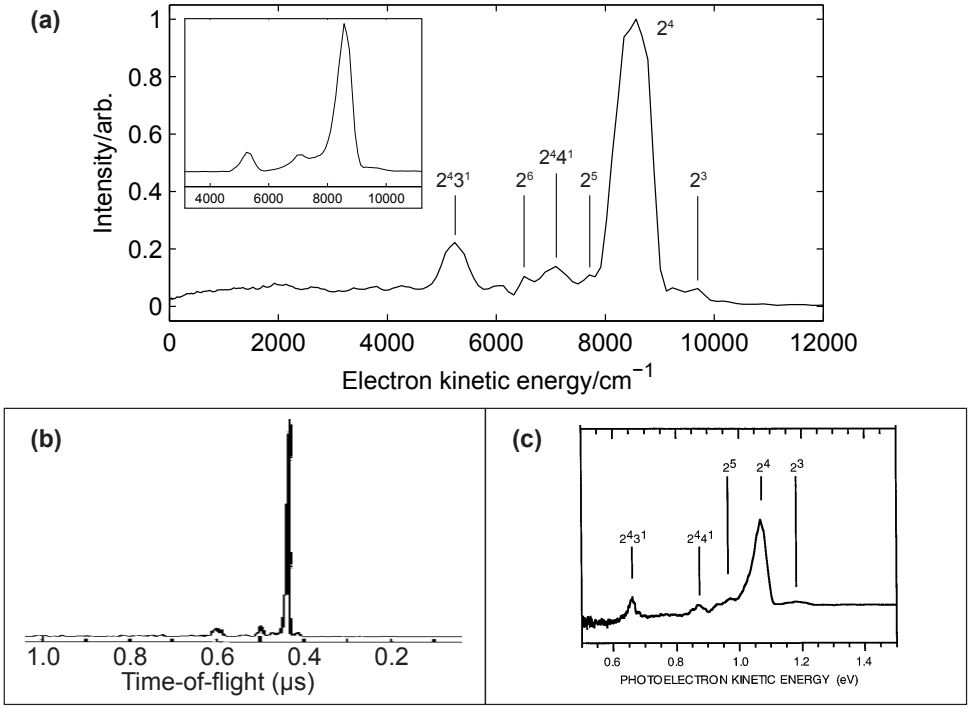

Figure 7.5: Photoelectron spectra recorded via $v_{2(i)} = 4$. (a) Imaging results, main spectrum from the image shown in Figure 7.4(c), inset spectrum from Figure 7.4(b). (b) Time-of-flight spectrum, reproduced from ref. [94]. (c) Spectrum recorded with magnetic bottle spectrometer, reproduced from ref. [7].

7.3.3 Photoelectron angular distributions

Figure 7.6 shows PADs extracted from the photoelectron images compared with those obtained from field-free time-of-flight (ToF) experiments (see refs. [31, 94]). The PADs correlate with the formation of $\widetilde{X}^2 A_2'' | v_{2(+)} = v_{2(i)}, N_{+K_+} \rangle$ cation states. Rotational resolution is not achieved in the 1-colour work, so these PADs contain contributions from all underlying rotational levels. The PAD recorded via the $1_0 \rightarrow 3_1$ pump transition is extracted from the image shown in Figure 7.4(b), and the $1_1 \rightarrow 3_2$ PAD from the image shown in Figure 7.4(c). The difference in quality between the source images is illustrated in the PADs by the size of the error bar output by the pBasex inversion process; in the former case the error bars are vanishingly small, while in the latter the lack of contrast in the photoelectron image leads to much larger error bars. The PADs recorded via the $1_1 \rightarrow 2_0$ and $1_1 \rightarrow 1_0$ pump transitions similarly show large error bars, they also originate from images which show good velocity-mapping, but low contrast and a significant background contribution. Because of these problems only the $1_0 \rightarrow 3_1$ PAD should be closely compared with the ToF result.

The $1_0 \rightarrow 3_1$ PAD obtained by imaging appears to be more anisotropic than the ToF result. The error bars on the ToF data points are small, but data was only recorded at 10° intervals for one quadrant ($0 \leq \theta \leq 90°$). The differences may therefore reflect the higher sensitivity of VMI, with data recorded for all quadrants ($0 \leq \theta \leq 360°$) with an

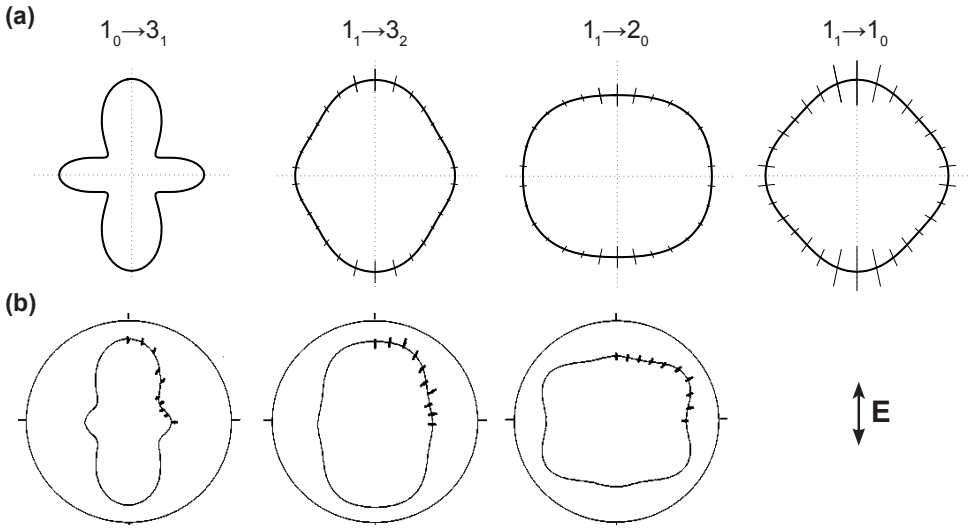

Figure 7.6: PADs correlated with the $\Delta v = 0$ ionizing transition, recorded via $\widetilde{X}^1A_1'|v_{2(g)} = 0, J_K\rangle \rightarrow \widetilde{B}^1E''|v_{2(i)} = 4, J_K\rangle$ pump transitions. (a) Imaging results. (b) Time-of-flight results, reproduced from ref. [94].

angular resolution of $< 1^\circ$ (see Section 3.2), to the fine details of the angular distribution. For instance, careful inspection of the ToF result shows that the depth of the four-fold minima would be sensitive to a small change in the data point recorded at $\theta = 30^\circ$ (the 4th data point from the horizontal axis); with many more data points the imaging result should be more robust.[3] It is not thought that saturation effects could be the cause of the observed difference because the experiments reported in ref. [31] include a careful study of laser power on the PADs.

Conversely, the remainder of the PADs shown in Figure 7.6 illustrate that images must still be carefully evaluated on their individual merits, and the possibility of artefacts which might affect the extracted PADs must be considered. In these cases the error bars are significant, but the results appear reasonable. However, given the large, isotropic background contribution and lack of contrast in the source images,[4] it is likely that in these cases the fine details of the angular distributions are washed out. The PADs thus appear more isotropic. Although this is consistent with the changes in the ToF results from left to right in Figure 7.6(b), the forms of the PADs do not so closely match those from ToF. Because the overall signal level is still good, as far as the inversion algorithm is concerned, the error bars are not entirely representative of this fact. Similar effects have been observed in photoelectron images due to detector inhomogeneity, incorrect threshold setting on the image acquisition software, and hot pixels on the CCD.

In summary, the PADs shown here are not thought to represent completely reliable results. They do, however, illustrate a qualitative similarity to PADs recorded in ToF experiments (more thorough testing of ToF and VMI results has been presented in the

[3] This, of course, also relies on a good source image and a reliable inversion method.

[4] In this instance background subtraction did not make a significant difference to the extracted PAD, showing that low contrast was the main problem.

literature, see Section 4.1.3 for further discussion on this point). More importantly, as mentioned above, the recording of 1-colour images provided a stepping-stone towards the real goal of 2-colour, slow-electron images, and a good test case for optimization of the experiment.

7.4 2-colour Photoelectron Images & Rotational Resolution

After optimizing the 1-colour photoelectron image a second, probe laser, was introduced as discussed above (Section 7.2). Due to the Rydberg nature of the $\widetilde{B}^1E''$ state ionizing transitions with $\Delta v_2 = 0$ dominate [188], so in all cases considered here $v_{2(i)} = v_{2(+)}$. For the wavelengths used in this study photoelectrons produced from (2+1) ionization are born with E_{KE} ~8000 cm^{-1}, while those created via a (2+1') process are restricted to much lower E_{KE} by the choice of λ_{probe}, typically $<$ 300 cm^{-1} for λ_{probe} =430 - 434 nm.

Figure 7.7(a) shows a photoelectron image recorded at sufficiently high electrostatic lens voltages to image both sets of photoelectrons ($V_r = 2700$ V, $V_e = 1874$ V; $\lambda_{pump} = 316.358$ nm, $\lambda_{probe} = 434$ nm). The central features, marked as regions 1 and 2 in the figure, appear in the presence of both pump and probe lasers, while the outer rings, marked 3 and 4, are due to electrons with much higher kinetic energy and represent pump only, (2+1), processes. In this case, these bands correspond to $\triangle v_2 = -1$ (ring 3) and $\triangle v_2 = 0$ (ring 4) ionizing transitions. No rotational structure can be resolved, but the large separation in velocity space is clear. Of the inner features, photoelectrons in region 1 arise from (2+1') processes, while the origin of the diffuse band, region 2, is unknown (a possible origin of these diffuse features is discussed in Section 7.4.2).

As discussed in Chapter 3, by dropping the electrostatic lens voltages it is possible to zoom-in on the low kinetic energy photoelectrons and maximize the resolution obtained in the velocity-mapped images. Figure 7.7(b) shows an image recorded under the same conditions as 7.7(a), but with the voltages lowered to $V_r = 160$ V, $V_e = 110$ V. This image corresponds to region 1 in 7.7(a). Three distinct rings can be seen in this image, these correspond to the formation of three different rotational levels in NH_3^+, $N_{+K_+} = 2_1, 3_1, 4_4$ (rotational assignments are discussed further in Section 7.5.1). In this example λ_{probe} is only sufficient to access these few rotational levels above the $\Delta v_2 = 0$ ionization threshold, and the ionization cross-section is consequently low leading to a weak 2-colour signal sitting on a relatively intense (but flat) 1-colour background (probe wavelength dependence is discussed in Sections 7.4.2 and 7.7).

7.4.1 Slow-electron VMI

Figure 7.7 illustrates that rotational resolution can be achieved in VMI; more quantitative data and analysis is presented in the following sections. At this point it is instructive to consider the practical limitations which were found during the initial 2-colour work. As already discussed, optimal resolution is achieved by using the whole area of the MCPs

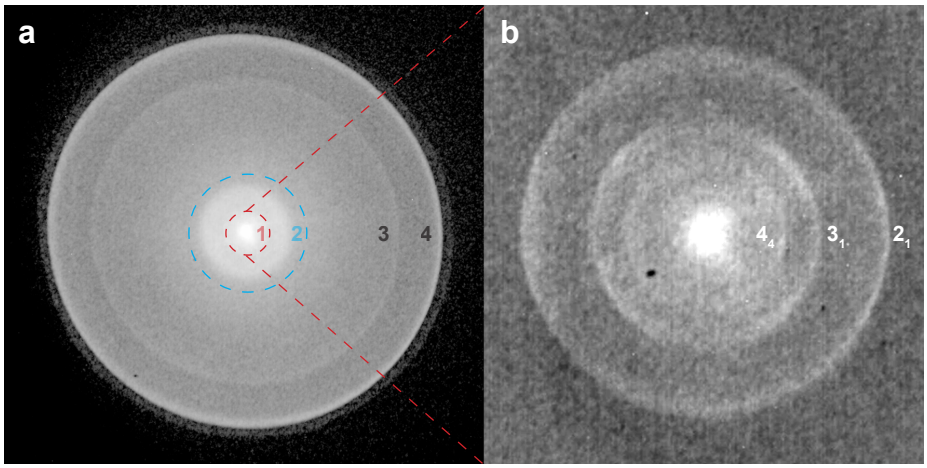

Figure 7.7: (a) Photoelectron image showing features originating from both 2-colour (regions 1 and 2) and 1-colour (rings 3 and 4) ionization processes ($V_r = 2700$ V, $V_e = 1874$ V; $\lambda_{pump} = 316.358$ nm, $\lambda_{probe} = 434$ nm). (b) As (a), but with $V_r = 160$ V, $V_e = 110$ V. This corresponds to region 1 in (a). Rotational features are resolved, and labelled N_{+K_+}.

to image the smallest dynamic (velocity) range. The best resolution should therefore correspond to the lowest VMI voltages and longest λ_{probe}. The only limitation on λ_{probe} arises from conservation of energy as shown in equation 4.17, although there is also the possibility of a lower ionization cross-section as the total energy approaches the ionization threshold which may render images hard to record due to decreased signal-to-noise ratio. In principle there should not be a limitation on V_r and V_e, apart from the necessity to project photoelectrons onto the active area of the detector. In practice, however, it was found that reducing the voltages below $V_r = 160$ V came at the expense of velocity mapping efficacy, and satisfactory velocity focusing could not be achieved. This problem, combined with the slight mis-alignment of the photoelectron images relative to the central axis of the spectrometer, meant that the full detector area could not be utilized, and "optimal" resolution was not achieved.

The most likely causes of this lower bound on the voltages applied to the electrostatic lens was small stray fields in the flight region of the spectrometer, and small inhomogeneities (aberrations) in the electrostatic optics. Low energy photoelectrons will be particularly sensitive to such effects, and at the time of these experiments there were some known problems with the design of the lens assembly. The cause of the off-axis alignment of the photoelectron image centre was thought to be due to mis-alignment of the holes in the three elements of the electrostatic lens, and the skimmer, relative to the central axis of the spectrometer.

Additionally, the precision (and stability) of the applied voltages becomes more critical at low V_r. The Stanford power supplies used in these experiments (PS300) had a resolution of 1 V, so may also have been a limiting factor. In work from Neumark's group developing the SEVI technique [42] voltages as low as $V_r = 50$ V were used, and typical resolutions on the order of $\Delta E/E = 10\%$. The best resolution obtained in this work was $\Delta E/E = 20\%$,

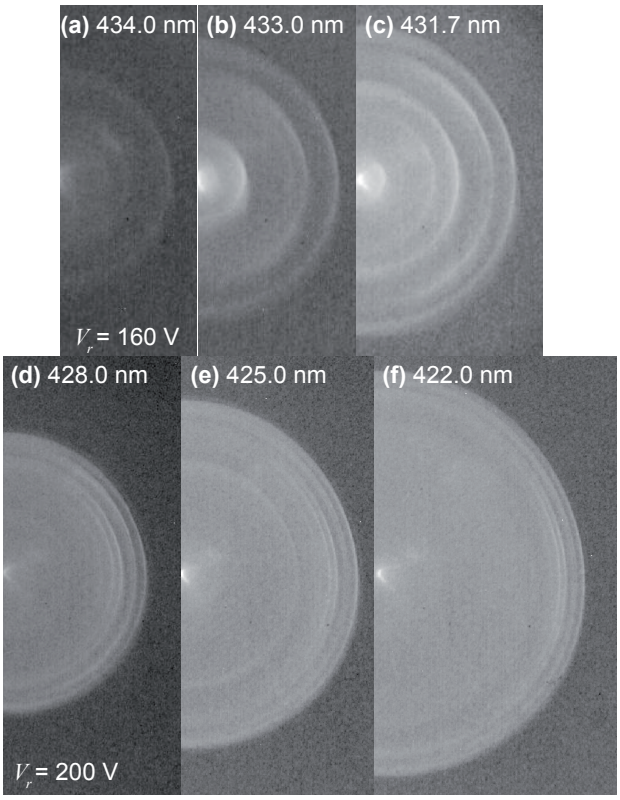

Figure 7.8: Images recorded for different λ_{probe}. For (a)-(c) $V_r = 160$ V, for (d)-(e) $V_r = 200$ V.

however this was sufficient to resolve the majority of rotational levels populated in NH_3^+.

7.4.2 Probe wavelength & energy resolution

As noted above, the longest λ_{probe} corresponds to the slowest photoelectrons and, therefore, the best energy resolution. Figure 7.8 shows this effect in more detail. The top row shows images recorded with $\lambda_{probe} = 434.0$, 433.0, 431.7 nm and $V_r = 160$ V. The good velocity resolution is apparent, individual rings - corresponding to individual ion rotational levels - are spatially separated. As λ_{probe} approached the $\triangle v = 0$ threshold the intensity of the photoelectron signal decreased. Figure 7.8(a) in particular shows very low contrast as a result of this. The bottom row of Figure 7.8 shows images recorded with shorter λ_{probe}. In order to fit cleanly onto the detector these images required slightly higher VMI voltages, $V_r = 200$ V. Individual rings can still be discerned, even at $\lambda_{probe} = 422.0$ nm, but the spatial separation is poorer and not all features are well resolved.

Figure 7.9 shows the spectra extracted from the images shown in Figure 7.8, plus an additional result recorded with $\lambda_{probe} = 420.0$ nm. In each case the spectra are normalized to the most intense feature. Rotational lines are well-resolved for spectra (a)-(d), while spectra (e)-(g) show much poorer resolution. The number of features observed changes with λ_{probe}; as the available energy is increased higher energy rotational levels can be populated in the ion. Three features are seen in (a), four in (b) and five in (c); rotational assignments are also shown in (c), and will be discussed further in Section 7.5.1. For

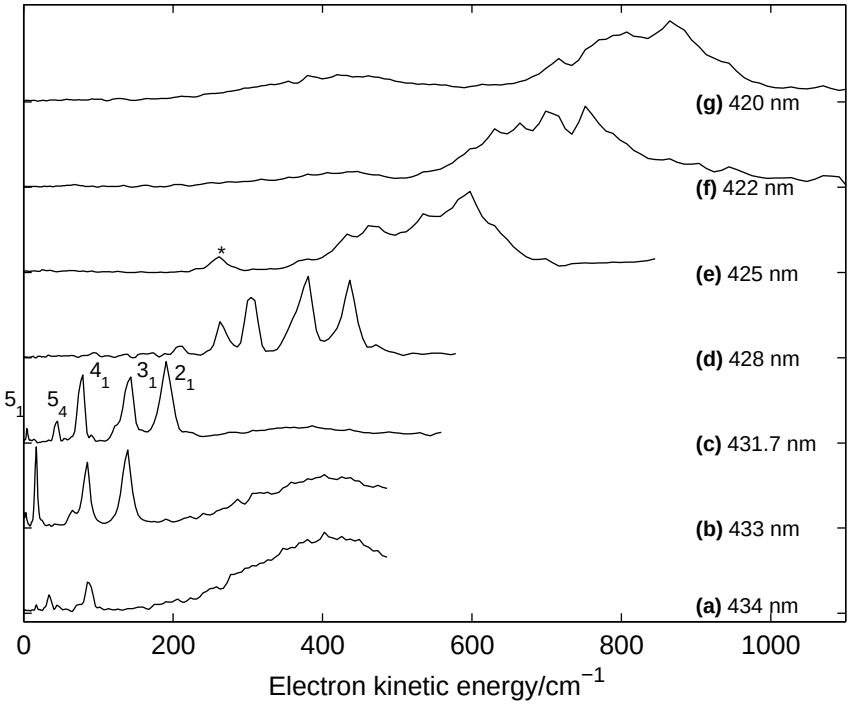

Figure 7.9: Spectra extracted from the images shown in Figure 7.8. All spectra are normalized to the most intense feature. (a)-(d) show well defined rotational features. Rotational assignments, N_{+K_+}, are shown for (c), and the feature marked * in (e) can be tentatively assigned as 6_1.

$\lambda_{probe} < 431.7$ nm no further rotational lines appear, with the exception of the feature marked with a * in (e). By comparison with MATI spectra [30], this feature is tentatively assigned as $N_{+K_+} = 6_1$. The increase in intensity of this feature at $\lambda_{probe} = 425.0$ nm may reflect the change in the ionization dynamics with λ_{probe}, and a rapid change in the dynamics with λ_{probe} would indicate the presence of a scattering resonance. Unfortunately data with small wavelength steps was not recorded in this region, so this observation awaits further experimental work.[5]

The spectra obtained from images (e) and (f) do not show rotational features clearly despite the fact that they can be seen in the raw images. This can be attributed to the variation in velocity-focus around the image. Near the horizontal axis the focus is good, but around the top of the image the focus is poor and the rings blur together. Because the pBasex inversion makes use of the whole image the radial spectrum essentially averages out the resolution, so the spectra are not as well-resolved as the images may suggest. In some cases extracting data from just one quadrant of an image may improve the resolution of the spectrum obtained, but this would depend on the exact nature of the imperfections in the original image. However, manipulation of the image prior to inversion may introduce other problems and artefacts, so it is preferable to obtain the best images experimentally and use these without additional manipulation.

In all spectra a diffuse band centered at $E_{KE} = 400$ cm^{-1} is present and, for (a),

[5]Rapid changes in line intensity were observed for the 1_1 line around $\lambda_{probe} = 431.4$ nm, this data is discussed briefly in Section 7.7.

is considerably more intense than the resolved rotational features. This diffuse feature was also present in Figure 7.7, marked as region 2. The origin of this feature is unknown, however the change in branching ratios between the diffuse band and the rotational lines suggests that it arises from a pathway which competes with direct ionization to $\widetilde{X}^2A_2''|v_{2(+)} = v_{2(i)}, N_{+K_+}\rangle$. As the probe energy increases above threshold, the cross-section for direct ionization increases and the diffuse band intensity decreases, consistent with the hypothesis of a competing ionization pathway. Interestingly, the diffuse band was only observed when both lasers were present, but the kinetic energy of the electrons forming the band *did not change with* λ_{probe} *or* λ_{pump}. Further work is needed in order to explore this observation, in particular investigation to establish which electronic states might be accessed through various combinations of pump and probe photons. If a specific process, and candidate electronic states, could be suggested further experimental work could be carried out to probe this behaviour further.

Returning to the question of resolution, it is apparent from the spectra in Figure 7.9 that some trade-off between energy resolution and dynamic range must be made. The spectrum obtained using $\lambda_{probe} = 431.7$ nm is close to optimum, but the 5_4 rotational line lies slightly too close to the centre of the photoelectron image. Due to the intense spot which appears in the centre, and the reduced number of data points for rings with small radii, data from the central region of the image ($r < 10$ pixels) can be unreliable. Based on this conclusion the experimental datasets which were subsequently recorded for different pump transitions (see following section) used a slightly shorter wavelength, $\lambda_{probe} = 431.3$ nm.

7.4.3 2-colour data overview

Having obtained rotationally-resolved photoelectron images, and optimised the velocity-mapping conditions and probe wavelength for best resolution, further experimental work was carried out to obtain datasets which would be sufficient for the in-depth analysis of the ionization dynamics which is the ultimate aim of all the work reported here.

Photoelectron images were recorded via pump transitions of the form $\widetilde{X}^1A_1'|v_{2(g)} = 0, J_{gK_g}\rangle \rightarrow \widetilde{B}^1E''|v_{2(i)} = \{3, 4\}, J_{iK_i}\rangle$, using $\lambda_{probe} = 431.3$ nm to access ion levels $\widetilde{X}^2A_2''|v_{2(+)} = v_{2(i)}, N_{+K_+}\rangle$. VMI voltages of $V_r = 160$ V and $V_e = 110$ V were used throughout. The largest experimental dataset was obtained via $v_{2(i)} = 4$; this data is presented in Section 7.5 and further analysed in Chapter 8. Photoelectron images were recorded via all of the transitions observed in the preliminary REMPI spectra (Figure 7.3(b)), with the exception of the $1_1 \rightarrow 3_0$ transition,[6] providing six photoelectron images. The raw photoelectron images are shown in Figure 7.10. The complete dataset was recorded twice during the experimental run to check for reproducibility. A sample of the data obtained via $v_{2(i)} = 3$ is presented in Section 7.6, although there is still work outstanding on the processing and analysis of this data so it is not discussed in depth.

[6] Photoelectron images were recorded via this transition, but the image intensity was very low and the images proved unreliable. The situation may have been improved by changing the molecular beam conditions, but this avenue was not pursued.

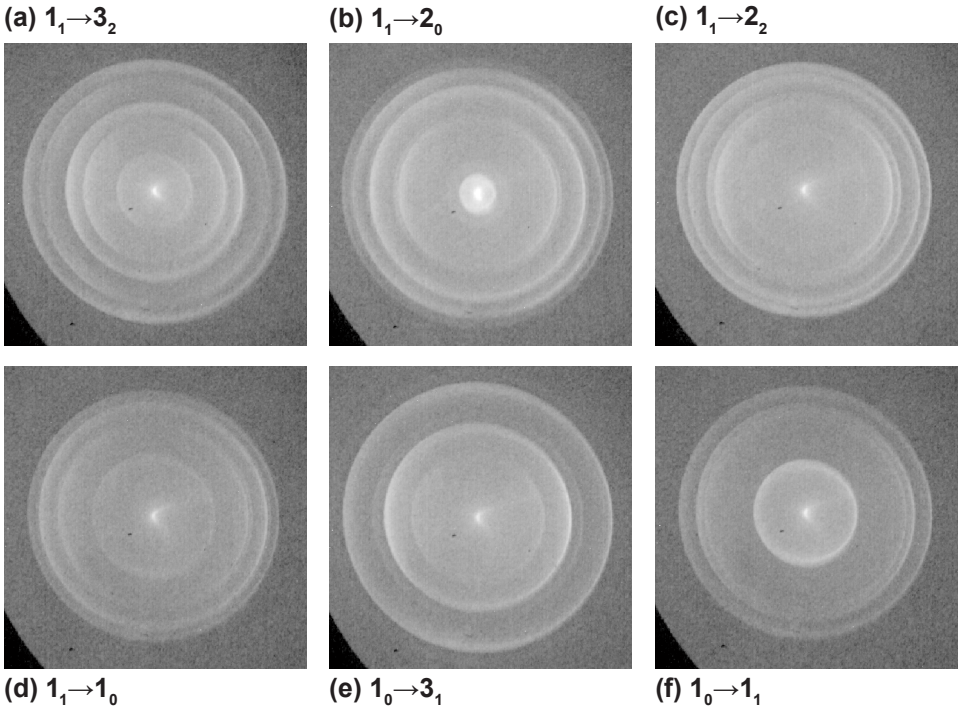

Figure 7.10: Raw photoelectron images recorded via $\widetilde{X}^1A_1'|v_{2(g)} = 0, J_{gK_g}\rangle \rightarrow \widetilde{B}^1E''|v_{2(i)} = 4, J_{iK_i}\rangle$ pump transitions with $\lambda_{probe} = 431.3$ nm. VMI voltages were $V_r = 160$ V and $V_e = 110$ V. All images are shown to the same scale, and labelled $J_{gK_g} \rightarrow J_{iK_i}$.

Towards the end of the experimental run a study was performed with the aim of probing the fine details of the dependence of the ionization dynamics on λ_{probe}, in this case images were recorded over the range $432 > \lambda_{probe} > 430.8$ nm in 0.1 nm steps. This data has yet to be fully analysed, but a sample is presented in Section 7.7. Of particular interest is the resonant behaviour of the 1_1 peak, similar to that suggested for the 6_1 feature in Section 7.4.2.

7.5 $v_2 = 4$ Dataset

7.5.1 Rotational spectra

Figure 7.11 shows the spectra obtained from the photoelectron images shown in Figure 7.10. The raw images were processed using pBasex, and the E_{KE} scaling of the resulting spectra were calibrated using the procedure detailed in Section 4.2. The calibrated spectra were then converted to an ion internal energy, E_{ion}, scale and required a further linear shift of 12 cm^{-1} to bring them into good agreement with calculated rotational line positions. This shows that non-linear effects in both the laser calibration and velocity mapping were negligible, but that the absolute calibration error of the probe wavelength was significant, $\triangle\lambda_{probe} = 0.22$ nm.

Rotational assignments are shown in Figure 7.11, and listed in Table 7.1(a) for para-

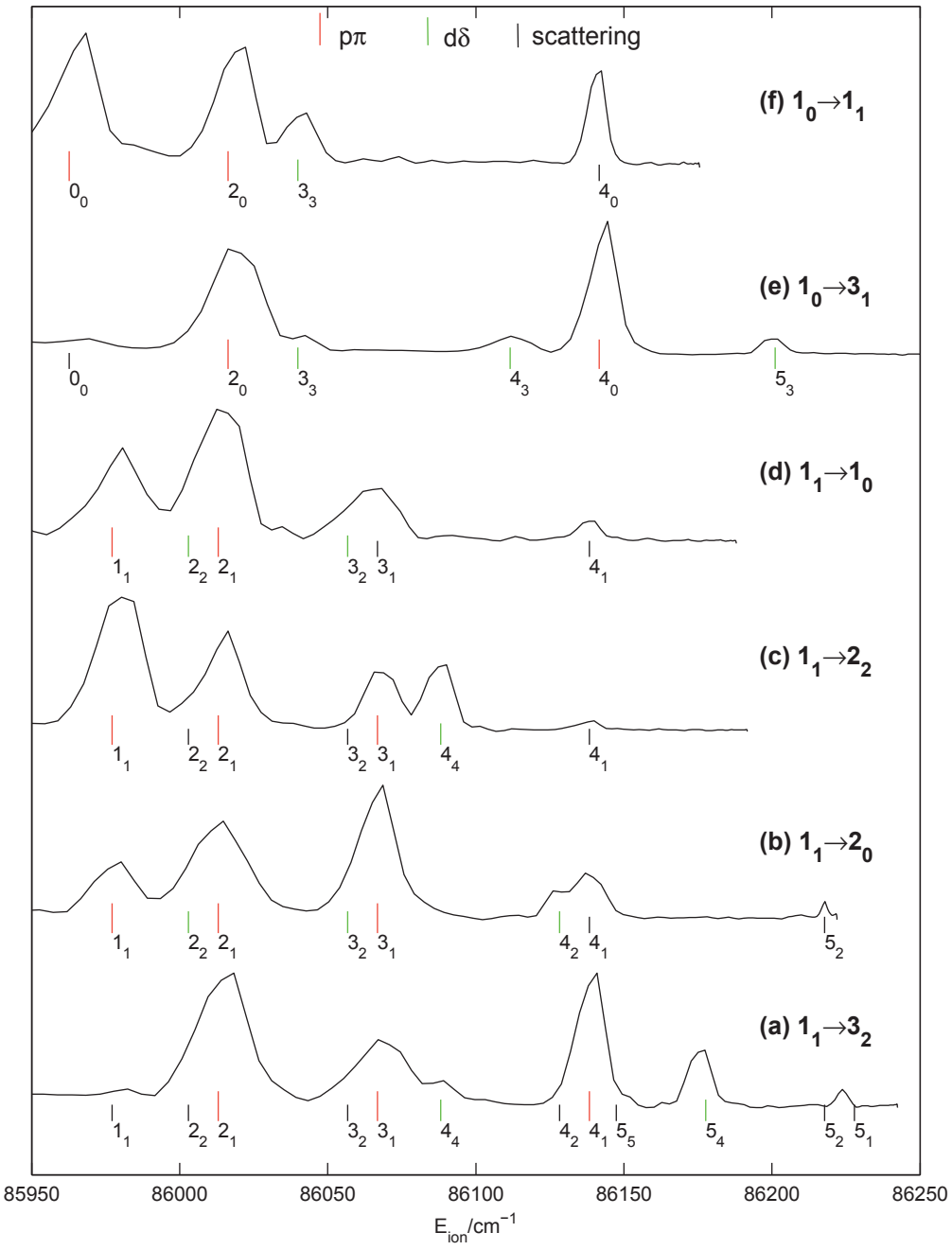

Figure 7.11: Photoelectron spectra extracted from the images shown in Figure 7.10, recorded via $\widetilde{X}^1A_1'|v_{2(g)} = 0, J_{gK_g}\rangle \rightarrow \widetilde{B}^1E''|v_{2(i)} = 4, J_{iK_i}\rangle$ pump transitions with $\lambda_{probe} = 431.3$ nm. Rotational assignments are shown, long red lines and shorter green lines represent levels accessible from the $p\pi$ and $d\delta$ Rydberg components, respectively, in the no-scattering case. Short black lines represent rotational levels which can only be populated via scattering of the Rydberg or photoelectron as discussed in the main text. Experimental data is shifted by (-)12 cm^{-1} to match calculated line positions, this is equivalent to an offset in the laser calibration $\triangle\lambda_{probe} = 0.22$ nm.

N_{+K_+}	Calc./cm^{-1}	Expt./cm^{-1}	Difference/cm^{-1}	Underlying features
1_1	85977	85982	5	
2_1	86013	86015	2	2_2
3_1	86067	86070	1	3_2
4_4	86088	86089	1	
4_2	86128	86127*	1	
4_1	86138	86138	0	4_2, 5_5
5_4	86178	86178	0	
5_2	86218	86218*	0	
5_1	86228	86224	4	

(a) Assignments and positions for data recorded via $1_1 \rightarrow 3_2$ (para), except * via $1_1 \rightarrow 2_0$, spectra shown in Figure 7.11(a) & (b). The final column lists *possible* underlying features.

N_{+K_+}	Calc./cm^{-1}	Expt./cm^{-1}	Difference/cm^{-1}
0_0	85963	85966	3
2_0	86016	86020	4
3_3	86040	86040	0
4_3	86112	86112*	0
4_0	86142	86141	1
5_3	86201	86200*	1

(b) Assignments and positions for data recorded via $1_0 \rightarrow 1_1$ (ortho), except * via $1_0 \rightarrow 3_1$, spectra shown in Figure 7.11(e) & (f).

Table 7.1: Rotational line assignments. Calibration uncertainty in experimental results is estimated as ± 5 cm^{-1}.

NH_3 and (b) for ortho-NH_3. Assignments were made with the aid of line positions calculated for an oblate symmetric top using rotational constants from ref. [189], and by reference to previously reported experimental spectra [28, 30]. The calibration error in the spectra was estimated to be ± 5 cm^{-1} (see Section 4.2), although this uncertainty is larger than the differences found between the measured and calculated line positions suggesting that the experimental data is actually slightly more accurate than expected.

In most cases single rotational levels are resolved in the spectra, and these can be unambiguously assigned. In the atomic picture outlined in Section 7.1.4 the majority of the lines can be assigned as originating from either the $p\pi$ ($\triangle N = 0, \pm 1$, $\Delta K = \pm 1$) or $d\delta$ ($\triangle N = 0, \pm 1, \pm 2$, $\Delta K = \pm 2$) Rydberg component, while population of other ion rotational levels must be due to scattering. Propensity rules suggest that the atomic-like lines will be most intense, while those arising from scattering will be much weaker. Such behaviour is indeed observed for most of the features seen in these spectra, and in the previously reported ZEKE [28] and MATI [29, 30] spectra (these spectra will be compared in detail in Section 8.2.2). The spectrum obtained via the $1_1 \rightarrow 3_2$ pump transition (Figure 7.11(a)) provides an illustrative example of this. The three most intense features are assigned as 2_1, 3_1 and 4_1, all of which are $p\pi$ 'allowed' in the atomic picture. The less

intense 4_4 and 5_4 features correlate with the $d\delta$ Rydberg component, and the much weaker 1_1 and 5_1 features arise from scattering. The observed intensities are thus consistent with the assignment of the $\tilde{B}$-state Rydberg character as primarily $p\pi$, and the application of the atomic-like propensity rules, while the presence of weak scattering features reflects the the molecular nature of the ionization process. These scattering channels would not be open in the atomic case; they reflect the scattering of the photoelectron from the short-range, non-central, molecular potential and the exchange of angular momentum between the outgoing electron and the ion core - hence the breakdown of the rotational spectator model.

In the spectra shown in Figure 7.11(a)-(d) (para-$\mathrm{NH_3}$) there are a few examples where more than one symmetry-allowed level underlies the observed feature. These are listed in Table 7.1(a). In these cases the line-profiles are consistent with the application of the atomic propensity rules, whereby population of $p\pi$ or $d\delta$ 'allowed' rotational levels can be assigned as the main contribution to the feature, and the other symmetry allowed levels *may* make small contributions to the wings of the peaks. This conclusion is verified by fitting Lorentzians to the peaks; for the features which may have contributions from underlying components the quality of the fit is almost identical for fitting with a single Lorentzian or two Lorentzians, and the second Lorentzian is typically found to contribute $< 10\%$ of the peak area. Because fewer rotational levels are present in ortho-$\mathrm{NH_3}$ there are no instances where multiple rotational levels may be unresolved in the spectra presented in Figure 7.11(e) & (f).

7.5.2 Photoelectron angular distributions

The PADs extracted from the photoelectron images are shown in Figure 7.12. These angular distributions are correlated with the formation of (for the most part) individual rotational levels of $\mathrm{NH_3^+}$, and these *rotationally-resolved* PADs exhibit a diverse range of forms. This behaviour is expected from equations 2.46 and 2.50, which show the complex dependence of the PAD on the angular momentum of the system, and define how changes in ΔN and ΔK will lead to different $\gamma_{N_+K_+l\lambda l'\lambda'}$ parameters. These PADs contain much more information than the vibronically-resolved PADs obtained in the acetylene experiments (see discussion in Section 6.2.2), and provide the necessary data for a very detailed insight into the photoionization dynamics.

In the case of the (2+1') REMPI scheme employed in these experiments the lab frame PADs can have contributions from four β_{LM} terms:

$$I(\theta) = \beta_{00}Y_{00} + \beta_{20}Y_{20} + \beta_{40}Y_{40} + \beta_{60}Y_{60} \tag{7.6}$$

The β_{LM} values corresponding to the PADs shown in Figure 7.12 are tabulated in Appendix C, along with experimental uncertainties. The error bars shown in Figure 7.12 represent the cumulative effect of the uncertainties in each β_{LM} parameter. PADs are labelled in Figure 7.12 according to which N_{+K_+} they correlate with, and these labels are further colour-coded according to the atomic-like propensity rules discussed in Sections

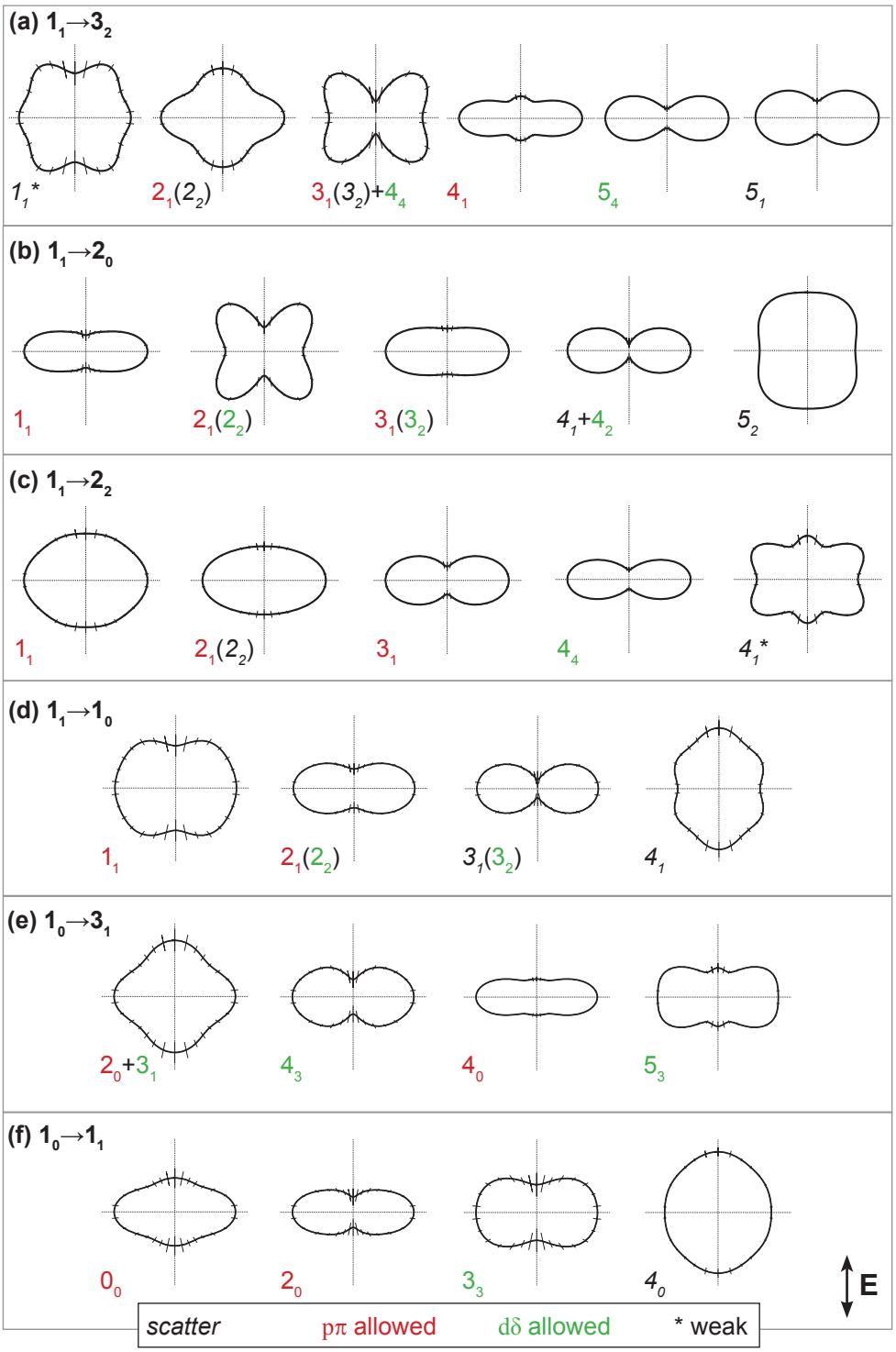

Figure 7.12: PADs extracted from the photoelectron images shown in Figure 7.10. Pump transitions are labelled $J_{gK_g} \rightarrow J_{iK_i}$, ion assignments ($N_{+K_+}$) follow those in Figure 7.11. In cases where the PAD correlates with more than one rotational level the most intense transition is listed first, followed by possible unresolved features in parentheses (as listed in Table 7.1), or by partially resolved features prefixed by $+$. Colour coding also follows Figure 7.11, with $p\pi$ allowed and $d\delta$ allowed levels in red and green respectively. Levels which can only be populated by scattering are shown in *italics*. Features which are particularly weak in the spectrum are marked *, in these cases the PADs may be less reliable than indicated by the error bars. Tabulated β values can be found in Appendix C.

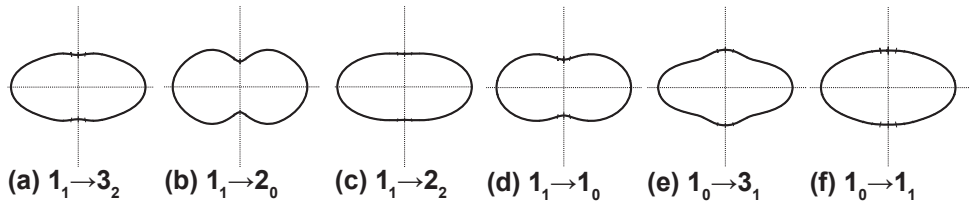

Figure 7.13: Rotationally-summed PADs corresponding to the photoelectron images shown in Figure 7.10.

7.1.4 and 7.5.1; the same colour-code was also used in Figure 7.11. PADs which are labelled in red therefore correlate with an ionizing transition which is $p\pi$ allowed, and those in green from transitions which are $d\delta$ allowed. More generally, these correspond to ionization to the even-l or odd-l continua respectively.

It is difficult to tease out any simple patterns from the complex behaviour of the PADs, but there are two general comments which can be made about those presented here. Firstly, the majority of the PADs show maxima perpendicular to the laser polarization, and this observation holds for PADs correlated with ionizing transitions to both the even-l or odd-l continua. Figure 7.13 shows a way to test this observation, whereby PADs are obtained by rotational summation of the data. In all cases the summed PAD is aligned perpendicular to the laser polarization. Additionally, these summed PADs can be directly compared with the equivalent PADs recorded in the 1-colour experiments, shown in Figure 7.6. The significant differences between these PADs can be attributed to the energy dependence of the dynamical parameters, which may change substantially between E_{KE}s of ∼8000 cm^{-1} and ∼300 cm^{-1}. In previous work [31] changes in the PAD recorded via $1_0 \rightarrow 3_1$ were also observed for $\lambda_{probe} \approx 360$ nm (when compared with the 1-colour PAD recorded under the same experimental conditions), which would produce E_{KE} ∼5000 cm^{-1}.

Secondly, the PADs which are correlated with scattering channels tend to show quite different structure to those correlated with the atomic-like channels. In particular, three of the PADs shown in Figure 7.12 have much larger β_{60} contributions than average: $1_1 \rightarrow 3_2 \rightarrow 1_1$ (panel (a)), $1_1 \rightarrow 2_2 \rightarrow 4_1$ (panel (c)) and $1_1 \rightarrow 1_0 \rightarrow 4_1$ (panel (d)). The angular momentum coupling of (l, l') into the lab frame PAD (see equation 2.52) dictates that for $\beta_{60} \neq 0$:

$$\begin{pmatrix} l & l' & 6 \\ 0 & 0 & 0 \end{pmatrix} \neq 0 \tag{7.7}$$

In all these cases l must be even (because $K_+ = 1$), hence there must be an even partial wave component $l > 2$ in these cases, i.e. $l = 4, 6, ...$ terms may be present. This is a signature of scattering, directly revealing the presence of higher-order terms in the asymptotic photoelectron wavefunction, $|\mathbf{k}, l\lambda m\rangle$, which would not be present in the no-scattering case. Some caution should be exercised here as two of the three ionizing transitions mentioned are weak, so there is the possibility of spurious β_{60} values arising in

the pBasex inversion and data extraction. The criterion set here is that if the uncertainty is greater than 50% then the β parameter should be regarded as undefined. For the PAD correlated with $1_1 \rightarrow 3_2 \rightarrow 1_1$ this is the case, and is reflected by the large error bars on the PAD. However, for the other two cases the β parameter is well defined and the link between β_{60} and scattering appears to hold. However, it should be noted that the situation is more complex than this because other PADs which are also correlated with scattering channels do not show significant β_{60} values, for example the PADs correlated with $1_1 \rightarrow 3_2 \rightarrow 5_1$ (Figure 7.12 panel (a)) and $1_1 \rightarrow 2_0 \rightarrow 4_1$ (panel (b)). Again this fact reflects the complicated dependence of the observed PAD on many factors, so although β_{60} values can only arise via scattering for even-l it is not necessarily the case that all PADs correlated with scattering will show significant β_{60} values.

The only example in this data of scattering correlated with odd-l is the $1_1 \rightarrow 2_0 \rightarrow 5_2$ ionizing transition. In this case the PAD shows much smaller β_{20} and β_{40} parameters than the average, but there are no direct conclusions which can be drawn from this single case. Further in-depth discussion of the PADs, and the dynamical parameters, will be presented in the following chapter.

7.6 $v_2 = 3$ Dataset

7.6.1 Rotational spectra

Photoelectron images recorded via pump transitions of the form $\widetilde{X}^1A_1'|v_{2(g)} = 0, J_{gK_g}\rangle \rightarrow \widetilde{B}^1E''|v_{2(i)} = 3, J_{iK_i}\rangle$, using $\lambda_{probe} = 431.3$ nm, allowed population of $\widetilde{X}^2A_2''|v_{2(+)} = 3, N_{+K_+}\rangle$ upon ionization. The raw images are shown in Figure 7.14. Because fewer intermediate states could be accessed, due to symmetry restrictions, only five pump transitions were used (as opposed to six in the $v_2 = 4$ data discussed above). At the time of writing this data is yet to be fully analysed, but a brief overview of the experimental spectra and PADs is presented here.

Figure 7.15 shows the spectra obtained from the photoelectron images. For $v_{2(+)}$ =odd and $\Delta v = 0$ the accessible rotational levels are the same as for $v_{2(+)}$ =even and $\Delta v = 0$, with the exception of *ortho*-NH_3^+ for which the allowed $K_+ = 0$ levels differ. In this case parity restrictions mean that only N =odd levels are allowed, as opposed to N =even for $v_{2(+)}$ =even. The expectation, therefore, is that for cases where the same rotational transitions can be accessed as for $v_{2(i)}$ =4, the rotational spectra will look similar unless there has been a significant change in the ionization dynamics between the two vibrational levels. Figure 7.15(b) and (d) can be compared directly with Figure 7.11(a) and (c). The former case shows the $1_1 \rightarrow 3_2$ transition, the latter $1_1 \rightarrow 2_2$.

For the $1_1 \rightarrow 3_2$ data the spectra are near identical. The only noticeable difference is the overlapped $3_1 + 4_1$ feature, which is slightly more intense in the $v_{2(+)}$ =3 data. For the $1_1 \rightarrow 2_2$ pump transition the 2_1 and 4_4 features are slightly less intense in the $v_{2(+)}$ =3 case, and the 4_1 feature slightly more intense. A more quantitative comparison of the branching ratios has yet to be made, but the magnitude of these changes suggests

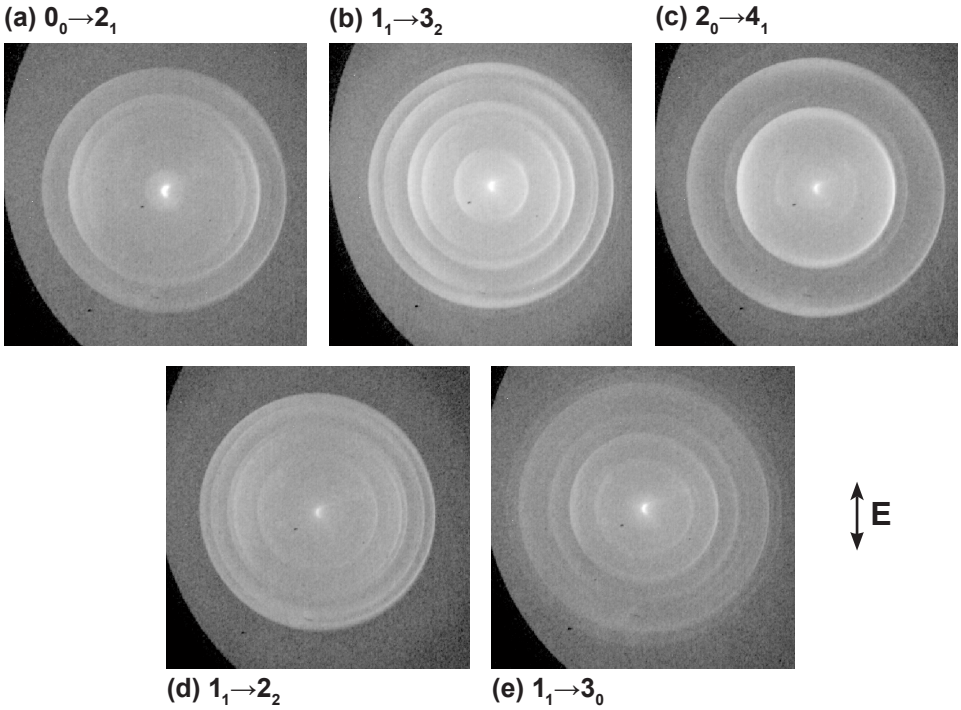

Figure 7.14: Raw photoelectron images for pump transitions $\widetilde{X}^1A_1'|v_{2(g)} = 0, J_{gK_g}\rangle \rightarrow \widetilde{B}^1E''|v_{2(i)} = 3, J_{iK_i}\rangle$ and $\lambda_{probe} = 431.3$ nm.

that there is only a small change in the ionization dynamics between the two cases.

One inconsistent result of the spectra shown here are the incompatibility of the rotational assignments for Figure 7.14(e). This spectrum corresponds to *para*-NH_3^+, so only the rotational levels labelled in the figure can be populated. However, using the same calibration as the other spectra presented in Figure 7.15, the features in the spectrum do not match well with the known line positions. One possibility is that a different calibration factor is required for this data, but as all of the data shown was recorded over a two day period with identical experimental conditions it is unclear why this should be the case. Another possibility is that the $1_1 \rightarrow 3_0$ pump transition assigned in the REMPI spectrum (Figure 7.3(a)) contained a significant contribution from another rotational transition. If this were the case then the photoelectron image recorded would contain contributions from two intermediate rotational levels, and this could lead to more observed features in the spectrum. Depending on the nature of the overlapped pump transition, the final spectrum may contain contributions from both *ortho* and *para*-NH_3^+, and show population of more ion rotational levels than could be accessed from a single intermediate level. Additionally, a second pump component might require different energy calibration upon conversion to E_{ion} to take into account a different intermediate state rotational energy. Because the spectrum in Figure 7.14(e) shows many rotational features, it seems likely that a blended pump transition is the source of the difficulty in assigning this spectrum. A candidate for the second intermediate level has yet to be found however.

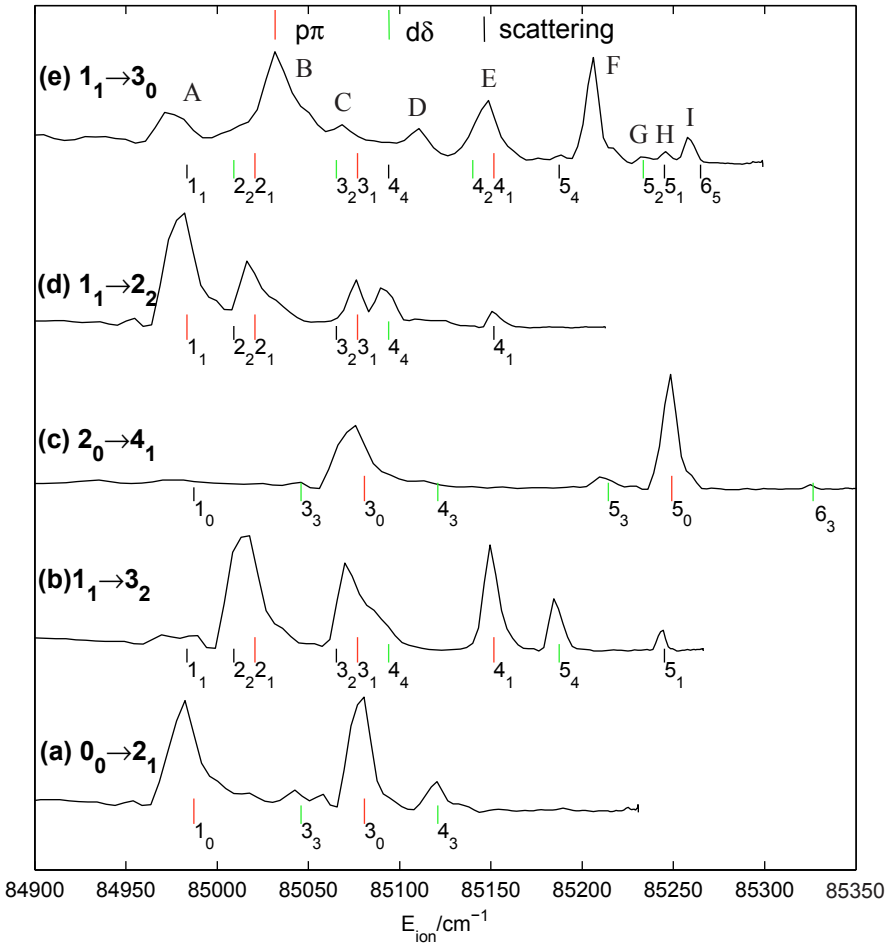

Figure 7.15: Photoelectron spectra extracted from the images shown in Figure 7.14, for pump transitions $\tilde{X}^1A_1'|v_{2(g)} = 0, J_{gK_g}\rangle \rightarrow \tilde{B}^1E''|v_{2(i)} = 3, J_{iK_i}\rangle$ and $\lambda_{probe} = 431.3$ nm. Rotational assignments are shown, long red lines and shorter green lines represent levels accessible from the $p\pi$ and $d\delta$ Rydberg components, respectively, in the no-scattering case. Short black lines represent rotational levels which can only be populated via scattering of the Rydberg or photoelectron as discussed in the main text. For (e) rotational assignments have not been successful, peaks are instead labelled A-I for reference.

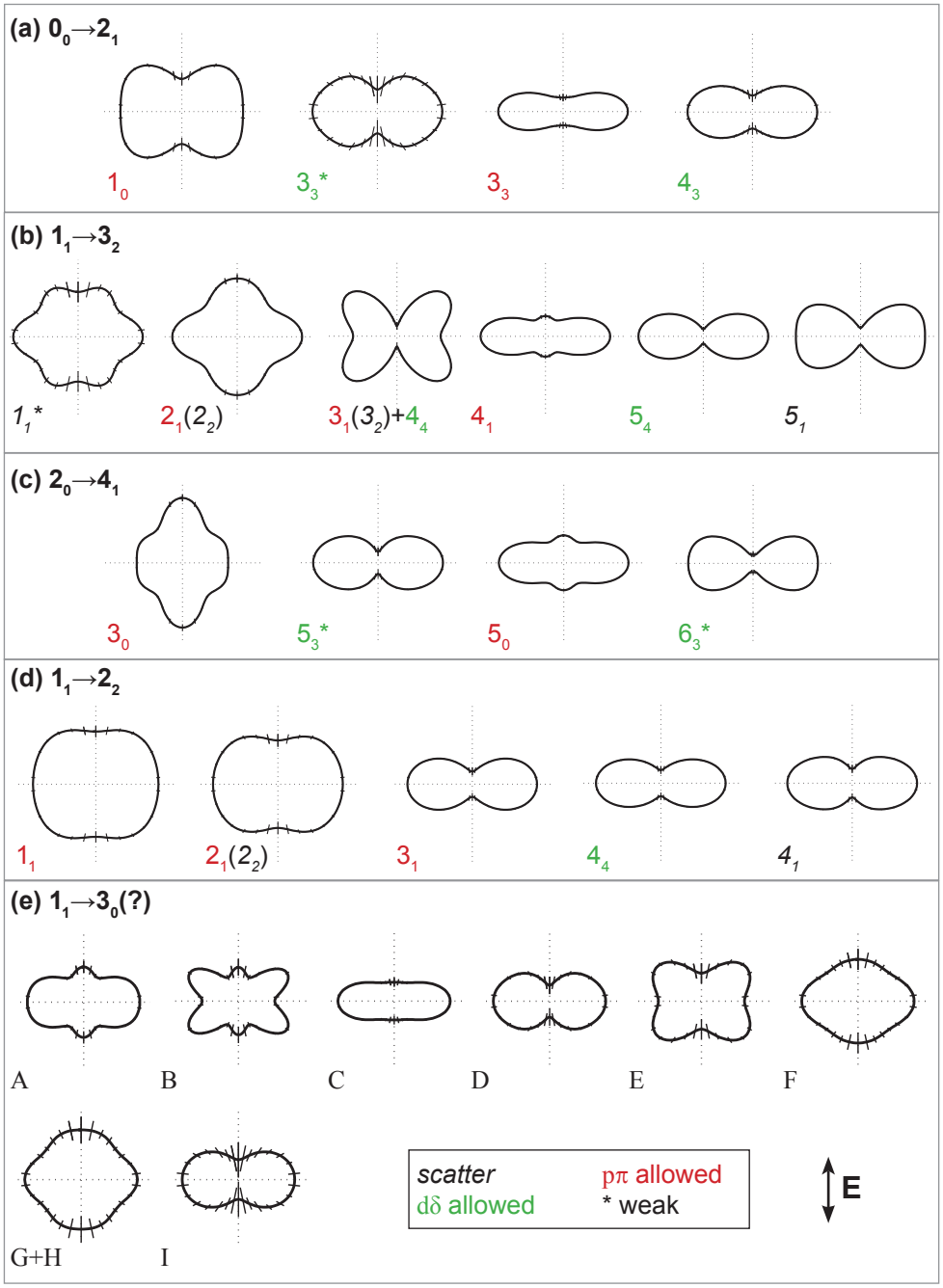

Figure 7.16: Photoelectron spectra extracted from the images shown in Figure 7.14, for pump transitions $\widetilde{X}^1A_1'|v_{2(g)} = 0, J_{gK_g}\rangle \rightarrow \widetilde{B}^1E''|v_{2(i)} = 3, J_{iK_i}\rangle$ and $\lambda_{probe} = 431.3$ nm.

7.6.2 PADs

PADs obtained from the $v_{2(+)} = 3$ images are shown in Figure 7.16. The PADs arising from pump transitions $1_1 \rightarrow 3_2$ (b) and $1_1 \rightarrow 2_2$ (d) can be compared with the same rotational pump transitions for the $v_{2(+)} = 4$ data, as shown in Figure 7.12(a) and (c). In the former case there is little change in the PADs between the two cases, with the exception of the PAD correlated with the 1_1 level. Population of this level involves scattering, and the feature in the spectrum is weak. Two conclusions could be reached from this, firstly that the scattering features may be more sensitive to small changes in the ionization dynamics; secondly, that the change in the PADs might be little more than a consequence of the large uncertainty in the PAD in the case of weak features in the photoelectron image.

For the $1_1 \rightarrow 2_2$ pump transition there are significant differences in the PADs for the formation of 1_1 and 2_1, and the scattering feature 4_1. In the first two cases the corresponding features in the spectrum are all strong, so the PADs are reliable in both datasets. The 4_1 feature is more intense in the $v_{2(+)} = 3$ data, so the PAD shown in Figure 7.16(d) correlated with this transition is likely to be more reliable than that shown in Figure 7.12(c). In particular the 4_1 PAD does not show a large β_{60} contribution in this dataset, unlike the equivalent PAD for the $v_{2(+)} = 4$ data. This is consistent with the previous discussion of the significance of β_{60} values in the PADs which are extracted from weak features in the spectrum (Section 7.5.2), and again most likely shows that the PAD extracted from the $v_{2(+)} = 4$ data has larger uncertainties than suggested by the error bars. Despite the possibly spurious 4_1 PAD in the $v_{2(+)} = 4$ data, the changes in the 1_1 and 2_1 PADs lead to the conclusion that there are some small changes in the photoionization dynamics between the two vibrational states.

Comparison of the rotational spectra and the PADs for the $1_1 \rightarrow 3_2$ and $1_1 \rightarrow 2_2$ pump transitions for $v_{2(i)} = 3$ and $v_{2(i)} = 4$ thus leads to the same conclusion, namely that there are some small changes in the photoionization dynamics between the two datasets. This data appears sensitive enough to reveal a vibrational dependence of the ionization dynamics, an effect which is expected to be small for the ionization of Rydberg states. The fact that only some of the rotational features in the spectrum, and associated PADs, appear sensitive to these changes suggests that any differences are small, and may only be reflected in certain $|l\lambda\rangle$ components.

7.7 Probe Wavelength Revisited

During the initial stages of this work images were recorded at many different λ_{probe}, over the range 420 - 434 nm, in order to optimise the experimental set-up for rotational resolution, and this work was discussed in Section 7.4.2. Later in the experimental run more careful studies were made over the range $\lambda_{probe} = 430.9 - 434$ nm, with the aim of obtaining data which could probe the effect of photoelectron kinetic energy on the dynamical parameters. Some of this data is briefly discussed here, although further work is needed before any final conclusions can be drawn.

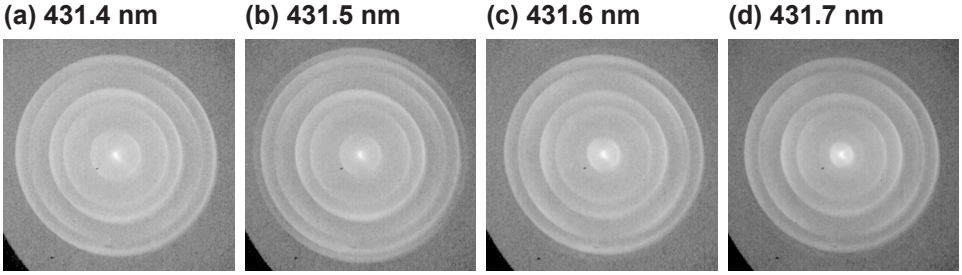

Figure 7.17: Raw images recorded at different λ_{probe}.

Figure 7.18 shows a selection of spectra obtained from images with different probe wavelengths. The total change in the photon energy across these spectra is 16 cm^{-1}. Over this range the dynamical parameters would not be expected to change significantly (see discussion in Section 4.3.1), with the exception of any resonant behaviour. The main features in the spectra, 2_1 and 4_1, do stay consistent in intensity over the range. On the other hand, significant changes are observed in the 1_1 and 3_1 features. In Figure 7.18(b) the 1_1 feature is markedly more intense, while the 3_1 feature is significantly more intense in spectrum (c). This behaviour was reproducible, and a similar increase of intensity in the 1_1 feature was also observed at λ_{probe} =431.2 nm. The increase in intensity can also be seen in the raw images, shown in Figure 7.17, where an extra ring is visible at the outer edge of the image recorded with λ_{probe} =431.5 nm.

These changes indicate that there is indeed some kind of resonant behaviour in this region, which may be attributed to a scattering resonance or the population of Rydberg levels, which converge on higher-lying ion levels but autoionize to form levels in the region under study [7, 30]. Further work is planned to examine this behaviour in more detail.

No significant changes were observed in the PADs as a function of λ_{probe}, with the exception of the PAD correlated with the 1_1 feature. As discussed in Section 7.6.2, changes in the PADs correlated with the weak 1_1 feature may be misleading. However, given the significant change in intensity in the rotational spectra, significant changes in the PAD correlated with this feature are expected [86]. Although the 3_1 feature also changes in intensity in the spectra shown in Figure 7.18, the corresponding PADs do not show significant changes. Again, further work is needed to draw firm conclusions from these observations, although the consistency of the PADs correlated with features which display no resonance behaviour in the spectrum reinforces the assertion that, in the absence of such resonances, the photoionization dynamics do not change over this wavelength region.

A final point of note on the spectra shown in Figure 7.18 is the apparent movement of the 5_1 feature in energy space as λ_{probe} increases. This is an artefact of the image processing and energy calibration procedure. Because of the $r^2 \rightarrow E$ mapping, data extracted from small r will be more sensitive to any errors in the energy calibration and, as mentioned previously, extra care must be taken with data from near the centre of the image.

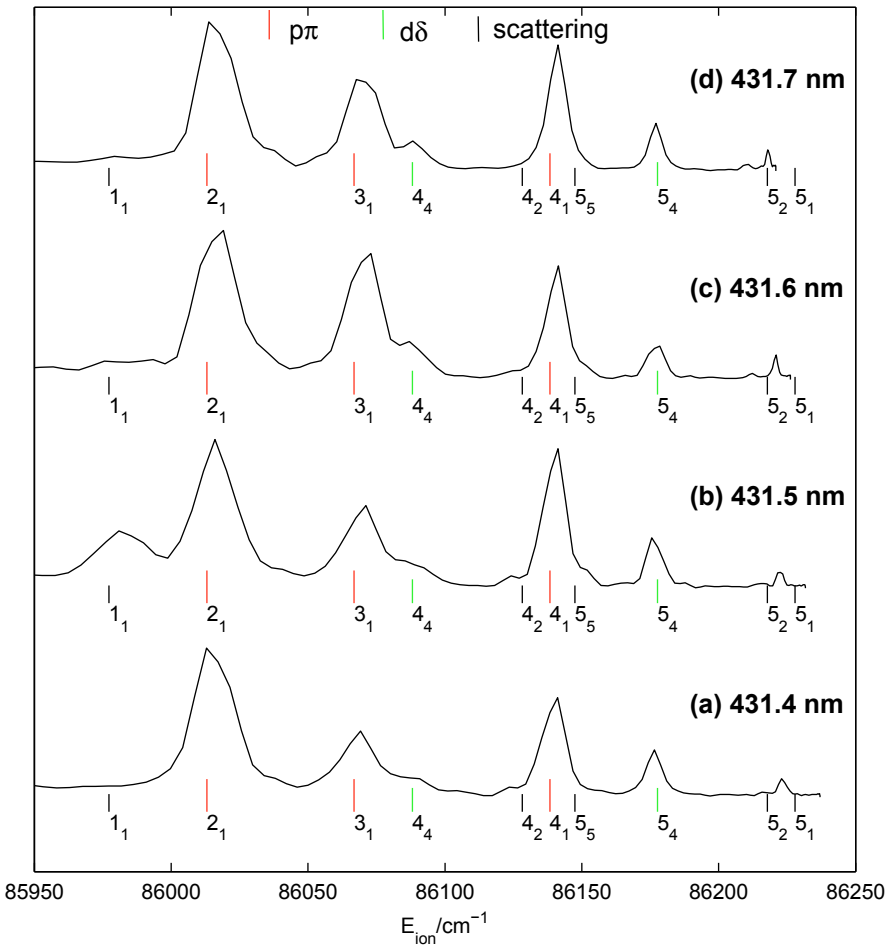

Figure 7.18: Spectra recorded at different λ_{probe}.

7.8 Conclusions

The experimental work presented in this chapter has demonstrated that rotational resolution can be achieved in VMI, and PADs correlated with the formation of individual ion rotational levels can be obtained with this technique. These PADs show a wide variety of forms, and provide extensive data which is suitable for analysis using partial wave decomposition techniques. Such an analysis is presented in the following chapter for the $v_2 = 4$ dataset. Rotational spectra, and the associated PADs, recorded via different intermediate vibrational levels revealed small changes in the ionization dynamics, and also highlight the sensitivity and wealth of information obtained experimentally. Data recorded for different probe wavelengths showed the presence of resonant behaviour in the ionization dynamics, but further work may be required to determine the exact nature of this behaviour.

Chapter 8

Ammonia II: Discussion & Partial Wave Analysis

In this chapter the photoionization dynamics of ammonia ($\widetilde{B}^1E''$) are investigated, based on the data presented in Chapter 7. Discussion of modelling of the scattering dynamics is presented, followed by further discussion of the $v_{2(i)} = 4$ data which was presented in Section 7.5. The rotational spectra are compared with previously reported ZEKE and MATI results, which may exhibit subtle differences in ionization dynamics. The partial wave decomposition of the ionization continuum is applied to analyse the dynamics quantitatively, and radial dipole matrix elements and phases are determined for ionization from $v_{2(i)} = 4$.

8.1 Application of Photoionization Theory to NH_3

8.1.1 Rotational spectator model

As a starting point the $\tilde{B}$-state can be treated as a Rydberg state and the rotational spectator approximation applied [31, 94]. This approximation was briefly outlined in the previous chapter (Section 7.1.4), and applied as an intuitive, zero-order model in discussion of the experimental data. In this description there is a single active Rydberg electron which is decoupled from the molecular core. Upon ionization the incident photon interacts with only this electron, so the angular momentum of the photon is coupled only to the photoelectron. In this model ionization is thus "atomic", there is no scattering of the outgoing photoelectron and the selection rules are the same as those for atomic ionization, $\Delta l = \pm 1$. In such a model the angular momentum coupling is described by:

$$\begin{aligned} C(lm\lambda M_i M_i^C \mu_\lambda) &= (-1)^{\mu_\lambda} \begin{pmatrix} N_i^C & l_{Ryd} & N_i \\ M_i^C & m_{Ryd} & -M_i \end{pmatrix} \begin{pmatrix} l & 1 & l_{Ryd} \\ -m & 0 & m_{Ryd} \end{pmatrix} \\ &\times \begin{pmatrix} N_i^C & l_{Ryd} & N_i \\ K_i^C & \lambda_{Ryd} & -K_i \end{pmatrix} \begin{pmatrix} l & 1 & l_{Ryd} \\ -\lambda & \mu_\lambda & \lambda_{Ryd} \end{pmatrix} \end{aligned} \tag{8.1}$$

Here the angular momentum of the prepared $\tilde{B}$-state rotational level, $|N_i K_i M_i\rangle$, is decoupled into a Rydberg electron, $|l_{Ryd}\lambda_{Ryd}m_{Ryd}\rangle$, and a molecular core $|N_i^C K_i^C M_i^C\rangle$. The decoupled molecular core is the nascent ion core in the rotational spectator model, hence:

$$\begin{aligned} N_i^C &= N_+ \\ K_i^C &= K_+ \\ M_i^C &= M_+ \end{aligned} \tag{8.2}$$

The Rydberg electron interacts with the incident photon, $|1\mu_\lambda 0\rangle$, upon ionization, and the photoelectron is described by $|l\lambda m\rangle$. The first two $3j$ symbols in equation 8.1 describe the lab frame coupling, while the second pair of $3j$ terms describe the molecular frame coupling. Angular momentum selection rules for photoionization in this coupling scheme can be extracted from these $3j$ terms, in particular:

$$\begin{aligned} \Delta N &= N_i - N_i^C = l_{Ryd}, l_{Ryd}-1, ..., -l_{Ryd} \\ \triangle K &= K_i - K_i^C = \lambda_{Ryd} \\ \Delta M &= M_i - M_i^C = m_{Ryd} \end{aligned} \tag{8.3}$$

These selection rules explicitly show how, in the rotational spectator coupling scheme, the rotational levels of the ion are determined by the character of the Rydberg electron in the $\tilde{B}$-state. Limits on N_+ and K_+ are therefore determined by $l_{Ryd} = 1, 2$ and $\lambda_{Ryd} = 1, 2$ for the $p\pi$ and $d\delta$ Rydberg components respectively, as given in the previous chapter (equations 7.4 and 7.5).[1] Similarly the angular momentum selection rules on the outgoing photoelectron partial-waves can be explicitly written from consideration of the relevant $3j$s and $\mu_\lambda = 0, \pm 1$:

$$\begin{aligned} l &= l_{Ryd}+1 \ldots l_{Ryd}-1 \\ \lambda &= \lambda_{Ryd}+1 \ldots \lambda_{Ryd}-1 \\ m &= m_{Ryd} \end{aligned} \tag{8.4}$$

8.1.2 Modelling scattering

Given that the $\tilde{B}$-state is an $n = 3$ Rydberg state, it may be expected that the simple, decoupled model presented above does not completely describe the ionization dynamics, and this was shown in the experimental data presented in the previous chapter by the presence of scattering features which would not be allowed in the rotational spectator model. Physically the Rydberg electron is likely to spend some time close to the molecular core, and thus experience the non-central (anisotropic) molecular potential. As mentioned previously (Section 7.1.2), in the core region l_{Ryd} and λ_{Ryd} are not good quantum numbers and in general a low-n Rydberg orbital would need to be expanded over many $|l_{Ryd}\lambda_{Ryd}\rangle$

[1] Although the terminology is slightly different this approach is very similar to the orbital ionization model described by Willitsch and Merkt [24].

terms to be well-described[2]; this electron-core interaction may be viewed in terms of angular momentum mixing or exchange. Symmetry restrictions placed upon this expansion showed that, for the $\tilde{B}$-state, only $p\pi$ and $d\delta$ components are expected to contribute significantly to the orbital character. The outgoing photoelectron will also experience the short range, anisotropic molecular potential, thus further scattering can occur during the ejection of the photoelectron. As before this reflects the fact that $|l\lambda\rangle$ are not good quantum numbers in this region; although the total angular momentum of the electron-ion system must be conserved there can be an exchange of angular momentum between the outgoing electron and the ion core. The one-electron wavefunction in this ion-core region can be described exactly by an *eigenchannel decomposition* of the continuum [93], which is closely related to the eigenchannel description of bound Rydberg electrons applied in MQDT (see Section A.2). Because the partial wave expansion is always valid asymptotically, the eigenchannel description is linked through a unitary transformation to the partial wave decomposition of the continuum. The treatments are thus equivalent, but provide physical insight into different parts of the problem and can be recognized as treating the same problem in either a close-coupled or asymptotic basis.

In modelling the ionization two different approaches could be employed depending on the assumptions made about the $\tilde{B}$-state. If the Rydberg character, as determined by ZEKE spectroscopy, is assumed to be accurate then one approach to modelling the ionization is to treat $|l_{Ryd}\lambda_{Ryd}\rangle$ as good quantum numbers and decouple the Rydberg electron from the core, as in the rotational spectator model. However, rather than assuming that there is no further interaction between the electron and the core upon ionization further coupling terms can be introduced to allow for scattering of the photoelectron. These terms are denoted N_t, K_t and M_t, signifying angular momentum transfer between the photoelectron and nascent ion core. Such a scheme is briefly discussed by D. Townsend [31], but it is not developed further. Although this may in principle provide a good description of the ionization process, and allow for both direct $(N_t, K_t = 0)$ and scattering $(N_t, K_t > 0)$ ionization processes, it does rely on a well-determined Rydberg character and a sequential ionization event.

A more general model can also be posited where the Rydberg character is not assumed, and *no assumptions about the intermediate state character are required*. In this case the coupling is the same as that described in Section 2.3, excluding spin. Angular momentum transfer terms are again used, but in this case there is no decoupling step into $|l_{Ryd}\lambda_{Ryd}\rangle$ and $|N_{Ryd}K_{Ryd}\rangle$, hence there is direct coupling between $|N_iK_i\rangle$ and $|N_+K_+\rangle$ and the overall angular momentum exchange between excitation and ionization is described. This scheme is advantageous in that no assumptions about $|N_{Ryd}K_{Ryd}\rangle$ need be made, and the coupling scheme still only requires four $3j$ terms. The disadvantage of this scheme is that it does not present such an appealing physical picture of sequential preparation of a Rydberg state followed by ionization - it does not distinguish between coupling of the Rydberg electron to the core and coupling of the photoelectron to the core, although whether such a distinction is valid is a matter of debate. This general model is used in

[2]Equivalently, the low-n Rydberg electron is not purely described by Hund's case (d) coupling.

K_i	Γ^i_{rve}	K_+	Γ^+_{rve}	l
0, 2	E"	1	E'	e
		2	E"	o
		4	E"	o
		5	E'	e

K_i	Γ^i_{rve}	K_+	Γ^+_{rve}	l
1	A'_2	0	A"$_2$	e
		3	A'_2	o
		6	A"$_2$	e

Table 8.1: Allowed partial wave parity (even/odd) for observed transitions with $v_{2(+)} = v_{2(i)} = 4$. (Left) *para*-NH_3, (right) *ortho*-NH_3.

this work and, as shown later, provides a good fit to the experimental results.

8.1.3 General symmetry selection rules

As discussed in Section 2.4, the application of symmetry rules places further strict limitations on the partial wave symmetries which are allowed in the photoelectron wavefunction. For ionization of ammonia from the $\tilde{B}$-state symmetry rules have been derived by several authors [27, 30, 31, 142]; in particular Signorell and Merkt [142] derived general rules for ammonia, based on equations 2.58 and 2.59. The application of these rules to ionizing transitions with $\Delta v_2 = 0$ and even-v_2, as applicable to the data analysed here, yields the rules shown in Table 8.1 (see also Figure 7.2). The key result here is that for the formation of a given K_+ level only odd- or even-l are allowed. Transitions which are $p\pi$-allowed in the atomic model correlate with even-l, and transitions $d\delta$-allowed correlate with odd-l.

8.2 Phenomenological Discussion of Scattering

8.2.1 Scattering features

In the spectra presented in Section 7.5 (recorded via $v_{2(i)} = 4$) there are a total of nine resolved features which arise from scattering. These features are listed in Table 8.2. In eight of these cases $\triangle K = \pm 1$; the exception is the $1_1 \rightarrow 2_0 \rightarrow 5_2$ ionizing transition for which $\triangle K = 2$. As shown in Table 8.1, for $v_{2(+)} = 4$ and *para*-NH_3, population of levels with $K_+ = 1$ must involve ionization to the even-l continuum, and population of $K_+ = 2$ ionization to the odd-l continuum. For *ortho*-NH_3, population of levels with $K_+ = 0$ must involve ionization to the even-l continuum. The eight scattering channels observed here with $\triangle K = \pm 1$ therefore all correlate with ionization to the even-l continuum, and only one scattering channel is correlated with odd-l. However, the assignment of the 5_2 feature may be incorrect (see Section 8.3.1); if so, this feature is actually assigned as 5_1, which would also correlate with even-l and $\Delta K = 1$.

In all cases the observed ΔN are only 1 or 2 units of angular momentum greater than those allowed in the atomic model (equations 7.4 and 7.5), and the observed ΔK are the same as those expected in the atomic model. The probability amplitude for angular momentum transfer is calculated from the angular momentum coupling factors discussed in Sections 2.3 and 8.1. A general observation of such coupling schemes is

Spectrum	Pump transition	Assignment	$\triangle N$	$\triangle K$	Intensity	l
a	$1_1 \rightarrow 3_2$	1_1	2	1	vw	e
		5_1	2	1	w	e
b	$1_1 \rightarrow 2_0$	4_1	2	1	m	e
		5_2*	3	2	w	o
c	$1_1 \rightarrow 2_2$	4_1	2	1	w	e
d	$1_1 \rightarrow 1_0$	3_1	2	1	m	e
		4_1	3	1	w	e
e	$1_0 \rightarrow 3_1$	0_0	3	1	vw	e
f	$1_0 \rightarrow 1_1$	4_0	3	1	s	e

Table 8.2: List of rotational features which arise from scattering. Spectrum labels correlate with Figure 7.11. Observed intensities are denoted vw - very weak; w - weak; m - medium; s - strong. Correlation with odd/even-l is also shown. 5_2 assignment may be incorrect, see discussion in main text.

that large transfers of angular momentum are less probable than small transfers, this is a consequence of angular momentum wavefunction overlap. Thus ionizing transitions with very large ΔN will have small geometrical factors and, assuming that the partial wave expansion is truncated at low l, will result in negligible matrix elements.

For even-l the allowed K_+ scattering channels ($K_+ = 5$ for *para*, $K_+ = 6$ for *ortho*, see Table 8.1) are only accessible by large ΔK processes and, by the same rationale applied to large ΔN scattering processes, the probability of large ΔK scattering may be expected to be small. For odd-l smaller ΔK scattering events are symmetry allowed, in particular processes with $\Delta K = 0$ are allowed for ionization from $K_i = 2$ levels (*para*-NH_3). The geometrical factors for these events might be expected to be more significant, but such scattering events were not observed in the experimental spectra. This is, however, not a definitive statement that they are not present because they may underlie more intense features in the spectrum (see Figure 7.5.1 and Table 7.1, also the fitted spectrum in Figure 4.5), and have been observed as very weak features in ZEKE [28] and MATI [30] spectra (see Section 8.2.2 for further comparison of these spectra).

All of the scattering features observed are weak, with the exception of the $1_0 \rightarrow 1_1 \rightarrow 4_1$ case (row (f) in Table 8.2). This feature is considerably more intense than any of the other ionizing transitions associated with scattering, and there is no obvious reason why this should be the case. It is possible that there is some kind of resonant enhancement of this feature at $\lambda_{probe} = 431.3$ nm, similar to the phenomena seen in the data presented in Section 7.7, but no data was obtained with different λ_{probe} so this remains speculative.

To summarize, the data shows many instances of scattering which changes ΔN, but no ΔK scattering (within the caveats mentioned above). The scattering features all correlate with even-l, with one possible exception. This appears to support a step-wise ionization picture, where the dominant $p\pi$ character in the $\tilde{B}$-state correlates directly with the even-l continuum, and the outgoing photoelectron is scattered within this continuum. Any even/odd l-mixing would be expected to produce more intense odd-l channels, and

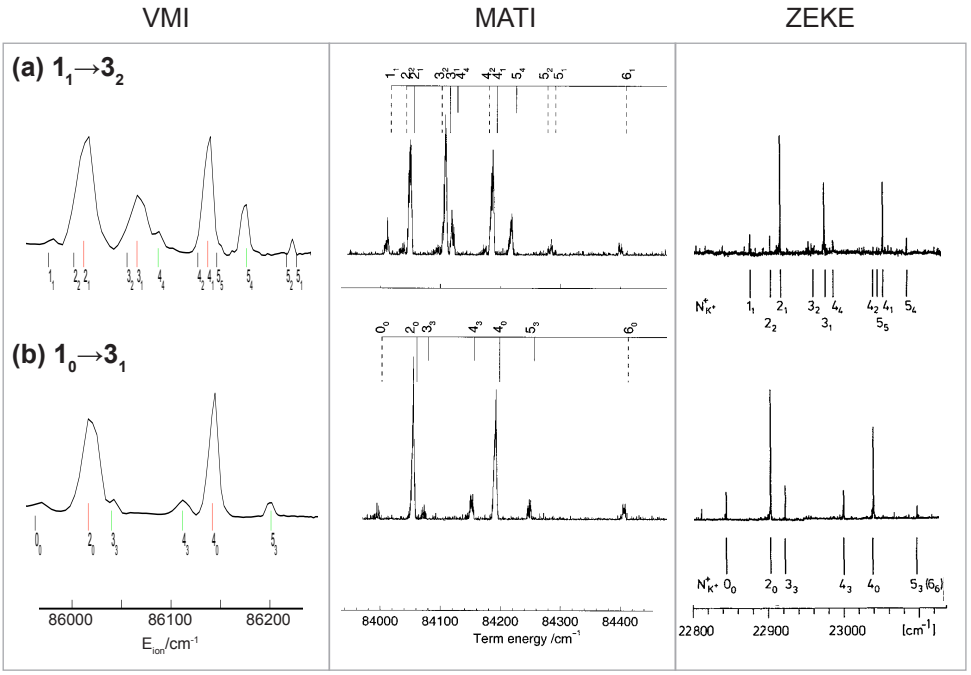

Figure 8.1: Comparison of spectra obtained from imaging, MATI (reproduced from ref. [30]) and ZEKE (reproduced from ref. [28]) for (a) $1_1 \rightarrow 3_2$ and (b) $1_0 \rightarrow 3_1$ pump transitions. Energy scales are reproduced from the source articles. The MATI & ZEKE spectra are recorded via $\tilde{B}|v_2 = 2\rangle$ and so are shifted relative to the imaging data recorded via $\tilde{B}|v_2 = 4\rangle$; rotational level spacing will also be slightly different. As shown in ref. [30] there is little change in rotational line intensities between spectra recorded via $v_2 = 2$ and $v_2 = 4$.

the $p\pi : d\delta$ ratio of the $\tilde{B}$-state character would not be expected to be reflected directly in the continuum.

8.2.2 Comparison with ZEKE/MATI spectra

It is instructive to compare the rotationally resolved spectra with ZEKE [28] and MATI [30] results. Comparison with these very high resolution techniques provides another method of verifying the peak assignments discussed in Section 7.5.1, and should also show whether weak features, which may not be resolved in the photoelectron images, may be present. Another question which may be at least partly addressed by such comparisons is how the different ionization paths in these techniques affect the dynamics.

Reproduced in Figure 8.1 are VMI, MATI [30] and ZEKE [28] spectra for two pump transitions. Overall there is reasonable agreement between the spectra, but there are also some interesting differences between them. Note that the MATI & ZEKE spectra are recorded via $\tilde{B}|v_2 = 2\rangle$ and so are shifted relative to the imaging data recorded via $\tilde{B}|v_2 = 4\rangle$; rotational level spacing will also be slightly different. As shown in ref. [30] there is little change in rotational line intensities between spectra recorded via $v_2 = 2$ and $v_2 = 4$.

The general conclusion from these spectra is that the same features are observed in all

cases, with the additional observation in the MATI data of higher-lying rotational levels (6_0, 6_1) which were not energetically accessible in the imaging experiments with $\lambda_{probe} = 431.3$ nm (although the 6_1 level was tentatively assigned in the spectrum recorded at $\lambda_{probe} = 425$ nm, as discussed in Section 7.4.2). Both the MATI and ZEKE spectra for the $1_1 \rightarrow 3_2$ case also show evidence of $K_+ = 2$ features, which arise from $\Delta K = 0$ ionizing transitions. As expected these are weak features in the spectra and, although they are not resolved in the imaging data, would not make significant contributions to the PADs extracted from the images.

The intensity ratios between the features are however very different in the three cases. For the $1_1 \rightarrow 3_2$ pump transition (Figure 8.1(a)) the most intense feature in the MATI spectrum is 3_1, while it is the least intense $p\pi$ allowed feature in the equivalent ZEKE and VMI results. In the VMI spectrum the 2_1 and 4_1 features are of almost equal intensity; the same features are of slightly different intensities in the MATI spectrum, and very different intensities in the ZEKE results. The 5_4 feature is much less intense in the ZEKE spectrum than in the VMI or MATI data. The spectra recorded via the $1_0 \rightarrow 3_1$ pump transition (Figure 8.1(b)) show fewer differences, although there are again significant changes in the intensities of the $p\pi$ allowed features; the 0_0 scattering feature is also considerably more intense in the ZEKE spectrum.

A more quantitative analysis is complex as it requires detailed understanding of the ionization pathways in the different cases. The VMI data might be considered to represent "direct", near-threshold photoionization as outlined in Section 2.3. The intensity distribution observed experimentally thus depends on the ionization matrix elements which describe the coupling of the initially prepared state to the ionization continuum.[3] The ionization process in the ZEKE & MATI techniques is the same (see Section 1.2.2), and involves photoexcitation to high-n Rydberg levels which undergo l-mixing to form long lived ZEKE states and are field-ionized (after a time delay) to produce the ZEKE signal. As described in Section 1.2.2 there are many factors which can influence the intensities seen in these experiments, and these involve both experimental conditions and inherent molecular properties. Differences in the observed intensities between ZEKE studies are therefore not surprising as the experimental conditions will be different, and differences between ZEKE and direct photoionization are also to be expected. Allowing for these considerations, the comparison of the results in Figure 8.1 suggests that the ionization dynamics are very similar in ZEKE and direct, near-threshold ionization. The qualitative picture of ionization from the $\tilde{B}$-state described by just two angular momentum components, and atomic-like propensity rules, still gives a good first approximation to the spectra. The implication here is that the rotational spectator ionization model is actually surprisingly good and models the dominant behaviour in both the ZEKE and direct photoionization processes. The strict symmetry selection rules on both the $\tilde{B}$-state character and the ionization channels are most likely responsible for the success of this simplified

[3] Additional perturbations to the ionization dynamics (or the free photoelectron wavefunction) may occur due to the **E**-fields in the ionization region, such effects are still a matter of debate but given the similarity of the spectra in this case, and the evidence of previous work in the group comparing field-free ToF and VMI results [35], it is not thought to be a significant issue in these results. It is still an intriguing question to explore, but one which is saved for future work.

description.

8.3 Extraction of Ionization Dynamics ($v_2 = 4$)

A quantitative determination of the dynamical parameters has been made from the data recorded via $\widetilde{X}^1A_1'|v_{2(g)} = 0, J_gK_g\rangle \rightarrow \widetilde{B}^1E''|v_{2(i)} = 4, J_iK_i\rangle$ pump transitions (Section 7.5) with $\lambda_{probe} = 431.3$ nm, using the fitting methodology detailed in Section 4.3. Results of the fit, and further discussion, are presented here.

8.3.1 Fit results

Fitted PADs are shown in Figure 8.2, and rotational spectra calculated from the fitted parameters in Figure 8.3. Experimental and calculated results are shown for all six pump transitions employed. The final fit conditions were as follows:

- All of the experimental data was used in the fit (28 PADs).
- PADs were intensity weighted, but the peak intensities were not fitted directly (i.e. $\beta_{00} = 1$).
- $l_{max} = 4$

These conditions were arrived at by following the systematic approach described in Section 4.3. In particular it was found that the fitting algorithm produced slightly better results when peak intensities were not fitted directly; this is because the large values for the peak intensities relative to the β-parameters tended to dominate the fit, skewing the fit in favour of accurate peak intensities at the expense of well-fitted PADs.[4] Weighting the PADs by peak intensities was a better approach as this still allowed the most intense features in the spectrum to make a larger contribution to χ^2, but not at the expense of PAD fitting.

Initial fitting was performed for $l_{max} = 3$. From angular momentum coupling $\Delta N_{max} = l + 1$, so $l_{max} = 3$ can describe all of the rotational peaks seen in the spectra, but satisfactory fits to the data could not be attained with $l_{max} = 3$. As discussed in Section 7.5.2, $l = 4$ is required to allow for the non-zero β_{60} contribution to some of the PADs associated with scattering of an even-l wave, and because destructive interference of partial waves can lead to near-zero intensities for large ΔN that are otherwise allowed by angular momentum coupling (see Section 4.3) the rotational spectra alone cannot rule out $l = 4$ terms. Fitting was therefore performed with $l_{max} = 4$, and also tested with $l_{max} = 5, 6$. It was found that, as expected, the PADs could still be well-fit setting $l_{max} = 5$ or 6. However, the intensities of $\Delta N > 3$ features in the calculated spectra were found to be very large in these fits, and this was the case even when intensities were directly fitted and set to zero for unobserved transitions, thereby weighting the fitting algorithm towards

[4] This problem may have been circumvented by weighting the β_{LM} and peak intensities differently in the fit, but this was not tried.

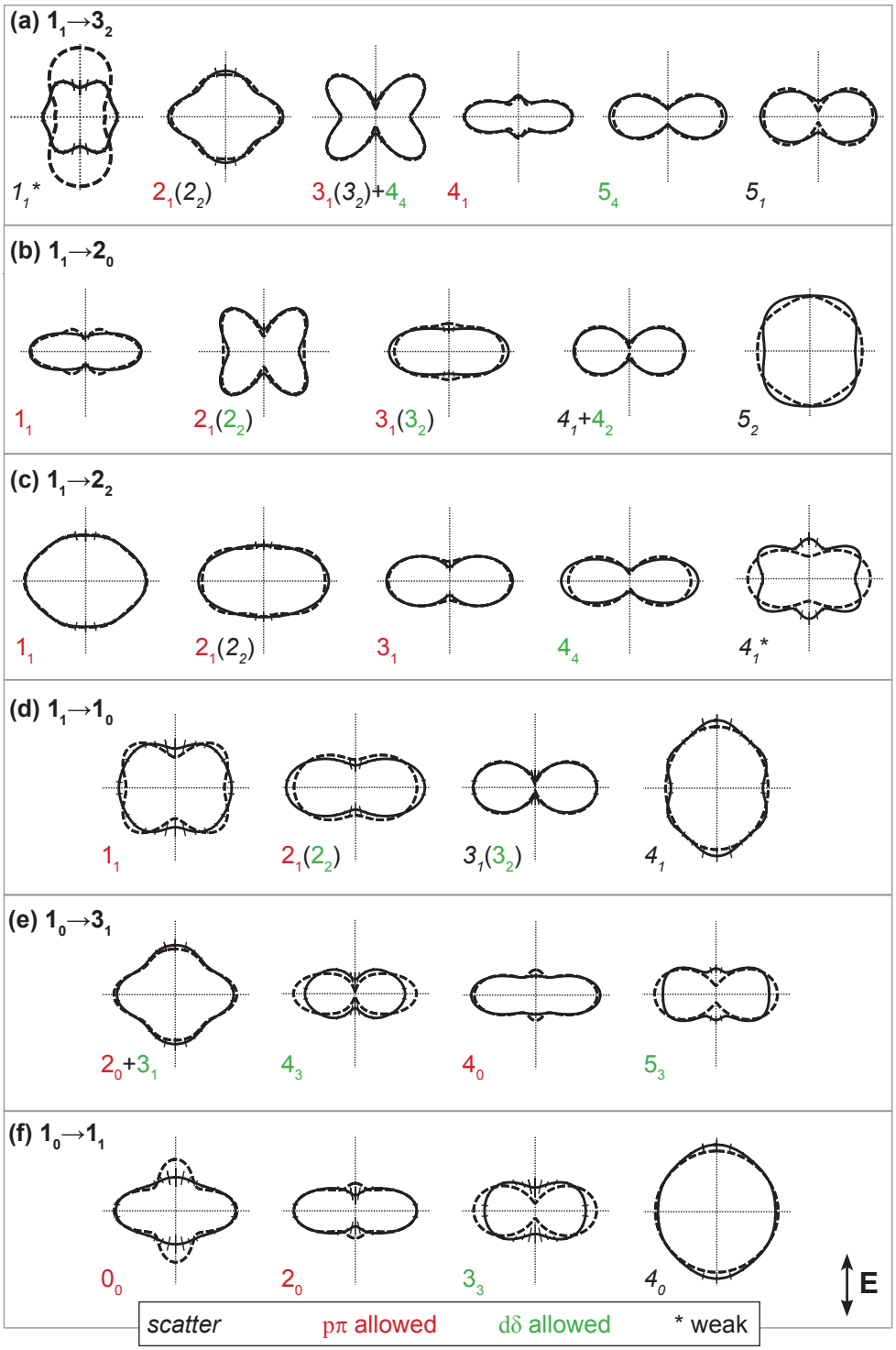

Figure 8.2: Experimental (solid lines) & fitted (dashed lines) PADs for $|0, J_K\rangle \rightarrow |4, J_K\rangle$ pump transitions.

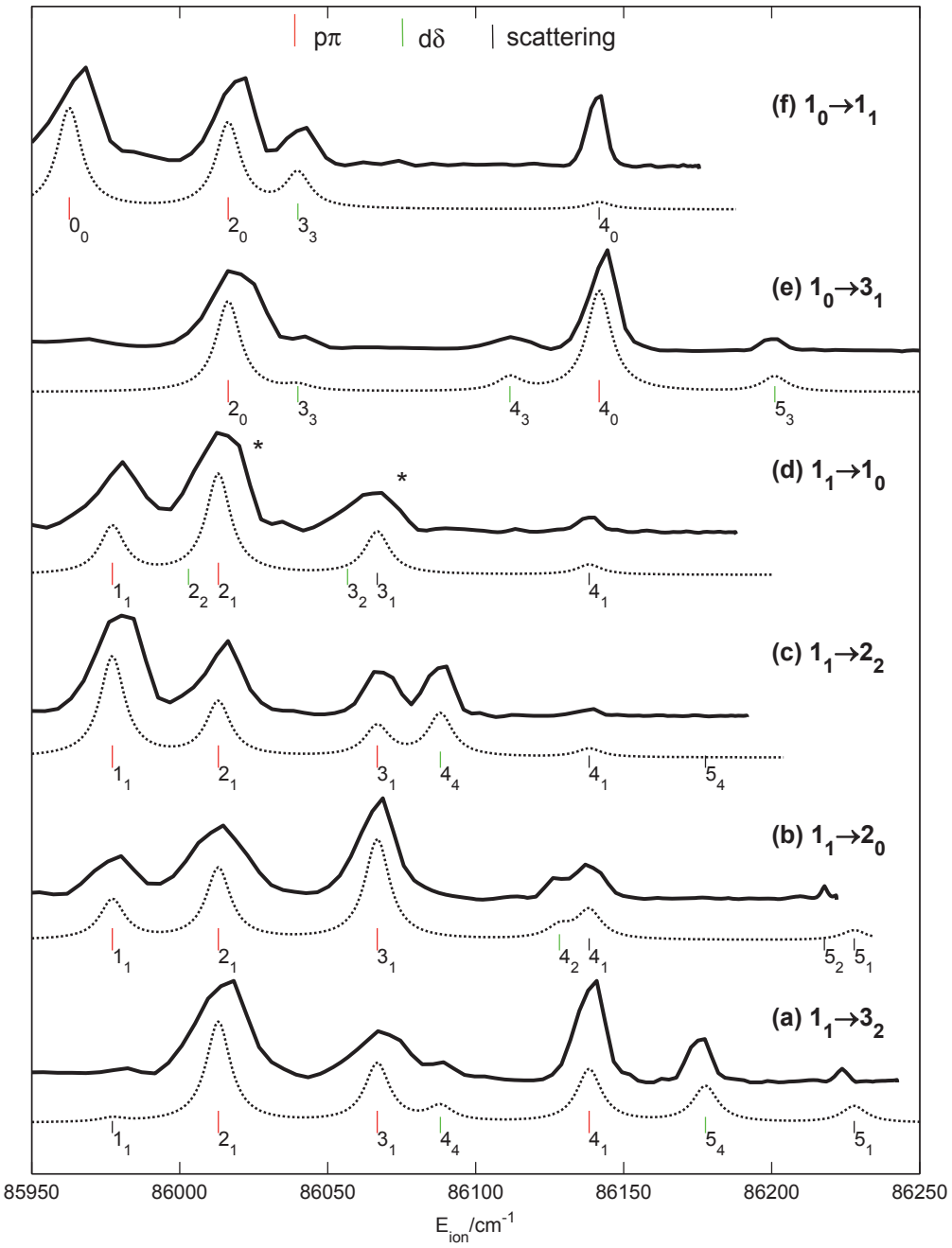

Figure 8.3: Experimental (solid lines) & calculated (dashed lines) rotational spectra for $|0, J_K\rangle \rightarrow |4, J_K\rangle$ pump transitions. Calculations made use of the fitted dynamical parameters listed in Table 8.3. All rotational features are plotted as Lorentzians, width 5 cm^{-1} (FWHM). Peaks marked * are comprised of two unresolved rotational features, but because the intensities of these features were summed before plotting the spectrum the peak profiles are not correct.

l	λ	$r_{l\lambda}$	$\eta_{l\lambda}$/deg	$r^2_{l\lambda}$/%	F_l/%
s	σ	0.357 (12)	0*	12.7 (17)	12.7 (17)
p	σ	-	-		13.0 (11)
	π	0.361 (8)	0*	13.0 (11)	
d	σ	0.137 (4)	31 (9)	1.9 (5)	53.0 (7)
	π	0.387 (2)	16 (3)	15.0 (3)	
	δ	0.601 (3)	149 (2)	36.1 (4)	
f	σ	-	-		10.7 (2)
	π	0.084 (1)	162 (3)	0.7 (1)	
	δ	0.143 (1)	153 (1)	2.1 (1)	
	ϕ	0.282 (1)	153 (1)	8.0 (1)	
g	σ	0.171 (7)	92 (9)	2.9 (10)	10.5 (17)
	π	0.276 (8)	64 (23)	7.6 (12)	
	δ	0.000 (5)	51 (169)	0.0	
	ϕ	-	-		
	γ	-	-		

Table 8.3: Fitted dynamical parameters. $r_{l\lambda}$ are normalized such that total x-section is unity. $r^2_{l\lambda}$ represent the partial x-sections for each $|l\lambda\rangle$ component, expressed as a percentage. F_l is the x-section for each l continua. Phases marked * are fixed as reference phases, one for even-l and one for odd-l. The phases are $\mathrm{mod}(360)$, the phase relationship between the odd and even continua, or the sign of the phases, cannot be deduced in this work. Components marked - are not allowed according to angular momentum coupling.

minimizing these features.[5] On the other hand, fits with $l_{max} = 4$ produced satisfactory results for both the fitted PADs and the calculated rotational spectra, leading to the conclusions that $l = 4$ terms were necessary, and that any $l > 4$ contributions can be assumed to be negligible. The sensitivity of the calculated rotational spectra to $l = 4$ contributions is discussed in Section 8.3.2.

As can be seen from Figures 8.2 and 8.3, the final results give a good fit to the PADs and rotational spectra across the whole dataset. The PADs arising from scattering and correlated with weak features (Figure 8.2(a)1_1, (c)4_1) are not so well fitted; this may be due to unreliable experimental PADs in some of these cases (see Section 7.5.2). The PADs correlated with the formation of the 0_0 and 3_3 levels shown in Figure 8.2(f) are also not quite so well fitted, but there are no obvious reasons for these discrepancies.

The rotational spectra are also well matched by the calculated spectra, with the striking exception of the 4_0 feature in Figure 8.3(f). In this instance there is significantly more scattering than observed in the other spectra. If this feature arises from a scattering resonance, as tentatively suggested in Section 8.2.1, the intensity would not be correctly modelled because the dynamical parameters are assumed to be constant over the dataset. The large difference between the calculated and recorded spectrum shown in Figure 8.3(f) corroborates this, but does not give any additional insight into the mechanism of the

[5] The same result was observed in the C_2H_2 work (Chapter 6), which also demonstrated that the presence of even a small percentage of high l in the photoelectron wavefunction can significantly change the calculated spectrum.

resonance. Also of note are the calculated intensities of the 5_1 and 5_2 features in Figure 8.3(b). Although the single feature in the experimental spectrum was previously assigned as 5_2, the calculated peak intensities suggest that it is in fact the 5_1 line, but appears at too low an energy in the spectrum due to calibration issues with data originating from near the centre of the photoelectron image - the same type of calibration artefact was illustrated in the data shown in Section 7.7, where the 5_1 feature was seen to move in energy space as it approached the centre of the image.

The final parameter set and associated uncertainties from the fitting are shown in Table 8.3. The magnitudes $r_{l\lambda}$ are normalized such that the total cross-section is unity. In this work only relative magnitudes can be determined because the absolute cross-section is not measured. The table also shows $r_{l\lambda}^2$, the relative cross-section for each $|l\lambda\rangle$ component, and the l-wave cross-section:

$$F_l = \sum_{\lambda} r_{l\lambda}^2 \tag{8.5}$$

Relative phases are split into even-l and odd-l because there is no interference between the two continua. In each case one phase is set to zero as a reference phase, and the final results are unsigned and $\mathrm{mod}(360)$.

Overall the d-wave dominates, with near equal contributions from the other allowed l-waves. The λ components of each wave show very different magnitudes; for the even-l continuum the phases of the λ components also show different phases, but for the odd-l continuum $\eta_{f\lambda}$ are similar and almost 180° out of phase with the p-wave. The considerable g-wave contribution would not be expected in the no-scattering model, and indicates that there is significant scattering of the outgoing photoelectron, as already suggested by qualitative analysis of the experimental results. The large uncertainties associated with the g-wave components arises because the PADs most sensitive to this contribution are those arising from scattering, which were also generally correlated with weak features in the spectrum and therefore large experimental errors. It should be noted that other PADs were also sensitive to the g-wave, so the possibility of spurious β_{LM} in the scattering cases (Section 7.5.2) does not invalidate the fit. This point is also reflected in the generally poor fit to the experimental PADs seen in the (weak) scattering channels, for example Figure 8.2(a) 1_1 and (c) 4_1.The following subsection discusses the uniqueness of this result, and further discussion is presented in subsection 8.3.3.

8.3.2 Uniqueness of fit & rotational spectra

Because of the large number of parameters involved in the fitting it is important to consider whether the final result presented above is unique. In the case of the acetylene fits discussed in Chapter 6, repeated fits yielded only one set of dynamical parameters, and the fit was immediately seen to be unique. In the fits performed for ammonia, statistical analysis of 5000 fits revealed the presence of several sets of parameters which yielded χ^2 values within 1% of the minimum obtained. Evaluation of the χ^2 surface in the region of each of these parameter sets always showed minima along every coordinate, showing that each parameter set was a local minimum, and that these minima could not

be differentiated on the basis of χ^2 alone because the 1% difference was not significant. However, the fitting made use of the PADs, but not the rotational spectra, so this did not present an insurmountable problem as more experimental data was available. As mentioned in the previous section, fitting directly to both the PADs and rotational spectra did not provide a good result due to the relative weighting of the two types of data, but calculation of rotational spectra did provide a way to cap l_{max} (as also seen in the acetylene case, Section 6.2.3). Similarly, further screening of the candidate parameter sets, as obtained by a fit to the PADs only, could make use of the rotational spectra.

One particular result from the candidate parameter sets was that a much larger g-wave contribution, as much as 34%, could be present. Physically this would be unexpected, but could not be ruled out from the fits to the PADs alone. Although the PADs correlated with scattering show the largest β_{60} values, and are therefore most sensitive to the g-wave contribution, other PADs were affected by $r_{g\lambda}$ and $\eta_{g\lambda}$ parameters and the overall χ^2 value was sensitive to the g-wave parameters. This can be contrasted with the case where a parameter is included in the fit which has negligible geometrical terms for the observed transition(s). In such a case the fit would be insensitive to the parameter, and a statistical analysis of repeated fits would reveal that the parameter could arbitrarily take any value. Similarly, the χ^2 surface would be invariant to such a parameter.

These considerations are illustrated in Figure 8.4, which shows the effect on the calculated rotational spectra, and a selection of PADs, of changing (a) the g-wave magnitudes and (b) the phase $\eta_{d\delta}$ relative to the values given in Table 8.3. Each spectrum in Figure 8.4(a) is calculated for $nr_{g\lambda}$, where n is a multiplier running from 1 - 10. As n is increased the intensity of the larger N_+ features is enhanced, while the lower-lying features die away (all spectra are normalized by area). The PADs for the 4_1 and 5_1 features change significantly. The 4_1 PAD is more sensitive to the changes; this may be attributed to small geometrical parameters involving $l = 4$, while the 5_1 PAD has a larger g-wave contribution initially, so is less sensitive to the increases in $r_{g\lambda}$. Because the odd:even l ratio is affected, the peaks correlated with odd-l also die away in the spectrum, but no changes are seen in the PADs because the partial wave composition of the odd-l continuum is not altered. This is shown in the 5_4 feature, which dies away in the spectrum but shows no change in the PAD. Figure 8.4(b) shows the effect of changing $\eta_{d\delta}$ away from the best-fit value. Again significant changes are observed in both the spectra and PADs, and again different rotational features demonstrate different sensitivities to the changes. The results shown in Figure 8.4 highlight the complexity of the fitting and the non-uniform response of the calculation; Figure 8.4(a) also shows that a large g-wave contribution was a genuine result of the fit and not just a reflection of an insensitivity to the g-wave components.

Comparison with the rotational spectra was found to provide an effective method for choosing a single parameter set from the candidates obtained from fitting. In particular, as might be intuitively expected, parameter sets with a larger g-wave contribution produced spectra with larger features for $\Delta N > 3$ transitions. This is shown in Figure 8.4(a), where the calculated rotational spectra are shown over a larger energy range than those obtained experimentally with λ_{probe} =431.3 nm, for which the highest-lying rotational

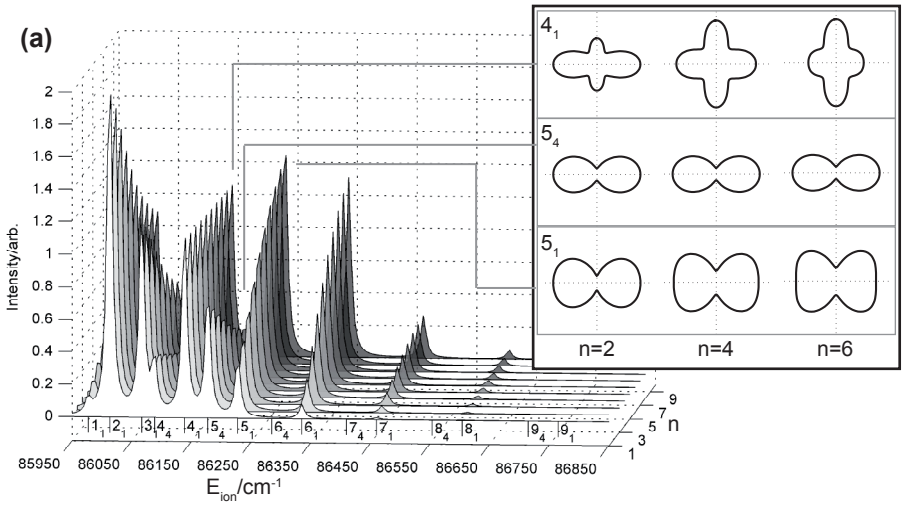

(a) Spectra calculated for $nr_{g\lambda}$, where the parameters for $n = 1$ are as shown in Table 8.3. Inset shows the PADs correlated with the 4_1, 5_4 and 5_1 features.

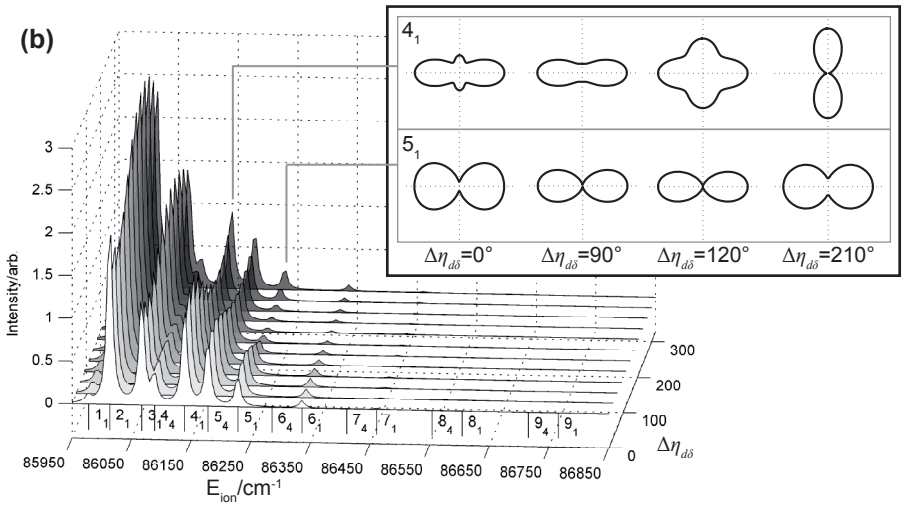

(b) Spectra calculated for $\Delta\eta_{d\delta}$, where the parameters for $\Delta\eta_{d\delta} = 0$ are as shown in Table 8.3. Inset shows the PADs correlated with the 4_1 and 5_1 features.

Figure 8.4: Illustration of sensitivity of rotational spectra and PADs to dynamical parameters. All spectra are normalized by area.

feature accessible was 5_1. There is little evidence for population of $N_+ > 5$ in the data recorded with shorted λ_{probe}, or in the ZEKE [28] and MATI [30] results, with the exception of the 6_1 feature observed in the MATI and tentatively assigned in the imaging data with λ_{probe} =425 nm (Section 7.4.2). The calculated spectrum corresponding to the best-fit parameter set (i.e. $n = 1$ in Figure 8.4(a)) corroborate this, showing a small 6_1 feature, but negligible population of $N_+ > 6$. As the g-wave multiplier is increased the 7_1 and 8_1 features grow in, and this is not consistent with the experimental data.

The single parameter set obtained after screening the calculated rotational spectra was further fine-tuned by direct fitting to the rotational spectra in addition to the PADs. This fitting used the already determined parameters as a starting point for the fit (as opposed to using randomized seed values) and capped the maximum change in these parameters

to 10%. This cap prevented the problems with the fit reproducing the rotational spectra at the expense of the PADs, as detailed above, but allowed enough flexibility to optimize the calculated spectra above the level of a by-eye comparison. The final parameter set obtained in this way is as listed in Table 8.3. While it is impossible to say with 100% certainty that these parameters are unique due to the complexity of the fit, the confidence in these parameters representing a unique result is high, and they have been tested as thoroughly as possible.

8.3.3 Discussion of dynamical parameters

The dynamical parameters obtained from the ionization of $\widetilde{B}$-state NH_3 present a much more complex picture than the acetylene case. Many partial wave components are allowed, and this makes it difficult to suggest a physically insightful picture of the ionization event. The main contribution to the photoelectron wavefunction is the $d\delta$-component, and this has a large phase shift of 149° relative to the s-wave. The $d\delta$-component has a large amplitude in the plane of the molecule, so might be expected to interact strongly with the short-range molecular potential. Similarly, the $d\sigma$ and $d\pi$ components might be expected to interact less strongly with the molecular potential, and show smaller non-Coulombic ($\delta_{l\lambda}$) phase contributions. However, this argument does not hold for the three f-wave components, which show almost identical phase shifts relative to the $p\pi$-wave. The fact that these phase shifts are close to the Coulomb phase shift, $\sigma_p - \sigma_f \approx 170°$, may indicate that there is only a small non-Coulombic contribution to the f-wave phase, although a large negative non-Coulombic contribution could yield the same final result within the constraints of the fitted $\eta_{l\lambda}$.

Both the d and f-wave show largest amplitude in the $\lambda = l$ component, $d\delta$ and $f\phi$ respectively. This indicates that the short-range eigenchannels with the largest amplitude in the plane of the molecule couple most strongly to the continuum. The g-wave parameters show the $g\pi$ component has the largest magnitude, and the pattern of the λ-component intensities is quite different from the d and f-waves. This may be the signature of scattering versus atomic-like ionization channels. The even:odd l ratio is 76:24, with uncertainty ± 2. Although this is the asymptotic l-wave ratio, it is similar to the values quoted by other authors for the $p\pi : d\delta$ $\widetilde{B}$-state composition (see Section 7.1.2), which may suggest that the short-range scattering does not cause further mixing of the odd and even-l continua [87]. This is consistent with the previous observation that only scattering associated with even-l is significant, and might provide some insight into the exact nature of the scattering potential. However, because of the complexity of the ionization dynamics further calculations are thought necessary to provide a more physical picture. In particular calculation of the photoelectron wavefunction, and MF-PAD, from the dynamical parameters determined here should provide a means of visualizing the dynamics. Similarly, an eigenchannel decomposition of the continuum might provide a clearer picture of the short-range dynamics [87, 93] (see also Appendix A). Electronic structure calculations of the intermediate and ion states may also assist in determining the nature of the scattering potential.

l	λ	$r_{l\lambda}$(i)	$r_{l\lambda}$(ii)	F_l/%	$\mu_{l\lambda}$	n	$\pi\mu_{l\lambda}$	$\pi\mu_{l\lambda}$/deg
s	σ	0.060	0.252	0.8	0.89	12-18	2.80	0*
p	π	0.315	0.237	8.4	0.81	9	2.54	0*
d	σ	0.217	0.929	56.5	0.06	>100	0.19	149
	π	0.217	0.929		0.00	>100	0	160
	δ	0.217	0.929		0.025	>100	0.08	156
f	π	0.402	0.303	34.2	0	-	0	146
	δ	0.402	0.303		0	-	0	146
	ϕ	0.402	0.303		0	-	0	146

Table 8.4: Magnitudes, $r_{l\lambda}$, of the radial dipole matrix elements reported in (i) ref. [31], and (ii) renormalized to include the $\widetilde{B}$-state character, as published in ref. [94]. Cross-sections F_l are also reproduced from ref. [94]. Quantum defects, $\mu_{l\lambda}$, used in refs. [31, 94], originally obtained from refs. [190, 191]. n is the principal quantum number for the Rydberg series for which $\mu_{l\lambda}$ was obtained. The final column shows the quantum defects redefined to match the phase convention followed in this work, in which even and odd-l are independent and terms * are set to zero. Note that these values do not include the Coulomb phases, so are not directly comparable with $\eta_{l\lambda}$.

The dynamical parameters obtained here are quite different from those found in the previous ToF work [31, 94], as reproduced in Table 8.4. In that case the lack of rotational resolution meant there was not sufficient experimental data to determine the magnitudes and phases, so the phases were approximated with the quantum defects [31, 94], $\mu_{l\lambda}$, obtained from spectroscopy of Rydberg series. These values are also reproduced in Table 8.4.[6] Magnitudes, $\boldsymbol{r}_{l\lambda}$, were assumed to be λ independent. Fitting was performed "by hand" within the rotational spectator model (Section 8.1), and made use of the six rotationally-summed PADs obtained experimentally. The fit was also fine-tuned to match the MATI spectra from ref. [192]. The $\widetilde{B}$-state character was assumed to be 85 % $p\pi$ and 15 % $d\delta$.

As discussed in Appendix A.3, the quantum defects are related to the non-Coulombic ("scattering") phase shifts which form part of the total phase, $\eta_{l\lambda}$, determined in this work. However, the energy dependence of the quantum defects was not allowed for in the previous work. Given that the experimental results were obtained at electron kinetic energies of ∼8000 cm^{-1}, the energy dependence of the dynamical parameters might be expected to lead to significant changes relative to the Rydberg series measurements. Indeed, significant changes in the dynamical parameters between E_{KE} ∼300 cm^{-1} and ∼8000 cm^{-1} have been qualitatively established in the comparison of 1-colour and 2-colour data discussed in Section 7.5.2.

In light of these numerous differences, lack of agreement between the dynamical parameters previously determined, and those reported here, is not surprising. However, the fact that the results determined from the ToF work agreed with the MATI spectra so well

[6] Note that there is some discrepancy between refs. [94] and [31] regarding the source of these quantum defects, and the values quoted in Table 8.4(b) for $n > 100$ appear to be from a personal communique as cited in ref. [31], but unpublished elsewhere in the literature.

is somewhat surprising. Furthermore, subsequent MQDT calculations, which made use of the dynamical parameters determined from the ToF work, also found good agreement with experimental results [30]. Because of the complex relationship between the magnitudes and phases, and the PADs and rotational spectra calculated from these parameters (see, for example, Figure 8.4), it is possible that a suitable set of magnitudes could be found to match the experimental PADs and MATI spectra when the phases were fixed to the quantum defects. It is unlikely, however, that this fit was unique because the parameter space in such fitting is very large and would contain many local minima for an ill-conditioned fit. The equivalence found in the fit of the parameters describing the ToF PADs and MATI spectra measured at very different E_{KE}s is likely an indication of this.

8.4 Conclusions

The analysis presented in this chapter has demonstrated that the rotationally-resolved photoelectron images obtained from the ionization of rovibrationally-prepared $\tilde{B}$-state NH_3 contain enough information to determine the dynamical parameters. Despite the complex nature of the problem, involving many partial waves, thorough evaluation of the parameters obtained has led to the conclusion that they represent a unique solution.

Comparison with ZEKE [28] and MATI [30] results showed that the dynamics of direct, near-threshold ionization are similar, if not identical, to those which govern the ZEKE ionization process. Although the dynamics appear to be similar in this case, the dependence of the feature intensities in ZEKE on the precise experimental conditions (see discussion in Section 1.2.2) suggests that the intensities observed in VMI experiments are likely to provide the most suitable experimental data for determination of the direct photoionization dynamics. Additionally, as observed in the previous chapter, the dynamics change significantly with photoelectron kinetic energy, so it is also the case that the dynamics far from threshold must be very different from those in the ZEKE case.

The main conclusion which can be drawn from the dynamical parameters obtained is the presence of scattering in this case of ionization from an $n = 3$ Rydberg state, indicating that interaction of the outgoing photoelectron with the molecular core is significant. This is a very different conclusion from previous results [31, 94] which were not sensitive to the small g-wave contribution. In that case the rotational spectator model was used, and many approximations were required in order to determine the dynamics - this was a direct consequence of the lack of rotational resolution in the experimental data. Because the dataset obtained in this work is much larger such approximations have been avoided, and the final dynamical parameter set is thought to be unique.

Chapter 9

Conclusions & Future Work

The work presented in this thesis has demonstrated a partial wave decomposition of the ionization continuum, in order to obtain "complete" information on the photoionization dynamics, can be achieved for polyatomic molecules. Dynamical parameters have been obtained for near-threshold ionization of $C_2H_2(\tilde{A}^1A_u, v_4 = 4)$ and $NH_3(\tilde{B}^1E'', v_2 = 4)$. In order to obtain these results extensive theoretical and experimental techniques have been employed and refined. In particular much work went into calculation of the angular momentum coupling parameters and development of a coherent fitting methodology. Experimental apparatus and techniques were also improved over the course of the acetylene and ammonia work to the point where rotationally-resolved photoelectron images were obtained in the latter case.

The results presented here represent the first successful determination of the dynamical parameters for a four-atom system, and for a non-linear polyatomic molecule. They also showed the first rotationally-resolved photoelectron images for a polyatomic molecule, although it should be noted that other investigators have obtained better absolute resolution in VMI [42].

9.1 Continuation of Experimental Work

There are several avenues which might be explored in future work. The most obvious, and immediately possible, is the continued analysis of the ammonia data with the aim of a quantitative comparison of the ionization dynamics for the two different vibrational levels probed, and a closer look at the data recorded for different probe wavelengths and, hence, photoelectron kinetic energies. Following on from this, further experiments to look at a wider range of probe wavelengths might be a possibility, as might further study of the diffuse band observed. The latter would require careful consideration of the possible causes of this band in order to plan suitable experiments, but time-resolved experiments may be a possibility. Ammonia also offers an ideal system to study ionization from different electronic states, in particular the $\tilde{C}$-state which lies close in energy to the $\tilde{B}$-state [191], but has almost purely $p\sigma$ character. MATI results recorded via the $\tilde{C}$-state show simpler rotational spectra indicative of this [30]. It would be interesting to see how similar the

scattering behaviour is in this case, and also to explore ionization from higher-n Rydbergs.

A final experimental strand based around ammonia is the repetition of the experiments using a (1+1') scheme. In this case pump wavelengths around 160 nm would be required, and are available from a recently constructed vacuum ultraviolet (VUV) source based around 4-wave mixing in a krypton gas cell. This would provide a way to access the same intermediate levels studied in the (2+1') experiments, but with a different alignment prepared by the absorption; experiments of this kind would therefore provide data which would allow the study of alignment effects when contrasted with the existing data. The downside of experiments using VUV light is that the generation process is very inefficient, and VUV is generated at extremely low powers. The overlap of the pump and probe laser beams is also very challenging - they must be counter-propagating and aligned *in vacuo*, so an equivalent plane set-up is not possible.

Work on acetylene may be revisited, with the aim of using a 2-colour scheme to obtain better resolution in the photoelectron images, and allow more detailed study of the higher-lying vibronic bands. Such a scheme was initially envisaged for this work, but during the initial phase of the experiments there were many problems obtaining a 2-colour ionization signal and 1-colour data was recorded instead. In light of the successful ammonia work, the problems experienced then should now be surmountable. Detailed study of the effects of isomerization, which can occur for $v_4 > 5$, on the ionization dynamics would also be possible in a 2-colour experiment.

The wavelengths required for acetylene also suggest that it would be a suitable candidate for an extension of the methodology of Elliott and coworkers, in which ionization is probed via interfering 1-photon and 2-photon ionization paths (refs. [81, 82, 83], see also further discussion in Section 1.4.2). Seideman and coworkers [193] have demonstrated that this technique can also be used to measure the Breit-Wigner phase of an intermediate state accessed by only one of the ionization paths.

Experimental work on H_2O_2 is also planned. In this case IR or visible wavelengths could be used to prepare rovibrational levels in the ground state prior to single-photon ionization using VUV light at around 130 nm. The aim would again be to obtain detailed information on the ionization dynamics, but this time from the electronic ground state. Rotational resolution should again be possible. Experiments could then move on to probe the vibrational dependence of the ionization dynamics, the electron kinetic energy dependence, or even the electronic state dependence of the ionization dynamics.

9.2 Experimental Development

Further development of the VMI spectrometer to include an Einzel lens is planned. This would provide further control over the photoelectron image obtained by decoupling the voltages set on the VMI electrostatic optics from the size of the final image. The resolution obtained experimentally could be improved by using the Einzel lens to magnify the photoelectron image to fill the detector, and the trade-off between velocity mapping efficiency and image size at low V_r, as observed in the ammonia work (Section 7.4), would

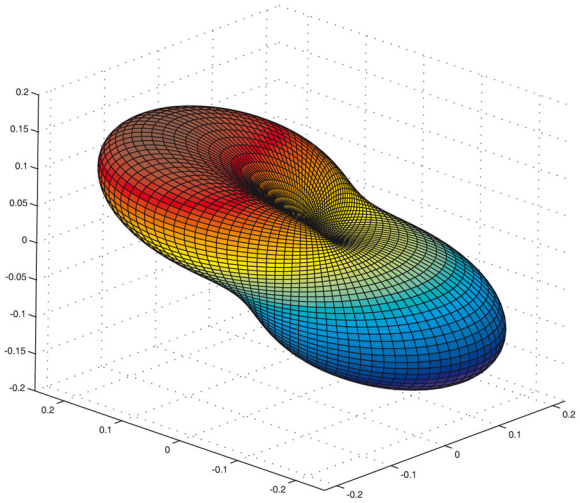

Figure 9.1: Photoelectron wavefunction calculated with equation 2.40 and dynamical parameters for acetylene (Table 6.1), plot shows the angular part of $|\phi_e|^2$.

no longer be a problem. This set-up would also allow the effect of the electric fields in the VMI region to be studied, different VMI voltages could be used and the magnification of the Einzel lens changed to maintain the same resolution in the final image. The use of an Einzel lens in this fashion has been demonstrated by Vrakking and co-workers in their "photoelectron microscope" work [194, 195, 196], where the effects of VMI fields at several kV on the near-threshold region of Xe were studied. In that work the Stark structure of the continuum was probed, and radial interference patterns originating from complex paths of below-threshold, field-ionized electrons in the combined ion-VMI electric field were observed in the photoelectron images.

Extension of the data-analysis capabilities of 2D imaging is also planned. Vallance and co-workers have developed a Fourier-moment inversion technique [41] which they have used with velocity-mapped ion images. This technique circumvents the cylindrical symmetry restriction imposed by current inversion methods (Section 4.1) by analysing several 2D images originating from the same 3D distribution, but projected along different vectors onto the detector. In this manner, somewhat akin to tomographic imaging, full 3D information can be reconstructed without the need to impose any symmetry restrictions. The technique should be readily extensible to photoelectron images, and allow for the recording of photoelectron angular distributions with a ϕ dependence, such as those obtained with non-cylindrical pump-probe polarization geometries.

9.3 Theoretical Work

Theoretical work based upon the analyses presented in this thesis is also planned. The dynamical parameters obtained should allow for the evaluation of the photoelectron wavefunction (equation 2.40) and calculation of MF-PADs, both of which should provide a more intuitive view of the photoionization dynamics. Figure 9.1 shows preliminary work

in this vein, the angular part of the asymptotic wavefunction calculated for acetylene. In light of recent work in which molecular orbital structure was tomographically reconstructed using experimental data obtained from electron-ion recombination experiments [108], the possibility of obtaining detailed information on molecular orbital structure from photoionization measurements is also an interesting goal to pursue.

Consideration of the data in the eigenchannel formalism [93] may present a more insightful parameterization of the ionization event. The dynamical parameters obtained in this work should also provide a good test for *ab initio* calculations; they offer a direct comparison for calculations of molecular and continuum wavefunctions, but as previously noted such calculations are challenging and would require collaborators with sufficient expertise.

This last point represents the major deficiency in the work presented here. Although the dynamical parameters have been determined for two polyatomic systems, the radial integrals are hard to interpret in a physically insightful manner. Similarly, the relation of the observed LF-PADs to the MF is complex, and again resists physical intuition. It is hoped that with the aid of molecular frame calculations a more tractable picture of molecular photoionization processes might be obtained.

Part III

Appendicies & Bibliography

Appendix A

Scattering Theory & Alternate Formalism

A.1 Scattering Theory

The partial wave expansion is a direct result from scattering theory. The consideration of scattering in spherical polar coordinates, assuming a central potential, leads to an outgoing spherical wave which can be considered as an expansion over l. The phase shift of this wave, relative to the incident wave, appears due to the interaction with the potential. The addition of a short-range, non-central component to the potential does not change the asymptotic result, but introduces an additional contribution to the phase shift. The treatment of photoionization presented in Section 2.3 is thus an extension of scattering theory, in which the photoionziation is treated as a "half-collision". Although not central to the work presented in this thesis, discussion of scattering theory is insightful because it reveals the physical origin of the partial wave phase shifts determined from the experimental results, and the relation of these phases to the short-range potential experienced by the outgoing photoelectron. The coordinate systems referred to here are the same as those shown in Figure 2.1.

A.1.1 General central potential

The general form of the Schrödinger equation (SE) for scattering from a central potential $U(r)$ is [125, 129]:

$$-\frac{\hbar^2}{2m}\nabla^2\Phi + U(r)\Phi = E\Phi \tag{A.1}$$

Here Φ are the eigenfunctions, and can be separated into radial and angular components in spherical polar coordinates,

$$\Phi = \sum_l A_l \frac{1}{r}\chi_l(r)P_l(\cos\theta) \tag{A.2}$$

where A_l are the expansion coefficients, $\chi_l(r)$ the radial wavefunctions and $P_l(\cos\theta)$ Legendre polynomials. The $P_l(\cos\theta)$ are axially symmetric, and degenerate with respect to m, the lab frame projection of l. The following treatment is considered in the molecular frame, so this extra complication can be omitted.

The radial part of the SE can be re-written in the form [129, 140]:

$$\frac{d^2\chi_l(r)}{dr^2} + \left(k^2 - \frac{l(l+1)}{r^2} - \frac{2mU(r)}{\hbar^2}\right)\chi_l(r) = 0 \tag{A.3}$$

Where k is the magnitude of the wave vector of the scattered wave. This form of the SE shows the key features of the scattering problem. The first term is the kinetic energy, and the second term is the *effective potential*, and contains contributions involving the wave vector, the angular momentum l and the scattering potential $U(r)$. This demonstrates that not only will the radial form of the scattered wavefunction be affected by the potential, but also by the total energy E ($\propto k^2$) *and* the angular momentum l. The term involving l, by analogy with classical scattering, is called the *centrifugal contribution*, and is primarily responsible for the truncation of the partial wave expansion to low l. This can be seen by considering the centrifugal contribution as a barrier in the effective potential which increases as $l(l+1)$, thus partial waves with high l are confined to small r and make no contribution to the scattered wavefunction.

Explicit forms of A_l and $\chi_l(r)$ can be considered in order to investigate the phase shift which occurs from scattering. For a general central potential the wavefunction can be written [140]:

$$\Phi = \sum_l \frac{(2l+1)}{kr} i^l e^{i\delta_l} \chi_l(r) P_l(\cos\theta) \tag{A.4}$$

$$\chi_l(r) \overset{r\to\infty}{\longrightarrow} \sin(kr - \frac{l\pi}{2} + \delta_l) \tag{A.5}$$

Here δ_l is the phase shift that occurs due to interaction with the scattering potential. This is reflected by the asymptotic form of χ_l which is the same as that for a free electron partial wave expansion, but with the inclusion of the scattering phase shift δ_l. The phase shift therefore carries information about the scattering potential. For $U > 0$ the potential is repulsive, the scattered wave is advanced (relative to $U = 0$) and the phase shift is negative, while for $U < 0$ the scattered wave is retarded and the phase shift is positive.[132, 140] In this way the sign and magnitude of the phase shift reveal information about the type of potential, and its magnitude.

A.1.2 Coulomb potential

In the case of a Coulomb potential equations A.9 and A.5 can be written in terms of the regular and irregular Coulomb functions, F_l and G_l, and the Coulomb phase shift σ_l:

$$F_l(r) \overset{r\to\infty}{\longrightarrow} \sin(kr - \frac{l\pi}{2} - \gamma\ln(2kr) + \sigma_l) \tag{A.6}$$

$$G_l(r) \overset{r\to\infty}{\longrightarrow} \cos(kr - \frac{l\pi}{2} - \gamma \ln(2kr) + \sigma_l) \tag{A.7}$$

$$\sigma_l = arg\Gamma(l + 1 - i\gamma) \tag{A.8}$$

In these equations Γ is the gamma function, and $\gamma = m_e Z/k$, where Z is the charge of the ion.[93] Assuming ionization of a neutral species, and working in atomic units, $\gamma = 1/k$. The boundary conditions at the origin dictate that only the regular Coulomb functions can contribute to the wavefunction, and the final form of the scattering wavefunction for a Coulomb potential is given by:

$$\Phi_c = \sum_l \frac{(2l+1)}{kr} i^l e^{i\sigma_l} F_l(r) P_l(\cos\theta) \tag{A.9}$$

As for the general central potential, the scattered wave has an associated phase shift, and the asymptotic form of the radial component is, as expected, very similar to equation A.5. Additionally, the phase shift has an analytic form in equation A.8.

A.1.3 Coulomb potential plus short-range potential

A more general case, which will be very important in the consideration in photoionization, is that of a short-range addition to the potential such as that which would be experienced by the outgoing photoelectron in the vicinity of the (ionized) species. In this case the problem can be treated as the Coulomb case (Section A.1.2), but with an additional short range contribution $U'(r)$.[140] The short range potential can be considered as a multipole potential,[93] so $U'(r) \to 0$ much faster than $U(r) \to 0$ as $r \to \infty$. A cut-off can therefore be assigned, such that $U'(r \geq r_c) = 0$, and the interaction defined as Coulombic beyond this region. The asymptotic form of the wavefunction is consequently similar to the Coulomb case (equation A.9), but the effect of the short-range part of the potential is to allow G_l to contribute, and to add an additional phase contribution:

$$\Phi_s = \sum_l \frac{(2l+1)}{kr} i^l e^{i(\sigma_l+\delta_l)} \chi_l^s(r) P_l(\cos\theta) \tag{A.10}$$

$$\chi_l^s(r \geq r_c) = \cos(\delta_l) F_l(r) + \sin(\delta_l) G_l(r) \tag{A.11}$$

$$\chi_l^s(r) \overset{r\to\infty}{\longrightarrow} \sin(kr - \frac{l\pi}{2} - \gamma \ln(2kr) + \sigma_l + \delta_l) \tag{A.12}$$

The mixing of the radial Coulomb solutions, $F_l(r)$ and $G_l(r)$, is therefore dependent on the short-range phase contribution δ_l, and the magnitude of this contribution can be viewed as a measure of how significantly the overall potential differs from a pure Coulomb field, i.e. $\delta_l \to 0$ as $U'(r) \to 0$. This definition is linked to the quantum defect, as discussed in Section A.3.

The total scattering phase shift is the sum of the Coulomb and short-range contribu-

tions:

$$\eta_l = \sigma_l + \delta_l \tag{A.13}$$

It is this total phase shift which is measured from analysis of the PADs, as discussed in Section 2.3. It is important to note here that the phase shifts are dependent on k. This is shown explicitly for σ_l by the appearance of $1/k$ in equation A.8. No analytic form is given for δ_l, this will depend on the precise details of $U'(r)$. However, the short-range potential can be treated as a black-box and physical arguments applied regarding the energy dependence. Such considerations are discussed by Park & Zare [93], who conclude that the dynamics inside the short-range are not very sensitive to the asymptotic photoelectron energy. Physically this is due to the deep Coulomb well in near the ion-core, so the kinetic energies in this region are always large and only changes to the asymptotic photoelectron energy which are significant with respect to the ionization potential will cause large changes in δ_l. This point is expanded upon further in Section 4.3.1.

A.1.4 Coulomb potential plus *non-central* short-range potential

In the preceding section all the potentials are central, i.e. only dependent on r. In a more general case, as applicable to photoionization of molecules, the short-range part of the potential may be non-central, and possibly highly anisotropic. Equation A.10 can be generalized to an axially-symmetric problem in the molecular frame, and the quantum number λ introduced as the projection of l onto this axis - usually chosen to be the principal symmetry axis of the molecule (see Figure 2.1).

$$\Phi = \sum_{l,\lambda} \frac{(2l+1)}{kr} i^l e^{i(\sigma_l + \delta_{l\lambda})} \chi^s_{l\lambda}(r) Y_{l\lambda}(\theta, \phi) \tag{A.14}$$

Here δ_l is replaced with $\delta_{l\lambda}$, the short-range phase shift for each partial wave component $(l,\, \lambda)$. $\chi^s_{l\lambda}(r)$ is defined as $\chi^s_l(r)$, except for the same substitution, $\delta_l \rightarrow \delta_{l\lambda}$. Similarly, equation A.13 can be rewritten as

$$\eta_{l\lambda} = \sigma_l + \delta_{l\lambda} \tag{A.15}$$

The form of $\Phi_{l\lambda}$ shown in equation A.14 can be compared with equation 2.40, recast slightly but essentially the same, and equation 2.41 which shows the wavefunction rotated into the lab frame. In this form of the scattering wavefunction there are more partial wave components (more scattering channels), and the wavefunction is inherently more complex. The Coulombic terms only show dependence on l, and reflect the spherically symmetric component of the potential as before. The short-range phase shifts now also reflect the anisotropy of the molecular potential, allowing for phase differences between the λ components of a given l-wave.

Further complications arise, however, because for a non-spherical potential l is not a good quantum number, and λ is only a good quantum number for cylindrically-symmetric potentials (e.g. homonuclear diatomic molecules). This means that l, and possibly λ, are

not good quantum numbers in the short-range region,[93] and l-mixing and λ-mixing can occur - hence the partial wave channels are not independent in this region. Additionally, electron-electron interactions in the short-range region can further reduce the symmetry, so even though λ is a good quantum number for a diatomic system under the independent electron approximation, λ-mixing may still occur in reality.

Because the asymptotic form is still exact, the short-range region can be considered as a black-box as in Section A.1.3, and the short-range phase will, as before, contain information on the precise nature of the potential experienced. The effect of the l-mixing at short range is that more l components may be expected to contribute to the scattered wavefunction than for the pure Coulomb case. In the case of photoionization this scattering can be interpreted as the short-range interaction of the outgoing photoelectron with the nascent ion core, and the exchange of angular momentum with the core gives rise to higher l in the photoelectron wavefunction. Equivalently, the short-range solutions to the potential comprise an expansion over the $|l,\, \lambda\rangle$ basis, and these are related to the asymptotic partial waves through a unitary transformation - this is the basis of the eigenchannel formalism discussed in Section A.2.

A.2 Relation to Eigenchannels

Park & Zare (ref. [93] and references therein) consider the eigenchannel approach, which can be considered as an extension of MQDT, and the relation of this formalism to both quantum defect theory (very briefly outlined above), and the partial wave expansion (as used throughout this work). In the eigenchannel approach the scattering wavefunction is expanded in the close-coupled, or eigenchannel basis,

$$\Phi_{eigenchannel} = \sum_{l,\lambda} i^l e^{i\sigma_l} Y_{l\lambda}(\theta,\phi) \sum_{\alpha_\lambda} U^{\lambda}_{l\alpha_\lambda} e^{-i\pi\tau^{\lambda}_{\alpha_\lambda}} \xi^{\lambda}_{\alpha_\lambda}(\mathbf{r};\, k,\, R) \tag{A.16}$$

The radial wavefunctions $\xi^{\lambda}_{\alpha_\lambda}(\mathbf{r};\, k,\, R)$ are given by:

$$\xi^{\lambda}_{\alpha_\lambda}(\mathbf{r} > r_c;\, k,\, R) = \frac{1}{\sqrt{2r}} \sum_{l"} U^{\lambda}_{l"\alpha_\lambda} [F_{l"}(r;\, k)\cos(\pi\tau^{\lambda}_{\alpha_\lambda}) - G_{l"}(r;\, k)\sin(\pi\tau^{\lambda}_{\alpha_\lambda})] Y_{l"\lambda}(\bar{\mathbf{r}}) \tag{A.17}$$

$U^{\lambda}_{l\alpha_\lambda}$ are electronic transformation matrix elements, $\tau^{\lambda}_{\alpha_\lambda}$ are the eigenphase shifts. Other symbols have the same meaning as previously, and the radial wavefunction $\xi^{\lambda}_{\alpha_\lambda}(\mathbf{r};\, k,\, R)$ is clearly very similar to χ^s_l defined in equation A.11, composed of a mix of regular and irregular Coulomb functions. The slightly more complex form arises because $\xi^{\lambda}_{\alpha_\lambda}(\mathbf{r};\, k,\, R)$ is derived in a matrix formalism, and its composition is defined in terms of the matrix elements $U^{\lambda}_{l"\alpha_\lambda}$. The properties of the electronic transformation matrix (see ref. [93] for full details) mean that $\xi^{\lambda}_{\alpha_\lambda}(\mathbf{r};\, k,\, R)$ are appropriate eigenfunctions for the scattering process. Additionally, the eigenchannels, indexed with α_λ, are independent and are not mixed by the scattering, so also constitute eigenfunctions for the short-range electron-core interaction. This has led to the eigenchannels being termed *continuum molecular orbitals*.

In this formalism $\tau^{\lambda}_{\alpha_\lambda}$ is the analytic continuation of the quantum defect for $E > 0$, and is analogous to δ_l in equation A.22. Park and Zare also show how the eigenchannel formalism is equivalent to open-channel MQDT [93], and both formalisms describe the close-coupled region. The eigenchannels also define the wavefunction asymptotically, so are related through a unitary transform to the partial wave expansion:

$$r_{l\lambda} e^{i\delta_{l\lambda}} = \sum_{\alpha_\lambda} U^{\lambda}_{l\alpha_\lambda} e^{-i\pi\tau^{\lambda}_{\alpha_\lambda}} M^{\lambda}_{\alpha_\lambda} \tag{A.18}$$

Here $M^{\lambda}_{\alpha_\lambda}$ are radial integrals linking the initial electronic orbital to the continuum molecular orbital α_λ, and hence define the electronic dipole matrix elements in the eigenchannel formalism. They are analogous to $r_{l\lambda}$, as defined in equation 2.47. The formalisms are thus closely related, but the eigenchannel approach further separates the photoionization dynamics into continuum ($U^{\lambda}_{l\alpha_\lambda}$, $e^{-i\pi\tau^{\lambda}_{\alpha_\lambda}}$) and molecular ($M^{\lambda}_{\alpha_\lambda}$) parameters, which can provide a more insightful parameterization of the photoionization event, and can also be used to determine the common continuum dynamics between different electronic states [93].

A.3 Relation to Quantum Defects

As shown by Seaton [197], the short-range phase contributions derived in scattering theory, δ_l, are equivalent to the quantum defects. Although quantum defect theory (QDT, or MQDT for the multichannel variant) is not the main focus of this work it is often applied to ionization problems, and appears extensively in the literature regarding NH_3, as discussed in Chapter 7, so will be introduced briefly here.

The quantum defect, μ_{nl}, is essentially a measure of how a central potential deviates from the pure Coulomb case. The quantum defect is defined by [198, 197]:

$$E_{nl} = \frac{-me^4}{2\hbar^2} \frac{Z^2}{v^2_{nl}} \tag{A.19}$$

Equation A.19 defines the energy levels, E_{nl}, for a hydrogenic system (i.e. a pure Coulomb potential) with charge Z and effective quantum number v_{nl}:

$$v_{nl} = n - \mu_{nl} \tag{A.20}$$

Where μ_{nl} is the quantum defect and n the principal quantum number, hence for $\mu_{nl} = 0$, $v_{nl} = n$ and the potential is Coulombic. As $n \to \infty$, $\mu_{nl} \to \mu_{\infty l}$, the limiting value of the quantum defect. This can be equated with the short-range phase at $E = 0$ [198]:

$$\pi\mu_{\infty l} = \delta_l(0) \tag{A.21}$$

Extending the quantum defect to $E > 0$, i.e. continuum states, requires knowledge of the analytic form of μ_{nl}. This may be determined by extrapolating from experimentally determined μ_{nl}, or through other methods such as perturbation theory [197]. In this case

the quantum defect is denoted $\mu_l(E)$ and:

$$\pi\mu_l(E) = \delta_l(E) \tag{A.22}$$

This description presents the barest introduction to MQDT, emphasizing the relation of the quantum defect to the scattering phase. The full treatment of photoionization within the MQDT framework treats the continuum wavefunctions in a similar way to the scattering theory results discussed above [197], the eigenchannels and long-range channels are derived using frame-transformation matrix elements to recast the scattering (or reactance) matrix elements, despite some subtle differences this is essentially the same approach as the eigenchannel formalism of Park & Zare [93] discussed above. Further details can be found in, for example, refs. [198, 197, 199, 200].

A.4 Orbital Ionization Model

The orbital ionization model, developed by Willitsch & Merkt [24], offers an intuitive picture of photoionization. The single-point expansion of the initial bound state is calculated using standard *ab initio* methods, and rotational line intensities are then calculated using standard angular momentum algebra in order to predict the photoelectron spectrum. The method is essentially the same as the rotational-spectator approximation detailed in Chapter 8.1, the difference being that it makes use of the calculated character of the bound state. It has been applied to several molecular systems, and compared to ZEKE results [22, 23, 24, 25, 26]. Like the rotational spectator model, it provides a good zero-order approximation, but neglects any scattering of the outgoing photoelectron, and although it uses input from electronic structure calculations it does not offer a complete treatment of ionization in the sense of the fully *ab initio* methods mentioned in Section 1.4.5.

Appendix B

β_{LM} Parameters from Acetylene Photoelectron Images

Tabulated here are the full set of β_{LM} parameters extracted from the photoelectron images recorded from for C_2H_2 via $V_0^5 K_0^1$ pump transitions, as detailed in Chapter 5.

Vibronic band	R_1		R_3		R_5	
	β_{20}	β_{40}	β_{20}	β_{40}	β_{20}	β_{40}
$\mathbf{0^0}\,^2\Pi_u$	0.135(24)	-0.070(20)	0.06(17)	-0.071(15)	0.195(16)	-0.12(14)
$\mathbf{4^1}\,^2\Sigma_u^-$	-0.100(10)	-0.053(9)	-0.183(10)	-0.001(9)	-0.025(16)	-0.061(14)
$\mathbf{4^1}\,^2\Delta_u$	-0.120(9)	0.049(8)	-0.181(12)	0.025(11)	-0.111(15)	-0.004(13)
$\mathbf{4^2}\,^2\Pi_u$	0.584(9)	0.063(8)	0.517(12)	0.050(11)	0.337(17)	0.015(15)
$\mathbf{4^3}\,^2\Sigma_u^- + \mathbf{4^3}\,^2\Delta_u$	-0.042(4)	-0.049(4)	-0.068(5)	-0.031(4)	-0.035(7)	-0.030(6)
$\mathbf{4^1 5^2}\,^2\Gamma_u$	-0.096(9)	-0.020(9)	-0.125(10)	-0.010(9)	-0.115(12)	-0.004(11)
$\mathbf{4^4}\,^2\Phi_u$	0.099(3)	-0.023(3)	0.107(4)	-0.020(4)	0.124(6)	-0.019(6)
$\mathbf{4^3}\,^2\Sigma_u^+ + \mathbf{4^3}\,^2\Delta_u$	-0.041(6)	-0.009(5)	0.008(7)	-0.012(7)	-0.021(6)	0.012(5)
?	0.095(4)	0.01(3)	0.074(5)	0.005(4)	0.024(8)	0.015(7)

Table B.1: β-parameters for R-branch pump transitions ($V_0^5 K_0^1$ band).

Vibronic band	Q_3*		Q_4		$Q_7 + P_2$		P_3	
	β_{20}	β_{40}	β_{20}	β_{40}	β_{20}	β_{40}	β_{20}	β_{40}
$\mathbf{0^0}\,^2\Pi_u$	0.17(19)	-0.07(16)	0.242(20)	-0.107(17)	0.153(20)	-0.12(16)	0.139(18)	-0.116(16)
$\mathbf{4^1}\,^2\Sigma_u^-$	-0.072(10)	-0.048(9)	0.05(11)	-0.099(10)	-0.044(14)	-0.106(13)	0.007(13)	-0.057(12)
$\mathbf{4^1}\,^2\Delta_u$	-0.077(11)	-0.003(10)	0.080(9)	0.000(9)	-0.046(14)	-0.03(13)	-0.032(16)	-0.019(14)
$\mathbf{4^2}\,^2\Pi_u$	0.508(12)	0.039(10)	0.299(12)	-0.036(11)	0.313(15)	-0.038(13)	0.235(16)	-0.007(14)
$\mathbf{4^3}\,^2\Sigma_u^- + \mathbf{4^3}\,^2\Delta_u$	-0.143(4)	-0.035(3)	-0.132(5)	-0.046(4)	-0.092(5)	-0.037(4)	-0.108(5)	-0.019(4)
$\mathbf{4^1 5^2}\,^2\Gamma_u$	-0.134(8)	-0.010(8)	-0.104(12)	-0.008(11)	-0.169(15)	0.003(14)	-0.145(12)	0.017(11)
$\mathbf{4^4}\,^2\Phi_u$	0.152(3)	-0.025(3)	0.249(4)	-0.039(4)	0.142(5)	-0.051(4)	0.179(4)	-0.029(3)
$\mathbf{4^3}\,^2\Sigma_u^+ + \mathbf{4^3}\,^2\Delta_u$	-0.039(6)	-0.007(5)	-0.011(6)	0.000(6)	-0.008(7)	-0.025(6)	0.004(7)	-0.018(6)
?	0.105(3)	0.004(3)	0.038(4)	-0.003(4)	0.088(6)	-0.003(6)	0.048(6)	0.007(5)

Table B.2: β-parameters for P, Q-branch pump transitions ($V_0^5 K_0^1$ band). *The Q_3 line is mixed, with a contribution from Q_1 and Q_2.

Appendix C

β_{LM} Parameters from Ammonia Photoelectron Images

Tabulated here are all β_{LM} values obtained from the ammonia experimental data (Chapter 7).

J_{gK_g}	J_{iK_i}	N_{+K_+}	β_{20}	β_{40}	β_{60}
0_0	2_1	1_0	-0.093(12)	-0.076(13)	*-0.006(11)*
		3_3	-0.204(30)	*-0.016(31)*	*-0.023(27)*
		3_0	-0.437(10)	0.144(12)	-0.027(10)
		4_3	-0.322(15)	*0.031(17)*	*-0.005(15)*
1_1	3_2	1_1	-0.058(21)	0.057(23)	-0.059(21)
		2_1	-0.071(9)	0.108(9)	-0.018(8)
		3_1	-0.079(8)	-0.212(9)	*0.003(8)*
		4_1	-0.399(6)	0.164(7)	-0.022(6)
		5_4	-0.436(6)	0.056(7)	*-0.006(6)*
		5_1	-0.350(4)	-0.057(4)	0.034(4)
2_0	4_1	3_0	0.022(8)	0.064(9)	0.048(8)
		5_3	-0.332(10)	*0.012(11)*	*-0.016(10)*
		5_0	-0.319(3)	0.136(4)	-0.014(3)
		6_3	-0.433(7)	*0.003(7)*	0.044(6)
1_1	2_2	1_1	-0.023(10)	-0.030(11)	*-0.006(10)*
		2_1	-0.078(12)	-0.031(13)	*-0.006(11)*
		3_1	-0.360(9)	0.025(10)	*0.002(9)*
		4_4	-0.365(9)	0.050(10)	*-0.009(9)*
		4_1	-0.315(10)	0.026(10)	-0.019(9)
1_1	3_0(?)	A	-0.226(16)	0.053(17)	0.039(15)
		B	-0.124(21)	-0.136(23)	0.130(20)
		C	-0.330(13)	0.103(14)	*-0.018(13)*
		D	-0.243(22)	*-0.014(24)*	*-0.016(21)*
		E	-0.051(24)	-0.127(25)	*0.020(22)*
		F	-0.104(25)	0.054(27)	*-0.012(24)*
		G+H	*-0.039(30)*	*0.053(32)*	*-0.021(28)*
		I	-0.240(48)	*-0.009(46)*	*0.001(41)*

Table C.2: β_{LM} extracted from the images shown in figure 7.14, recorded via $\widetilde{X}^1A_1'|v_{2(g)} = 0, J_{gK_g}\rangle \rightarrow \widetilde{B}^1E''|v_{2(i)} = 3, J_{iK_i}\rangle$ pump transitions with $\lambda_{probe} = 431.3$ nm.

J_{gK_g}	J_{iK_i}	N_{+K_+}	β_{20}	β_{40}	β_{60}
1_1	3_2	1_1	*0.022(24)*	*-0.022(26)*	-0.051(23)
		2_1	-0.100(16)	0.102(17)	*-0.022(15)*
		$3_1 + 4_4$	-0.066(25)	-0.165(27)	*-0.012(24)*
		4_1	-0.364(10)	0.161(11)	-0.025(10)
		5_4	-0.420(9)	0.051(10)	*0.008(8)*
		5_1	-0.288(8)	*0.010(8)*	*-0.007(7)*
1_1	2_0	1_1	-0.352(16)	0.098(17)	*-0.028(15)*
		2_1	0.043(15)	-0.173(16)	*-0.025(15)*
		3_1	-0.284(10)	0.070(11)	*-0.014(9)*
		$4_1 + 4_2$	-0.399(13)	0.040(15)	*-0.012(13)*
		5_2	0.080(3)	-0.043(3)	*0.000(3)*
1_1	2_2	1_1	-0.079(13)	*0.019(13)*	*-0.008(12)*
		2_1	-0.178(11)	0.039(12)	*-0.008(10)*
		3_1	-0.330(11)	0.033(12)	*-0.012(11)*
		4_4	-0.431(8)	0.092(8)	-0.017(7)
		4_1	-0.118(15)	-0.062(16)	0.081(14)
1_1	1_0	1_1	-0.057(21)	*-0.031(22)*	*-0.015(20)*
		2_1	-0.289(15)	0.036(16)	*-0.007(14)*
		3_1	-0.363(22)	*0.011(24)*	*-0.002(21)*
		4_1	0.081(19)	*-0.019(19)*	0.036(17)
1_0	3_1	$2_0 + 3_1$	-0.055(24)	0.072(25)	*-0.009(22)*
		4_3	-0.246(20)	*-0.004(22)*	*-0.020(19)*
		4_0	-0.379(7)	0.138(8)	-0.025(7)
		5_3	-0.250(11)	*-0.006(12)*	0.047(10)
1_0	1_1	0_0	-0.199(24)	0.082(26)	*-0.016(23)*
		2_0	-0.325(23)	0.062(25)	*-0.026(21)*
		3_3	-0.185(25)	*-0.026(28)*	*0.008(24)*
		4_0	0.027(9)	*0.006(10)*	*0.007(9)*

Table C.4: β_{LM} extracted from the images shown in figure 7.10, recorded via $\widetilde{X}^1A_1'|v_{2(g)} = 0, J_gK_g\rangle \rightarrow \widetilde{B}^1E''|v_{2(i)} = 4, J_iK_i\rangle$ pump transitions with $\lambda_{probe} = 431.3$ nm.

Bibliography

[1] S. T. Pratt, *Reports on Progress in Physics*, 1995, **58**, 821–883.

[2] K. Wang, J. A. Stephens and V. McKoy, *The Journal of Physical Chemistry*, 1993, **97**, 9874–9881.

[3] K. Wang and V. McKoy, *Annual Review of Physical Chemistry*, 1995, **46**, 275–304.

[4] P. Kruit and F. H. Read, *Journal of Physics E: Scientific Instruments*, 1983, **16**, 313–324.

[5] E. de Beer, W. J. Buma and C. A. de Lange, *The Journal of Chemical Physics*, 1993, **99**, 3252–3261.

[6] S. Pratt, P. Dehmer and J. Dehmer, *Journal of Chemical Physics*, 1991, **95**, 6238–6248.

[7] S. T. Pratt, *The Journal of Chemical Physics*, 2002, **117**, 1055–1067.

[8] K. Wang, J. A. Stephens, V. McKoy, E. de Beer, C. A. de Lange and N. P. C. Westwood, *The Journal of Chemical Physics*, 1992, **97**, 211–221.

[9] N. P. L. Wales, W. J. Buma, C. A. de Lange, H. Lefebvre-Brion, K. Wang and V. McKoy, *The Journal of Chemical Physics*, 1996, **104**, 4911–4919.

[10] K. Wang and V. McKoy, *The Journal of Chemical Physics*, 1991, **95**, 8718–8724.

[11] J. Xie and R. N. Zare, *Chemical Physics Letters*, 1989, **159**, 399 – 405.

[12] M. C. R. Cockett, *Chemical Society Reviews*, 2005, **34**, 935–948.

[13] E. W. Schlag, *ZEKE Spectroscopy*, Cambridge University Press, 1998.

[14] A. Ellis, M. Feher and T. Wright, *Electronic and Photoelectron Spectroscopy Fundamentals and Case Studies*, Cambridge University Press, 1st edn., 2005.

[15] W. A. Chupka, *The Journal of Chemical Physics*, 1993, **98**, 4520–4530.

[16] T. P. Softley and R. J. Rednall, *The Journal of Chemical Physics*, 2000, **112**, 7992–8005.

[17] S. R. Procter, M. J. Webb and T. P. Softley, *Faraday Discussions*, 2000, **115**, 277–294.

[18] K. Müller-Dethlefs and E. W. Schlag, *Angewandte Chemie International Edition*, 1998, **37**, 1346–1374.

[19] U. Hollenstein, R. Seiler, H. Schmutz, M. Andrist and F. Merkt, *Journal Of Chemical Physics*, 2001, **115**, 5461–5469.

[20] C. J. A. Hammond, *Ph.D. thesis*, University of Nottingham, 2008.

[21] K. S. Haber, Y. Jiang, G. Bryant, E. Grant, H. Lefebvre-Brion and E. R. Grant, *Physical Review A*, 1991, **44**, R5331–R5334.

[22] R. Seiler, U. Hollenstein, T. P. Softley and F. Merkt, *The Journal of Chemical Physics*, 2003, **118**, 10024–10033.

[23] S. Willitsch, U. Hollenstein and F. Merkt, *The Journal of Chemical Physics*, 2004, **120**, 1761–1774.

[24] S. Willitsch and F. Merkt, *International Journal of Mass Spectrometry*, 2005, **245**, 14–25.

[25] U. Hollenstein, F. Merkt, L. Meyer, R. Seiler, T. P. Softley and S. Willitsch, *Molecular Physics*, 2007, **105**, 1711–1722.

[26] A. M. Schulenburg and F. Merkt, *The Journal of Chemical Physics*, 2009, **130**, 034308.

[27] K. Müller-Dethlefs, *The Journal of Chemical Physics*, 1991, **95**, 4821–4839.

[28] W. Habenicht, G. Reiser and K. Müller-Dethlefs, *The Journal of Chemical Physics*, 1991, **95**, 4809–4820.

[29] H. Dickinson, D. Rolland and T. Softley, *Philosophical Transactions of the Royal Society of London A*, 1997, **355**, 1585–1606.

[30] H. Dickinson, D. Rolland and T. P. Softley, *The Journal of Physical Chemistry A*, 2001, **105**, 5590–5600.

[31] D. Townsend, *Ph.D. thesis*, University of Nottingham, 1999.

[32] S. W. Allendorf, D. J. Leahy, D. C. Jacobs and R. N. Zare, *The Journal of Chemical Physics*, 1989, **91**, 2216–2234.

[33] O. Hemmers, S. B. Whitfield, P. Glans, H. Wang, D. W. Lindle, R. Wehlitz and I. A. Sellin, *Review of Scientific Instruments*, 1998, **69**, 3809–3817.

[34] D. J. Leahy, K. L. Reid and R. N. Zare, *The Journal of Chemical Physics*, 1991, **95**, 1757–1767.

[35] S. Bellm and K. L. Reid, *Chemical Physics Letters*, 2004, **395**, 253–258.

[36] R. Weinkauf, F. Lehrer, E. W. Schlag and A. Metsala, *Faraday Discussions*, 2000, **115**, 363–381.

[37] *Imaging in Molecular Dynamics: Technology and Applications*, ed. B. J. Whitaker, Cambridge University Press, Cambridge, 2003.

[38] D. W. Chandler and P. L. Houston, *Journal of Chemical Physics*, 1987, **87**, 1445–1447.

[39] A. T. J. B. Eppink and D. H. Parker, *Review of Scientific Instruments*, 1997, **68**, 3477–3484.

[40] D. H. Parker and A. T. J. B. Eppink, *The Journal of Chemical Physics*, 1997, **107**, 2357–2362.

[41] M. J. Bass, M. Brouard, A. P. Clark and C. Vallance, *Journal Of Chemical Physics*, 2002, **117**, 8723–8735.

[42] A. Osterwalder, M. J. Nee, J. Zhou and D. M. Neumark, *The Journal of Chemical Physics*, 2004, **121**, 6317–6322.

[43] M. J. Nee, A. Osterwalder, J. Zhou and D. M. Neumark, *The Journal of Chemical Physics*, 2006, **125**, 014306.

[44] C. J. Hammond and K. L. Reid, *Physical Chemistry Chemical Physics*, 2008, **10**, 6762–6769.

[45] A. M. D. Lee, *Ph.D. thesis*, Queen's University, Kingston, Ontario, Canada, 2007.

[46] A. Stolow and J. G. Underwood, in *Advances in Chemical Physics*, ed. S. A. Rice, 2008, vol. 139, ch. Time-Resolved Photoelectron Spectroscopy of Nonadiabatic Dynamics in Polyatomic Molecules.

[47] A. Vredenborg, W. G. Roeterdink and M. H. M. Janssen, *Review of Scientific Instruments*, 2008, **79**, 063108.

[48] U. Becker, *Journal of Electron Spectroscopy and Related Phenomena*, 1998, **96**, 105 – 115.

[49] J. H. D. Eland, M. Takahashi and Y. Hikosaka, *Faraday Discussions*, 2000, **115**, 119–126.

[50] A. Yagishita, K. Hosaka and J.-I. Adachi, *Journal of Electron Spectroscopy and Related Phenomena*, 2005, **142**, 295 – 312.

[51] M. Lebech, J. C. Houver, A. Lafosse, D. Dowek, C. Alcaraz, L. Nahon and R. R. Lucchese, *The Journal of Chemical Physics*, 2003, **118**, 9653–9663.

[52] J. A. Davies, R. E. Continetti, D. W. Chandler and C. C. Hayden, *Physical Review Letters*, 2000, **84**, 5983–5986.

[53] R. E. Continetti, *Annual Review of Physical Chemistry*, 2001, **52**, 165–192.

[54] P. Downie and I. Powis, *The Journal of Chemical Physics*, 1999, **111**, 4535–4547.

[55] U. Becker, O. Gessner and A. Rüdel, *Journal of Electron Spectroscopy and Related Phenomena*, 2000, **108**, 189 – 201.

[56] I. Thomann, R. Lock, V. Sharma, E. Gagnon, S. T. Pratt, H. C. Kapteyn, M. M. Murnane and W. Li, *The Journal of Physical Chemistry A*, 2008, **112**, 9382–9386.

[57] C. Z. Bisgaard, O. J. Clarkin, G. Wu, A. M. D. Lee, O. Gessner, C. C. Hayden and A. Stolow, *Science*, 2009, **323**, 1464–1468.

[58] C. N. Yang, *Physical Review*, 1948, **74**, 764–772.

[59] D. Dill, *The Journal of Chemical Physics*, 1976, **65**, 1130–1133.

[60] S. N. Dixit and V. McKoy, *The Journal of Chemical Physics*, 1985, **82**, 3546–3553.

[61] K. L. Reid, *Annual Review of Physical Chemistry*, 2003, **54**, 397–424.

[62] K. L. Reid, D. J. Leahy and R. N. Zare, *The Journal of Chemical Physics*, 1991, **95**, 1746–1756.

[63] K. L. Reid, D. J. Leahy and R. N. Zare, *Physical Review Letters*, 1992, **68**, 3527–3530.

[64] B. Ritchie, *Physical Review A*, 1976, **13**, 1411–1415.

[65] J. Cooper and R. N. Zare, *The Journal of Chemical Physics*, 1968, **48**, 942–943.

[66] J. Cooper and R. N. Zare, in *Lectures in Theoretical Physics: Atomic Collision Processes, Vol. XI-C*, ed. K. T. M. S. Geltman and W. E. Brittin, Gordon and Breach, New York, 1969, ch. Photoelectron Angular Distributions, pp. 317–337.

[67] H. D. Cohen and U. Fano, *Physical Review*, 1966, **150**, 30–33.

[68] J. L. Hall and M. W. Siegel, *The Journal of Chemical Physics*, 1968, **48**, 943–945.

[69] J. A. Duncanson, M. P. Strand, A. Lindgård and R. S. Berry, *Physical Review Letters*, 1976, **37**, 987–990.

[70] B. Schmidtke, M. Drescher, N. A. Cherepkov and U. Heinzmann, *Journal of Physics B: Atomic, Molecular and Optical Physics*, 2000, **33**, 2451–2465.

[71] M. P. Strand, J. Hansen, R.-L. Chien and R. S. Berry, *Chemical Physics Letters*, 1978, **59**, 205 – 209.

[72] J. C. Hansen, J. A. Duncanson, R.-L. Chien and R. S. Berry, *Physical Review A*, 1980, **21**, 222–233.

[73] R.-l. Chien, O. C. Mullins and R. S. Berry, *Physical Review A*, 1983, **28**, 2078–2084.

[74] N. A. Cherepkov, *Journal of Physics B: Atomic and Molecular Physics*, 1979, **12**, 1279–1296.

[75] N. Cherepkov, *Journal of Electron Spectroscopy and Related Phenomena*, 2005, **144-147**, 1197 – 1201.

[76] U. Heinzmann, *Journal of Physics B: Atomic and Molecular Physics*, 1980, **13**, 4353–4366.

[77] U. Heinzmann, *Journal of Physics B: Atomic and Molecular Physics*, 1980, **13**, 4367–4381.

[78] G. Snell, B. Langer, M. Drescher, N. Müller, B. Zimmermann, U. Hergenhahn, J. Viefhaus, U. Heinzmann and U. Becker, *Physical Review Letters*, 1999, **82**, 2480–2483.

[79] S. J. Smith and G. Leuchs, in *Advances in Atomic and Molecular Physics*, Academic Press, 1988, ch. Angular Correlations in Multiphoton Ionization of Atoms, pp. 157–218.

[80] Z.-M. Wang and D. S. Elliott, *Physical Review Letters*, 2000, **84**, 3795–3798.

[81] Y.-Y. Yin and D. S. Elliott, *Physical Review A*, 1993, **47**, 2881–2887.

[82] Y.-Y. Yin, C. Chen, D. S. Elliott and A. V. Smith, *Physical Review Letters*, 1992, **69**, 2353–2356.

[83] Y.-Y. Yin, D. S. Elliott, R. Shehadeh and E. R. Grant, *Chemical Physics Letters*, 1995, **241**, 591 – 596.

[84] D. Dill, *Physical Review A*, 1973, **7**, 1976–1987.

[85] H. Park and R. N. Zare, *The Journal of Chemical Physics*, 1993, **99**, 6537–6544.

[86] H. Park, I. Konen and R. N. Zare, *Physical Review Letters*, 2000, **84**, 3819–3822.

[87] H. Park and R. N. Zare, *The Journal of Chemical Physics*, 1996, **104**, 4568–4580.

[88] O. Geßner, Y. Hikosaka, B. Zimmermann, A. Hempelmann, R. R. Lucchese, J. H. D. Eland, P.-M. Guyon and U. Becker, *Physical Review Letters*, 2002, **88**, 193002.

[89] J. Adachi, K. Ito, H. Yoshii, M. Yamazaki, A. Yagishita, M. Stener and P. Decleva, *Journal of Physics B: Atomic, Molecular and Optical Physics*, 2007, **40**, 29–47.

[90] R. R. Lucchese, A. Lafosse, J. C. Brenot, P. M. Guyon, J. C. Houver, M. Lebech, G. Raseev and D. Dowek, *Physical Review A*, 2002, **65**, 020702.

[91] W. Li, J. Houver, A. Haouas, F. Catoire, C. Elkharrat, R. Guillemin, L. Journel, R. Montuoro, R. Lucchese, M. Simon and D. Dowek, *Journal of Electron Spectroscopy and Related Phenomena*, 2007, **156-158**, 30 – 37.

[92] W. B. Li, R. Montuoro, J. C. Houver, L. Journel, A. Haouas, M. Simon, R. R. Lucchese and D. Dowek, *Physical Review A (Atomic, Molecular, and Optical Physics)*, 2007, **75**, 052718.

[93] H. Park and R. N. Zare, *The Journal of Chemical Physics*, 1996, **104**, 4554–4567.

[94] D. Townsend and K. L. Reid, *The Journal of Chemical Physics*, 2000, **112**, 9783–9790.

[95] K. L. Reid and J. G. Underwood, *The Journal of Chemical Physics*, 2000, **112**, 3643–3649.

[96] J. G. Underwood and K. L. Reid, *The Journal of Chemical Physics*, 2000, **113**, 1067–1074.

[97] T. Suzuki, *Annual Review of Physical Chemistry*, 2006, **57**, 555–592.

[98] M. Tsubouchi and T. Suzuki, *The Journal of Chemical Physics*, 2004, **121**, 8846–8853.

[99] J. G. Underwood, B. J. Sussman and A. Stolow, *Physical Review Letters*, 2005, **94**, 143002.

[100] Y.-I. Suzuki and T. Suzuki, *Molecular Physics*, 2007, **105**, 1675–1693.

[101] D. Akoury, K. Kreidi, T. Jahnke, T. Weber, A. Staudte, M. Schoffler, N. Neumann, J. Titze, L. P. H. Schmidt, A. Czasch, O. Jagutzki, R. A. C. Fraga, R. E. Grisenti, R. D. Muino, N. A. Cherepkov, S. K. Semenov, P. Ranitovic, C. L. Cocke, T. Osipov, H. Adaniya, J. C. Thompson, M. H. Prior, A. Belkacem, A. L. Landers, H. Schmidt-Bocking and R. Dorner, *Science*, 2007, **318**, 949–952.

[102] F. Martin, J. Fernandez, T. Havermeier, L. Foucar, T. Weber, K. Kreidi, M. Schoffler, L. Schmidt, T. Jahnke, O. Jagutzki, A. Czasch, E. P. Benis, T. Osipov, A. L. Landers, A. Belkacem, M. H. Prior, H. Schmidt-Bocking, C. L. Cocke and R. Dorner, *Science*, 2007, **315**, 629–633.

[103] E. Surber, R. Mabbs and A. Sanov, *The Journal of Physical Chemistry A*, 2003, **107**, 8215–8224.

[104] R. Mabbs, E. Surber, L. Velarde and A. Sanov, *The Journal of Chemical Physics*, 2004, **120**, 5148–5154.

[105] X.-P. Xing, X.-B. Wang and L.-S. Wang, *The Journal of Physical Chemistry A*, 2009, **113**, 945–948.

[106] C. Bartels, C. Hock, J. Huwer, R. Kuhnen, J. Schwobel and B. von Issendorff, *Science*, 2009, **323**, 1323–1327.

[107] M. F. Kling and M. J. Vrakking, *Annual Review of Physical Chemistry*, 2008, **59**, 463–492.

[108] J. Itatani, J. Levesque, D. Zeidler, H. Niikura, H. Pepin, J. C. Kieffer, P. B. Corkum and D. M. Villeneuve, *Nature*, 2004, **432**, 867–871.

[109] J. Levesque, J. Itatani, D. Zeidler, H. Pépin, J.-C. Kieffer, P. B. Corkum and D. M. Villeneuve, *Journal of Modern Optics*, 2006, **53**, 185–192.

[110] S. N. Dixit and P. Lambropoulos, *Physical Review A*, 1983, **27**, 861–874.

[111] T. Seideman, *The Journal of Chemical Physics*, 1997, **107**, 7859–7868.

[112] V. Kumarappan, L. Holmegaard, C. Martiny, C. B. Madsen, T. K. Kjeldsen, S. S. Viftrup, L. B. Madsen and H. Stapelfeldt, *Physical Review Letters*, 2008, **100**, 093006.

[113] C. Cornaggia, *Physical Review A (Atomic, Molecular, and Optical Physics)*, 2008, **78**, 041401.

[114] S. Bauch and M. Bonitz, *Physical Review A (Atomic, Molecular, and Optical Physics)*, 2008, **78**, 043403.

[115] R. Guillemin, O. Hemmers, D. W. Lindle, E. Shigemasa, K. Le Guen, D. Ceolin, C. Miron, N. Leclercq, P. Morin, M. Simon and P. W. Langhoff, *Physical Review Letters*, 2002, **89**, 033002.

[116] F. Lépine, S. Zamith, A. de Snaijer, C. Bordas and M. J. J. Vrakking, *Physical Review Letters*, 2004, **93**, 233003.

[117] P. Bolognesi, D. Toffoli, P. Decleva, V. Feyer, L. Pravica and L. Avaldi, *Journal of Physics B: Atomic, Molecular and Optical Physics*, 2008, **41**, 221002 (5pp).

[118] T. Seideman, *Annual Review of Physical Chemistry*, 2002, **53**, 41–65.

[119] A. V. Davis, R. Wester, A. E. Bragg and D. M. Neumark, *The Journal of Chemical Physics*, 2003, **118**, 999–1002.

[120] O. Geßner, A. M. D. Lee, J. P. Shaffer, H. Reisler, S. V. Levchenko, A. I. Krylov, J. G. Underwood, H. Shi, A. L. L. East, D. M. Wardlaw, E. t. H. Chrysostom, C. C. Hayden and A. Stolow, *Science*, 2006, **311**, 219–222.

[121] T. Osipov, C. L. Cocke, M. H. Prior, A. Landers, T. Weber, O. Jagutzki, L. Schmidt, H. Schmidt-Böcking and R. Dörner, *Physical Review Letters*, 2003, **90**, 233002.

[122] I. Powis, *The Journal of Chemical Physics*, 1995, **103**, 5570–5589.

[123] S. M. Bellm, J. A. Davies, P. T. Whiteside, J. Guo, I. Powis and K. L. Reid, *The Journal of Chemical Physics*, 2005, **122**, 224306.

[124] R. R. Lucchese, G. Raseev and V. McKoy, *Physical Review A*, 1982, **25**, 2572–2587.

[125] P. W. Atkins and R. S. Friedman, *Molecular Quantum Mechanics*, Oxford University Press, 3rd edn., 1997.

[126] J. M. Hollas, *High Resolution Spectroscopy*, John Wiley & Sons, Chichester, UK, 2nd edn., 1998.

[127] P. R. Bunker and P. Jensen, *Molecular Symmetry and Spectroscopy*, NRC Research Press, Ottawa, 2nd edn., 1998.

[128] E. Hecht, *Optics*, Addison Wesley, 4th edn., 2002.

[129] A. M. Rae, *Quantum Mechanics*, Taylor & Francis, 5th edn., 2008.

[130] C. Gerry and P. Knight, *Introductory Quantum Optics*, Cambridge University Press, 2005.

[131] T. Seideman, *Physical Review A*, 2001, **64**, 042504.

[132] R. N. Zare, *Angular Momentum: Understanding spatial aspects in chemistry and physics*, John Wiley & Sons, 1988.

[133] J. M. Hollas, *Modern Spectroscopy*, John Wiley & Sons, 3rd edn., 1997.

[134] G. Racah, *Physical Review*, 1942, **62**, 438–462.

[135] D. J. Leahy, K. L. Reid and R. N. Zare, *The Journal of Physical Chemistry*, 1991, **95**, 8154–8158.

[136] C. Z. Bisgaard, *Ph.D. thesis*, University of Aarhus, 2006.

[137] B. Friedrich, D. P. Pullman and D. R. Herschbach, *The Journal of Physical Chemistry*, 1991, **95**, 8118–8129.

[138] K. Blum, *Density Matrix Theory and Applications*, Plenum Press, New York, 2nd edn., 1996.

[139] N. Chandra, *Journal of Physics B: Atomic and Molecular Physics*, 1987, **20**, 3405–3415.

[140] A. Messiah, *Quantum Mechanics Volume I*, North-Holland Publishing Company, 1970.

[141] L. Landau and E. Lifshitz, *Quantum Mechanics (Non-relativistic Theory)*, Pergamon Press, 3rd edn., 1977.

[142] R. Signorell and F. Merkt, *Molecular Physics*, 1997, **92**, 793–804.

[143] K. L. Reid and D. J. Leahy, *betalm.for and gamma.for*, Fortran code, 1991.

[144] K. L. Reid and I. Powis, *The Journal of Chemical Physics*, 1994, **100**, 1066–1074.

[145] N. Chandra, *Journal of Physics B: Atomic and Molecular Physics*, 1987, **20**, 3417–3426.

[146] W. C. Wiley and I. H. McLaren, *Review of Scientific Instruments*, 1955, **26**, 1150–1157.

[147] Photek, *Dual GM1kV User Manual*, 1st edn., 2003.

[148] D. Townsend, M. P. Minitti and A. G. Suits, *Review of Scientific Instruments*, 2003, **74**, 2530–2539.

[149] D. A. Chestakov, S.-M. Wu, G. Wu, D. H. Parker, A. T. J. B. Eppink and T. N. Kitsopoulos, *The Journal of Physical Chemistry A*, 2004, **108**, 8100–8105.

[150] J. L. Wiza, *Nuclear Instruments and Methods*, 1979, **162**, 587–601.

[151] *Scientific Detector Products Technical Brief 3 - Spatial Resolution*, Burle inc. technical report, 2008.

[152] Basler Vision Technologies, *Basler A302f Camera User's Manual*, 2002.

[153] B.-Y. Chang, R. C. Hoetzlein, J. A. Mueller, J. D. Geiser and P. L. Houston, *Review of Scientific Instruments*, 1998, **69**, 1665–1670.

[154] *http://www.mumetals.com*, Magnetic shield corporation technical report, 2008.

[155] G. A. Garcia, L. Nahon, C. J. Harding, E. A. Mikajlo and I. Powis, *Review of Scientific Instruments*, 2005, **76**, 053302.

[156] W. Li, S. D. Chambreau, S. A. Lahankar and A. G. Suits, *Review of Scientific Instruments*, 2005, **76**, 063106.

[157] G. A. Garcia, L. Nahon and I. Powis, *Review of Scientific Instruments*, 2004, **75**, 4989–4996.

[158] C. J. Dasch, *Applied Optics*, 1992, **31**, 1146–1152.

[159] V. Dribinski, A. Ossadtchi, V. A. Mandelshtam and H. Reisler, *Review of Scientific Instruments*, 2002, **73**, 2634–2642.

[160] M. Staniforth, *Personal communication*, 2007.

[161] P. R. Bevington and D. K. Robinson, *Data Reduction and Error Analysis for the Physical Sciences*, McGraw-Hill, New York, 2nd edn., 1992.

[162] H. Park, D. J. Leahy and R. N. Zare, *Physical Review Letters*, 1996, **76**, 1591–1594.

[163] T. Teramoto, J. Adachi, K. Hosaka, M. Yamazaki, K. Yamanouchi, N. A. Cherepkov, M. Stener, P. Decleva and A. Yagishita, *Journal of Physics B: Atomic, Molecular and Optical Physics*, 2007, **40**, F241–F250.

[164] T. Teramoto, J. Adachi, M. Yamazaki, K. Yamanouchi, M. Stener, P. Decleva and A. Yagishita, *Journal of Physics B: Atomic, Molecular and Optical Physics*, 2007, **40**, 4033–4046.

[165] S. M. Bellm and K. L. Reid, *Physical Review Letters*, 2003, **91**, 263002.

[166] C. K. Ingold and G. W. King, *Journal of the Chemical Society*, 1953, 2702–2755.

[167] J. K. G. Watson, M. Herman, J. C. Van Craen and R. Colin, *Journal of Molecular Spectroscopy*, 1982, **95**, 101–132.

[168] J. Watson, J. V. Craen, M. Herman and R. Colin, *Journal of Molecular Spectroscopy*, 1985, **111**, 185–197.

[169] K. Tsuji, C. Terauchi, K. Shibuya and S. Tsuchiya, *Chemical Physics Letters*, 1999, **306**, 41–47.

[170] E. Ventura, M. Dallos and H. Lischka, *Journal of Chemical Physics*, 2003, **118**, 1702–1713.

[171] T. Suzuki, Y. Shi and H. Kohguchi, *Journal of Chemical Physics*, 1997, **106**, 5292–5295.

[172] D. H. Mordaunt, M. N. R. Ashfold, R. N. Dixon, P. Loffler, L. Schnieder and K. H. Welge, *Journal of Chemical Physics*, 1998, **108**, 519–526.

[173] M. Peric and S. D. Peyerimhoff, *Journal of Chemical Physics*, 1995, **102**, 3685.

[174] S. Pratt, P. Dehmer and J. Dehmer, *Journal of Chemical Physics*, 1993, **99**, 6233–6244.

[175] S.-J. Tang, Y.-C. Chou, J. J.-M. Lin and Y.-C. Hsu, *Journal of Chemical Physics*, 2006, **125**, 133201.

[176] G. Herzberg, *Molecular Spectra and Molecular Structure Volume II: Infrared and Raman Spectra of Polyatomic Molecules*, Krieger Publishing Company, Florida, 1991.

[177] P. Rupper and F. Merkt, *Review of Scientific Instruments*, 2004, **75**, 613.

[178] J. Yang and Y. Mo, *Journal of Physical Chemistry A*, 2006, **110**, 11001–11009.

[179] M.-F. Jagod, M. Rosslein, C. M. Gabrys, B. D. Rehfuss, F. Scappini, M. W. Crofton and T. Oka, *Journal of Chemical Physics*, 1992, **97**, 7111–7123.

[180] G. Herzberg, *Molecular Spectra and Molecular Structure III: Electronic Spectra and Electronic Structure of Polyatomic Molecules*, Van Nostrand Reinhold Company, New York, USA, 1966.

[181] J. K. G. Watson, *Journal of Molecular Spectroscopy*, 2001, **207**, 276–284.

[182] J. E. Reutt, L. S. Wang, J. E. Pollard, D. J. Trevor, Y. T. Lee and D. A. Shirley, *The Journal of Chemical Physics*, 1986, **84**, 3022–3031.

[183] L. Avaldi, G. Dawber, R. I. Hall, G. C. King, A. G. McConkey, M. A. MacDonald and G. Stefani, *Journal of Electron Spectroscopy and Related Phenomena*, 1995, **71**, 93 – 105.

[184] A. N. Petelin and A. A. Kiselov, *International Journal of Quantum Chemistry*, 1972, **6**, 701.

[185] J. Pitarch-Ruiz, J. Sanchez-Marin and D. Maynau, *J. Comput. Chem.*, 2003, **24**, 609.

[186] P. Hockett and K. L. Reid, *Journal of Chemical Physics*, 2007, **In Press**, year.

[187] M. N. R. Ashfold, R. N. Dixon, R. J. Stickland and C. M. Western, *Chemical Physics Letters*, 1987, **138**, 201 – 208.

[188] R. J. S. Morrison, W. E. Conaway and R. N. Zare, *Chemical Physics Letters*, 1985, **113**, 435 – 440.

[189] G. Reiser, W. Habenicht and K. Müller-Dethlefs, *The Journal of Chemical Physics*, 1993, **98**, 8462–8468.

[190] D. T. Cramb and S. C. Wallace, *The Journal of Chemical Physics*, 1994, **101**, 6523–6528.

[191] S. R. Langford, A. J. Orr-Ewing, R. A. Morgan, C. M. Western, M. N. R. Ashfold, A. Rijkenberg, C. R. Scheper, W. J. Buma and C. A. de Lange, *The Journal of Chemical Physics*, 1998, **108**, 6667–6680.

[192] D. Rolland, *Ph.D. thesis*, University of Oxford, 1999.

[193] J. A. Fiss, A. Khachatrian, K. Truhins, L. Zhu, R. J. Gordon and T. Seideman, *Physical Review Letters*, 2000, **85**, 2096–2099.

[194] C. Nicole, I. Sluimer, F. Rosca-Pruna, M. Warntjes, M. Vrakking, C. Bordas, F. Texier and F. Robicheaux, *Physical Review Letters*, 2000, **85**, 4024–4027.

[195] H. L. Offerhaus, C. Nicole, F. Lepine, C. Bordas, F. Rosca-Pruna and M. J. J. Vrakking, *Review of Scientific Instruments*, 2001, **72**, 3245–3248.

[196] F. Lépine, C. Bordas, C. Nicole and M. J. J. Vrakking, *Physical Review A*, 2004, **70**, 033417.

[197] M. J. Seaton, *Reports on Progress in Physics*, 1983, **46**, 167–257.

[198] M. J. Seaton, *Monthly Notices Of The Royal Astronomical Society*, 1958, **118**, 504–518.

[199] C. Greene, U. Fano and G. Strinati, *Physical Review A*, 1979, **19**, 1485–1509.

[200] C. Greene and C. Jungen, *Advances in Atomic and Molecular Physics*, 1985, **21**, 51–121.

List of Figures

1.1 Photoelectron spectra and calculated spectra for HBr. (a) Ionization from $f^3\Delta_2(v=0)$ Rydberg state, prepared via $S(9)$ rotational transition, (b) corresponding *ab initio* result; (c) Ionization from $F^1\Delta_2(v=0)$ Rydberg state, prepared via $Q(10)$ rotational transition, (d) corresponding *ab initio* result. Figure reproduced from ref. [9]. 14

1.2 Schematic of the convergence of Rydberg series to different (rotational) states of the ion. Figure reproduced from ref. [12]. 15

1.3 (a) & (b) ZEKE results for ionization of of HCl via $F^1\Delta_2(v=0)$ Rydberg state, prepared via $S(0)$ rotational transition, (c) calculated spectrum for the same transition, (d) ZEKE results for different pump transitions as labelled. Spectra (a) and (d) reproduced from ref. [5], (b) & (c) from ref. [10] (original data for (b) was reported in ref. [21]). 17

1.4 Schematic of the VMI set-up. The electrostatic lens focuses the Newton spheres onto the microchannel plates as a function of their initial velocity. Note that the action of the lens also compresses the Newton spheres in the y-direction. The 2D projection of the original 3D distribution is visualized by the phosphor screen. 19

1.5 Illustration of electrostatic potential surfaces for (a) single-centre system, (b) four-centre linear system, (c) four-centre non-linear system. Potentials shown in (b) and (c) are highly anisotropic at short-range, but tend to pure Coulomb potentials asymptotically. 24

1.6 $\mathrm{N}(1s^{-1})$ and $\mathrm{O}(1s^{-1})$ MF-PADs at 418.3 eV and 550.5 eV, for a molecule aligned parallel, perpendicular, at the magic angle (54.7°) with respect to linearly polarized light, and for a molecule aligned perpendicular to the propagation axis of right-circularly polarized light. Reproduced from ref. [92]. 25

1.7 Calculated PADs for (2+1) ionization of sodium. Laser intensities are given in MW/cm^2. Reproduced from ref. [110]. 28

2.1 (a) Spatial coordinates. (b) Angular momentum vector diagrams. 33

2.2 Lab frame alignments after (a) one-photon excitation, (b) two-photon excitation. In all cases $J_g = 10$ In most cases ΔK does not affect the alignment, the exception being the case for $\Delta J = 0$, $\Delta K = 0$ which is forbidden in the one-photon case. 38

3.1 VMI spectrometer schematic and images. 51
3.2 (Left panel) Comparison of different electrostatic lens configurations. (Right panel) Action of velocity-mapping electrostatic optics. Particles are velocity-mapped at the focal plane. Right panel reproduced from ref. [39]. 52
3.3 (a) MCP chevron stack operation, based on ref. [150]. (b) Detector response and limiting cases, see text for details. 55
3.4 Characteristics of a VMI lens. R is the ring radius, S the residual spread in position, N the magnification factor and V_e/V_r the velocity-mapping voltage ratio. All quantities are plotted versus L, the length of the flight tube (or, equivalently, the distance of the detector from the ionization region). In all cases the ionization region was modelled as a line-source with Gaussian intensity distribution width 2.12 mm, V_r =1000 V and E_{KE} =1 eV. The laser focus was set at $p = 0.5$, defined as half-way between the repeller ($p = 0$) and extractor plates ($p = 1$) for (a) and (b), but was varied in (c) and (d). Reproduced from ref. [39]. Note that the axes are defined differently from the convention used in this thesis. 59
3.5 $\Delta E/E$ behaviour as a function of VMI voltages. The simulations used a source region 0.5x0.5x4 mm. Reproduced from ref. [155]. 60
3.6 Plots showing the behaviour of E and dE. (a) Analytic and (b) experimental. 61
3.7 Schematic of the experimental set-up for (a) 1-colour and (b) 2-colour work. 64

4.1 Simulated 3D & 2D photoelectron distributions. (Top) Image (a) shows the central slice through a 3D photoelectron velocity sphere for an isotropic angular distribution with a Lorentzian radial profile. Image (b) shows a 2D projection of the velocity sphere, using a 250 x 250 pixel array. (Bottom) Cuts through the central row ($z = 125$) of images (a) and (b), as marked in the images by the dashed line. Coordinate systems used in the text are defined, the general Cartesian axes (x, y, z) are the same as those previously defined (Figure 2.1), cylindrical coordinates (ρ, z) in the plane $z = z_n$, and polar coordinates (r, θ) in the plane of the detector. 70
4.2 Example of pBasex extracted radial and β_L spectra. Error bars are shown on the β_L data. In regions of low intensity in the radial spectrum, the β_L spectrum shows oscillatory behaviour and large error bars, this is a result of undefined angular functions in these regions. Over features in the radial spectrum the β_L values are well-behaved with small error bars; these regions provide meaningful anisotropy parameters over which an intensity-weighted average can be found, yielding the β_L parameters for the feature. 74

4.3 Illustration of inversion methods. (a) Raw photoelectron image; (b) Abel-inverted image; (c) pBasex inverted image. Data shown is from acetylene work (Chapter 5), $V_0^5 K_0^1 R_1$ pump transition. 75
4.4 Radial & angular data comparison for pBasex and Abel inversion methods. 76
4.5 Illustration of pixellation and fitting to pBasex extracted data. (a) Experimental data, fit and residual. (b) Lorentzian components of the fit, peaks marked * represent the position of known features which may underlie the intense peaks, but are ambiguous in this data. The quality of the fit is almost identical if they are omitted. Data shown is from ammonia work (Chapter 7), $v_2 = 4$, $1_1 \rightarrow 3_2$ pump transition. 78
4.6 Polar plots of PAD extracted from Abel and pBasex inverted data. (a) Abel data, extracted from the inverted image in 1° steps, and fitted form (equation 1.4). Centre-line noise has not been removed in the plot although it was ignored for the purposes of fitting. Error bars are plotted on each data point as $\sqrt{N}$. Note that the data is symmetrized by the inversion process. (b) pBasex derived PAD. Error bars are calculated from the uncertainties in each β_{LM} parameter and plotted at 12° intervals, but *do not represent data points*. PAD shown is 3_1 example from Figure 4.4(b). 79
4.7 Illustration of the conversion from $r \rightarrow E$ space for two identical Lorentzian peaks in r (velocity) space. Peak heights are preserved in the unscaled conversion, division by r normalizes the energy spectrum to peak area. . . 80
4.8 Illustration of χ^2 mapping and response. Data used is from ammonia, see chapter 8. 86

5.1 Overview of the (1+1) REMPI scheme used. 90
5.2 Vibrational modes and vibrational symmetry of C_2H_2 in linear and *trans*-bent geometries. Based on ref. [6]. 91
5.3 Composite REMPI scan over λ = 207 - 216.5 nm. Features are labelled by mode, quanta and K_i, e.g. $\mathbf{3}^5$ denotes $v_{3(i)} = 5$, and the sub-bands $K_i = 1, 2$ are marked. 94
5.4 Examples of experimental (blue) & simulated (red) REMPI spectra in the region of (a) $V_0^4 K_0^1$ and (b) $V_0^5 K_0^1$. Experimentally a 10% mixture of C_2H_2 seeded in Ar was used. In the simulations T_{rot} = 5 K. 95
5.5 REMPI spectra recorded using neat C_2H_2 in the region of the $V_0^4 K_0^1$ (top) and $V_0^5 K_0^1$ (bottom) bands. The data is shifted by 0.8 cm^{-1} to agree with the calculated line positions. 96
5.6 (top) Photoelectron images and recorded via pump transitions (a) $V_0^4 K_0^1 R_1$ (b) $1_0^1 V_0^2 K_0^1 R_1$ (c) $V_0^5 K_0^1 R_1$ (d) $V_0^6 K_0^1 R_1$. Non-linear intensity scaling has been applied to enhance the contrast of the outer features in images (b)-(d). (bottom) Photoelectron spectra extracted from the images. . . . 97
5.7 Photoelectron spectra recorded via pump transitions (a) $V_0^4 K_0^1 R_1$, (b) $1_0^1 V_0^2 K_0^1$, (c) $V_0^5 K_0^1 R_1$, and vibronic band assignments. 98

5.8 Photoelectron spectra in the region of $\mathbf{4}^{1}\,^{2}\Sigma_u^-$ vibronic band. Five different pump transitions, $V_0^4K_0^1(R_{1,3,5,7,9})$ are shown. For $J_i \geq 6$ rotational lines of alternate N_+ levels become partially resolved. 101
5.9 Photoelectron images recorded via pump transitions $V_0^4K_0^1(R_{1,3,5,7,9})$, and PADs correlated with the formation of the $\mathbf{4}^{1}\,^{2}\Sigma_u^-$ vibronic state of $C_2H_2^+$ (inner ring of the photoelectron images). PADs for pump transitions $V_0^4K_0^1(Q_{3,5,7})$ are shown in Figure 6.1. 101
5.10 Vibronically-resolved PADs recorded via the $V_0^5K_0^1R_1$ pump transition. Vibronic bands are labelled as detailed in the text, and * denotes PADs correlated with vibronic bands for which K_+= odd. 103
5.11 PAD response to pump transition for the $\mathbf{4^1}\,^{2}\Sigma_u^-$, $\mathbf{4^3}\,^{2}\Sigma_u^- + \mathbf{4^3}\,^{2}\Delta_u$ (lower component) and $\mathbf{4^4}\,^{2}\Phi_u$ vibronic bands. * Mixed with Q_1 and Q_2. 105

6.1 Experimental (solid lines) and fitted (dashed lines) PADs for the formation of the $\mathbf{4}^{1}\,^{2}\Sigma_u^-$ vibronic band following pump transitions $V_0^4K_0^1(Q,R)$. . . 110
6.2 Calculated PADs for pump transitions $V_0^4K_0^1$ (a) R_1, (b) R_5 (c) Q_2 and (d) Q_6. Intermediate state alignments are shown in terms of the relative population of M_i levels in each case. 112
6.3 Calculated rotationally-resolved PADs. (left panel) Major contributions to the calculated PAD for the lowest J_i (a) R-branch and (b) Q-branch pump transitions observed experimentally. (right panel) Calculated PADs for the J_i=4, (a) R-branch and (b) Q-branch pump transitions. 113
6.4 Comparison of calculated and experimental rotationally-resolved photoelectron spectra. (a) ZEKE spectra reproduced from ref. [175]. (b) & (c) Calculated rotational spectra with $l_{max} = 3$ and $l_{max} = 5$ respectively. (d) Photoelectron spectra from photoelectron images (see Chapter 5). (e) & (f) Calculated spectra as (b) & (c) but with broader peaks to match imaging data. 114
6.5 Experimental (a) and calculated (b) & (c) PADs as a function of K_+. Experimental PADs were recorded via the $V_0^5K_0^1R_1$ pump transition. Calculated PADs are shown for (b) all $r_{l\lambda} = 1$, all $\eta_{l\lambda} = 0$; (b) all $r_{l\lambda} = 1$, $\eta_{l\lambda} = 0$ except $\eta_{f(\lambda>0)} = \pi$. 119
6.6 Calculated rotational spectra for the $\mathbf{4}^{1}\,^{2}\Delta_u$ vibronic band. The spin-orbit splitting was set to -30 cm^{-1}. 122

7.1 Schematic of (2+1) and (2+1') REMPI via the $\widetilde{B}$-state. The rotational structure of each electronic state is illustrated, see main text for details. The highest occupied molecular orbital (HOMO) for the $\widetilde{X}^1A_1'$ state is also illustrated, as calculated using the Gaussian package. No calculations have been run for the $\widetilde{B}^1E''$ or $\widetilde{X}^2A_2''$ electronic states. 126
7.2 Ionization pathways from $\tilde{B}|v_2 = 4, 3_2\rangle$. Solid lines show the levels accessible in the rotational-spectator, or atomic-like, ionization model; dashed lines show rotational levels which may be accessed by scattering. 129

7.3 REMPI spectra. (a) $v_{2(i)} = 3$ region, (b) $v_{2(i)} = 4$ region. Transitions are labelled $N_{gK_g} \rightarrow N_{iK_i}$. Experimental data are shifted to match calculated line positions, see text for details. 132

7.4 Photoelectron images. (a) & (b) recorded via $\widetilde{X}^1A_1'|v_{2(g)} = 0, 1_0\rangle \rightarrow \widetilde{B}^1E''|v_{2(i)} = 4, 3_1\rangle$ pump transition, (c) via via $\widetilde{X}^1A_1'|v_{2(g)} = 0, 1_1\rangle \rightarrow \widetilde{B}^1E''|v_{2(i)} = 4, 3_2\rangle$. (a) Shows distortion due to insufficient detector shielding. (b) Image with good contrast. (c) Image showing poor contrast, but sharper features. 134

7.5 Photoelectron spectra recorded via $v_{2(i)} = 4$. (a) Imaging results, main spectrum from the image shown in Figure 7.4(c), inset spectrum from Figure 7.4(b). (b) Time-of-flight spectrum, reproduced from ref. [94]. (c) Spectrum recorded with magnetic bottle spectrometer, reproduced from ref. [7]. 135

7.6 PADs correlated with the $\Delta v = 0$ ionizing transition, recorded via $\widetilde{X}^1A_1'|v_{2(g)} = 0, J_K\rangle \rightarrow \widetilde{B}^1E''|v_{2(i)} = 4, J_K\rangle$ pump transitions. (a) Imaging results. (b) Time-of-flight results, reproduced from ref. [94]. 136

7.7 (a) Photoelectron image showing features originating from both 2-colour (regions 1 and 2) and 1-colour (rings 3 and 4) ionization processes ($V_r = 2700$ V, $V_e = 1874$ V; $\lambda_{pump} = 316.358$ nm, $\lambda_{probe} = 434$ nm). (b) As (a), but with $V_r = 160$ V, $V_e = 110$ V. This corresponds to region 1 in (a). Rotational features are resolved, and labelled N_{+K_+}. 138

7.8 Images recorded for different λ_{probe}. For (a)-(c) $V_r = 160$ V, for (d)-(e) $V_r = 200$ V. 139

7.9 Spectra extracted from the images shown in Figure 7.8. All spectra are normalized to the most intense feature. (a)-(d) show well defined rotational features. Rotational assignments, N_{+K_+}, are shown for (c), and the feature marked * in (e) can be tentatively assigned as 6_1. 140

7.10 Raw photoelectron images recorded via $\widetilde{X}^1A_1'|v_{2(g)} = 0, J_{gK_g}\rangle \rightarrow \widetilde{B}^1E''|v_{2(i)} = 4, J_{iK_i}\rangle$ pump transitions with $\lambda_{probe} = 431.3$ nm. VMI voltages were $V_r = 160$ V and $V_e = 110$ V. All images are shown to the same scale, and labelled $J_{gK_g} \rightarrow J_{iK_i}$. 142

7.11 Photoelectron spectra extracted from the images shown in Figure 7.10, recorded via $\widetilde{X}^1A_1'|v_{2(g)} = 0, J_{gK_g}\rangle \rightarrow \widetilde{B}^1E''|v_{2(i)} = 4, J_{iK_i}\rangle$ pump transitions with $\lambda_{probe} = 431.3$ nm. Rotational assignments are shown, long red lines and shorter green lines represent levels accessible from the $p\pi$ and $d\delta$ Rydberg components, respectively, in the no-scattering case. Short black lines represent rotational levels which can only be populated via scattering of the Rydberg or photoelectron as discussed in the main text. Experimental data is shifted by (-)12 cm^{-1} to match calculated line positions, this is equivalent to an offset in the laser calibration $\triangle\lambda_{probe} = 0.22$ nm. 143

7.12 PADs extracted from the photoelectron images shown in Figure 7.10. Pump transitions are labelled $J_{gK_g} \rightarrow J_{iK_i}$, ion assignments ($N_{+K_+}$) follow those in Figure 7.11. In cases where the PAD correlates with more than one rotational level the most intense transition is listed first, followed by possible unresolved features in parentheses (as listed in Table 7.1), or by partially resolved features prefixed by $+$. Colour coding also follows Figure 7.11, with $p\pi$ allowed and $d\delta$ allowed levels in red and green respectively. Levels which can only be populated by scattering are shown in *italics*. Features which are particularly weak in the spectrum are marked *, in these cases the PADs may be less reliable than indicated by the error bars. Tabulated β values can be found in Appendix C. 146

7.13 Rotationally-summed PADs corresponding to the photoelectron images shown in Figure 7.10. 147

7.14 Raw photoelectron images for pump transitions $\widetilde{X}^1A_1'|v_{2(g)}=0, J_{gK_g}\rangle \rightarrow \widetilde{B}^1E''|v_{2(i)}=3, J_{iK_i}\rangle$ and $\lambda_{probe}=431.3$ nm. 149

7.15 Photoelectron spectra extracted from the images shown in Figure 7.14, for pump transitions $\widetilde{X}^1A_1'|v_{2(g)}=0, J_{gK_g}\rangle \rightarrow \widetilde{B}^1E''|v_{2(i)}=3, J_{iK_i}\rangle$ and $\lambda_{probe}=431.3$ nm. Rotational assignments are shown, long red lines and shorter green lines represent levels accessible from the $p\pi$ and $d\delta$ Rydberg components, respectively, in the no-scattering case. Short black lines represent rotational levels which can only be populated via scattering of the Rydberg or photoelectron as discussed in the main text. For (e) rotational assignments have not been successful, peaks are instead labelled A-I for reference. 150

7.16 Photoelectron spectra extracted from the images shown in Figure 7.14, for pump transitions $\widetilde{X}^1A_1'|v_{2(g)}=0, J_{gK_g}\rangle \rightarrow \widetilde{B}^1E''|v_{2(i)}=3, J_{iK_i}\rangle$ and $\lambda_{probe}=431.3$ nm. 151

7.17 Raw images recorded at different λ_{probe}. 153

7.18 Spectra recorded at different λ_{probe}. 154

8.1 Comparison of spectra obtained from imaging, MATI (reproduced from ref. [30]) and ZEKE (reproduced from ref. [28]) for (a) $1_1 \rightarrow 3_2$ and (b) $1_0 \rightarrow 3_1$ pump transitions. Energy scales are reproduced from the source articles. The MATI & ZEKE spectra are recorded via $\tilde{B}|v_2=2\rangle$ and so are shifted relative to the imaging data recorded via $\tilde{B}|v_2=4\rangle$; rotational level spacing will also be slightly different. As shown in ref. [30] there is little change in rotational line intensities between spectra recorded via $v_2=2$ and $v_2=4$. 160

8.2 Experimental (solid lines) & fitted (dashed lines) PADs for $|0, J_K\rangle \rightarrow |4, J_K\rangle$ pump transitions. 163

8.3 Experimental (solid lines) & calculated (dashed lines) rotational spectra for $|0, J_K\rangle \rightarrow |4, J_K\rangle$ pump transitions. Calculations made use of the fitted dynamical parameters listed in Table 8.3. All rotational features are plotted as Lorentzians, width 5 cm^{-1} (FWHM). Peaks marked * are comprised of two unresolved rotational features, but because the intensities of these features were summed before plotting the spectrum the peak profiles are not correct. 164

8.4 Illustration of sensitivity of rotational spectra and PADs to dynamical parameters. All spectra are normalized by area. 168

9.1 Photoelectron wavefunction calculated with equation 2.40 and dynamical parameters for acetylene (Table 6.1), plot shows the angular part of $|\phi_e|^2$. 174

List of Tables

3.1 Typical operating voltages for MCP and phosphor screen 53

4.1 Evaluation of extracted β_{LM} parameters for (a) experimental and (b) simulated images. Uncertainties in pBasex results are shown in parenthesis, and parameters in italics have >50 % error and can be regarded as undefined. Uncertainties have not been calculated for the Abel derived results (see Section 4.1.4). 77

5.1 Vibronic state assignments. E_{vib} values are derived from Lorentzian peak fits to the experimental spectra, and averaged over all spectra obtained via the $V_0^5K_0^1$ and $1_0^1V_0^2K_0^1$ vibronic bands. Values in parentheses represent the error assigned from the standard deviation of this analysis. Literature values quoted from Pratt et. al. [174] show experimental uncertainties in parentheses; the values from Tang et. al. [175] have been rounded to zero decimal places and the quoted experimental errors are omitted at this level of accuracy, representing an error in the second decimal place. The values in the final column, taken from ref. [173], are from *ab initio* calculations and no uncertainties are given in the source article. 99

5.2 Normalized β_{LM} parameters for PADs correlated with the formation of the $4^1\,^2\Sigma_u^-$ vibronic band via $V_0^4K_0^1(J_i)$. Values in parentheses are errors in the final digit. Parameters shown in *italics* are undefined with respect to the experimental errors (> 50% error) and can be regarded as zero. . 102

6.1 Fitted dynamical parameters. $r_{l\lambda}$ are normalized such that the total cross-section is unity. $\eta_{l\lambda}$ are relative to $\eta_{p\sigma}$, which is fixed at zero. Γ_l represents the degree of parallel character, $r_{l\lambda}^2$ the partial cross-section and F_l the l-wave cross-section. 111

6.2 Calculated and experimental branching ratios (%) for $V_0^4 K_0^1$ R-branch (left) and Q-branch (right) pump transitions. For the R-branch CI are the full calculated results including $\Delta N = \pm 3$ features, *CII* shows calculated values excluding $\Delta N = \pm 3$ features and *CIII* shows calculated values after summing $\Delta N = \pm 1, \pm 3$ features. *CII* and *CIII* can be compared directly with the experimentally derived results, *CIII* should provide a better match for low J_i, and *CII* for higher J_i where $\Delta N = \pm 3$ features do not underlie the $\Delta N = \pm 1$ features. 115

6.3 Fitted dynamical parameters, as Table 6.1 but for $l_{max} = 5$. $r_{l\lambda}$ are normalized such that the total cross-section is unity. $\eta_{l\lambda}$ are relative to $\eta_{p\sigma}$, which is fixed at zero. Γ_l represents the degree of parallel character, $r^2_{l\lambda}$ the partial cross-section and F_l the l-wave cross-section. Uncertainties in the fit have not been calculated for these results, but will be of similar magnitude to those given for the $l_{max} = 3$ case shown in Table 6.1. These parameters were used to calculate the rotational spectra shown in Figure 6.4, panels (c) and (f). 116

6.4 Fitted dynamical parameters, as Table 6.1 but for fitting to three different datasets as discussed in the text. $\eta_{l\lambda}$ are relative to $\eta_{p\sigma}$, which is fixed at zero. $r^2_{l\lambda}$ is the partial cross-section (%) and F_l the l-wave cross-section (%). 121

7.1 Rotational line assignments. Calibration uncertainty in experimental results is estimated as ± 5 cm^{-1}. 144

8.1 Allowed partial wave parity (even/odd) for observed transitions with $v_{2(+)} = v_{2(i)} = 4$. (Left) *para*-NH_3, (right) *ortho*-NH_3. 158

8.2 List of rotational features which arise from scattering. Spectrum labels correlate with Figure 7.11. Observed intensities are denoted vw - very weak; w - weak; m - medium; s - strong. Correlation with odd/even-l is also shown. 5_2 assignment may be incorrect, see discussion in main text. 159

8.3 Fitted dynamical parameters. $r_{l\lambda}$ are normalized such that total x-section is unity. $r^2_{l\lambda}$ represent the partial x-sections for each $|l\lambda\rangle$ component, expressed as a percentage. F_l is the x-section for each l continua. Phases marked * are fixed as reference phases, one for even-l and one for odd-l. The phases are $\mathrm{mod}(360)$, the phase relationship between the odd and even continua, or the sign of the phases, cannot be deduced in this work. Components marked - are not allowed according to angular momentum coupling. 165

8.4 Magnitudes, $r_{l\lambda}$, of the radial dipole matrix elements reported in (i) ref. [31], and (ii) renormalized to include the $\widetilde{B}$-state character, as published in ref. [94]. Cross-sections F_l are also reproduced from ref. [94]. Quantum defects, $\mu_{l\lambda}$, used in refs. [31, 94], originally obtained from refs. [190, 191]. n is the principal quantum number for the Rydberg series for which $\mu_{l\lambda}$ was obtained. The final column shows the quantum defects redefined to match the phase convention followed in this work, in which even and odd-l are independent and terms * are set to zero. Note that these values do not include the Coulomb phases, so are not directly comparable with $\eta_{l\lambda}$. 170

B.1 β-parameters for R-branch pump transitions ($V_0^5K_0^1$ band). 185

B.2 β-parameters for P, Q-branch pump transitions ($V_0^5K_0^1$ band). *The Q_3 line is mixed, with a contribution from Q_1 and Q_2. 186

C.2 β_{LM} extracted from the images shown in figure 7.14, recorded via $\widetilde{X}^1A_1'|v_{2(g)} = 0, J_{gK_g}\rangle \rightarrow \widetilde{B}^1E''|v_{2(i)} = 3, J_{iK_i}\rangle$ pump transitions with $\lambda_{probe} = 431.3$ nm. 188

C.4 β_{LM} extracted from the images shown in figure 7.10, recorded via $\widetilde{X}^1A_1'|v_{2(g)} = 0, J_gK_g\rangle \rightarrow \widetilde{B}^1E''|v_{2(i)} = 4, J_iK_i\rangle$ pump transitions with $\lambda_{probe} = 431.3$ nm. 189